

TRIBOLOGICAL PERFORMANCE OF ASHLESS ANTIWEAR ADDITIVES
UNDER EXTREME PRESSURE CONDITIONS

by

BOHOON KIM

Presented to the Faculty of the Graduate School of
The University of Texas at Arlington in Partial Fulfillment
of the Requirements
for the Degree of

DOCTOR OF PHILOSOPHY

THE UNIVERSITY OF TEXAS AT ARLINGTON

December 2009

Copyright © by BOHOON KIM 2009

All Rights Reserved

DEDICATION

To my parents JungKuk Kim and YoungSik Kim for their endless belief and love to me

To my wife MinYoung Jeun for her eternal love, her outstanding support, and confidence to me

ACKNOWLEDGEMENTS

I would like to express the deepest appreciation to my advisor, Dr. Pranesh Aswath, who has the attitude and the substance of a genius: he continually and convincingly conveyed a spirit of adventure in regard to research and scholarship, and an excitement in regard to teaching. Without his guidance and persistent help this dissertation would not have been possible. I would like to thank my committee members, Dr. Roger Goolsby, Dr. Ronald Elsenbaumer, Dr. Yaowu Hao, and Dr. Daejong Kim for their encouraging words, thoughtful criticism, and time and attention during busy semesters.

I also wish to thank all the faculty members of the Department of Materials Science and Engineering at the University of Texas at Arlington for their generous sharing of their knowledge and resources throughout my graduate studies. I would like to thank the MSE staff, Mrs. Jennifer Standlee, who has always greeted and talked to me with a great smile and a warm heart and has been more than helpful in many instances, and Mrs. Libia Cuauhti for their assisting me with the administrative tasks necessary for completing my doctoral program. I am also grateful to Dr. Jiechao Jiang and Dr. David Yan for training on numerous equipments in the Characterization Center for Materials and Biology as well as their significant help and contribution with the TEM work. I thank the Hysitron Corporation for sharing of resources and expertise with regards to nano mechanical testing. I especially thank Dr. Yongfeng Hu and Dr. Lucia Zuin of the Canadian Light Source of the University of Saskatchewan, Canada and Dr. Narayan Appathurai of the Synchrotron Radiation Center of the University of Wisconsin at Madison for their technical support and help with the XANES studies. Special thanks to the Platinum Research Organization team, Mr. Cork Jaeger, Dr. Harold Shaub, Mr. Matt Hawkins, and Mr. David Owen for their practical guidance and sponsorship of this research effort.

I would like to thank with my heart to my former and current colleagues, Dage (elder brother) Xin Chen, Predating Artist Ramoun Mourhatch, Chatterbox Anuradha Somayaji, Cat Mom Hande Demirkiran, TLCL legend Mihir Patel, ZingZing Man Eray Erkan, Butterfly Arunya Suresh, Prude Hansika Parekh, HipHop Warrior Tonye Adeogba, Crybaby Beibei Wang, and Migratory Bird Shruti Gandhi in the Tribology Lubrication and Coating Lab. Also, my deepest gratitude goes to my Korean younger brothers in the MSE, Emil Boy HyunJu Zin, All Su Soo Kim, Lucky Boy JungMin Kim, One Bite HyunUk Kim, and Prospective Student JaeHo Jung and my friends in the MSE, Point Guard Liangshan Chen, Spoiled Boy Punnapob Punnakitikashem, Long Leg Shih-Hsin (Mark) Chang, Dragonfly Vishwas Bedekar, and others.

I am extremely grateful to Dr. JaeHoon Yu, Dr. Esther Yang, Dr. JeongBong Lee, and Dr. InMu Haw for showing me their sublime humanity and leadership as a senior in human life.

I am also greatly appreciating their excellent help, support, and love to my mentors, Mr. Brian Eberhard and Mrs. Dana Eberhard who show me the real charity and love to others, to my godfather Mr. SangWu Lee Abel who takes care of me like his son, and to my great friends JinSeok Lim, ManKyu Han, JunSeok Kim, SunHo Choi, HoChul Shin, InKee Hong, SeungHo Yoo, YeonHo Jang, SoYeop Kim, DongKyu Kim, KunHee Han, WoonKi Na, JeaGuan Kim, HyunMo Son, Maria Son, KwanTae Kim, and Sophia Lee, who love and trust me forever.

I would sincerely like to thank my two elder sisters, SeongHee Kim and KeunAh Kim, and their family, and my parents-in-law JungHwa Jeun and ByungSook Yoo, sister-in-law HaeWon Jeun, brother-in-law YiJun Jeun for their countless love and belief.

Last, I with true heart want to thank my parents, JungKuk Kim and YoungSik Kim, without whom I would never have been able to achieve so much. I really wish my father may get well soon and live longer with me. I want to express all my respects to them. I especially wish to express my love for my wife, MinYoung Jeun who only knows the real price of this dissertation as we suffered and paid it together. I thank for her endless love, patience, and understanding.

December 10, 2009

ABSTRACT

TRIBOLOGICAL PERFORMANCE OF ASHLESS ANTIWEAR ADDITIVES UNDER EXTREME PRESSURE CONDITIONS

BOHOON KIM, PhD

The University of Texas at Arlington, 2009

Supervising Professor: Dr. Pranesh B. Aswath

Zinc dialkyl dithiophosphate (ZDDP) has been used in engine oil for several decades as an antiwear additive. However, ZDDP is the primary source of P, S and Zn in the exhaust, which results in frequent maintenance or replacement of exhaust gas treatment systems. The use of ashless additives is more desirable because of recent environmental regulations.

The main goal of this research was to develop a fundamental understanding of how ashless compounds protect the tribological surface in comparison to ZDDP. X-ray absorption near edge structure spectroscopy (XANES) has been performed on tribo and thermal films in order to investigate the chemical properties of films generated from ashless antiwear additives like chemical structure as well as chemical composition. In order to achieve this objective, three approaches were used.

First, the relationships between ashless thiophosphates and wear properties under extreme pressure were examined. Ashless antiwear additives properly form their tribofilms on

the sliding steel surface, reacting with iron (Fe) which is originated from the substrate. The tribofilms consist of iron phosphates, iron sulfides, and iron sulfates that have lower reduced modulus and hardness compared to tribofilms from ZDDP. However, they are still sufficiently stiff to prevent asperity contact and provide antiwear behavior. In addition, the thickness of protective tribofilms formed with ashless thiophosphates was found to be thicker than the ones formed when ZDDP was used under identical tribological conditions.

Secondly, in order to understand the mechanism of tribofilm generation of metal free additives, a fundamental understanding of thermal decomposition of ashless antiwear chemistries and their influence on thermal film formation was derived. The decomposed P- and S- containing products of ZDDP reacted with the metal surface and their own metal cations forming thermal films. In case of metal free dithiophosphates, sulfur species initially formed on the surface very fast, and then, phosphate species formed and diffused into the thermal film. It was one of the reasons why DDP-2 had better antiwear protection. While, DDP-1 with low thermal stability suffered from the oxidation and hydrolysis of thermal film and oil, which was related with poor wear performance. The amine phosphate showed the cross-link of phosphates and the oxidation of thermal film (iron nitrate or nitrite), resulting in its stick-slip behavior and big wear volume. The distinction of wear performance of different chemistries could be interpreted by these different mechanisms of formation of thermal films.

Thirdly we examined how ashless fluorinated compounds may influence the formation and the characteristics of tribofilms and in proxy the wear properties. While the general form of the tribofilms were essentially the same with and without the presence of PTFE, an important distinction was the presence of a layer of PTFE on the surface of the tribofilm that prevented its oxidation of the tribofilm and yielded better wear performance.

TABLE OF CONTENTS

ACKNOWLEDGEMENTS	iv
ABSTRACT	vi
LIST OF ILLUSTRATIONS.....	xiii
LIST OF TABLES	xxi
Chapter	Page
1. INTRODUCTION	1
1.1 Motivation for This Research	3
1.2 Objectives of This Research	4
1.3 Structure of This Research	6
2. BACKGROUND	8
2.1 Boundary Lubrication	8
2.2 Lubricants and Lubricant Additives	10
2.3 Lubrication Mechanisms	13
2.3.1 Decomposition Mechanisms of Antiwear Additives	13
2.3.1.1 Thermal Degradation of ZDDP.....	14
2.3.2 Film Formation Mechanisms of Antiwear Additives	16
2.3.3 Review of Previous Studies for Tribofilms	18
2.4 Tribological Wear Tester	19
2.4.1 UTA-built BOCLE	20
2.5 XANES (X-ray Absorption Near-Edge Structure) Spectroscopy.....	21
2.5.1 Introduction of XANES	21
2.5.2 Principle of XANES	22

2.5.3 Data Acquisition of XANES	25
2.5.4 Previous Studies of XANES	26
2.6 Nano Mechanical Properties of Tribofilms	27
2.6.1 Principle of Nano-Indentation Test.....	27
2.6.2 Previous Studies of Nano Indentation.....	30
3. PROPERTIES OF TRIBOFILMS FORMED WITH ASHLESS DITHIOPHOSPHATE AND ZINC DIALKYL DITHIOPHOSPHATE UNDER EXTREME PRESSURE CONDITIONS	31
3.1 Introduction	32
3.2 Experimental Details.....	33
3.2.1 Materials and Tribological Test	33
3.2.2 Analysis of Tribofilm	35
3.3 Results and Discussion	37
3.3.1 Tribological Wear Data.....	37
3.3.2 Tribofilm Characterization Using Secondary Electron Microscopy and Energy Dispersive Spectroscopy	38
3.3.3 Comparison of FIB (Focused Ion Beam) Image	40
3.3.4 XANES (X-ray Absorption Near Edge Structure Spectroscopy) Analysis of Tribofilms.....	41
3.3.4.1 Phosphorus L edge XANES Spectral Analysis	41
3.3.4.2 Phosphorus K edge XANES Spectral Analysis.....	43
3.3.4.3 Sulfur L edge XANES Spectral Analysis	44
3.3.4.4 Sulfur K edge XANES Spectral Analysis.....	45
3.3.5 Transmission Electron Microscopy of Wear Debris from Tribological Tests.....	46
3.3.6 Mechanism of Formation of Oxide Nanoparticles in the Wear Debris	49
3.3.7 Nano-Indentation of Tribofilms	51
3.3.8 Nano-Scratch of Tribofilms.....	54

3.3.9 Scanning Nano-Wear Tests of Tribofilms	56
3.3.10 Phenomenological Model of Tribofilm Formation	56
3.4 Conclusion	57
4. TEM ANALYSIS OF WEAR DEBRIS FROM TRIBOLOGICAL TESTS: ASHLESS ANTIWEAR COMPOUNDS	59
4.1 Introduction.....	59
4.2 Experimental Details	61
4.2.1 Materials.....	61
4.2.2 Tribological Testing Procedure	62
4.2.3 Evaluation of Tribological Test.....	63
4.3 Results and Discussion.....	64
4.3.1 Analysis of Wear Properties.....	64
4.3.2 <i>SEM Analysis of Wear Track</i>	70
4.3.3 <i>TEM Analysis of Wear Track</i>	70
4.4 Conclusion.....	71
5. XANES ANALYSIS OF THERMAL FILMS FORMED FROM ASHLESS ANTIWEAR COMPOUNDS COMPARING WITH ZDDP: ASHLESS DIALKYL DITHIOPHOSPHATES	73
5.1 Introduction.....	73
5.2 Experimental Details.....	77
5.2.1 Materials and Sample Preparations.....	77
5.2.2 Data Acquisition and Analysis.....	78
5.3 Results and Discussion	79
5.3.1 Thermal Film Thickness.....	79
5.3.2 XANES Analysis of Thermal Film	83
5.3.2.1 Phosphorus Characterization.....	85
5.3.2.2 Sulfur Characterization.....	99
5.3.3 Surface Morphology	110

5.3.4 Mechanism of Thermal Film Formation and Phenomenological Model	112
5.4 Conclusion	125
6. ANES ANALYSIS OF THERMAL FILMS FORMED FROM ASHLESS ANTIWEAR COMPOUNDS COMPARING WITH ZDDP: ASHLESS AMINE PHOSPHATES.....	126
6.1 Introduction.....	126
6.2 Experimental Details	128
6.2.1 Materials and Sample Preparations.....	128
6.2.2 Data Acquisition and Analysis.....	129
6.3 Results and Discussion	130
6.3.1 Thermal Film Thickness.....	130
6.3.2 XANES Analysis of Thermal Film	132
6.3.2.1 Phosphorus Characterization.....	134
6.3.2.2 Nitrogen Characterization.....	142
6.3.3 Surface Morphology	143
6.3.4 Mechanism of Thermal Film Formation and Phenomenological Model	143
6.4 Conclusion	147
7. TRIBOLOGICAL AND XANES ANALYSIS OF TRIBOFILMS FORMED WITH NANOSCALE PTFE.....	149
7.1 Introduction.....	149
7.2 Experimental Details	150
7.2.1 Test Materials.....	150
7.2.2 Tribological Tests and Tribofilm Analysis.....	151
7.3 Results and Discussion	152
7.3.1 Tribological Performance	152
7.3.2 XANES Analysis of Tribofilm	155

7.3.2.1 Phosphorus and Sulfur Characterization	155
7.3.2.2 Zinc, Oxygen, and Fluorine Characterization.....	164
7.3.3 Morphology Analysis of Tribofilm	167
7.3.4 Mechanism and Phenomenological Model	168
7.4 Conclusion	174
8. CONCLUSION	175
REFERENCES	179
BIOGRAPHICAL INFORMATION	189

LIST OF ILLUSTRATIONS

Figure	Page
1.1 GF-5 Performance Requirements. GF-5 is an Upcoming Passenger Car Engine Oil Specification.	3
2.1 Stribeck Curve and Lubrication Regimes.....	9
2.2 Friction Surface Contact Model	10
2.3 Chemical Structure of Neutral Zinc Dialkyl Dithiophosphate (ZDDP)	14
2.4 Schematic of Lab-made BOCLE. (a) Loading Setup of the BOCLE: The Vertical Load is Applied Pneumatically from the Top of the Machine. The Vertical Load Cell Measures the Applied Load. The Fiction Load Cell Measures the Fiction Load. (b) Fiction Load Measurement: The Fiction Load Cell Measures the Horizontal Force Resisting the Rotation of the Steel Ring, Which is Applied in the Horizontal Direction on the Scuffing Ball	20
2.5 Schematic Illustration of an X-ray Absorption Spectrum, Showing the Structured Absorption of Both the XANES and the EXAFS	22
2.6 Typical Experimental Apparatus for XAS Measurements. Incident and Transmitted Intensities are Measured Using an Ion Chamber. A Variety of Detectors can be Used to Measure X-ray Fluorescence Intensity for Samples	23
2.7 The Photoelectric Effect, in which an X-ray is Absorbed and a Core-Level Electron is Promoted out of the Atom.	24
2.8 Decay of the Excited State: X-ray Fluorescence (a) and the Auger Effect (b). In Both Cases, the Probability of Emission (X-ray or Electron) is Directly Proportional to the Absorption Probability	25
2.9 Load Function and Load Displacement Curve. (a) Trapezoidal Load Function for Single Nano Indentation Test; It Consists of Loading, Holding, and Unloading Segments. (b) Load-Displacement Curve of Nano Indentation.....	28
3.1 Chemical Structures of (a) the Neutral ZDDP and (b) the Ashless DDP	34
3.2 Comparison of Tribological Data for Wear Tests with ZDDP and Ashless DDP at a Phosphorous Level of 0.1 wt %. (a) Coefficient of Friction as a Function of Number of Cycles and (b) Wear Volume at the End of the Test. Tests were Conducted under Boundary Lubrication with a 1/4 Inch Ball of WC on a 52100 Steel Cylinder. Contact Load is 24 kg for Duration of 15,000 Cycles.	36

3.3 Effect of Concentration of Phosphorous, Load, and Nature of Antiwear Agent on Wear Volume. All Tests were Conducted for Duration of 25,000 Cycles. (a) ZDDP and (b) Ashless DDP	38
3.4 Scanning Electron Microscope (SEM) Image of Wear Track and Energy Dispersive Spectroscopy (EDS) Using X-rays of Wear Track from (a) ZDDP and (b) Ashless DDP. Both Tests were Conducted at a load of 24 kg for Duration of 15,000 Cycles.	39
3.5 Focused Ion Beam (FIB) Cross-Section of the Tribofilm Formed at the End of the Test Conducted at a Load of 24 kg for 15,000 Cycles: (a) ZDDP Tribofilm and (b) Ashless DDP Tribofilm.....	40
3.6 XANES Spectra at the P L-edge of the Tribofilms Formed from ZDDP and Ashless DDP. The Spectra of the Model Compounds of Fe and Zn Phosphates are Superimposed: (a) Total Electron Yield and (b) Fluorescence Yield	42
3.7 XANES Spectra at the P K-edge of the Tribofilms Formed from ZDDP and Ashless DDP. The Spectra of the Model Compounds of Fe and Zn Phosphates are Superimposed: (a) Total Electron Yield and (b) Fluorescence Yield	43
3.8 XANES Spectra at the S L-edge of the Tribofilms Formed from ZDDP and Ashless DDP. The Spectra of the Model Compounds of Fe and Zn Sulfates and Sulfides are Superimposed: (a) Total Electron Yield and (b) Fluorescence Yield.....	44
3.9 XANES Spectra at the S K-edge of the Tribofilms Formed from ZDDP and Ashless DDP. The Spectra of the Model Compounds of Fe and Zn Sulfates and Sulfides are Superimposed: (a) Total Electron Yield and (b) Fluorescence Yield.....	46
3.10 Bright Field Transmission Electron Microscopy (TEM) of the Wear Debris Harvested at the Ends of a Wear Test Conducted with ZDDP at a Load of 24 kg for Duration of 5000 Cycles: (a) 20,000× Magnification Bright Field Image, (b) 200,000× Magnification Bright Field Image, and (c) Selected Area Diffraction Pattern of Wear Debris.	47
3.11 Bright Field Transmission Electron Microscopy (TEM) of the Wear Debris Harvested at the Ends of a Wear Test Conducted with Ashless DDP at a Load of 24 kg for Duration of 5000 Cycles: (a) 20,000× Magnification Bright Field Image, (b) 200,000× Magnification Bright Field Image, and (c) Selected Area Diffraction Pattern of Wear Debris.....	48
3.12 Gibbs Free Energy and Enthalpy of Formation of Different Oxides of Iron as a Function of Temperature.....	50
3.13 Ellingham Diagram for the Formation of Oxides as a Function of Temperature. Also, the Regions of Stabilities of the Various Different Oxides of Fe. are Shown in the Diagram.	51
3.14 Plots of (a) Hardness and (b) Reduced Modulus as a Function of Contact Depth for Peak Indentation Loads Ranging from 25 μN to 1500 μN for Tribofilms Generated from ZDDP and Ashless DDP in Mineral Oil.	52
3.15 Scratch Test with Ramp Force of 5000 μN on Tribofilms from ZDDP and Ashless DDP in Mineral Oil. (a) Lateral Force versus Lateral Displacement; (b) Coefficient of Friction versus Lateral Displacement, and (c) Vertical Applied Force versus Vertical Displacement.	53

3.16 Three-Dimensional Graphical SPM Images of the Tribofilm Surfaces after Scanning Wear Tests. The Three-Dimensional Wear Images and the Cross-Sectional Profiles: (a) of ZDDP and (b) of Ashless DDP.	55
3.17 Phenomenological Model of Tribofilms Constructed Based on SEM, EDS, FIB, Nano-Indentation, Nano-Scratch, Nano-Wear, and XANES Spectroscopy Data: (a) Ashless DDP Tribofilm and (b) ZDDP Tribofilm.....	58
4.1 Wear Properties of Six Different Ashless Antiwear Agents. a) Friction Coefficient of DDPs and AP, b) Friction Coefficient of TPPTs, c) Test Temperature of All Samples, and d) Profilometric Traces of the Wear Traces of All Six Tests	65
4.2 Wear Volume of All Six Ashless Antiwear Additives All Tested at a Load of 24Kg for a Period of 15000 Cycles. (* DDP-1 was measured at the failed point.).....	66
4.3 Secondary Electron Scanning Electron Microscopy Images of the Wear Track for Six Different Additives. Each Picture Consists of 25 KeV 200X SEM Image (Bigger Picture) and 10KeV 1,000X SEM Image (Smaller Picture). a) DDP-1, b) DDP-2, c) AP-1, d) A-TPPT, e) B-TPPT, and f) H-TPPT	68
4.4 TEM Images of the Wear Debris after 5000 Cycles Test for All Six Ashless Antiwear Additives. 20,000 X Low Magnification, 200,000 X High Magnification, and the Diffraction Pattern. a) DDP-1, b) DDP-2, c) AP-1, d) A-TPPT, e) B-TPPT, and f) H-TPPT	69
5.1 Cross-Section Images of Thermal Film Thicknesses Formed from Different Chemistries with the Variation of Time. a) the Thickness of Thermal Film of ZDDP, b) the Thickness of Thermal Film of DDP-1, and c) the Thickness of Thermal Film of DDP-2.....	81
5.2 Plots of Thermal Film Growth as a Function of Time. a) the Plots of Thermal Film Growth of Three Different Chemistries, b) the Logarithm of Thickness of Thermal Film Formed from ZDDP, c) the Logarithm of Thickness of Thermal Film Formed from DDP-1, and d) the Logarithm of Thickness of Thermal Film Formed from DDP-2.....	82
5.3 Cross-Section Images of Thermal Film Thicknesses Formed from Different Chemistries at 4 Hour.....	83
5.4 XANES Spectra of the TEY and FLY modes at the K edge of Phosphorus Model Compounds: $Zn_3(PO_4)_2$ and $FePO_4$	84
5.5 XANES Spectra of the TEY and FLY modes at the P K edge of Thermal Films Formed from ZDDP as Baking Time.	86
5.6 XANES Spectra of the TEY and FLY modes at the P K edge of Thermal Films Formed from DDP-1 as Baking Time	86
5.7 XANES Spectra of the TEY and FLY modes at the P K edge of Thermal Films Formed from DDP-2 as Baking Time.	88
5.8 XANES Spectra of the TEY and FLY modes at the P K edge of 4 hour Thermal Films Formed from ZDDP and Four Different Ashless Thiophosphates	88

5.9 XANES Spectra of the TEY and FLY modes at the L edge of Phosphorus Model Compounds. a) TEY and FLY modes of Model Compounds: $Zn_3(PO_4)_2$, $FePO_4$ and $Fe_4(P_2O_7)_3$, b) FLY mode of Raw Materials.	90
5.10 The Linear Background Subtraction and the Deconvolution of Polyphosphate Spectra of Three Model Compounds and Two Different Thermal Films: $Zn_{20}P_{33}O_{116}$, $Zn_3(PO_4)_2$, $FePO_4$, ZDDP 4 hour Thermal Film, and DDP-4 4 hour Thermal Film (from Top to Bottom).	91
5.11 Standard of Chain Length of Polyphosphate Using the a/c Ratio, Relative Peak (a) Intensity Normalized to Peak (c) at P L edge Spectra. a) Two Different Relative a/c Ratios of Various Chain Length of Zinc Polyphosphates, the Left Y Axis is Related to Height a/c Ratio and the Right Y Axis is for the Area a/c Ratio. b) Relative Height a/c Ratios of Iron Phosphate and Iron Pyrophosphate as Two Model Compounds of Iron Phosphate.....	92
5.12 XANES Spectra of the TEY and FLY modes at the P L edge of Thermal Films Formed from ZDDP as Baking Time	94
5.13 XANES Spectra of the TEY and FLY modes at the P L edge of Thermal Films Formed from DDP-1 as Baking Time	94
5.14 XANES Spectra of the TEY and FLY modes at the P K edge of Thermal Films Formed from DDP-2 as Baking Time.	95
5.15 XANES Spectra of the TEY and FLY modes at the P L edge of 4 hour Thermal Films Formed from ZDDP and Four Different Ashless Thiophosphates.	95
5.16 Chain Length Comparisons of Phosphate Films by a/c Ratio Comparison as Different Chemistries with Time. The Relative Ratios are Presented in order of ZDDP, DDP-1, DDP-2 and All 4 hour Thermal Films from Top to Bottom	97
5.17 XANES Spectra of the TEY and FLY modes at the S K edge of Model Compounds.....	98
5.18 XANES Spectra of the TEY and FLY modes at the S K edge of Thermal Films Formed from ZDDP with Baking Time.....	100
5.19 XANES Spectra of the TEY and FLY modes at the S K edge of Thermal Films Formed from DDP-1 with Baking Time.....	100
5.20 XANES Spectra of the TEY and FLY modes at the S K edge of Thermal Films Formed from DDP-2 with Baking Time.....	101
5.21 XANES Spectra of the TEY and FLY modes at the S K edge of 4 hour Thermal Films Formed from ZDDP and Four Different Ashless Thiophosphates	101
5.22 Example of K edge XANES Spectra where Both Phosphorus and Sulfur Coexist.....	102
5.23 Relative S/P Ratio-1 of All Thermal Films Generated from Various Thiophosphate Additives and the Percentage of Sulfide at Sulfur Species in Thermal Films. a) Relative S/P Ratio and Sulfide % of ZDDP and b) Relative S/P Ratio and Sulfide % of DDP-1,	105

5.24 Relative S/P Ratio-2 of All Thermal Films Generated from Various Thiophosphate Additives and the Percentage of Sulfide at Sulfur Species in Thermal Films. a) Relative S/P Ratio and Sulfide % of DDP-2, and d) Relative S/P Ratio and Sulfide % of 4 hour Thermal Films of Different Chemistries	106
5.25 XANES Spectra of the (a) TEY and (b) FLY modes at the S L edge of Model Compounds and (c) FLY modes at the S L edge of Unreacted Raw DDPs.	108
5.26 XANES Spectra of the TEY and FLY modes at the S L edge of Thermal Films Formed from ZDDP as Baking Time	109
5.27 XANES Spectra of the TEY and FLY modes at the S L edge of Thermal Films Formed from DDP-1 as Baking Time	109
5.28 XANES Spectra of the TEY and FLY modes at the S L edge of Thermal Films Formed from DDP-2 as Baking Time	110
5.29 XANES Spectra of the TEY and FLY modes at the S L edge of 4 hour Thermal Films Formed from ZDDP and Four Different Ashless Thiophosphates	110
5.30 Optic Images of Surface Morphology of 4 hour Baked Thermal Films Using the Optic Profilometer, Wyko NT 9100. Magnification is 100X. a) Bare Steel Surface, b) ZDDP 4 hour Thermal Film, c) DDP-1 4 hour Thermal Film, and d) DDP-2 4 hour Thermal Film	111
5.31 Phenomenological Model of ZDDP Thermal Films. Top Picture is 10 minute ZDDP Thermal Film and Bottom Picture is 4 hour ZDDP Thermal Film.....	115
5.32 Phenomenological Model of DDP-1 Thermal Films. Top Picture is 10 minute DDP-1 Thermal Film and Bottom Picture is 4 hour DDP-1 Thermal Film.....	120
5.33 Phenomenological Model of DDP-2 Thermal Films. Top Picture is 10 minute DDP-2 Thermal Film and Bottom Picture is 4 hour DDP-2 Thermal Film.....	122
5.34 Phenomenological Model of DDP-3 and DDP-4 Thermal Films. Top Picture is 4 hour DDP-3 Thermal Film and Bottom Picture is 4 hour DDP-4 Thermal Film.....	124
6.1 Common Chemical Structure of Amine Phosphate. Phosphate and Amine Group are Connected by Hydrogen Bond. a) Dibasic Amine Phosphate and b) Monobasic Amine Phosphate	129
6.2 Cross-Section Images of Thermal Film Thicknesses Formed from a) AP-1 and b) ZDDP	131
6.3 Cross-Section Images of Thermal Film Thicknesses Formed from Different Chemistries at 4 hour	132
6.4 Plots of Thermal Film Growth as a Function of Time. a) Plots of Thermal Film Growth of Three Different Amine Phosphate Chemistries and ZDDP, b) Logarithm of Thickness of Thermal Film Formed from AP-1, and c) Logarithm of Thickness of Thermal Film Formed from ZDDP	133

6.5 XANES Spectra of the TEY and FLY modes at the P K edge of Model Compounds: Zn ₃ (PO ₄) ₂ , FePO ₄ , and (NH ₄) ₂ HPO ₄	134
6.6 XANES Spectra of the TEY and FLY modes at the P L edge of Thermal Films Formed from AP-1 as Baking Time.....	135
6.7 XANES Spectra of the TEY and FLY modes at the P K edge of 4 hour Thermal Films Formed from Three Different Amine Phosphate Additives Comparing with ZDDP 4 hour Thermal Film	135
6.8 XANES Spectra of the TEY and FLY modes at the P L edge of Model Compounds as well as of Raw Amine Phosphate Additives. a) TEY and FLY Spectra of Model Compounds: Zn ₃ (PO ₄) ₂ , FePO ₄ , and (NH ₄) ₂ HPO ₄ and b) FLY Spectra of Three Different Amine Phosphate Raw Materials	137
6.9 The a/c Ratio Comparison of Model Compounds and Raw Materials at the FLY mode	137
6.10 XANES Spectra of the TEY and FLY modes at the P L edge of Thermal Films Formed from AP-1 as Baking Time.....	138
6.11 Example for Energy Shift of the White Line Peak Because of the Variation of Chain Length of Iron Phosphate. A Longer Chain Iron Polyphosphate Has Lower Energy Range of Main Peak.....	139
6.12 The a/c Ratio Comparison of AP-1 Thermal Films as a Function of Time as a Function of Time at the TEY and FLY mode.....	140
6.13 XANES Spectra of the TEY and FLY modes at the P L edge of 4 hour Thermal Films Formed from ZDDP and Three Different Ashless Amine Phosphates	140
6.14 The a/c Ratio Comparison as Different Chemistries at 4 hour. The Relative Ratios are Presented in order of ZDDP, AP-1, AP-2 and AP-3.....	141
6.15 XANES Spectra of the TEY and FLY modes at the N K edge of Model Compound, (NH ₄) ₂ HPO ₄ , and of 4 hour Thermal Films Formed from Three Amine Phosphates	141
6.16 Nitrogen K edge XANES Spectra of NO ₂ (Nitrite) and NO ₃ (Nitrate). N and O 1s Photo Emission Spectra for the Adsorption of NO ₂ on Polycrystalline Zinc at 100K	142
6.17 Topographical Surface Images (47 μm X 63 μm) of 4 hour Baked Thermal Films Using the Optic Profilometer, Wyko NT 9100. a) Bare Steel Surface, b) ZDDP 4 hour Thermal Film, c) AP-1 4 hour Thermal Film, d) AP-2 4 hour Thermal Film, and e) AP-3 4 hour Thermal Film.....	144
6.18 Phenomenological Model of AP-1 Thermal Films. Top Picture is 10 minute AP-1 Thermal Film and Bottom Picture is 4 hour AP-1 Thermal Film	146
7.1 a) the Chemical Structure of Polytetrafluoroethylene (PTFE) and b) the Schematic of a Functionalized PTFE Particle.....	151

7.2 A Plot of Wear Volume Data vs. Type of Formulations. Three Different Types of Antiwear Additives, ZDDP, F-ZDDP, and Acidic Ashless Dithiophosphate, were Tested with 0.08 wt% P in Base Stock with/without 0.33 wt % irradiated PTFEs. Test Condition: a 1/4" Ball of WC on a 52100 Steel Cylinder, 24Kg Applied Load, and 15,000 Cycles.....	152
7.3 XANES Spectra of the TEY and FLY modes at the Phosphorus L edge. a) TEY and FLY mode of Model Compounds: $Zn_3(PO_4)_2$, $FePO_4$, and $Fe_4(P_2O_7)_3$, b) TEY mode of Tribofilms Formed from Six Solutions, and c) FLY mode of Tribofilms Formed from Six Solutions.....	154
7.4 Relative a/c Ratios of P L edge TEY and FLY modes of Six Different Samples. The Height Intensity Ratio is Adopted like Previous Chapters	156
7.5 XANES Spectra of the TEY and FLY modes at the Phosphorus K edge. a) TEY and FLY mode of Model Compounds: $Zn_3(PO_4)_2$, and $FePO_4$, b) TEY mode of Tribofilms Formed from Six Solutions, and c) FLY mode of Tribofilms Formed from Six Solutions.....	157
7.6 XANES Spectra of the TEY and FLY modes at the Sulfur L edge. a) TEY and b) FLY mode of Model Compounds: Three Metal Sulfides and Three Metal Sulfates, c) TEY mode of Tribofilms Formed from Six Solutions, and d) FLY mode of Tribofilms Formed from Six Solutions	158
7.7 XANES Spectra of the TEY and FLY modes at the Sulfur K edge. a) TEY and b) FLY mode of Model Compounds: Three Metal Sulfides and Three Metal Sulfates, c) TEY mode of Tribofilms Formed from Six Solutions, and d) FLY mode of Tribofilms Formed from Six Solutions	160
7.8 Relative S/P Ratios of K edge TEY and FLY modes of Six Different Samples and the Percentage of Sulfide out of Whole Sulfur Containing Compounds	162
7.9 XANES Spectra of the TEY and FLY modes at the Zinc L edge. a) TEY and b) FLY mode of Model Compounds, c) TEY and FLY modes of Tribofilms Formed from ZDDP and F-ZDDP with and without PTFE	163
7.10 XANES Spectra of the TEY and FLY modes at the Oxygen K edge. a) TEY and b) FLY mode of Model Compounds, c) TEY mode of Tribofilms Formed from Six Solutions, and d) FLY mode of Tribofilms Formed from Six Solutions	166
7.11 XANES Spectra of the TEY and FLY modes at the Fluorine K edge. a) TEY spectra of F Model Compounds as well as Tribofilms Formed from Antiwear Additives with PTFE and b) FLY Spectra of F Model Compounds as well as Tribofilms Formed from Antiwear Additives with PTFE	167
7.12 Morphological Images of Tribofilms Formed from Six Formulations. a)~f) 200X SEM Image of Each Antiwear Additive with/without PTFE, g) 2000X SEM Image of Region-1, h) 2000X SEM Image of Region-2, i) 5000X SEM Image of Region-1, j) 5000X SEM Image of Region-2, k) 3D Optic Profilometer Image of Region-1, and l) 3D Optic Profilometer Image of Region-2 at Tribofilm from F-ZDDP with PTFE	169
7.13 Phenomenological Model of Tribofilms Formed from ZDDP / F-ZDDP in Absence and in Presence of PTFE. Top Picture is Tribofilm of ZDDP/F-ZDDP itself and Bottom Picture is Tribofilm of ZDDP/F-ZDDP with PTFE	172

7.14 Phenomenological Model of Tribofilms Formed from DDP-2 in Absence and in Presence of PTFE. Top Picture is Tribofilm of DDP-2 itself and Bottom Picture is Tribofilm of DDP-2 with PTFE..... 173

LIST OF TABLES

Table	Page
2.1 Lubricant Additives and Their Tasks and Examples	11
2.2 Specifications of BOCLE Tester.....	21
3.1 The Calculated d_{hkl} Spacings for the Ring Patterns Observed in Figure 3.10(c) and 3.11(c) Compared to Observed Values for Three Types of Iron Oxide.	48
4.1 The Chemical Structures and Properties for Six Different Antiwear Ashless Additives.....	62
5.1 Chemical Structures and Properties of Samples	76
5.2 Chemical Composition and Size of Steel Coupons	77
5.3 Inorganic Model Compounds for the Phenomenological Models	113
6.1 Properties of Ashless Amine Phosphates	129
7.1 Inorganic Model Compounds for the Phenomenological Models	170

CHAPTER 1

INTRODUCTION

The science of tribology has been part of human civilization since prehistoric times. However, the research into tribology as a field of science began in earnest in the 17th century with the development of axles and bearings. [1] Even though the scientific study of tribology has a long history, tribology is still in an imperfect science due to limitations in surface analytical techniques and major differences in experimental methods. [2] Recent rapid progresses in advanced analytical characterization tools and techniques over the last couple of decades have provided tribologists with many opportunities to develop a better understanding of tribology. [3,4]

Tribology, which deals with science of friction, wear, and lubrication, is concerned with interacting surfaces moving relative to each other. [5] Tribology is a multi-discipline field including mechanical engineering, materials science and engineering, chemical engineering, physics, chemistry among others. [6] In addition, tribology is a field of science which provides solutions to problems of great economic significance such as reliability, maintenance, and wear of technical equipment ranging from household appliances to spacecraft. [2]

The recent development of high performance machines has put significant demands on the development of lubricants and coatings to prevent catastrophic wear and reduce friction. [5] The internal combustion engine is no exception. The rapid development new technologies like fuel injection, electronic engine management, multi-valve engines, variable valve timing, and catalyst conversion have resulted in higher operating speeds, higher temperatures and severe mechanical stresses. [7] The appropriate choice of lubricants can mitigate the problems generated from harsher operating conditions in internal combustion engine by reducing the

extent of wear and friction increasing the durability of engine. In addition, stringent legislative regulations by the Environmental Protection Agency (EPA) for increasing fuel economy and reducing exhaust emissions have provided the stimulus for a number of studies aimed at improving the performance and properties of the lubricants in automobile engines. [8] Since catalytic converters became a part of exhaust systems in the 1970s, many studies have been aimed at developing formulations of engine oil to reduce the harmful tailpipe emission by reducing the amount of phosphorous and sulfur that tend to contribute towards the degradation of the life and performance of the catalytic converter. [9,10]

Today's GF-4 specification developed by ILSAC (International Lubricant Standardization and Approval Committee) in 2004 addresses some of the compositional limitations of oil: sulfur less than 0.5 weight % and phosphorus from 0.06 wt% min. to 0.08 wt% max.. [11] Recently, ILSAC GF-5 specification targeted for model year 2011 vehicles are expected to improve passenger car performance from the sparkplug to the tailpipe. [12] New lubricants must provide improvements relative to ILSAC GF-4 balancing three different categories; fuel economy and fuel economy retention, engine oil robustness, and protection of emission control systems. [13] Figure 1.1 shows representative performance requirements of engine lubricants. In particular, lubricant and additive industries are focusing on engine oil robustness and emission system durability. In addition as shown in figure 1.1, piston cleanliness, engine sludge protection and turbocharger protection are important aspects of engine performance that require optimization of engine oil formulation. This involves the judicious development and use of various additives because detergents and dispersants which are used to clean engine parts and prevent sludge buildup may have negative impacts on fuel economy by competing for metal surface with friction modifiers.[14] In case of emission system durability closely connected to the lifetime of catalytic converter, phosphorus retention in engine area and not in the emission system is emphasized even if the amount of elemental phosphorous has not been reduced from GF-4 level (0.06 wt% min ~ 0.08 wt% max). [14] It is desired to keep

phosphorus off the catalytic converter to reduce emission and to keep it in the engine to protect against wear. Therefore, new upgrades and technologies of antiwear additives and other lubrication additives suitable for this regulation are required.

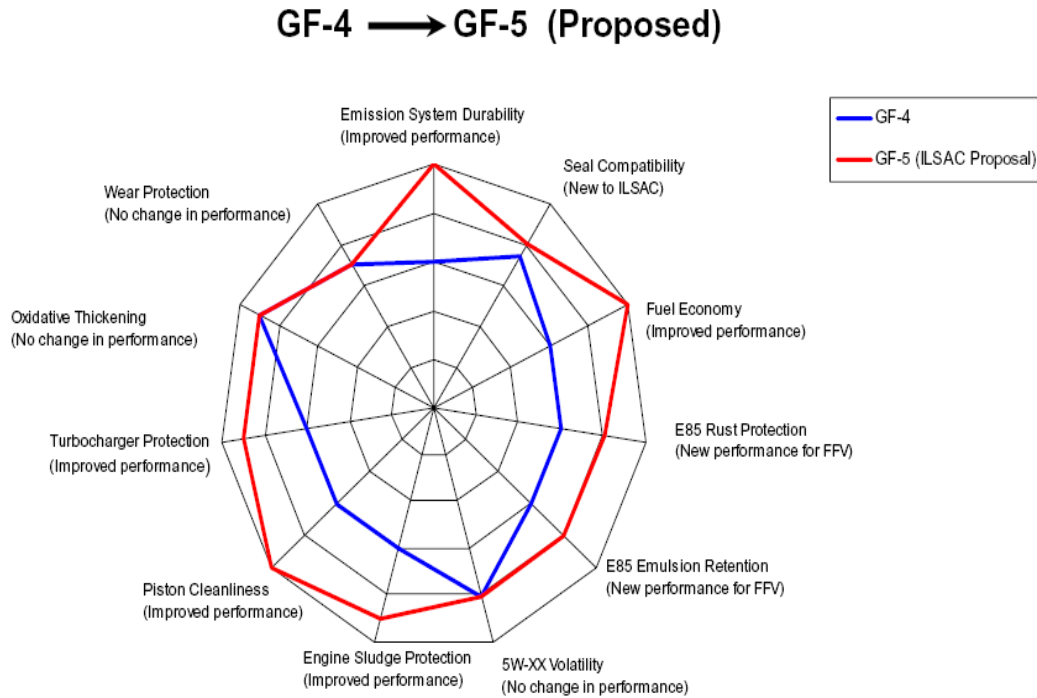


Figure 1.1 GF-5 Performance Requirements. GF-5 is an Upcoming Passenger Car Engine Oil Specification. [14]

1.1 Motivation for This Research

Zinc dialkyl dithiophosphates (ZDDP) have been widely used as an antiwear additive in engine oils since 1944 when the original ZDDP patents were filed. [15] ZDDP is outstanding at forming chemical reaction films at high temperatures and physisorbed films at lower temperatures on the surfaces. [16] ZDDP is also an economical antiwear additive compared to other additives. [17] However, in spite of these prominent merits, ZDDP has some drawbacks. The demerits of ZDDP are problems with toxicity, waste disposal, filter clogging, pollution, and deposition on the lubricated surfaces. [16] In particular, the antiwear additives with metal elements like Zn in ZDDP are susceptible to hydrolysis. Therefore, the contamination of the

engine oil with water can lead to the breakdown of the bond that holds zinc oxide. This reaction results in clogging filters, catalysts, and traps, depositing all ash forming elements on the surface of substrates, and degrading performance. [18] As a consequence, the pressure drop across the trap or the catalyst converter is increased and the harmful emissions aren't converted into the harmless products. This requires more frequent maintenance or replacement in order to keep high levels of effectiveness and durability in the various exhaust gas treatment systems. [19] The use of environmentally friendly ashless additives without any heavy metal elements is desirable because of the environmental and toxicological considerations. Development of metal-free additives is part of the new trend in engine oils these days. Therefore, the mechanism study of ashless antiwear additives in comparison to ZDDP becomes essential.

1.2 Objectives of This Research

Many researchers around the world have been actively involved in studying the antiwear behavior of ZDDP containing oils to understand the mechanism of tribofilm formation which has yet to be completed. Barnes [20], Spikes [21], and Nicholls and Kasrai [15] provided insight into the overall picture of ZDDP by their comprehensive reviews. Recently, advanced analytical characterization tools and techniques provide opportunities to elucidate the complicated chemistry of lubrication and the chemical nature of tribofilms generated from various lubricants. Many studies [22-26] have explained the mechanism of tribofilm formation and the chemical properties of tribofilms generated from ZDDP by using X-ray absorption near edge spectroscopy (XANES). Mourhatch and Aswath [27] and Pereira et al. [28] studied the mechanical properties of tribofilm of ZDDP by nano indentation. Martin [29] and Kasrai et al. [24,30] invaluablely found that the film has a bilayer structure with different chain length of phosphates. Mourhatch and Aswath [27] have recently provided valuable phenomenological model of tribofilm formed from ZDDP. In addition, Zhang et al. [4] and Najman et al. [31] studied

the mechanisms and the chemical and mechanical properties of tribofilm formed from ashless antiwear additives comparing with ZDDP. In spite of the wealth of information concerning the reaction behavior of ZDDP during wear, many questions about the mechanism of ZDDP still remain unresolved. The chemical mechanism of formation of the tribofilm, the reacting species for the tribofilm, tribofilm kinetics, etc. are still in the controversy. [21] Moreover, in case of ashless antiwear additives, many more questions about their tribological performance remain unanswered. The influence of hydrocarbon and functional groups on the tribological properties and the relationship among other additive species in addition to above same issues related to ZDDP are waiting to be solved. Therefore, the main goal of this research is to develop a fundamental understanding of how ashless compounds protect the tribological surfaces in comparison to ZDDP. In order to better understand the antiwear mechanisms of antiwear ashless additives, this study has been divided into three parts.

In the first part of this research, the relationship among ashless thiophosphates, amine phosphate, and triphenyl phosphorothionate chemistries and their wear properties under extreme pressure have been studied. The main intent in this section is to examine if the absence of cationic species in the antiwear additive has any influence on the formation of tribofilm. Normally, zinc cation of ZDDP has an important role to form an amorphous glass film consisting of phosphates and sulfides and to make tribofilms cross-link. [15,21] In this study, we will examine how metal-free antiwear additives form tribofilms on the surface of substrates, in particular under the extreme pressure. In addition, the role of sulfur in the chemistries and the influence of the chain length of alcohols on the formation of tribofilm will be examined. (in Chapter 3 and 4)

In the second part of this research, in order to better understand the comprehensive mechanism of tribofilm formation from metal free additives, fundamental issues related to thermal decomposition of ashless antiwear chemistries and their influence on thermal film formation will be studied. Jones and Coy [32] and H. Spikes [21] have suggested that the

tribofilm formation of ZDDP started from the thermal degradation of ZDDP. Fuller, Kasrai, and Bancroft [23] studied the thermal film formed from ZDDP by X-ray absorption spectroscopy. However, there is no study to explain the mechanism of formation of tribofilm generated from ashless antiwear additives with thermal degradation process. Thus, correlations between thermal film formation and antiwear tribofilm formation will be investigated in this section. (in Chapter 5 and 6)

The third section of study examines how ashless fluorinated compounds influence the formation and the characteristics of tribofilms and in proxy, the wear properties. Only a few studies, Palios et al. [33] and Rico et al. [34], have studied the effectiveness of PTFE powder as an antiwear additive in oil applications. However, nobody has so far proposed a clear mechanism of antiwear performance. In this study, the role of functionalized polytetrafluoroethylene (PTFE) as an ashless fluorinated compounds in wear protection and tribofilm formation will be investigated. The relationship between functionalized PTFE and ashless thiophosphates will also be examined and compared with the case of ZDDP. (in Chapter 7)

1.3 Structure of This Research

This dissertation consists of eight chapters. An outline and summary of each chapter are exposed here.

Chapter 1, introduction: This chapter introduces the motivation and objectives behind this whole research. It also provides the readers with brief concepts about tribology and the necessity of studying and improving the properties of antiwear additives and other lubrication additives.

Chapter 2, background: This chapter provides a detailed background on boundary lubrication, engine lubrication and antiwear additives, and the structure, chemistry and antiwear mechanism of ZDDP and other ashless additives. In addition, the tribological testing

methods and the characterization tools and principles are reviewed.

Chapter 3 compares the properties of tribofilms formed with ashless dithiophosphate and zinc dialkyl dithiophosphate under extreme pressure conditions. Both tribofilms of ash (or zinc) and ashless dialkyl dithiophosphates are comparatively analyzed using SEM, FIB, XANES, TEM, and nano mechanical tests.

Chapter 4 discusses TEM studies of wear debris generated from six ashless antiwear additives. First of all, tribological results tested with six ashless additives are analyzed, and then each wear debris generated during the tribological testing is tested under the conventional TEM in order to study the mechanism of formation of tribofilm and the creation of wear particles.

Chapter 5 examines the chemistry of thermal films formed from ashless dithiophosphate antiwear additives using XANES. Thermal films produced through thermal decomposition are studied in order to better understand the comprehensive mechanism of tribofilm generation. The nature of each thermal film in each different chemical group is identified using XANES analysis techniques.

Chapter 6 studies the chemistry of thermal films formed from ashless amine phosphate antiwear additives using XANES. The growth kinetics and chemical structure and information of thermal films are provided by XANES spectroscopy and SEM to help understand the film formation of metal and sulfur free additives.

Chapter 7 focuses on the role of functionalized PTFE in wear protection and tribofilm formation accompanied with ZDDP, Fluorinated ZDDP, and ashless dialkyl dithiophosphate (DDP). The tribological results for wear performance and the XANES analysis for chemical information of their tribofilms are presented and discussed.

Chapter 8: conclusions: This chapter concludes on the dissertation.

CHAPTER 2

BACKGROUND

2.1 Boundary Lubrication

A lubrication system is made up of moving surfaces under load with a lubricant in between. [35] The interposed lubricant film can be a solid like graphite, MoS_2 , a solid-liquid dispersion, a liquid, a liquid-liquid dispersion (greases) or under some special circumstances a gas. Lubricants have four major functions such as friction and wear reduction, heat removal, suspension of contaminants, and protection of oxidation and corrosion. [36] Lubrication is attained by utilizing the physical and chemical properties of the lubricating fluid. Physical properties such as density, viscosity, heat capacity, thermal conductivity, and the temperature–pressure–viscosity relationships determine the ability of the lubricant to operate under hydrodynamic or elastohydrodynamic lubrication. Chemical properties such as solvency, dispersancy, detergency, antiwear, anticorrosion, frictional properties, and antioxidant capacity are crucial to successful boundary lubrication. Some properties are controlled by the chemical composition of the base oils, and some properties are controlled by chemical additives designed for that purpose. [35]

There are three types of lubrication regimes in the lubrication area depending on different variables like load, amount of lubricant, surface roughness etc. In the early part of the 20th century, Stribeck presented the relationship between the friction coefficient (f) and viscosity of the lubricating oil (η), load (F_N), and velocity (V) using the Stribeck curve shown in figure 2.1. This curve succinctly explains the characteristics of different lubrication regions, including hydrodynamic lubrication, elastohydrodynamic lubrication and mixed lubrication, and boundary lubrication. [5]

In hydrodynamic lubrication like zone (C) in figure 2.1, the fluid completely isolates the friction surfaces [$h \gg R$, where h is the fluid film thickness and R is the surface roughness], and internal fluid mechanics alone determines tribological characteristics. In elastohydrodynamic lubrication [$h \approx R$] (zone (B)), fluid viscosity, the viscosity-pressure coefficient and the elastic coefficient of the solid surface are the most dominant factors. In contrast, the boundary lubrication mode [$h \rightarrow 0$ and $h < R$] in zone (A) is mainly characterized only by interactions in the contact between friction surfaces and the lubricant (including additives) instead of hydrodynamic effects of lubricating oil or rheological characteristics of bulk. [5]

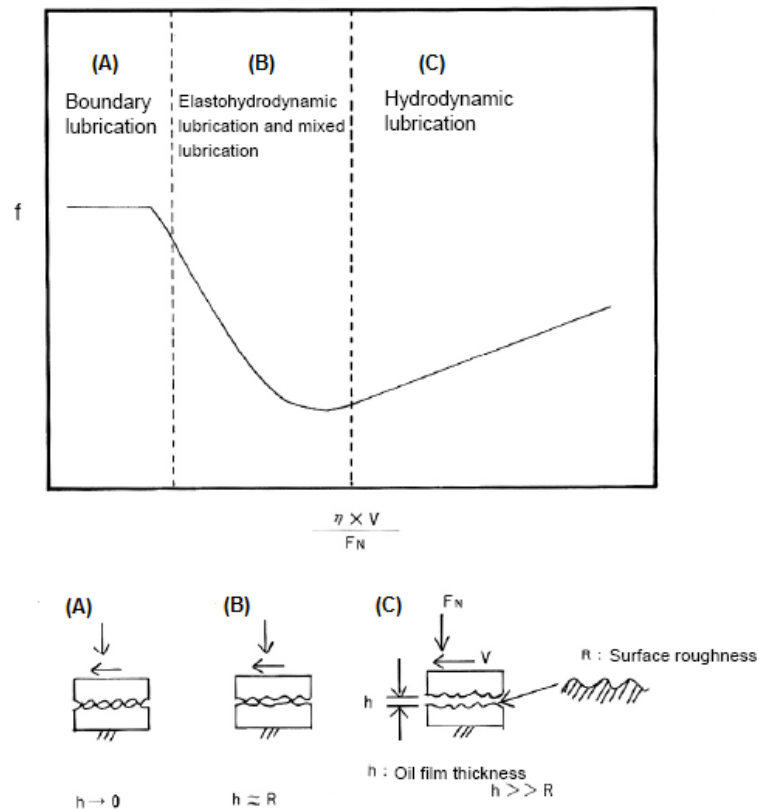


Figure 2.1 Stribeck Curve and Lubrication Regimes [5]

Boundary lubrication is defined as the lubrication regime where the average oil film thickness (h) is less than the composite surface roughness (R) and the surface asperities come into contact with each other under relative motion as shown in figure 2.2. [37,38] Under

boundary lubrication, asperities from one surface collide with the asperities of the other sliding surface. These collisions produce localized elastic and plastic deformations and sometimes fracture depending on the load and the material properties. These collisions accompany very high but short-lived local temperature excursions and create active abraded surfaces with very high surface energy. [2] Both flash temperatures and nascent surfaces can induce direct chemical reactions between the surface and the lubricants. Thus, the properties of lubricants and lubricant additives have critical influences upon the regime of boundary lubrication.

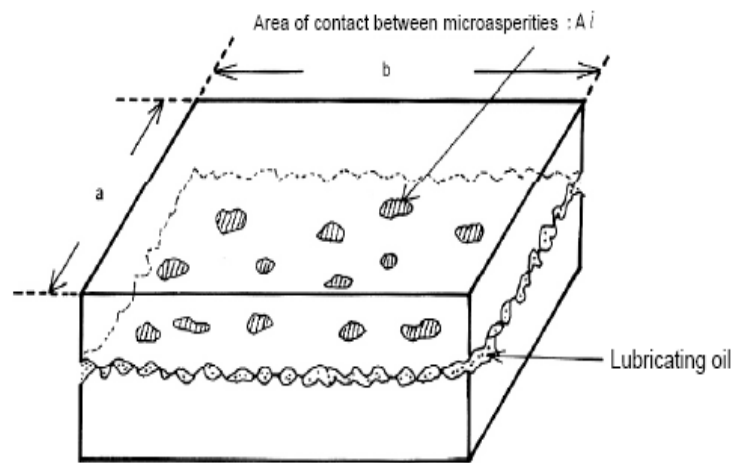


Figure 2.2 Friction Surface Contact Model [5]

2.2 Lubricants and Lubricant Additives

Lubricants play an important role in reducing the wear and friction and can potentially increase the efficiency and life of automobile engines. Additives are used to supplement the limitations of lubricants and to enhance the performance of base oils. [6] The bases oils as main lubricants must be viscous enough to maintain a lubricant film under operating conditions but should be as fluid as possible to remove heat and to avoid power loss due to viscous drag. It should also be stable under thermal and oxidative stresses, have low volatility and possess some ability to control friction and wear by itself. The ability to dissolve chemical additives but to be inert toward metal surfaces, rubber seals and gaskets are all very important characteristics.

[35] The common lubricants are base oils which are mineral oils derived from petroleum stock. In addition, synthetic oils artificially developed in order to provide superior oxidative properties are gradually replacing mineral base stocks. [2] Lubricant additives are added to oils in a small amount to improve the lubricating capacity and durability of the oil. Each lubricant additive has its own primary purpose. Table 2.1 shows each additive's role for the overall mechanism of lubrication in oils with common examples.

Table 2.1 Lubricant Additives and Their Tasks and Examples [2,22,39]

Lubricant Additive	Main Task	Examples
Antioxidants	Preventing peroxides and stabilizing radicals (enhancing oxidation stability of oil)	Alkylated Diphenol Amine, Hindered Phenol
Antiwear Additives	Preventing wear in mild condition	Zinc Dialkyl Dithiophosphate (ZDDP), Tricresylphosphate (TCP)
Extreme Pressure Additives	Preventing wear in severe condition	Dibenzylidisedisulphide, Sulfurized Derivatives, Molybdenum Disulphide
Adsorption or Boundary Additives	Preventing slip-stick phenomena	Sulphurized Fatty Acid Derivatives, Phosphonic Acids
Detergents	Protecting oils against sludge formation	Calcium Sulfonate
Dispersants	Dispersing particles	Polyisobutylene (PIB) Succinimide
Corrosion and Rust Inhibitors	Preventing corrosion or rust of engine surface and bearings	Barium Sulfonates, Calcium Phenates
Viscosity Index Improvers	Reducing difference in viscosities at different temperatures	Olefin Co-polymers, Polymethacrylates
Friction Modifiers	Performing lower friction behavior on surfaces	Organomolybdenum, Molybdenum Dithiocarbonates
Foam Inhibitors	Retarding the formation of foam in oil	Hydrogen and silicon compounds
Pour Point Depressants	Preventing the generation of wax crystals at low temperatures	Polymethacrylates

Antiwear properties are among the most important characteristics of lubricants. Wear can occur by reasons such as metal to metal contact, corrosion, and abrasion by solids and third bodies. Antiwear additives are designed to reduce wear when the sliding surfaces are exposed to low or moderate pressures, while extreme pressure additives work in a more severe pressure environment. [22] Tonck et al. have categorized two different types of antiwear behaviors depending on the chemical nature of the antiwear additives. [40] First antiwear action is the tribochemical reaction leading to formation of tribofilms by chemical reaction processes involving an active participation of both the contact surface material(s) and environmental factors (atmosphere, water etc) and their chemical interaction with the antiwear additive. In this case depending on the type of the additives, two types of mechanisms are observed [40]:

- a. Additives chemically react with the surface directly, e.g. sulfur and chlorine chemical compounds, fatty acids, fluorinated compounds.
- b. Antiwear action by the additives occurs through thermal and/or oxidative degradation process of the additive e.g. metal dithiophosphates (ZDDP or MoDDP) and phosphorus containing organic compounds.

Second category is about polymeric and non-sacrificial films. In this case, contact surfaces do not chemically participate in the formation of the antiwear film, although they may catalyze the process. This process also involves formation of high molecular weight compounds through polymerization process with complex esters, solid lubricant additive like oil soluble molybdenum compounds, borate additives, double bond containing molecules, polytetrafluoroethylenes (PTFEs), etc.

There are several different types of antiwear additives that are currently used in oil formulations. Usually phosphorus additives like zinc dialkyl dithiophosphate (ZDDP), ashless dialkyl dithiophosphate, and other phosphate esters are used as antiwear additives. Of all antiwear additives, zinc dialkyl dithiophosphate has so far been the most commonly used in the engine oil due to its excellent antiwear and anti-oxidant properties while ashless dialkyl

dithiophosphates, phosphates esters, and amine phosphates have recently been used as possible replacements to ZDDPs. Like ZDDP, these phosphorus additives function by chemisorptions to the operating surface. [2] As one of friction reducers, PTFE oil additives with particle size below 20 micron size in suspensions in a liquid carrier are used in commercial engine lubricants for examples, Slick 50, Lubrilon, etc. The PTFE invented by DuPont provides the lowest friction coefficient of all solid compounds (lower than 0.2). Because static friction coefficient and dynamic one are nearly identical, it doesn't have stick-slip effect on the surface. [41] This property makes PTFEs the most suitable solid lubricant in engine application.

2.3 Lubrication Mechanisms

In this section, some mechanisms accepted commonly for the decomposition of antiwear additives and the film formation mechanisms proposed by some researchers will be reviewed. With large amount of research efforts, there are a number of decomposition mechanism studies and tribological film formations related to zinc dialkyl dithiophosphates (ZDDPs) while very few studies have been conducted on ashless antiwear additives. Thus, the decomposition mechanisms and the film formation mechanisms of ZDDPs will mainly be introduced here and then the previous studies related to tribofilms generated from antiwear additives will briefly be presented in the end of section.

2.3.1. Decomposition Mechanisms of Antiwear Additives

Even though many studies have tried to resolve the decomposition mechanism of antiwear additives, especially ZDDP, none of them are comprehensive due to the complex chemistry of the additive and variants that exist together with multiple test methodologies and characterization techniques in use. [21,32,42,43] Different mechanisms have been proposed for the same end products identified by different authors. Thermal degradation, surface adsorption, oxidation by hydro peroxide, radical reactions, hydrolysis, and chemical reaction with FeO and oxygen in the air, or a combination of the above are some examples of the proposed

mechanism. [15] All proposed mechanisms have reached one important conclusion that decomposed products of antiwear additives are glassy and insoluble products which consist mainly of phosphates with some amount of sulfides, even if they are produced by different decomposition processes. This study is based on the thermal degradation mechanism of ZDDP. Hence, the thermal decomposition mechanism is reviewed here.

2.3.1.1 Thermal Degradation of ZDDP

ZDDPs are degraded at high temperatures by thermal or thermo-oxidative process resulting in zinc phosphates, alkyl sulfides, mercaptans, hydrogen sulfide, and olefins. [32] The mechanism of thermal decomposition of ZDDP was examined in 1981 by Coy and Jones with using NMR spectroscopy and later summarized by Spikes in his comprehensive review. [21] In order to elucidate the thermal decomposition process of ZDDP, the chemical structure of neutral ZDDP is presented in figure 2.3.

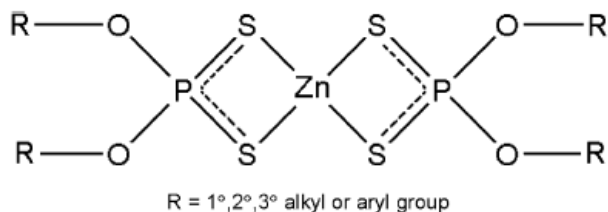
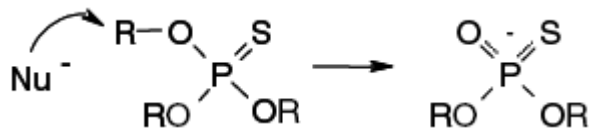


Figure 2.3 Chemical Structure of Neutral Zinc Dialkyl Dithiophosphate (ZDDP) [15]

The exchange of alkyl groups between S and O in ZDDP molecules is the initial reaction. A key chemical feature of organo thiophosphates is that they become strong alkylating agents which are reacting with a nucleophile Nu⁻ of the form in equation 2.1. Autocatalytic realkylation occasionally occurs after this reaction like equation 2.2. Mercaptides are appropriate nucleophiles.

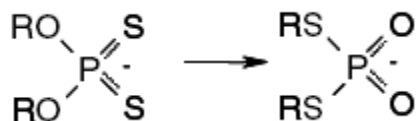


Equation 2.1 Nucleophilic Attack [21,32]



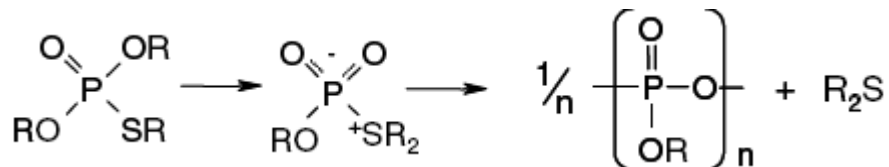
Equation 2.2 Realkylation [21,32]

Sometimes, thiophosphates alkylate themselves without any other nucleophiles. Dithiophosphates, $(RO)_2PSS^-$ are also strong alkylating agents and they cause the O/S exchange leading to dithionylphosphate, $(RS)_2POO^-$ in equation 2.3. In this alkylation reaction, alkyl groups can be easily exchanged between different molecules at high temperature.



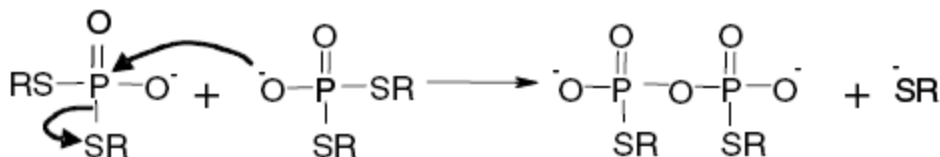
Equation 2.3 O/S Exchange [21,32]

As shown in equation 2.4, RS groups in thionyl or dithionyl phosphates are easily removed by attack of a phosphoryl group from neighboring molecule to form a polyphosphate.

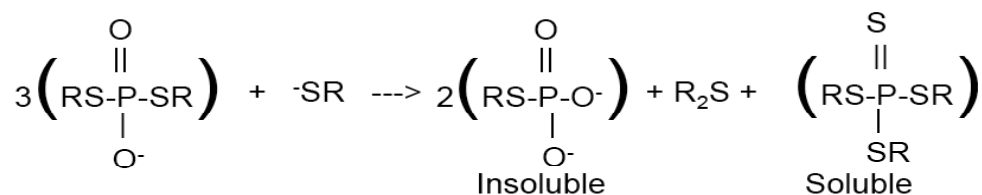


Equation 2.4 Formation of Polyphosphate [21,32]

Also, the dithiophosphate generated from self-alkylation reaction polymerize to form the polythiophosphate, which result from nucleophilic attacks from other dithionylphosphates and phosphonium species (RS^-) like equation 2.5 and 2.6. Then, sulfur elements are eliminated by hydrolysis or the formation of an ultraphosphate network glass.



Equation 2.5 Formation of Polythiophosphate-1 [21,32]



Equation 2.6 Formation of Polythiophosphate-2 [21,32]

All reactions start from the fact that the sulfur in thiophosphoryl prefer to bond to tetrahedral carbon and sub-group metals, while oxygen likes to react with protons and phosphorus. Thus, these reactions replace P-S, P=S and C-O bonds by C-S, P-O, and P=O bonds. Finally, the decomposition products from the degradation of ZDDP in oil solution consist of polyphosphates and a mixture of alkyl sulfides. [21,32]

2.3.2. Film Formation Mechanisms of Antiwear Additives

Some insights on the film formation mechanisms are deduced from chemical reaction of degradation products from ZDDPs. Spedding and Wakins in their studies showed that the hydrolytic decompositions products of ZDDP are chemically absorbed on the metal surface while ZDDP itself isn't. In addition, they found that these decomposed products act as the precursors of antiwear action of ZDDP by interacting with metal surface. These precursors become fusible glassy compounds including phosphate, sulfide, and iron oxide as a ternary eutectic to give the antiwear performance. [43,44]

Willermet et al. [42] have proposed the most detailed mechanism for film formation of ZDDP. Their suggestion is a four-step process such as follows:

1. Adsorption of ZDDP on metallic surfaces.
2. Reaction of ZDDP with the metallic surface to form species of phosphates and phosphothionic moieties bound to the metal surface.
3. Formation of phosphate film precursors from antioxidant reactions of ZDDP.

4. Condensation of the phosphates/phosphothionates species occur and are then terminated by zinc-containing compounds or other metal ions in solution (such as from detergents).

The authors conclude that phosphates are formed through oxidative decomposition process.

Yin et al. [24,45] modified Willermet's mechanism slightly and proposed a new three-step thermo-oxidative process mechanism using XANES analysis.

1. ZDDP is physisorbed on steel.
2. Thermal-oxidative process with oxygen or organic peroxides (from the oxidation of hydrocarbon base oil) results in the decomposition of ZDDP producing zinc metaphosphate (a long chain polyphosphate), $\text{Zn}(\text{PO}_3)_2$, and small amounts of zinc sulfides.
 - 3a. The formation of pyrophosphates (FeZnP_2O_7).
 - 3b. The formation of orthophosphates ($\text{Fe}_2\text{Zn}(\text{PO}_4)_2$).

If the temperature is high or if there is a lack of metal ions in solution, step 2 at fast reaction rate, which involves the formation of metaphosphates, governs. However, if the reaction is slow owing to low reaction temperatures or an abundance of iron and zinc cations, then step 3a and 3b are proceeding to form pyrophosphates or orthophosphates. The authors suggested that long chain polyphosphates form first and then with extended rubbing short chain polyphosphates form by interacting with the metal cations while Willermet et al. [42] suggested that short chain polyphosphate form first and then long chain polyphosphate is next by polymerization.

Suominen-Fuller et al. [23] slightly modified the three step film formation mechanism of Yin to a five step mechanism for the decomposition of ZDDP and the formation of a polyphosphate film on steel by using XANES spectroscopy. The authors proposed the presence of intermediate phosphate isomers, named as a linkage-isomer (LI), in solution.

1. ZDDP is adsorbed onto the metal surface.

2. ZDDP (in solution) is converted to phosphate intermediate termed Linkage Isomer (in solution).
3. LI (in solution) is adsorbed to the metal surface.
4. Thermal-oxidation of adsorbed LI and ZDDP occurs by either O₂ or ROOH to form long-chain polyphosphates Zn(PO₃)₂.
5. With continued rubbing, in the presence of water from the base oil, hydrolysis of polyphosphates occurs, creating short-chain polyphosphates.

The authors also proposed that if step 3 occurs rapidly in the absence of ZDDP oil-soluble decomposition products, then colloidal and short chain polyphosphates dominantly form and deposit on the surface.

All the mechanisms presented above have important similarities although there are some significant differences. First, in all approaches ZDDP is in solution and any of its decomposition products chemically or physically adsorbs to the metal surface covered with oxide layers. Second is that thermal oxidative process happens to degrade antiwear additives like ZDDP. Third, final products, that is, tribological films are composed of phosphates and sulfur compounds. [46] To sum up, even if there are various mechanisms and theories proposed about antiwear reaction of antiwear additives, the fruitful agreements of film formation of antiwear additives have helped develop the understanding of how antiwear additives work.

2.3.3. Review of Previous Studies for Tribofilms

There have been many studies devoted to examining the nature of tribofilms formation from antiwear additives on steel substrates. [3,15,20,21,27,28,47,48] A number of studies on the composition and the chemical structure of tribofilm generated from antiwear additives are available. [4,22-24,45,47,49-53] This section reviews some of the previous studies on tribofilm formation.

Normally, tribofilms form at much lower temperatures than thermal films. Even at room temperature, tribofilms can be formed slowly. Typically the rate of film formation increases with

increasing temperature. [54] Tribofilms form on the rubbing areas in actual sliding conditions. [54,55] Tribofilms have similar chemical composition as thermal films, but are mechanically stronger. [23,30,56] They grow and stabilize to a thickness of about 50~150 nm on steel surfaces. [54,57] Tribofilms form initially as separate patches on steel surfaces and then gradually develop to form an almost continuous, but still pad-like structure that are separated by deep valleys. The pads consist mainly of glassy phosphates, with a thin metal polyphosphate in outer layer while with metal pyro or orthophosphate in the bulk. [29,45] In the case of tribofilm of ZDDP, it is revealed that the film has a bi-layer structure with long chain Zn polyphosphates at the surface and short chain polyphosphates in the bulk area. [4] The outer parts of the pad formed from ZDDP have mainly Zn cations but there is an increasingly large proportion of Fe towards the metal surface. [29] Within the pads there is negligible thiophosphate but sulfur is present as zinc sulfide. [21,30] On the metal surface below these pads there may be a sulfur-rich layer of zinc or iron sulfide. [58].

2.4 Tribological Wear Tester

A number of tribological testers have been designed and used in lubricant evaluation. There are many different factors to affect the outcome of a tribological test such as the characteristics of the testing materials, the type of lubricant, contact geometry, surface roughness, environment of the test (in air or nitrogen), and mechanical variables (load, speed, etc.). [27] Thus, designing and planning the tribological test are important in order to obtain reliable results which are close to real wear and friction data produced from real equipments. Even though tribological tests in laboratories are hardly realistic and representative of the real components and condition, laboratory-scale tests are good methods to predict the performance of various lubricants to a certain extent. [39] As dependable tribological models for evaluation of lubricity of engine oil, there are a ball-on-cylinder lubricity evaluator (BOCLE), high frequency reciprocating rig (HFRR), SRV, 4-ball wear tester (ASTM D-2266), etc. Wear testers used in this

study are ball on cylinder lubricity evaluation (BOCLE) testers based on ASTM method D5001 which is the standard test method for measurement of lubricity of aviation turbine fuels. A lab-built ball on cylinder testing equipment has been used for this study.

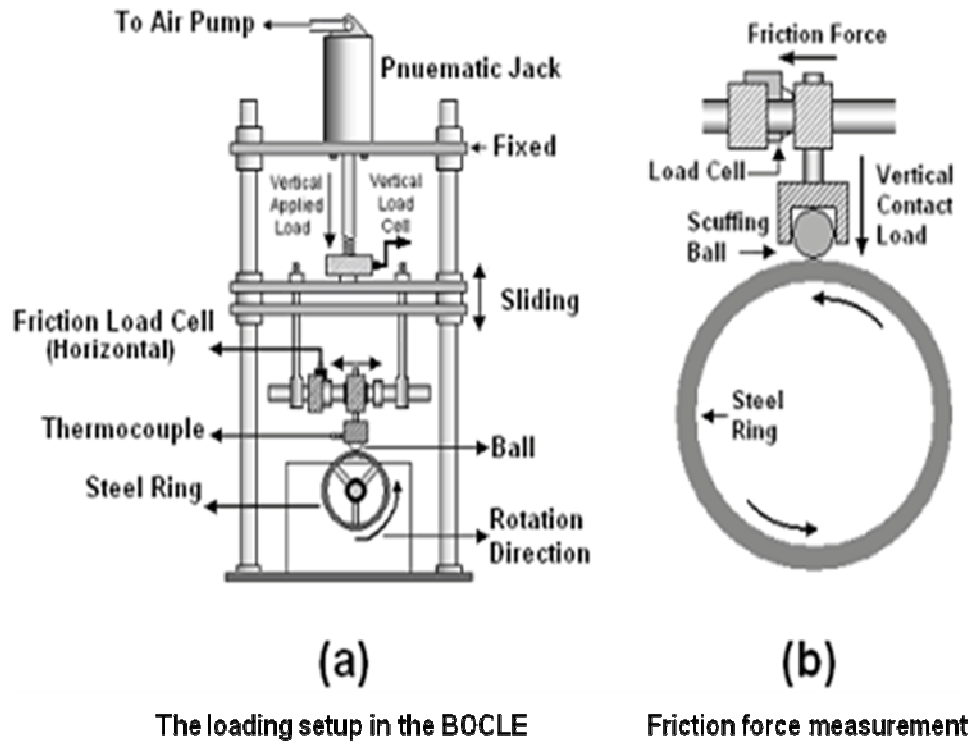


Figure 2.4 Schematic of Lab-made BOCLE. (a) Loading Setup of the BOCLE: The Vertical Load is Applied Pneumatically from the Top of the Machine. The Vertical Load Cell Measures the Applied Load. The Fiction Load Cell Measures the Fiction Load. (b) Fiction Load Measurement: The Fiction Load Cell Measures the Horizontal Force Resisting the Rotation of the Steel Ring, Which is Applied in the Horizontal Direction on the Scuffing Ball. [27,39]

2.4.1 UTA-built BOCLE

The unique Ball-on-Cylinder type of tribological testing unit was designed and built In order to simulate boundary lubrication conditions. The effects of the factors influencing the performance of the tribofilm such as contact pressure, speed, chemistry and surface roughness can be studied with this tribo tester. Figure 2.4 shows the schematic of home-built BOCLE. The BOCLE unit is designed to capture real time data like scuffing load, frictional force (and hence coefficient of friction) and near contact point temperature. The maximum contact load possible

in this machine is 36 Kg and is controlled by the pneumatic pump on the top as illustrated in figure 2.4(a). The coefficient of friction is measured by calculating the ratio of the applied vertical load obtained from the applied load assembly and the horizontal load of the friction load cell generated by sliding the ball holder on the steel ring. The temperature of contact point is also measured by the thermocouple closely located at the scuffing ball. The contact temperature is correlated with friction events during the wear test to a large extent. The limited amount of oil (50 ml) used in the test system together with the relatively high scuffing loads used, can simulate boundary lubrication condition and extreme pressure condition. Table 2.2 explains the specifications of the lab-made ball-on-cylinder lubricity evaluator.

Table 2.2 Specifications of BOCLE Tester [39]

Parameter	UTA Lab-made BOCLE
Ring type / Diameter	Timken bearing ring 50 mm
Ball type / Diameter	Tungsten carbide (grade 25) 6.35 mm
Applied loads range / mechanism	60~280 N Pneumatic
Measured variables	Coefficient of friction Temperature
Rotating speed	700 rpm

2.5 XANES (X-ray Absorption Near-Edge Structure) Spectroscopy

2.5.1 Introduction of XANES

X-ray absorption spectroscopy (XAS) is a current representative non-destructive analysis technique. Because its experimental setup simply requires a monochromatically tunable light source and an electron energy analyzer and it can probe the local geometric and electronic structure of selected matter, X-ray absorption spectroscopy (XAS) is widely used nowadays. [53] The experiment is usually performed at synchrotron radiation sources, which

provide intense and tunable X-ray beams. Samples can be in the gas-phase, solution, or condensed matter like solids. [59]

X-ray absorption spectroscopy broadly consists of two distinguished regions as describes in figure 2.5. The absorption edge is not simply a discontinuous increase in absorption. It has important structures both in the neighborhood of the edge jump and well above the edge. [60] The adjacent structure within about 50~100 eV of the edge is referred to as X-ray absorption near-edge structure spectroscopy (XANES). The oscillated regions for about 1000 eV or more above the edge are called as extended X-ray absorption fine structure (EXAFS). Although the distinction between XANES and EXAFS is ambiguous and they have same physical principles, the XANES and EXAFS regions are usually analyzed differently. The XANES is sensitive to oxidation state and geometry, but is not analyzed quantitatively, while the EXAFS is sensitive to the radial distribution of electron density around the absorbing atom and is used for quantitative determination of bond length and coordination number. [60]

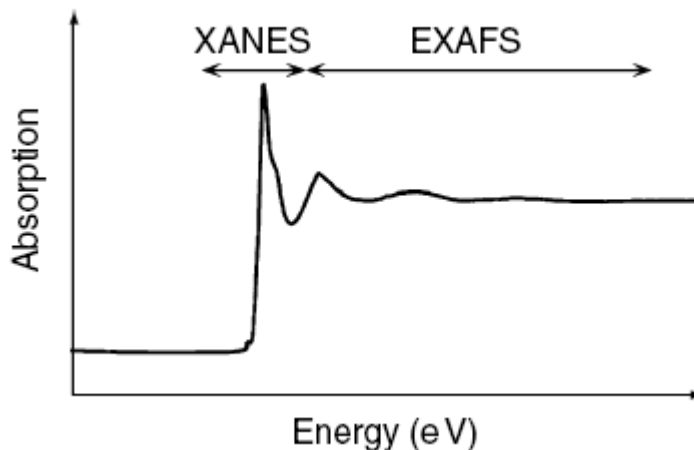


Figure 2.5 Schematic Illustration of an X-ray Absorption Spectrum, Showing the Structured Absorption of Both the XANES and the EXAFS. [60]

2.5.2 Principle of XANES

When the x-rays bombard a target, the oscillating electric field of the electromagnetic radiation interacts with the electrons bound in an atom. Either the radiation will be scattered by

these electrons or absorbed and excite the electrons like figure 2.6. [61] The XANES principle is based on the determination of the x-ray absorption coefficient (μ) depending on the photon energy ($h\nu$) at a fixed angle of illumination (θ). As the optical excitation of a core level electron requires the binding energy E_B as minimum photon energy, the transgression of this energy coincides with an increased absorption coefficient. [62] This leads to the formation of absorption edge. A narrow parallel monochromatic x-ray beam of intensity (I_0) passing through a sample of thickness (x) in figure 2.6 gets a transmitted x-ray intensity (I_t) and a fluorescence x-ray intensity (I_f). The relationship is given by the following expression.

$$\ln \frac{I_0}{I_t} = \mu \times x \quad \text{and} \quad \frac{I_f}{I_0} \propto \mu$$

Equation 2.7 Relationship for the Linear Absorption Coefficient μ

Where μ is the linear absorption coefficient of sample, which depends on the types of atoms and the density ρ of material and x is the samples thickness. This equation directly measures the probability of exciting a core level electron.

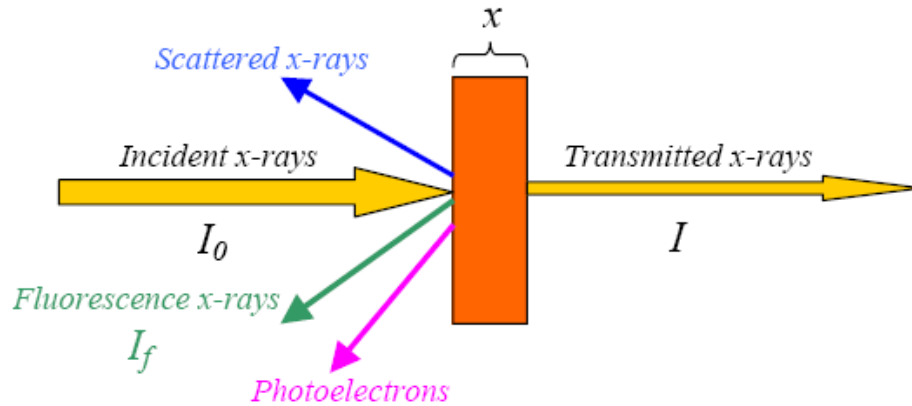


Figure 2.6 Typical Experimental Apparatus for XAS Measurements. Incident and Transmitted Intensities are Measured Using an Ion Chamber. A Variety of Detectors can be Used to Measure X-ray Fluorescence Intensity for Samples. [61]

As depicted in figure 2.7, a photon with sufficient energy enables the photoexcitation of a core level electron (K,L, or M shell) beyond the continuum (vacuum level, E_V). The atom is left in an

excited state with an empty electronic level (a core hole). The electron ejected from the atom is called the photo-electron.

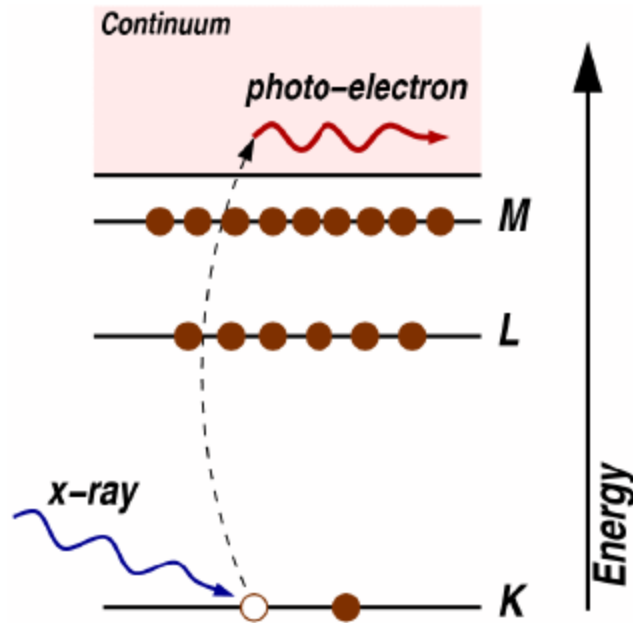


Figure 2.7 The Photoelectric Effect, in which an X-ray is Absorbed and a Core-Level Electron is Promoted out of the Atom. [63]

Then, the excited core-hole will relax back to a ground state of the atom. A higher level core electron drops into the core hole, and fluorescent x-ray and Auger electron (or secondary electron) are emitted such as figure 2.8. If an x-ray with energy is equal to the difference of the core-levels like figure 2.8(a), this is called as x-ray fluorescence. Auger and secondary electron emission occur when an electron is promoted to the continuum from another core-level as shown in figure 2.8(b). [63] X-ray fluorescence and auger emission occur at discrete energies that are characteristic of the absorbing atom and can be used to identify the absorbing atom. The auger and secondary electron emissions provide a total electron yield mode (TEY mode) which detects all electrons emitted as a result of photo absorption. In a fluorescence yield mode (FLY or FY mode), the fluorescence radiation is detected. [59]

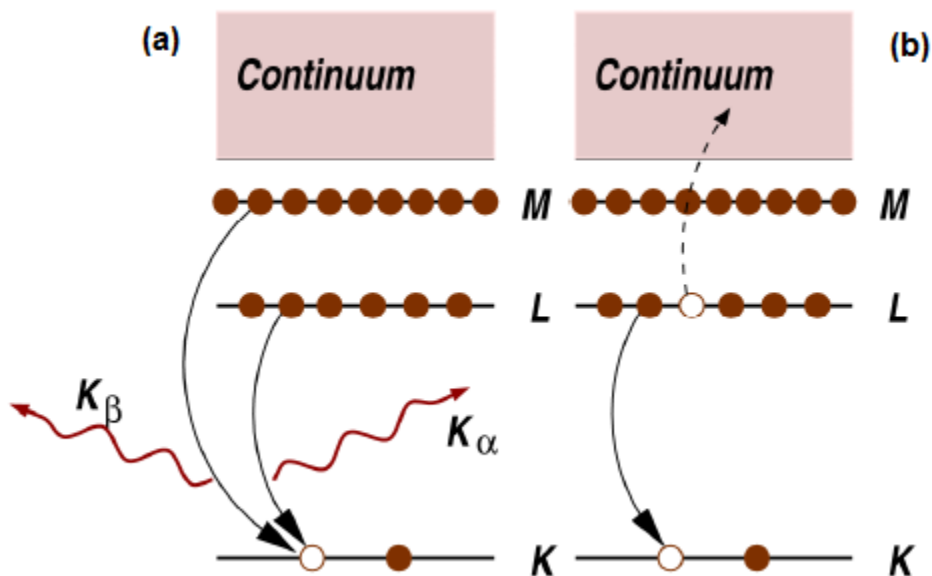


Figure 2.8 Decay of the Excited State: X-ray Fluorescence (a) and the Auger Effect (b). In Both Cases, the Probability of Emission (X-ray or Electron) is Directly Proportional to the Absorption Probability. [63]

2.5.3 Data Acquisition of XANES

The XANES experiments were run at two different beam lines in two different synchrotron facilities depending on the energy range. For phosphorus (P) and sulfur (S) K-edge spectra of higher energy range, The Canadian double crystal monochromator (DCM) beamline at the Synchrotron Radiation Center (SRC) at the University of Wisconsin–Madison in Stoughton, Wisconsin was used. The DCM beamline covers the range of 1500 to 4000 eV with 0.3 eV for P and S scan step of resolution. The beam spot size is 2 mm by 2 mm (horizontal by vertical). [64] In case of P and S L-edge spectra of lower energy range, the variable line spacing plane grating monochromator (VLS-PGM) beamline at the Canadian Light Source (CLS) facility in Saskatoon, Saskatchewan, Canada was run. Its energy range is between 5.5 and 250 eV with 0.1 eV scan step of resolution at both P and S peaks. The PGM beam spot size is 500 μm by 500 μm . Zinc (Zn) L-edge, iron (Fe) L-edge, oxygen (O) K-edge, and fluorine (F) K-edge were tested at the high resolution spherical grating monochromator (SGM) beamline in the CLS

facility. It covers the energy range between 250 to 2000 eV with 0.1 eV scan step in 1000 μm by 100 μm spot size. [65]

As already explained in the previous section, there are two detection modes that have different sampling depths. The total electron yield (TEY) mode obtains some information of the surface layers while the fluorescence yield (FLY) mode gets the data concerned with the bulk of the matter beyond the outer surface layers. This accessibility of two separated modes with layer difference provides huge benefits to study chain length, chemical composition, and structural environment variation of tribofilms according to the depth. [39] In K-edge spectra, the maximum depth of the TEY is about 50 nm, while the FLY mode has about 300~500 nm depth. The L-edge with lower energy maximally probes about 5~7 nm in the TEY mode and about 50 nm in FLY mode. [66]

2.5.4 Previous Studies of XANES

Chemical analyses of the tribofilms formed by ZDDP have progressed since 1990s using X-ray absorption near-edge spectroscopy (XANES). [21] XANES has two main advantages. First, it can provide quite clear discrimination between atoms of the same elements having only very slight differences in their electronic and thus chemical environment. Another is that it has different modes of operation that enable both very thin surface layers to be analyzed separately on the same specimen. On the other hands, its disadvantage is that spectra have to be interpreted by comparison with reference chemicals and it is not quantitative. [21] XANES works has provided the critical information about tribological films formed by functional lubrication oil formulations. Kasrai et al. [67] provided the chain length information of phosphate antiwear films using XANES. XANES spectroscopy was used to measure the thickness of antiwear films from ZDDP. [3,57] Also, XANES technique provided the chemical nature of P and S in the antiwear films. [4,23,24,30,57,67] With this technique, it was found that the pads in the antiwear film consist of a thin surface film, rich in quite long chain polyphosphate on top of shorter chain poly- or orthophosphate glass material. [24,25,30,56,66] Moreover, thermal films

have similar composition to tribofilms formed on rubbed surfaces from XANES spectroscopy. [23,30,68] Recently, tribofilms generated from ashless antiwear additives have been compared with ZDDP and with one another. [4,31,47,49-52] Najman et al. [31,47,50] found that ashless thiophosphates formed short chain iron phosphates and iron sulfides on the rubbed surface by XANES spectroscopy.

2.6 Nano Mechanical Properties of Tribofilms

The Hysitron TriboIndenter, a high-resolution nano-mechanical testing instrument, is an ideal technique to study mechanical properties of the tribofilms and the thermal films whose mechanical properties are still unknown. There are three types of nano-mechanical tests, i.e. nano-indentation, nano-scratch, and scanning nano-wear tests. Recently mechanical properties of tribofilms generated from ZDDP like hardness and reduced modulus have been studied using nano indentation mode as a valuable tool. [58,69,70] However, most of these studies have remained limited to the nano-indentation. The scanning nano wear and nano scratch tests performed on the tribofilms and the thermal films are somehow a new technique to analyze the mechanical properties of films. Some of the mechanical properties like adhesion and integrity of tribofilms or thermal films can be induced from nano scratch test. The result of nano wear test provides the resistance of tribofilms against shear forces and the structural continuity of the tribofilm. Nano-mechanical test were performed both at the University of Texas at Arlington on a Hysitron Ubi 1 nano-mechanical testing system and also at Hysitron corporation's nano-mechanics research laboratory in Minneapolis, MN.

2.6.1 Principle of Nano-Indentation Test

In nano indentation, a nano-size of hard tip whose mechanical properties are known like diamond is pressed into a sample whose properties are unknown. [71] As normal force is applied to an indenter tip, the tip penetration into the sample is increased according to the material of sample. During the indentation process, the depth of penetration and the applied load are recorded, and then the area of the indent is determined using the known geometry of

the indentation tip. The load-displacement curve is calculated and plotted on a graph with these data. These curves are used to obtain mechanical properties of the tribological films such as the hardness and the reduced modulus.

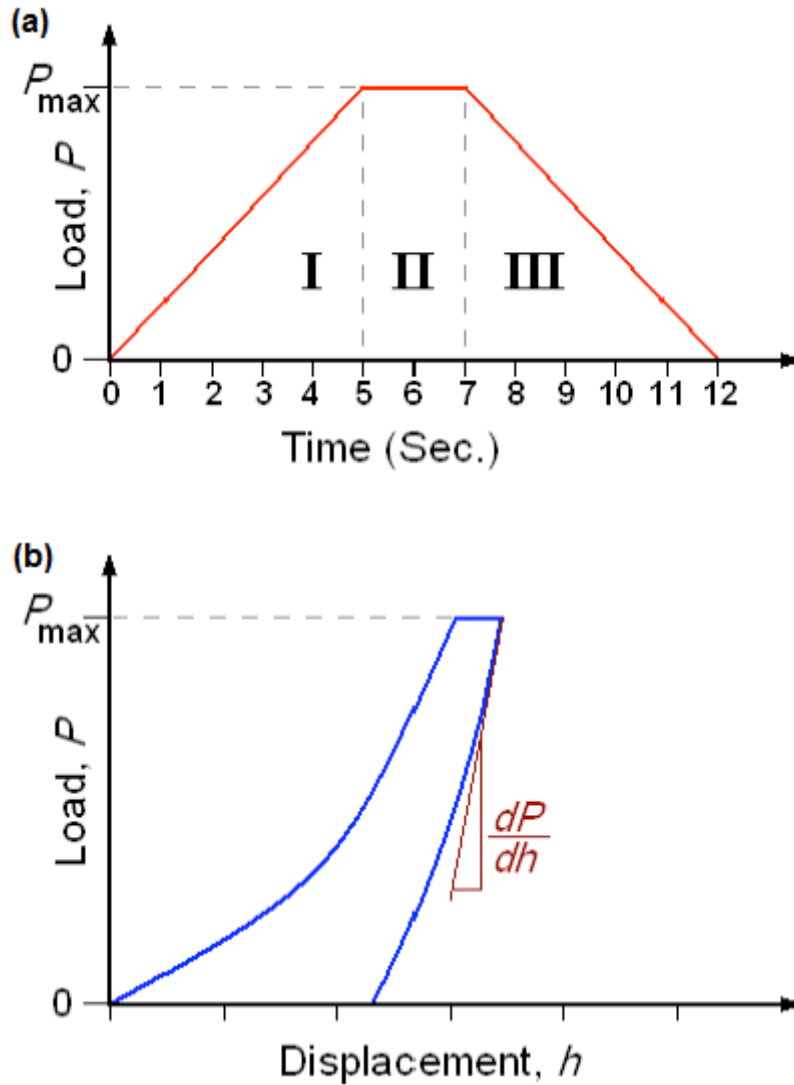


Figure 2.9 Load Function and Load Displacement Curve. (a) Trapezoidal Load Function for Single Nano Indentation Test; It Consists of Loading, Holding, and Unloading Segments. (b) Load-Displacement Curve of Nano Indentation. [39]

Figure 2.9(a) shows the trapezoidal load function which is used in this study. The single indent test with a trapezoidal load function is divided into a 5 second loading segment, a 2 second holding segment at the user-defined load, and a 5 second unloading segment. First

information that can be obtained from a single trapezoidal nano indentation is the reduced modulus of the material. Figure 2.9(b) shows the load-displacement curve of the single nano indent test. The reduced modulus is measured from the slope of the load-displacement curve at the early stages of unloading segment. This calculation for the reduced modulus is based on the Oliver-Pharr analysis. [71,72] The slope of the curve (dP / dh) upon unloading is indicative of the stiffness (S) of the contact. This value generally includes a contribution from both the material being tested and the response of the test device itself. The stiffness of the contact can be used to calculate the reduced modulus of elasticity E_r as

$$E_r = \frac{1}{\beta} \frac{\sqrt{\pi}}{2} \frac{S}{\sqrt{A(h_c)}}$$

Equation 2.8 The Reduced Modulus and the Stiffness of the Contact.

where, $A(h_c)$ is the area of the indentation at the contact depth h_c (the depth of the residual indentation), and β is a geometrical constant on the order of unity. The reduced modulus E_r is converted to the elastic modulus E_s of tested sample with the following equation:

$$\frac{1}{E_r} = \frac{(1 - \nu_i^2)}{E_i} + \frac{(1 - \nu_s^2)}{E_s}$$

Equation 2.9 The Conversion Equation of the Reduced and the Elastic Modulus.

here, the subscript i indicates a property of the indenter material (here, diamond tip) and ν is Poisson's ratio. The subscript s indicates a property of the sample.

Second mechanical property that can be induced from a nano indentation test is the hardness of the material. The hardness is related to the maximum load to the indentation area. Before the nano indentation tests, the TriboIndenter need to be calibrated for compliance and tip abnormalities, using the regular method of measuring a succession of indents into a silica sample at different penetration depths to calculate the tip area function. [73] This tip area function is used to calculate the hardness of material. The equation of the hardness is like below:

$$H = \frac{P_{\max}}{A_r}$$

Equation 2.10 The Hardness of Material.

Where P_{\max} is the maximum load to the indentation area, and A_r is the area obtained from the tip area function as the indenter depth.

2.6.2 Previous Studies of Nano Indentation

Nanoindentation, couples with topographical imaging, is a powerful method of differentiating components of heterogeneous materials on the basis of their local mechanical properties. [74] The physical properties of hardness and stiffness of ZDDP films, which are likely to determine the film's mechanical survival as well as the stresses experienced by the substrate, have been estimated by nano-indentation techniques. [21,28,48,70,75-77] Komvopoulos et al. [70] found the phosphate tribofilm exhibited an average hardness of 6.0 GPa and reduced elastic modulus of 122.7 GPa compared to 12.5 GPa and 217. GPa of the steel substrate, respectively. This reflects an inherent ability of the tribofilms to plastically deform, thereby protecting the substrate from sliding wear. Nicholls et al. [75] also reported that a large antiwear pad had a reduced modulus of about 80.5 GPa. This allowed for the correlation between the elastic response of the film and the polyphosphate chain length to be made. Some studies measured a ZDDP thermal film to have an indentation modulus of 35 GPa and a hardness of 1.5 GPa [78] and a ZDDP tribofilm to have an indentation modulus of 90 GPa and a hardness of 3.5 GPa [58]. Pereira et al. [28] studied the temperature dependent mechanical modulus of antiwear films formed by ZDDP additives on 52100 steel. They found that below 150 °C, the indentation modulus is relatively constant at about 100 GPa and at 200 °C, a significant decrease in modulus to about 70 GPa is observed with having enough stiff to prevent asperity contact and provide antiwear behavior. [28] Recently, Mourhatch and Aswath [39,76] found the tribofilms formed from ZDDP consist of two different layers, a harder top layer covering a softer and thicker layer underneath using nano indentation techniques. They showed the tribological nature of tribofilms of ZDDP for protecting the sliding surface. [76]

CHAPTER 3

PROPERTIES OF TRIBOFILMS FORMED WITH ASHLESS DITHIOPHOSPHATE AND ZINC DIALKYL DITHIOPHOSPHATE UNDER EXTREME PRESSURE CONDITIONS

Tribological and nanoscale properties of tribofilms from ashless dialkyl dithiophosphates (DDPs) were compared with zinc dialkyl dithiophosphates (ZDDPs) in this study. The tribosurfaces generated from these chemistries were examined using scanning electron microscopy and energy dispersive spectroscopy. The wear debris harvested from the wear tests was examined in a transmission electron microscope in bright field mode with selected area diffraction to examine the crystallinity and nature of the debris particles. Thickness of the tribofilms was measured using the focused ion beam cross-section microscopy indicating that the tribofilms formed by ashless dithiophosphates are significantly thicker than those formed by ZDDP. Nano-mechanical properties of the tribofilms including hardness and reduced modulus, scratch and nano-wear performance of the ashless dithiophosphate were compared to the secondary ZDDP. The overall results indicate that the wear performance of the ashless DDP is comparable or better than when ZDDP is used. The analytical techniques indicate that the tribofilms formed with ashless DDPs are thicker than those formed from ZDDP; however, the hardness and modulus of the tribofilm are lower in the case of ashless DDPs. XANES analysis indicate that in both tribofilms, phosphates are present as short chain phosphates. Ashless DDPs yield iron phosphates while ZDDP yielded a mix of iron and zinc phosphates. Both tribofilms have greater proportion of phosphates compared to sulfur species. The sulfur near the surface is mostly in the form of sulfates while the material in the interior is a mixture of sulfates and sulfides.

3.1 Introduction

Several additives in engine oils are necessary to improve the efficiency of engines by reducing friction and wear as well as by protecting the oil from oxidation. [17,20,21,79] As both an antiwear and an antioxidant additive, zinc dialkyl dithiophosphate (ZDDP) has been used in engine oil for several decades. [15,21] However, in spite of its outstanding properties, ZDDP is the primary source of P, S and heavy metal Zn in the exhaust. [16,80-82] Moreover, the zinc in ZDDP can easily hydrolyze and deposit as activated Zn complex on surfaces of parts within the engine. [18,19,80,83] More frequent maintenance and replacement of oil are needed to retain power and performance of the engine. Development of metal-free additives is part of a new trend in engine oils in Europe, Japan, and North America [16,19,80,81,83-92] Ashless phosphorus-containing antiwear additives have been found to be particularly effective at reducing friction and inhibiting wear. [90] Phosphates, phosphites, thiophosphates, metal phosphates, and amine phosphates are common examples of phosphorus additives that are used in the lubricant industry as additives. [91].

Camenzind et al. [18] demonstrated that an ashless dialkyl dithiophosphate can have superior antiwear and antioxidation performance under extreme pressure conditions (four-ball test) and exhibit improved compatibility and stability under hydrolysis condition. Ribeaud [19] found that oils made with zinc-free antiwear additives tend to have a lower friction than those containing ZDDP using a mini traction machine. On the other hand Zhang et al. [3] compared wear behavior of ashless dialkyl dithiophosphate with ZDDP. They found ZDDPs have better wear protection compared with ashless dithiophosphates and a combination of ZDDP and ashless dithiophosphate can provide very good wear protection. Najman et al. [51] also determined that ZDDP provides better wear protection than ashless thiophosphates when used without other types of additives present in the base oil. Another study [31] compared dialkyl dithiophosphates with another ashless additive, triaryl monothiophosphate. They found the tribofilm of ashless dialkyl dithiophosphates to be comprised of a thick film with pad-like

structures that are wide in area and micro-chemically heterogeneous, with areas of varying polyphosphate chain length. [31] While significant inroads have been made in the development of ashless antiwear additives, a comprehensive comparison of their behavior in comparison to ZDDP is still required.

In this study the tribological behavior of an ashless DDP was compared to ZDDP under extreme pressure and boundary lubrication conditions. In order to get a better understanding on the role played by the tribofilms formed on the surface with wear behavior, the tribosurfaces were examined using scanning electron microscopy and energy dispersive spectroscopy. Wear debris harvested from the wear tests was examined by transmission electron microscope in bright field mode with selected area diffraction to examine the crystallinity of the wear debris. Thickness of the tribofilms was measured using the focused ion beam cross-section microscopy. Nano-mechanical properties including hardness and reduced modulus, scratch and nano-wear performance of the tribofilms formed from the ashless dithiophosphate were compared to the secondary ZDDP. The chemical structure of tribofilms was also investigated using X-ray near edge absorption structure (XANES) spectroscopy.

3.2 Experimental Details

3.2.1. Materials and Tribological Test

A secondary ZDDP (7.2 wt % P) consisting of both basic and neutral forms of ZDDP and an ashless dialkyl dithiophosphate (9.3 wt % P) were used in this study, the structure of the two compounds is shown in figure 3.1. Two blends were formulated with each antiwear additive, one with a nominal composition of 0.1 wt % P and the other with a composition of 0.05 wt % P in 100 neutral base oil without any other additives present.

An in-house-made ball on cylinder lubricity evaluator (BOCLE) was used to conduct the boundary lubrication tests for all formulations. Test protocols of the BOCLE are detailed in an earlier study. [27,76] Tungsten carbide balls of 0.25 in. (6.25 mm) diameter of Rockwell C

hardness of 78 (HRC) were used as the scuffing tribological component. Timken hardened steel bearing rings of 50 mm outside diameter with 62 HRC Rockwell hardness were used as the rotating cylinder. In order to nullify the possible effects of residual machining lubricants and contamination, both components (ring and ball) were cleaned, brushed and ultrasonically cleaned using acetone and hexane. In order to simulate a boundary lubrication regime, only 50 μ l of oil solution was applied along the line of contact by the scuffing ball on the outer circumferential surface of the ring using a surgical syringe. The surface roughness (Ra) of substrate was fixed to the relatively tight range of 0.2–0.4 μ m in order to control the effect of surface finish. To study the effect of test duration, wear tests were run for 5000, 15,000, and 25,000 cycles for both formulations (ZDDP and DDP in base oil) at a rotating speed of 700rpm (109.96 m/min). The effect of contact load on extent of wear was also investigated by conducting tribological tests at contact loads of 20, 22, 24, and 26 kg loads. A profilometer (Mahr M1 Perthometer) was used to measure the profile of the wear track at 60° intervals around the ring. The average of 18 measurements from three wear tests for each tribological condition was used to determine the average and standard deviation of wear volume.

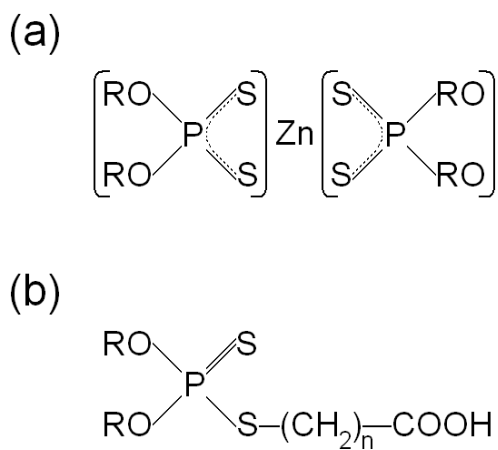


Figure 3.1 Chemical Structures of (a) the Neutral ZDDP and (b) the Ashless DDP.

3.2.2. Analysis of Tribofilm

The surface morphologies of the wear track on the ring were examined in secondary electron mode using a scanning electron microscope (SEM, JEOL-JSM-IC845A) and chemical composition of tribofilms were investigated by energy dispersive X-ray Spectroscopy (EDS, 20 keV and 25 cm working distance). Thickness of tribofilms was measured by cross-sectioning the tribofilm using a focused ion beam microscope (FIB, Zeiss Leo FIB 1540XB). Samples for the SEM and FIB test were prepared by cutting a small portion of tested rings using a diamond blade with base oil as lubricant to prevent contamination of the surface. Once cut, the samples were ultrasonically cleaned with a mixture of hexane and acetone to remove any base oil that may have remained on to the surface.

A Nano-indenter (Hysitron Triboscope™) was used to probe the nanoscale mechanical properties (e.g. hardness and reduced elastic modulus) of the tribofilms formed on the wear track generated on the surface of the rings during wear tests. Nano-indentation tests were run using a NorthStar cube corner diamond probe with a tip radius of less than 40 nm. For nano-scratch tests and nano-scanning-wear tests, the probe (tip) used was a 90° conical probe with a 2 µm tip radius. Normal force and normal displacement were measured during nano-indentation tests. Lateral force and displacement was measured in addition to normal force and displacement in scratch and scanning nano-wear tests. Nanoindentation tests were conducted to measure the hardness and the reduced elastic modulus of tribofilms as a function of thickness of these films. Nano-scratch and scanning nano-wear tests were primarily used to investigate the mechanical integrity of tribofilms, their adhesion and their layer structure. The Triboindenter was also used in Scanning Probe Microscopy (SPM) mode to obtain topographical information from the generated wear area at the end of scanning nano-wear tests.

The chemical structure, chemical composition and the bonding environment of certain atoms (e.g. P and S) present in the tribofilms, were probed by the X-ray Absorption Near Edge Structure (XANES) Spectroscopy. XANES phosphorus and sulfur K-edge spectra were obtained

on the double crystal monochromator (DCM) beam line in the Synchrotron Radiation Center (SRC) at the University of Wisconsin, Madison. Its analysis range is between 1500 eV and 4000 eV. Phosphorus and sulfur L-edge spectra were gained on the variable line spacing plane grating monochromator (VLS PGM) beam line at the Canadian Light Source (CLS), Saskatoon, Canada with an analysis range from 5.5 eV to 250 eV. Both fluorescence yield (FY) mode and total electron yield (TEY) mode were used to probe the chemical structure in the bulk and surface regions of the film, respectively. Spectra from tribofilm samples were compared with those obtained from model compounds for accurate analysis.

The characterization of wear debris generated during wear tests was carried out using a Transmission Electron Microscope (JEOL TEM-ASID 1200EX). The wear debris generated throughout the wear tests, originate from tribosurfaces normally covered by tribofilms, therefore TEM characterization of this debris can provide an insight in crystallinity and morphology of the tribofilms. Wear debris were collected after a 5000 cycle test in order to study wear events in early stages of tribofilm formation. Spent oil with the wear particles was collected using a plastic film and transferred to an ultra thin carbon film supported on a copper grid. The residual oil was then washed off using acetone and hexane, conveniently leaving the wear debris trapped on the carbon film for probing by TEM.

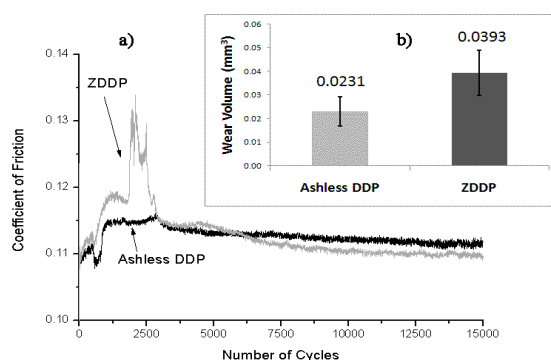


Figure 3.2 Comparison of Tribological Data for Wear Tests with ZDDP and Ashless DDP at a Phosphorous Level of 0.1 wt %. (a) Coefficient of Friction as a Function of Number of Cycles and (b) Wear Volume at the End of the Test. Tests were Conducted under Boundary Lubrication with a 1/4 Inch Ball of WC on a 52100 Steel Cylinder. Contact Load is 24 kg for Duration of 15,000 Cycles.

3.3 Results and Discussion

3.3.1. Tribological Wear Data

Figure 3.2 is the coefficient of friction versus test duration and the measured wear volume from ZDDP and ashless DDP, tested on the BOCLE. The wear tests were run under 24 kg scuffing load (3.56 GPa Hertzian contact load) for 15,000 cycles. The reported wear volume is the average value measured from three tests with six measurements in each test. In each case the tribofilm is formed at around 2500 cycles beyond which, the presence of tribofilms results in steady and relatively unchanging values of coefficient of friction. Friction events at the beginning of wear tests were observed to be smoother in the case of Ashless DDP while, for ZDDP, fluctuations in the friction are more pronounced and severe in initial stages of the test (Figure 3.2). The high shearing forces present as well as rising contact point temperature during the early stages of wear tests result in decomposition of antiwear additives and the formation of tribofilms on the steel substrates. The tribofilm reduces the fluctuation in coefficient of friction as surface asperities are covered by smoother tribofilms minimizing severe asperity interactions between the tribosurfaces and preventing/reducing the amount of wear in the process. Smaller increase of coefficient of friction in the case of DDP indicates that ashless DDP can break down under far less severe shearing and thermal conditions than ZDDP to form tribofilms. In terms of wear performance, the wear volume of ashless DDP is smaller than that of ZDDP. These differences in wear volume result from the fact that initial friction fluctuations are far less severe in the case of DDP than ZDDP.

The effect of applied scuffing load in wear tests on the amount of wear was also investigated as shown in figure 3.3. Test duration in all these tests was set at 25,000 cycles instead of 15,000 cycles for better differentiation. The wear volumes for both of the additives follow a similar pattern. However, it can be seen that under similar conditions, in all cases, ashless DDP generates smaller wear volume than ZDDP confirming the observations shown in figure 3.2. For lower loads (3.35 GPa and 3.46 GPa), the wear performance is close for the two

chemistries at both concentrations, however, under higher test loads (3.56 GPa and 3.66 GPa), solutions with the higher concentration of both ZDDP and DDP continue to provide wear protection while at the lower concentrations, the measured wear volumes significantly increase when concentration of the antiwear additive is reduced suggesting insufficient amount of antiwear additive.

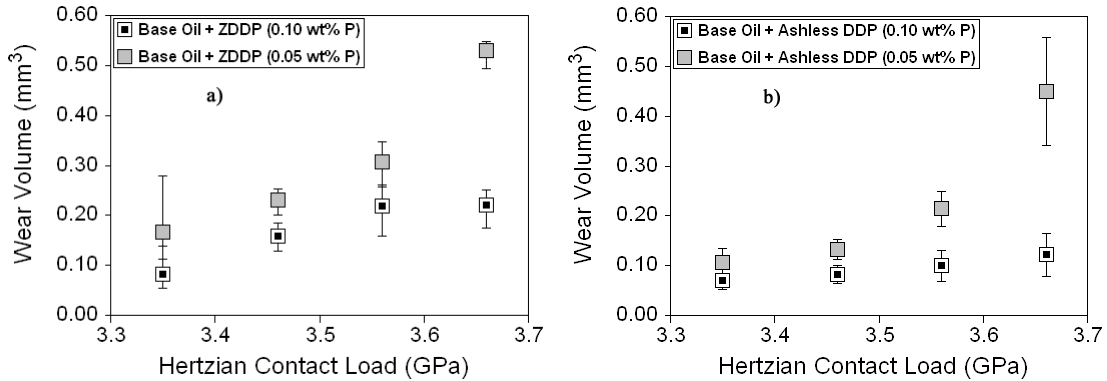


Figure 3.3 Effect of Concentration of Phosphorous, Load, and Nature of Antiwear Agent on Wear Volume. All Tests were Conducted for Duration of 25,000 Cycles. (a) ZDDP and (b) Ashless DDP.

3.3.2. Tribofilm Characterization Using Secondary Electron Microscopy and Energy Dispersive Spectroscopy

Figure 3.4(a) and (b) is the secondary electron image of the tribofilm surface and energy dispersive X-ray spectrum from a region within the wear track. In both images, the tribofilms are relatively uniform, with just a few scratches where the film has been removed by interaction with wear debris. The scratches are caused by the sliding of wear debris generated during the test, resulting in some trenching.

The energy dispersive spectroscopy analysis was conducted in spot mode from the center region of the tribofilm. In previous studies, Zhang et al. [4] found the tribofilm of ZDDP at low loads had mostly Zn cations rather than Fe with XANES analysis. Kasrai and co-workers have also drawn similar conclusions. [3,4,15,57] However, in this study, very little Zn was found by energy dispersive spectroscopy. On the other hand, strong Fe peaks were observed in both cases where the origin of the Fe peak may be a combination from both the tribofilm and the

substrate. In this case an accelerating voltage of 20 kV was used to energize the electrons in the SEM. The interaction depth from which characteristic X-rays are produced is a strong function of atomic number of the elements in the volume.

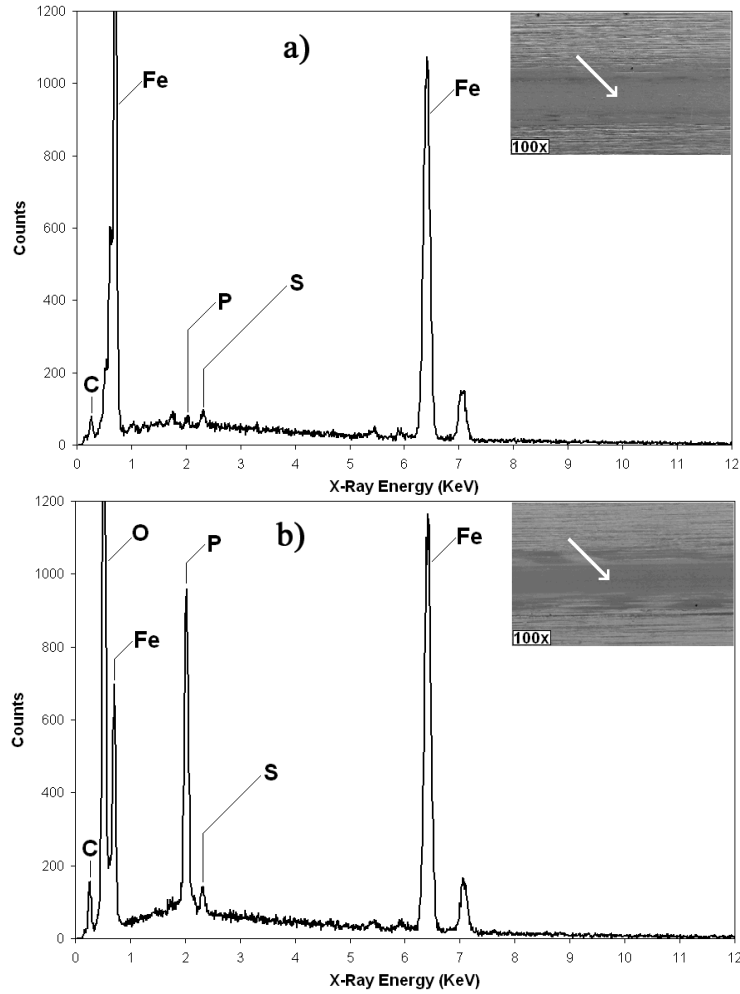


Figure 3.4 Scanning Electron Microscope (SEM) Image of Wear Track and Energy Dispersive Spectroscopy (EDS) Using X-rays of Wear Track from (a) ZDDP and (b) Ashless DDP. Both Tests were Conducted at a load of 24 kg for Duration of 15,000 Cycles.

The tribofilms are complex entities of Fe, O, P and S as well as Zn in the case of ZDDP, while a single valued interaction volume is difficult to estimate, it is reasonable to expect that the depth from which characteristic X-rays are produced in this case is in the range of 500nm or larger. In case of ZDDP, similar amounts of P and S are observed in the tribofilm and the dominant peak

is from the Fe substrate indicating that the tribofilms are relatively thin. On the contrary, ashless DDP has stronger phosphorus peak than sulfur peak. In addition, the intensities of oxygen and carbon from DDP are higher than ones from ZDDP. This indicates that the thickness of the tribofilm formed in the case of DDP is much larger than the one formed from ZDDP as much more of the EDS signal is coming from the tribofilm and less from the substrates. In addition, the tribofilm from DDP appears to consist of phosphates as opposed to sulfides/sulfates due to the large difference in peak intensities of the P and S in the tribofilm.

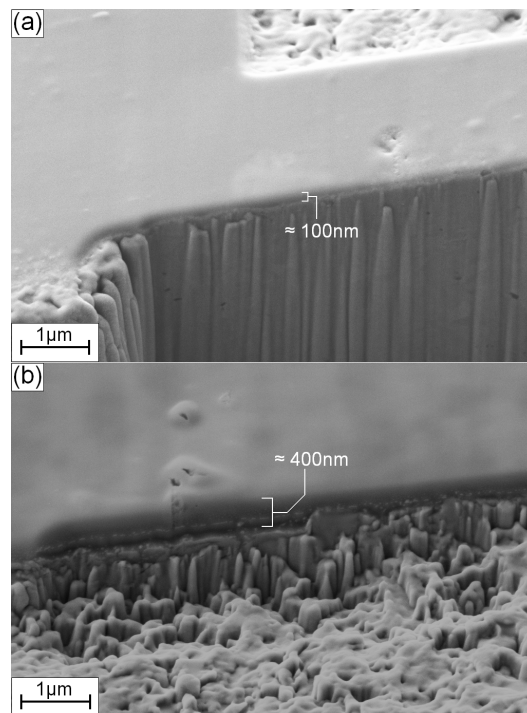


Figure 3.5 Focused Ion Beam (FIB) Cross-Section of the Tribofilm Formed at the End of the Test Conducted at a Load of 24 kg for 15,000 Cycles: (a) ZDDP Tribofilm and (b) Ashless DDP Tribofilm.

3.3.3 Comparison of FIB (Focused Ion Beam) Image

A gallium ion beam was used to sputter a rectangular trench 8 μm by 10 μm in area on the wear track. A secondary electron image was taken of the trench at an angle of 54° relative to the surface to determine the thickness of the tribofilm. The tribofilm surface is extremely smooth and uniform as shown in figure 3.5(a) and (b). The tribofilm formed with DDP

is approximately 400nm thick while the tribofilm from ZDDP is approximately 100nm thick. The larger thickness measured directly using FIB complements the EDS data that also suggests thicker tribofilm formed with DDP. The 100 nm thick tribofilm formed with ZDDP is consistent with observations in several studies using spacer measurements in the mini traction machine [54,93,94], Auger depth profiling [29,95], X-ray absorption spectroscopy [57] and nano-indentation [27,96]. This indicates that when ashless DDP is used at extreme pressures, thick protective tribofilms are formed, which may be responsible for the improved wear performance.

3.3.4 XANES (X-ray Absorption Near Edge Structure Spectroscopy) Analysis of Tribofilms

ZDDP and DDP mixtures in base oil were tested under boundary conditions for 5000 and 15,000 cycles at a load of 24 kg. All XANES spectra were acquired in two modes, the total electron yield (TEY) mode for chemical information of surface or near surface regions and the fluorescence yield (FLY) mode for chemical property of bulk of tribofilm. The sampling depths for tribofilms in the TEY of phosphorus and sulfur are around 5 nm at the L-edge and around 50nm at the K-edge while the sampling depths of the FLY mode are about 50nm at the L-edge and about 400nm at the K-edge. [57]

3.3.4.1 Phosphorus L edge XANES Spectral Analysis

The FLY spectra and the TEY spectra of tribofilms generated from ZDDP and ashless DDP at the end of 5000 and 15,000 cycles together with model compounds, FePO_4 , $\text{Zn}_3(\text{PO}_4)_2$, and $\text{Fe}_4(\text{P}_2\text{O}_7)_3$ are shown in figure 3.6(a) and (b). In previous studies [97-99], the phosphate chain length of tribofilms was determined from P Ledge XANES spectra. The ratio of the intensity of first pre-edge to the white line indicates the phosphate chain length: if the pre-edge intensity is much smaller than main peak it indicates a short chain polyphosphate, on the other hand larger pre-edge peaks suggest a long chain polyphosphate [31,97,100]. All pre-edge peaks in our tribofilms show little or no pre-edge. It is concluded that tribofilms tested in this study consist of short chain polyphosphates and/or mono phosphates. In model compounds of figure 3.6(a) and (b), two differences are observed, the position of all peaks and the width of

iron phosphate and iron pyrophosphate. Iron phosphates have a slightly higher energy states than zinc phosphates (white line peaks for iron pyrophosphate, $\text{Fe}_4(\text{P}_2\text{O}_7)_3$ is at 139.3 eV, iron phosphate, FePO_4 is at 139 eV and $\text{Zn}_3(\text{PO}_4)_2$ is at 138.7 eV). A short chain polyphosphate, iron pyrophosphate ($\text{Fe}_4(\text{P}_2\text{O}_7)_3$), has relatively wider white line than an iron phosphate (FePO_4). Comparing the characteristics of model compounds with two tribofilms from ZDDP and DDP at 5000 cycles, it is clear that the tribofilm formed from DDP lies close to an iron phosphate while the tribofilm from ZDDP matches $\text{Zn}_3(\text{PO}_4)_2$. On the other hand at the end of 15,000 cycles both tribofilms have phosphorous in the form of iron pyrophosphate. This result is quite different from other previous studies [30,31,75,97,100,101] where at lower contact loads it has been shown that the primary phosphates formed are long chain polyphosphates of Zn with very little evidence of iron phosphates of any kind. In this study, by virtue of the high Hertzian contact load in the BOCLE tester, Fe atoms react with the decomposition products of ZDDP or DDP resulting in the formation of short chain iron pyrophosphates and iron phosphates.

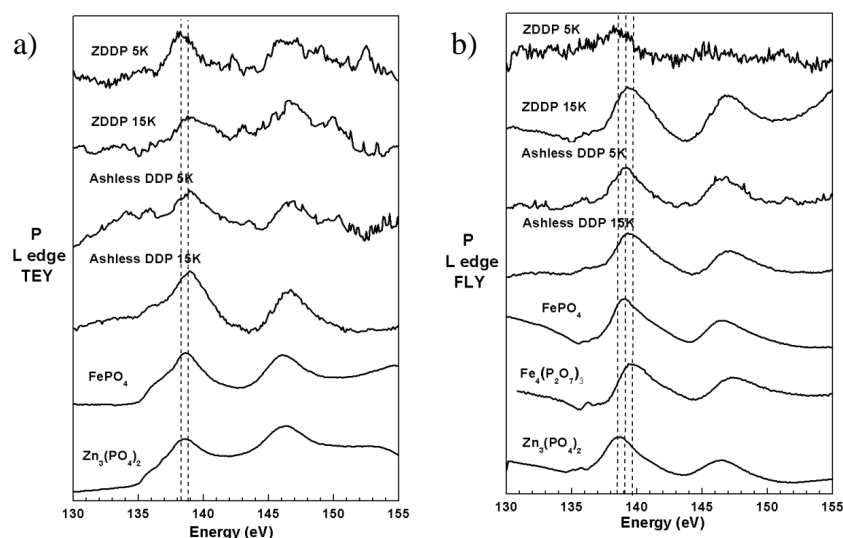


Figure 3.6 XANES Spectra at the P L-edge of the Tribofilms Formed from ZDDP and Ashless DDP. The Spectra of the Model Compounds of Fe and Zn Phosphates are Superimposed: (a) Total Electron Yield and (b) Fluorescence Yield.

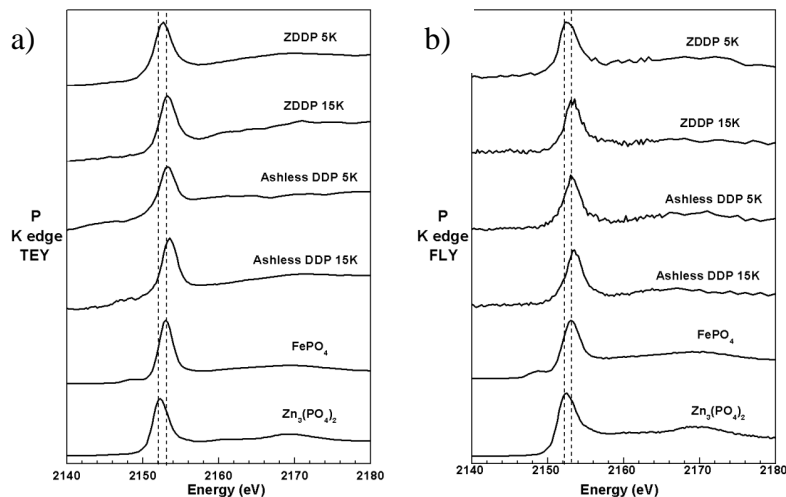


Figure 3.7 XANES Spectra at the P K-edge of the Tribofilms Formed from ZDDP and Ashless DDP. The Spectra of the Model Compounds of Fe and Zn Phosphates are Superimposed: (a) Total Electron Yield and (b) Fluorescence Yield.

3.3.4.2 Phosphorus K edge XANES Spectral Analysis

The single intense (white) peak is shown in each sample and in the standards in figure 3.7(a) and (b). This white line in P K-edge is obtained by the transitions of the core phosphorous 1s electrons to unoccupied p-like valence states. There are two differences between the two model compounds, zinc phosphate and iron phosphate. First, the location of main peak of iron phosphate is a slight higher energy than the one for zinc phosphate (FePO₄ peak is at 2151.6 eV while the Zn₃(PO₄)₂ peak is at 2150 eV). The K-edge spectra also indicate that at 5000 cycles the phosphates formed from DDP are iron phosphates while the ones formed from ZDDP are closer to zinc phosphates. At 15,000 cycles the outcome is also similar to the L-edge spectra and it suggests that both the tribofilms are primarily composed of Fe phosphates. Second, iron phosphate has a small pre-edge peak that is more noticeable in the FLY spectrum. In both tribofilms in FLY mode at 15,000 cycles, the pre-edge peak of iron phosphate is not clearly elucidated; however, in TEY mode the DDP peak has a clear pre-edge while it is not that clear in the case of ZDDP tribofilm. However, all white lines in FLY and TEY modes are close to the position of the intense peak for iron phosphates. This is clear evidence that iron phosphates

are dominantly formed in the tribological test of longer duration. This result is also contrary to earlier studies [28,30,97,100-102] that have shown that the primary constituents of tribofilms are polyphosphates of Zn. The tribological conditions here are more severe with much larger Hertzian contact loads and are responsible for the incorporation of Fe into the tribofilm and the formation of short chain Fe polyphosphates. It is also evident at the earlier stages of the tribological test, the phosphates formed when ZDDP is used are closer to zinc phosphates while at later times iron phosphates dominate.

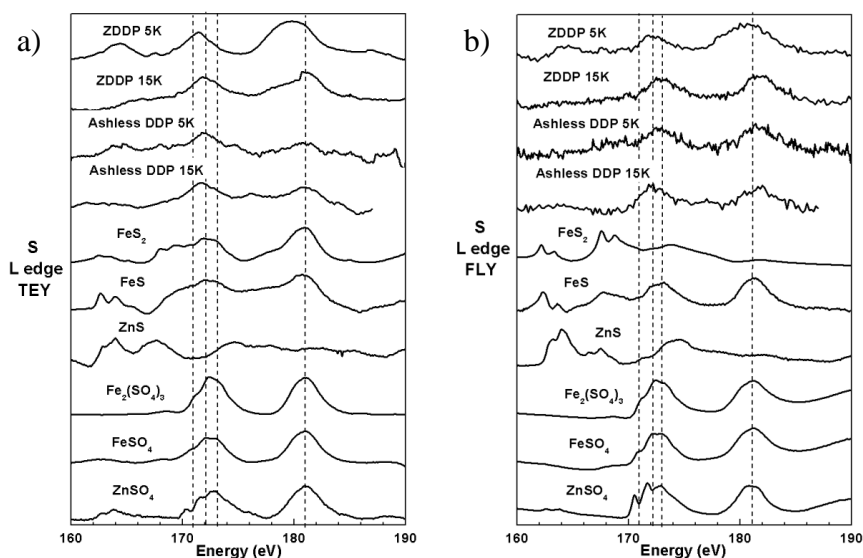


Figure 3.8 XANES Spectra at the S L-edge of the Tribofilms Formed from ZDDP and Ashless DDP. The Spectra of the Model Compounds of Fe and Zn Sulfates and Sulfides are Superimposed: (a) Total Electron Yield and (b) Fluorescence Yield.

3.3.4.3 Sulfur L edge XANES Spectral Analysis

The sulfur L-edge spectra recorded in FLY and TEY mode are shown in figure 3.8(a) and (b). Six different model compounds are compared with tribofilms generated from ZDDP and ashless DDP. There are two categories in model compounds; sulfide series like ZnS, FeS, and FeS₂ and sulfate series such as ZnSO₄, FeSO₄, and Fe₂(SO₄)₃. All sulfates and sulfides have unique features to distinguish them from one another except FeSO₄ and Fe₂(SO₄)₃. Model compounds, iron sulfide (FeS) and iron sulfate (FeSO₄ or Fe₂(SO₄)₃) have two main peaks, but

iron sulfide has a sharp peak at lower energy that is missing in the sulfates. Zinc sulfate has three small peaks at first main peak.

Once the sulfur peaks of tribofilms are carefully analyzed both tribofilms have sulfates and sulfides. The peak at 162.2 eV in the ZDDP tribofilm most likely corresponds to the ZnS peak and to a lesser extent the FeS peak. The small peak at 165.6 eV corresponds to ZnS. However, the peak at 171.6 eV does not belong to ZnS, it likely belongs to a combination of FeS and $\text{ZnSO}_4/\text{FeSO}_4$. The final peak at 179.8 eV is closer in location to FeS than the sulfate peak; however, we cannot rule out an overlap of the two peaks. This complex mix of peaks suggests that the sulfur is present as a mixture of sulfides and sulfates of both Zn and Fe. This result is different from the previous researches [28,103,104] where all sulfurs exist in the status of zinc or iron sulfide. On the other hand when DDP is used there is no Zn in the tribofilm and near the surface (TEY) there is a mixture of FeS and Fe sulfates while deeper down (FLY) it appears that the sulfates dominate. However, the noisy nature of the sulfur L-edge spectra in the DDP tribofilm indicates that very little sulfur is present and based on the P L-edge spectrum there is much more phosphorous present.

3.3.4.4 Sulfur K edge XANES Spectral Analysis

Figure 3.9(a) and (b) is the sulfur K-edge spectra in TEY and FLY mode of the model compounds and tribofilms from ZDDP and DDP. In these plots the K-edge spectra of all sulfates in model compounds are identical while peaks of sulfide compounds are differentiated. The sulfur signals of both tribofilms in FLY mode are weaker than ones in TEY mode. This indicates that more sulfur is present near the surface than in the bulk of tribofilm. In addition, tribofilms of both ZDDP and DDP, throughout the thickness, are comprised of a mixture of sulfide and sulfate. In the TEY mode, clear sulfate peaks are observed because plenty of oxygen is available in the surface region and sulfur exists in its oxidized form as sulfate, but in addition there is clear evidence for the presence of sulfides as well. In case of DDP, the metal cation is Fe. The sulfur compounds formed are iron sulfide and iron sulfate while in the ZDDP tribofilms

in addition to ZnSO_4 , FeS and ZnS are also present. It is also evident that the amount of these sulfur compounds in the bulk of the tribofilm is limited as the relative intensities of the S peaks are smaller than the phosphorous peaks at the K-edge.

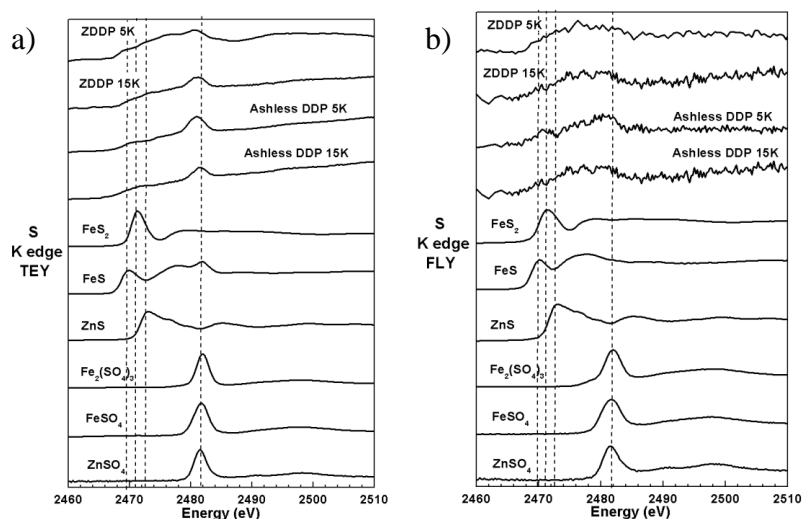


Figure 3.9 XANES Spectra at the S K-edge of the Tribofilms Formed from ZDDP and Ashless DDP. The Spectra of the Model Compounds of Fe and Zn Sulfates and Sulfides are Superimposed: (a) Total Electron Yield and (b) Fluorescence Yield.

3.3.5 Transmission Electron Microscopy of Wear Debris from Tribological Tests

The wear debris formed at the early stages of the tribological tests are nothing but the tribofilms that has been sheared off and may include some of the oxide by-products that are formed by the oxidation of the substrate and/or the tribofilm. Hence, analysis of the debris provides important insights into the chemistry of the tribofilm [27,96,99,105]. Wear debris were collected after a 5000-cycle test in order to study the initial process of tribofilm formation and placed on a polymer film and repeatedly washed with hexane and acetone to remove any oil residue. A 120 keV transmission electron microscope (TEM) was used to characterize the wear debris. Figure 3.10 and 3.11 show bright field images of low magnification (20,000 \times) and high magnification (200,000 \times), and X-ray diffraction patterns for wear debris from the tribological tests with ZDDP and ashless DDP. Both ZDDP and ashless DDP have well defined amorphous

glass film at the low magnification image, figure 3.10(a) and 3.11(a). In the high magnification pictures, figure 3.10(b) and 3.11(b), nanoscale particles as well as glass film are also observed. By analysis of diffraction pattern, comparing d spacings in figure 3.10(c) and 3.11(c) with ones of model compounds as shown in Table 1, these small particles are identified as crystalline particles of iron oxides. The crystallinity of particles harvested in the wear debris from ZDDP was identified as Fe_3O_4 in a previous study [27]. Fe_3O_4 (magnetite) has an inverse spinel structure with oxygen atoms in the cubic close packed sites and trivalent Fe occupying the tetrahedral sites and a mixture of trivalent and divalent Fe occupying the octahedral sites of the close packed cubic oxygen lattice [106]. However, the diffraction pattern from wear debris from ashless DDP is more complex than the ones from ZDDP. Several iron oxides, FeO, Fe_2O_3 , and Fe_3O_4 , were observed as described in Table 1 when DDP was used. Fe_2O_3 (Hematite) has the corundum structure (Al_2O_3) with approximately hexagonal close packed array of oxygen atoms with the Fe^{3+} ions occupying two thirds of the octahedral sites between the oxygen atoms [107]. Ferrous oxide or FeO exhibits the rock salt structure where the iron atoms are octahedrally coordinated by oxygen atoms and vice versa.

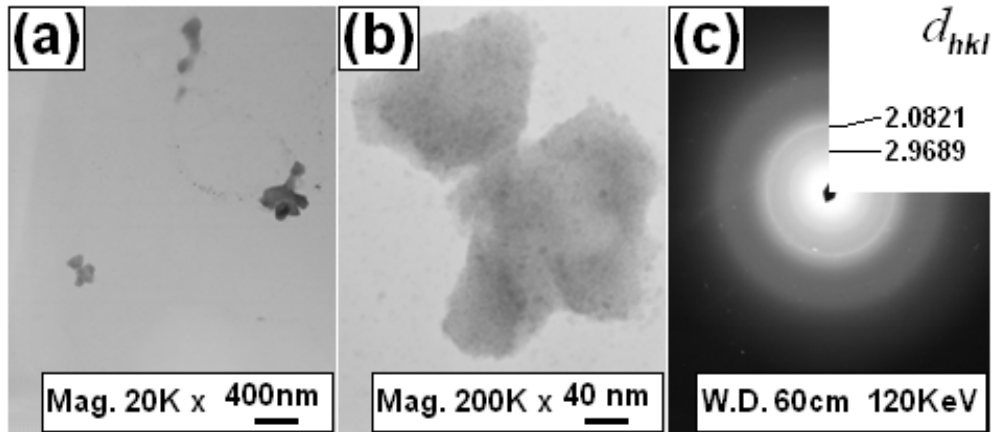


Figure 3.10 Bright Field Transmission Electron Microscopy (TEM) of the Wear Debris Harvested at the Ends of a Wear Test Conducted with ZDDP at a Load of 24 kg for Duration of 5000 Cycles: (a) 20,000 \times Magnification Bright Field Image, (b) 200,000 \times Magnification Bright Field Image, and (c) Selected Area Diffraction Pattern of Wear Debris.

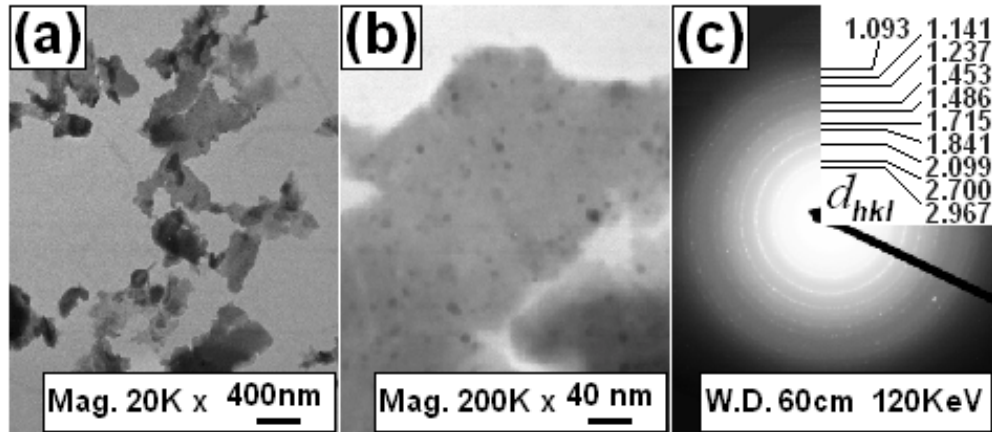


Figure 3.11 Bright Field Transmission Electron Microscopy (TEM) of the Wear Debris Harvested at the Ends of a Wear Test Conducted with Ashless DDP at a Load of 24 kg for Duration of 5000 Cycles: (a) 20,000× Magnification Bright Field Image, (b) 200,000× Magnification Bright Field Image, and (c) Selected Area Diffraction Pattern of Wear Debris.

Table 3.1. The Calculated d_{hkl} Spacings for the Ring Patterns Observed in Figure 3.10(c) and 3.11(c) Compared to Observed Values for Three Types of Iron Oxide.

d Spacing (Å)									
Fe₃O₄		Fe₂O₃		FeO		Observed Values			
						ZDDP	Ashless DDP		
d (Å)	I(f)	d (Å)	I(f)	d (Å)	I(f)	Fe₃O₄	Fe₃O₄	Fe₂O₃	FeO
2.967	30	3.684	30	1.525	100	2.9689	2.9670		1.5246
2.532	100	2.700	100	1.512	100			2.7000	
2.099	20	2.519	70	1.301	20	2.0821	2.0993		
1.715	10	2.207	20	1.294	60		1.7146	2.2070	
1.616	30	1.841	40	1.291	60			1.8406	
1.485	40	1.694	45	1.250	20		1.4845	1.6941	
1.328	4	1.599	10	1.237	60				1.2366
1.281	10	1.486	30	1.074	60			1.4859	1.0738
1.266	4	1.454	30	0.992	20			1.4538	
1.122	4	1.312	10	0.987	20				
1.093	12	1.260	8	0.982	60		1.0930		
0.970	6	1.141	7	0.967	100			1.1411	
0.939	4	1.104	7	0.957	100			1.1035	
0.880	6	1.056	7						
0.812	6	0.961	5						

3.3.6 Mechanism of Formation of Oxide Nanoparticles in the Wear Debris

Oxide nanoparticles with a typical size of 20nm are dispersed within otherwise amorphous wear debris. The wear debris is nothing but pieces of the tribofilm that have been sheared off. The origin of the nanoparticles could be from a couple of sources: (i) Oxidation of asperity particles of iron that are subsequently incorporated into the tribofilm. (ii) Intrinsic oxidation of the constituents of the tribofilm resulting in the nanocrystallites of oxides. The former mechanism would result in the formation of particles of varying size as there is little control on the size of the asperities that are oxidized. In addition, it is quite possible that some of the particles may not be completely oxidized prior to their incorporation into the debris. However, it is evident from the TEM and SAD analysis that most of the particles are approximately 20nm in diameter and none of them have any metallic Fe incorporated in them. Hence the likely mechanism for the formation of the nanoparticles is the intrinsic reaction of the Fe and O present in the wear debris together with available oxygen dissolved in the lubricant and during contact of debris with air. Formation of these Fe oxides from within an amorphous matrix involves a complex interplay between the kinetics of oxidation and thermodynamic stability of the oxides and the interfacial energy between the oxide particles and the amorphous matrix. Complicating the analysis is the fact that the composition of the matrix (wear debris) is constantly evolving during the test as more of the antiwear additive is decomposing and being incorporated into the tribofilm and the wear debris. However, a first principle analysis on the enthalpy of formation of the various oxides and thermodynamics of the oxidation process will provide us with some insight on the observed results.

The wear debris of tribofilms from ZDDP primarily contains Fe_3O_4 while the debris from tribofilms of DDP is largely made up of Fe_3O_4 , but also contain FeO and Fe_2O_3 . Figure 3.12 is a plot of standard enthalpy and free energy of formation of various oxides of Fe as a function of temperature. From the enthalpy of formation of oxides it is evident that formation of Fe_3O_4 is the most exothermic with the largest negative enthalpy of formation followed by Fe_2O_3

and FeO. In addition, the free energy of formation of Fe_3O_4 is the most negative indicating that it is the most stable oxide. This would suggest that the most likely oxide to form is Fe_3O_4 . Examining the Ellingham diagram shown in figure 3.13, it is evident that at temperatures below 800K the formation of Fe_3O_4 from FeO is favored. The conversion of Fe_3O_4 to its higher oxidation state of Fe_2O_3 is also not favored under ideal conditions. Even if the activity of oxygen is taken as 0.2 (in air) and that of FeO is as low as 0.2 the formation of Fe_3O_4 is still favored over FeO. In the case of ZDDP the formation of Fe_3O_4 as the only oxide is favored as it is thermodynamically the most stable oxide possible. On the other hand the wear debris from tribofilms formed from ashless DDP have a mixture of the three oxides with Fe_3O_4 being the dominant oxide. The higher Fe content in the tribofilm here may favor the formation of FeO as an intermediate stage oxide and there is some conversion of Fe_3O_4 to Fe_2O_3 . However, even in this case the dominant oxide is still Fe_3O_4 .

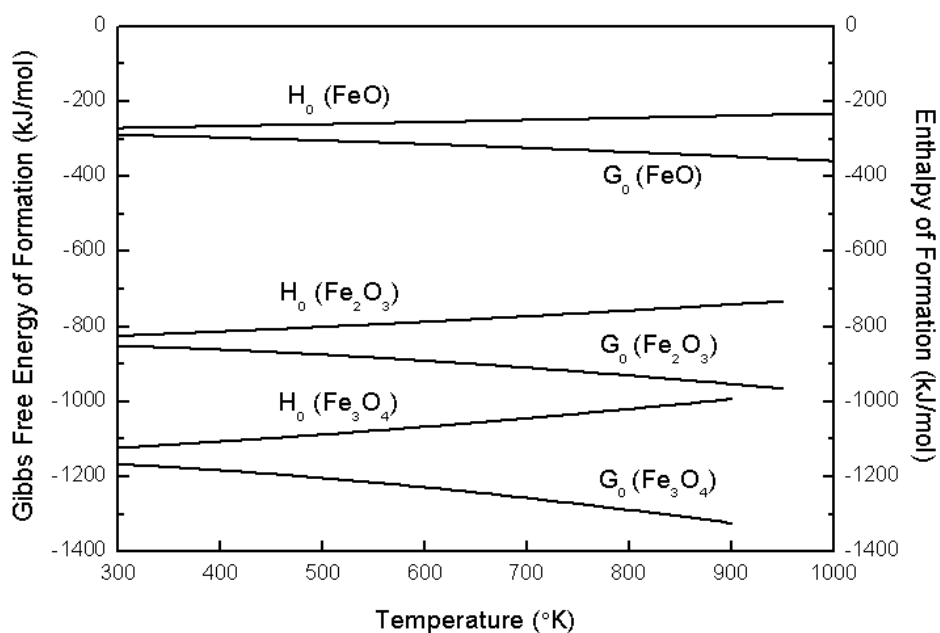


Figure 3.12 Gibbs Free Energy and Enthalpy of Formation of Different Oxides of Iron as a Function of Temperature.

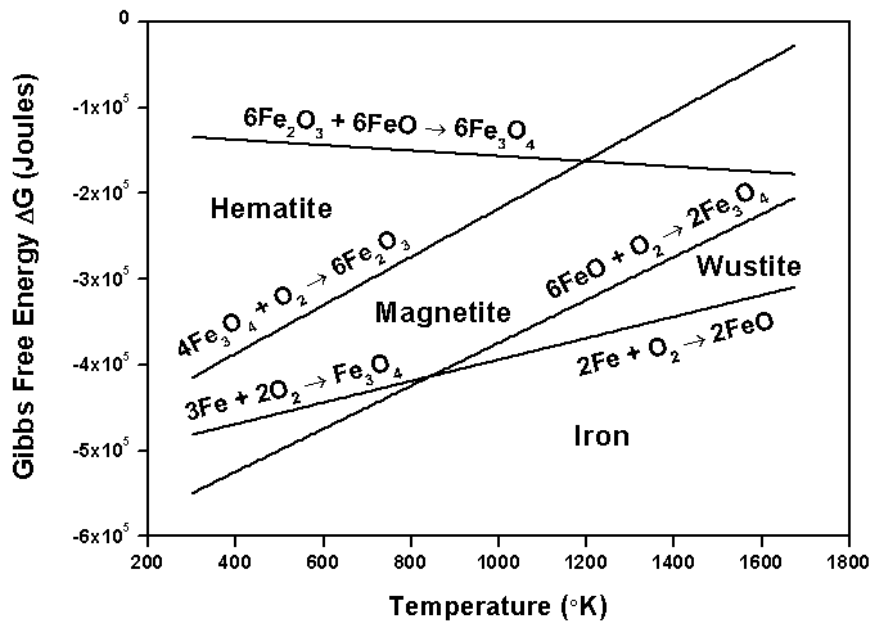


Figure 3.13 Ellingham Diagram for the Formation of Oxides as a Function of Temperature. Also, the Regions of Stabilities of the Various Different Oxides of Fe. are Shown in the Diagram.

3.3.7 Nano-Indentation of Tribofilms

Nano-indentation tests were carried out using a Hysitron Triboindenter equipped with a NorthStar cube corner probe with a tip radius smaller than 40 nm. Tribofilm samples were generated running wear tests for 15,000 cycles under 24 kg load. Indentations were carried out using a trapezoidal load function (load as a function of time) with a 5 s linear loading segment, a 2 s holding segment (at the maximum indentation load) and a 5 s linear unloading segment. Ten indentations were performed on each sample with peak loads ranging from 15 μN to 1500 μN . The reduced elastic modulus and hardness of the tribofilm are measured during each indentation. Figure 3.14(a) and (b) shows the plots of hardness and reduced modulus as a function of vertical displacement in tribofilms from ZDDP and ashless DDP. In the case of ZDDP, the hardness decreases from 20 GPa at the surface region (<5 nm) to 8 GPa at the depth of 50 nm. Beyond 50 nm, the hardness remains almost constant close to 8 GPa that is close to the

hardness of the steel substrate indicating the substrate effect dominating the measured values. In case of ashless DDP, the hardness values remain at around 5 GPa throughout the tested thickness. This data is also consistent with the observations made using the FIB where the thickness of the ashless DDP tribofilms was found to be around 400 nm. Therefore, even up to 300nm of vertical tip displacement into the tribofilm, the measured hardness values are not affected by the steel sub substrate in the case of tribofilms formed from ashless DDP. A similar trend is observed when looking at reduced elastic modulus of the two samples. The ZDDP tribofilm has a reduced elastic modulus of about 230 GPa that decreases rapidly to 125 GPa with increasing depth from the surface region to the depth of 50nm beyond which the substrate effect becomes pronounced and the measured reduced elastic modulus increases to that of the steel substrate, i.e. 200 GPa. The reduced modulus of ashless DDP remains between 100 GPa and 140 GPa and never reaches the reduced modulus of steel through the tested thickness. All things considered, the surface of tribofilm of ZDDP is harder but the bulk is more compliant. On the other hand in the case of ashless DDP, all areas of the tribofilm are smoother and the hardness and reduced modulus are lower than ZDDP.

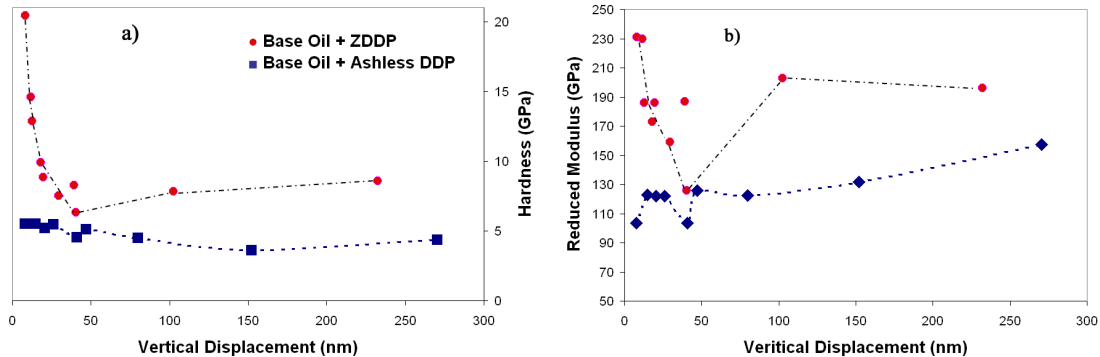


Figure 3.14 Plots of (a) Hardness and (b) Reduced Modulus as a Function of Contact Depth for Peak Indentation Loads Ranging from 25 μN to 1500 μN for Tribofilms Generated from ZDDP and Ashless DDP in Mineral Oil.

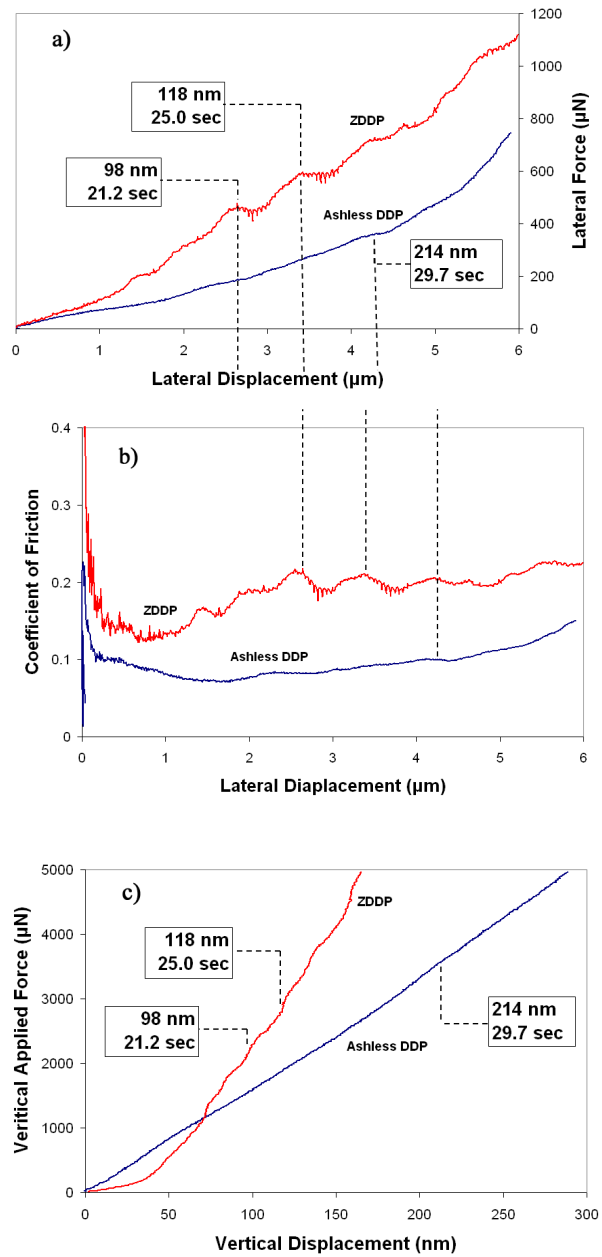


Figure 3.15 Scratch Test with Ramp Force of 5000 μN on Tribofilms from ZDDP and Ashless DDP in Mineral Oil. (a) Lateral Force versus Lateral Displacement; (b) Coefficient of Friction versus Lateral Displacement, and (c) Vertical Applied Force versus Vertical Displacement.

3.3.8 Nano-Scratch of Tribofilms

Nano-scratch tests were performed in order to study the tribofilms' resistance to scratch. This is of particular importance as the wear debris composed of oxides and other hard constituents when trapped between two contacting bodies results in scratch and breakdown of the tribofilm. The intrinsic resistance of the tribofilm to scratch provides important insights into the resistance to breakdown of the tribofilm, thickness of the tribofilm and its delamination characteristics.

The probe used to perform the scratch tests was a 2 μm radius conical tip with 90° tip angle. The load function used for scratch tests dictated that while the tip moved a lateral distance of 6 μm at a constant speed, the applied normal force would increase linearly from 0 μN to 5000 μN . In each scratch test, vertical displacement (tip penetration depth) and the lateral resistance force, i.e. the force resisting the lateral movement of the tip, were measured. Figure 3.15(a) and (b) shows the plots of lateral displacement versus the lateral force and coefficient of friction which was calculated by the ratio of measured lateral force to applied force. Figure 3.15(c) shows the graph of vertical force as a function of vertical displacement. Here, the vertical load is controlled and the vertical displacement is the measured response. As the tip moves laterally, the linear increase in the applied normal force results in a progressively deeper scratch. During scratch tests, with increasing depth of scratch, resistance against the lateral movement of the tip, i.e. the measured lateral force, increases due to increased contact area and pile-up of material in front of the probe. The measured lateral forces in the case of ZDDP tribofilm are larger than the values measured for ashless DDP tribofilm. Figure 3.15(b) shows the coefficient of friction as a function of lateral displacement. While the measured value of the coefficient of friction for ZDDP tribofilm averages around 0.2, for ashless DDP this value hovers around 0.1 which can be explained by the more compliant nature of the tribofilm generated by the ashless DDP which is also evident in the relatively smaller values of measured hardness and reduced elastic modulus as shown in figure 3.14. Both ZDDP and DDP tribofilms have

higher coefficient of friction at the initial stages of each scratch test, which can be the result of the surface being harder than the bulk of the tribofilm. For the ZDDP tribofilm, the coefficient of friction values drop at several points (figure 3.15(b)) while the DDP tribofilm exhibits a smooth coefficient of friction versus lateral displacement graph. These drop points in the coefficient of friction graphs can be explained by cracking of the tribofilm and delamination of tribofilms. The two main drop points in ZDDP tribofilm, both occur at depths close to 100 nm, which is the observed average thickness of the film in this case (FIB data), and can be attributed to separation of tribofilm from the substrate under shearing force of the scratch test resulting in sudden drop in the amount of force required to move the tip in the lateral direction. In case of the ashless DDP tribofilm, the penetration of the probe into the DDP tribofilm increases constantly and in a relatively linear fashion. Here, due to presence of a much thicker tribofilm (>400 nm), the probe remains inside the tribofilm and away from the substrate during the entire scratch test. Thus, the measured properties of the tribofilm are not affected by delamination of the tribofilm. The smaller overall lower vertical displacement of the tip in the case of ZDDP tribofilm is also a result of the presence of a harder and less compliant film.

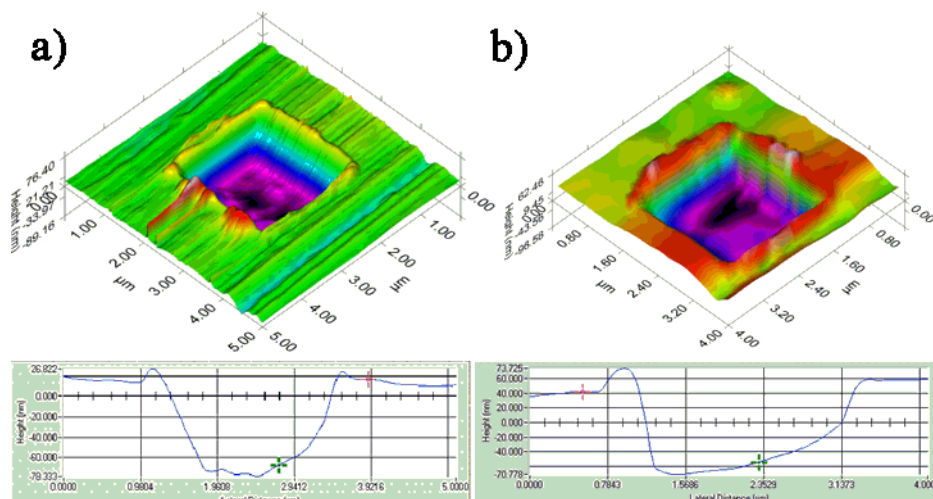


Figure 3.16 Three-Dimensional Graphical SPM Images of the Tribofilm Surfaces after Scanning Wear Tests. The Three-Dimensional Wear Images and the Cross-Sectional Profiles: (a) of ZDDP and (b) of Ashless DDP.

3.3.9 Scanning Nano-Wear Tests of Tribofilms

Figure 3.16 shows the 3-dimensional images obtained from an area of each tribofilm on which, scanning nano-wear tests were performed using the Triboindenter. Scanning nano-wear tests were run in the SPM (scanning probe microscopy) mode under a constant normal force of 75 μN on an area of 2 μm by 2 μm . SPM images of the post-wear area (figure 3.16) were obtained by scanning a larger area, encompassing the worn area with the tip exerting a nominal force of 1 μN necessary to capture the topographic data of the surface while being small enough not to damage or wear the surface any further. The depth of the wear scar in both cases (ZDDP and DDP tribofilms) is around 95 nm. Although the amount of material removed is the same for both tribofilm samples, but since the DDP tribofilm is about 400nm thick, the removal of 100nm (depth) of materials still leaves more than 75% of the tribofilm thickness intact, keeping the substrate from exposure while in the case of ZDDP tribofilm, this amount of material removal (100 nm) will inevitably result in the exposure of the surface and the loss of antiwear properties of the film.

3.3.10 Phenomenological Model of Tribofilm Formation

Figure 3.17 shows the phenomenological models of antiwear tribofilms generated from ZDDP and ashless DDP based on insights obtained from the different characterization techniques employed in this study. The thickness of ZDDP tribofilm is around 100 nm and the thickness of DDP tribofilm is around 400 nm based on FIB observations which is also confirmed by nano-mechanical testing of the two tribofilms. EDX spectroscopy confirms the presence of P, S, oxygen and carbon in both tribofilm samples. The relative amount of phosphorus to sulfur was found to be higher in the DDP tribofilm than in the ZDDP tribofilm. The EDS spectra obtained from DDP tribofilm also displays higher intensity peaks of oxygen and carbon in comparison to ZDDP tribofilm due to higher amounts of phosphates inside the tribofilm as well as the possible presence of more organic compounds on the surface. XANES spectroscopy data obtained from the two tribofilms provides valuable chemical information for developing

phenomenological models of the tribofilms. The tribofilms generated from both ZDDP and DDP mostly consist of short chain iron pyrophosphates. Sulfur is present as mostly iron sulfates with small amount of iron sulfides. The hardness and stiffness data from nano-indentation test suggest that the tribofilm of ZDDP consists of a 15 nm-thick surface crust consisting of possibly highly cross-linked polyphosphates with relatively higher hardness and a more compliant bulk underneath the harder crust. DDP tribofilms on the other hand, are composed of a relatively uniform and compliant phosphate glass matrix through the thickness of the film. The summary of the above observations is illustrated in the models of the two tribofilms shown in figure 3.17(a) and (b).

3.4 Conclusion

Ashless DDP had better antiwear performance than ZDDP in the Ball on Cylinder tester under the extreme pressure conditions used in this study. The morphology, thickness, mechanical properties, and chemical composition of tribofilms formed from ZDDP and ashless DDP formed under extreme pressure testing conditions were investigated with various analytical techniques, i.e. SEM, EDX, FIB, TEM, nano-mechanical testing, and XANES. It was found that the thickness of the ZDDP tribofilm is about 100nm and it chemically consists of short chain pyrophosphates and iron sulfates with small amounts of iron and zinc sulfide. The surface region of this tribofilm is harder and stiffer while the bulk is softer and more compliant. This structure is the key to antiwear properties of ZDDP tribofilms since the harder crust protects the film from scratching and material removal while the compliant bulk dissipates the energy of possible impact on the tribofilm. On the other hand, the ashless DDP forms tribofilms (under the testing conditions of this study) that are significantly thicker (400 nm) and are similar to ZDDP tribofilms in chemical structure. The tribofilm of DDP is uniform and compliant (compared to the steel substrate) through its thickness and thus protects the surface by effectively covering the substrate.

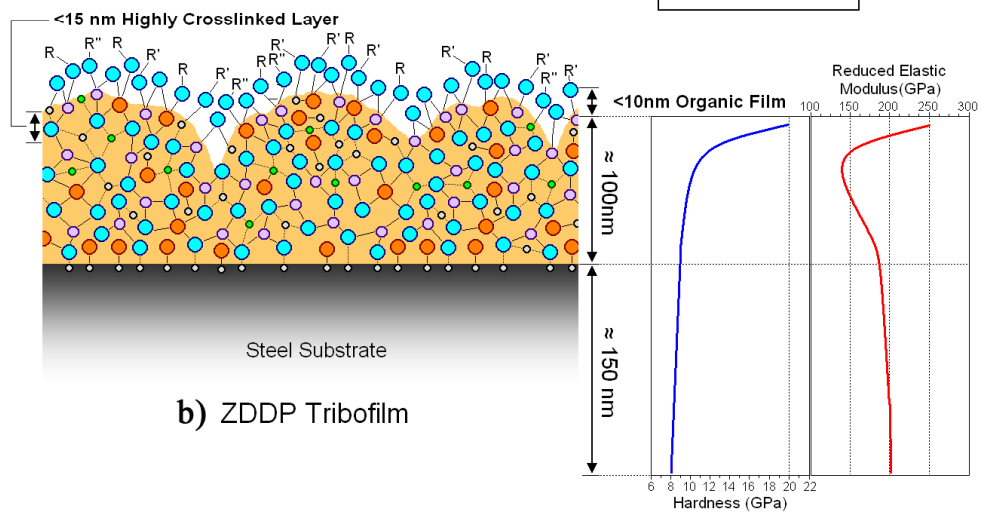
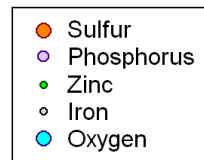
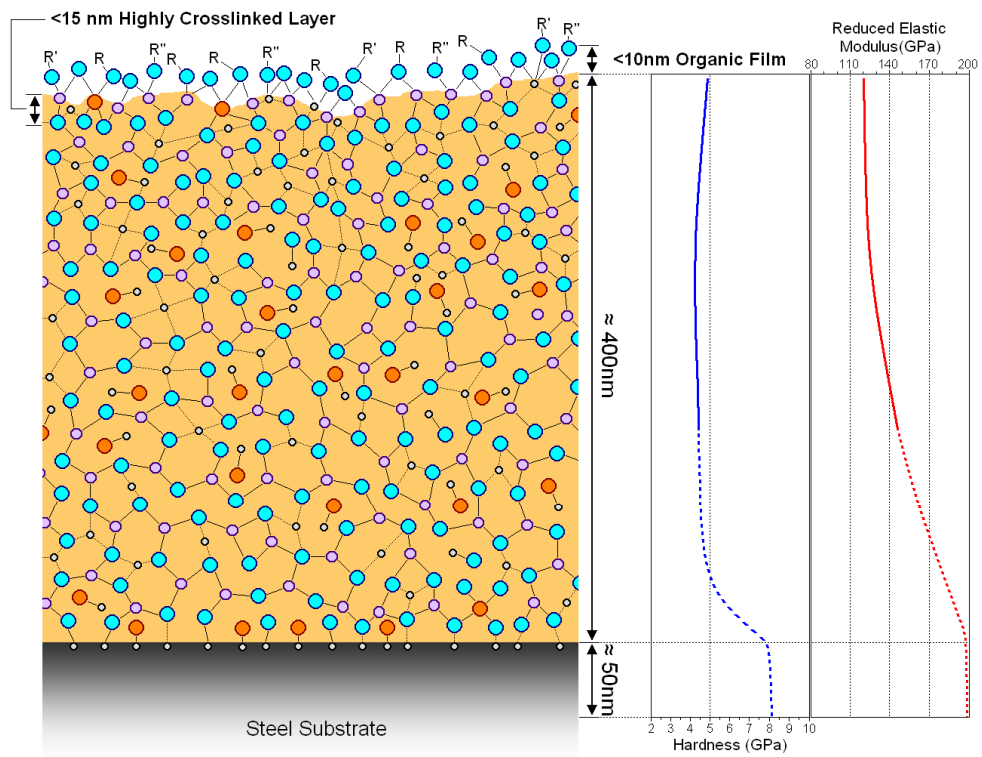


Figure 3.17 Phenomenological Model of Tribofilms Constructed Based on SEM, EDS, FIB, Nano-Indentation, Nano-Scratch, Nano-Wear, and XANES Spectroscopy Data: (a) Ashless DDP Tribofilm and (b) ZDDP Tribofilm.

CHAPTER 4

TEM ANALYSIS OF WEAR DEBRIS FROM TRIBOLOGICAL TESTS: ASHLESS ANTIWEAR COMPOUNDS

Surfaces of catalytic converters are often deactivated by the deposits of P and S as well as metallic and organometallic deposits. Recent approaches have included developing formulations lower in phosphorous and sulfur as well as using ashless antiwear agents. In this study, six different ashless antiwear agents, including an ashless neutral dialkyl dithiophosphate (DDP-1), an acidic dialkyl dithiophosphate (DDP-2), an alkylated triphenyl phosphorothionate (A-TPPT), a butylated triphenyl phosphorothionate (B-TPPT), a triphenyl phosphorothionate (H-TPPT), and an amine phosphate (AP-1) were studied. These antiwear agents all at a nominal composition of 0.1 wt. % P were diluted in base oil and wear performance was examined using a ball on cylinder tribometer where a limited quantity of oil (50 μ l) was used in boundary layer and a contact load of 24 Kg was used. Of the chosen antiwear agents the acidic dialkyl dithiophosphate offers the best wear protection followed by the alkylated triphenyl phosphorothionate, the butylated triphenyl phosphorothionate, the triphenyl phosphorothionate, and the amine phosphate. The amine phosphate has the worst wear performance and the neutral dialkyl dithiophosphate had the shortest time to failure. The wear surface was examined in a scanning electron microscope (SEM) and wear debris harvested from the wear test was examined in a transmission electron microscope (TEM).

4.1 Introduction

Lubricants have an important role to reduce the wear and the friction and to increase the efficiency and the life of automobile engines. Additives are used to supplement the limitations of lubricants and to enhance the performance of base oils. [6,91] These antiwear

additives, extreme pressure additives, detergents, antioxidant, dispersants, and viscosity improvers are examples of lubrication additives. [15] Recently, as the regulation of EPA (Environmental Protection Agency) has become stricter, the use of environmental friendly ashless additives without heavy metal element in engine applications becomes trendy.

Recently the wear behavior of ashless antiwear agents as possible replacements to metal contained antiwear have been examined. Najman et al. [31,47,49] have showed that diaryl phosphate, triaryl phosphate, amine phosphate, dialkyl dithiophosphate, and triphenyl phosphorothionate have potentialities for extreme-pressure and antiwear performance. They have compared their tribological properties and chemical compositions of their tribofilms using atomic force microscopy (AFM), X-ray absorption near edge structure spectroscopy (XANES), and X-ray photoelectron emissions microscopy (X-PEEM). Zhang et al. [3,4] compared ZDDP with an ashless neutral dialkyl dithiophosphate (DDP) about thickness, morphology, and chemical constitution of their tribofilm. They concluded that antiwear performance of ZDDP is superior to neutral ashless dialkyl dithiophosphate, but the combination of ZDDP and DDP is sufficient to provide very good wear protection. Camenzind et al. [18] found that an ashless acidic dialkyl dithiophosphate has superior antiwear performance with high resistibility of oxidation and hydrolysis. Heuberger and his companion [108] tested oils containing triphenyl phosphorothionates substituted with alkyl chains of three different lengths under boundary condition. They reported the effects of load, temperature, and additive chain length for tribofilm formation and their reaction mechanisms. Finally, they found alkylated phosphorothionates have thinner films in comparison with ZDDP because of a lack of counter-ions in the system. [108]

The study of wear debris provide with the clue to understand the mechanism of formation of tribofilm and the properties of tribofilm because wear debris are portions of reaction film which are taken out by the frictional movement. Several researchers have studied the nature of wear debris by transmission electron microscope (TEM) analysis. A prior study using FeF₃ as an additive to catalyze the decomposition of ZDDP in a wear test found evidence of

Fe₂O₃ in the wear debris. [109] Martin also reported in his TEM study that tribofilms are composed of very thin flake shape amorphous glasses and mixture of iron and iron oxide, especially Fe₂O₃. [110,111] Recently Mourhatch and Aswath [27] found the crystallines in the tribofilm and the wear debris are close to Fe₃O₄. However, any researches haven't yet reached clear conclusion so far.

In this study, the mechanism of antiwear behavior under boundary lubrication conditions was studied using six different ashless antiwear agents. Boundary lubrication tests with a limited amount of lubricant were conducted to evaluate the antiwear performance. The tribological surface was examined using scanning electron microscopy. The wear debris from the boundary lubrication tests was examined in a transmission electron microscope to characterize the nature of the tribofilms forms.

4.2 Experimental Details

4.2.1 Materials

Six different ashless antiwear chemistries were studied under boundary lubrication conditions. We separate six samples into three different categories. A neutral ashless dialkyl dithiophosphate (DDP-1) and an acidic ashless dialkyl dithiophosphate (DDP-2) are included in ashless dialkyl dithiophosphate group. An amine phosphates (AP-1) is in the amine phosphate group alone. An alkylated triphenyl phosphorothionate (A-TPPT, R=H or p-nonyl), a butylated triphenyl phosphorothionate (B-TPPT, R=H or tertiary butyl), and a triphenyl phosphorothionate (H-TPPT, R=H) belong to the triphenyl phosphorothionate group. The difference among triphenyl phosphorothionates is concerned with the lengths of corresponding alkyl chain which are mentioned in the above parenthesis. The structure and other physical and chemical properties of these materials are shown in table 4.1. Each of the antiwear chemistries was diluted in a 100 N base oil to yield a concentration of 0.1 wt % phosphorus.

Tungsten carbide balls that are 6.25 mm (1/4 inch) in diameter and Rockwell hardness of 78 HRc hardness are used as the stationary part and Timken roller bearing rings (Model M12610) that have 50 mm (2 inch) diameter and Rockwell hardness of 62 HRc hardness is the moving part. The balls and rings are cleaned very well with hexane, acetone, and also brushed and ultrasonic-cleaned to remove any traces of machining oil on the rings and any contaminants on the balls.

Table 4.1 The Chemical Structures and Properties for Six Different Antiwear Ashless Additives [112-117]

Sample	Additive	Chemical Structure	Flash Point	Decomposition Temp.	Temp. for 50% wt. Loss
DDP-1	Neutral DDP		114 °C	80°C-250°C	180 °C
DDP-2	Acidic DDP		162 °C	125°C-240°C	210 °C
AP-1	Amine Phosphate		135 °C	125°C-260°C	240 °C
H-TPPT	TPPT		>200 °C	225°C-400°C	250 °C
B-TPPT	Butylated TPPT		162 °C	180°C-320°C	290 °C
A-TPPT	Alkylated TPPT		108 °C	125°C-350°C	325 °C

DDP: Dialkyl Dithiophosphate, TPPT : Triphenyl Phosphorothionate

4.2.2 Tribological Testing Procedure

A Ball-On-Cylinder Lubricity Evaluator (BOCLE) designed and built at the University of Texas at Arlington was used to conduct the tribological tests under boundary lubrication. Prior to the application of the test oil chemistry the contact surface was prepared by using mineral base oil and a minor load of 6 Kg for a duration of 2000 cycles. The surface was cleaned with

acetone and hexane to remove any debris and remnant oil without removing the ring from the test fixture. Subsequently, 50 μl of oil was used in each test, and delivered using a surgical syringe at the point of contact between the ball and the ring. The ring was then rotated manually to ensure an even distribution of oil in the contact area between the ball and cylinder. The details of the experimental setup are provided in detail by Mourhatch and Aswath. [76] The measured properties include coefficient of friction, contact temperature, scuffing load and number of cycles.

The applied load was increased from 6 Kg to 24 Kg gradually over 2000 cycles of at the start of the test to ensure that no scuffing occurred during the start of the test. Once the test load reached 24 Kg it was maintained constant for the duration of the test. All tests were conducted at a rotation speed of 700 RPM (109.96 meters/minute). Duration of the test was fixed at 15,000 cycles unless the oil failed prior to that period. After completion of testing, a stylus profilometric trace was conducted using a Mahr M1 Perthometer to get the surface profile of the wear scar at 6 locations at 60° intervals along the surface of the ring. The wear cross section was used to calculate the wear volume at the end of the test.

4.2.3 Evaluation of Tribological Test

The nature of the wear occurring at the surface is best studied by examining the surface of the wear tracks. A Hitachi S-3000N Scanning Electron Microscope (SEM) was used to get secondary electron images of the wear track.

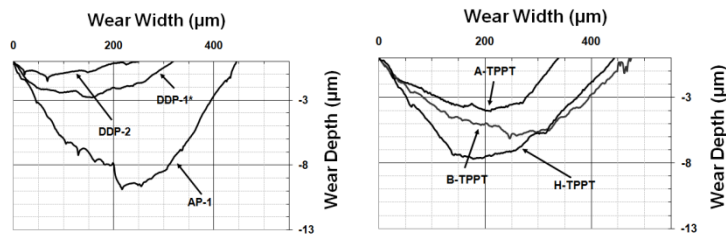
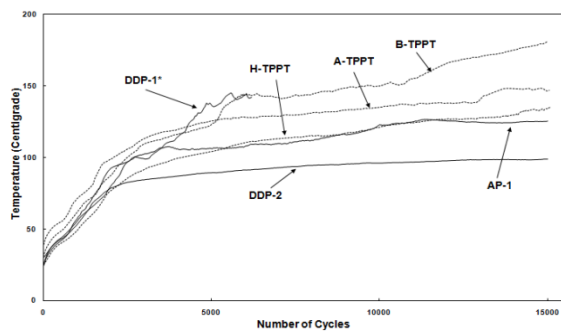
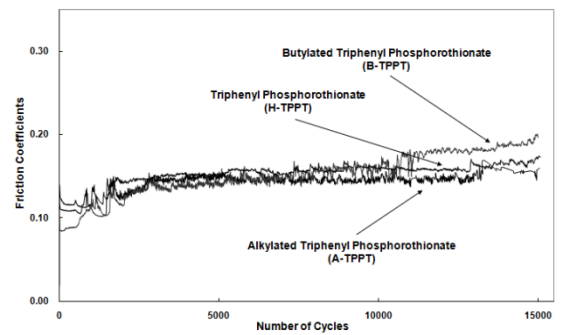
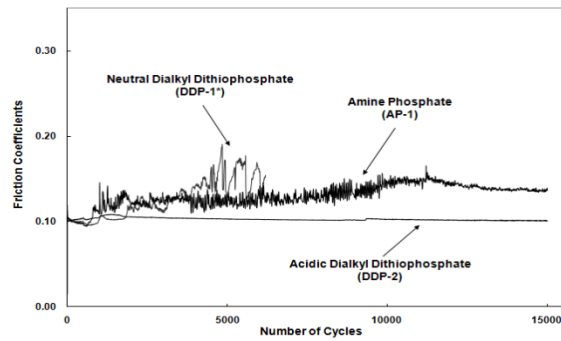
Wear debris carries information on the chemistry, crystallinity and morphology of the protective tribofilms formed on the surface. [109] All tests were run for a period of 5000 cycles at 700 rpm at load of 24 Kg using 50 μl of oil as described earlier and the wear debris was harvested using a piece of flexible plastic film placed in contact with the ring as it was manually rotated to recover the debris after the end of the test. The oil containing the debris was placed on a 3 mm copper grid coated with a carbon film. The oil in the debris was washed away using hexane solvent. The deposited debris was immediately introduced into the chamber of the

transmission electron microscope (TEM). A JEOL TEM-ASID (1200EX), 120KV was used in all cases. The bright field images at low magnification (20,000 X magnification) were obtained to examine the debris morphology and size. The bright field images of high magnification (200,000 X magnification) were acquired to investigate the structure of the wear debris and the presence of substructure formed in the tribofilm. In addition, the electron beam diffraction patterns of debris (at a camera constant of 60 cm) were obtained to examine the crystallinity and nature of the phases present in the tribofilms.

4.3 Results and Discussion

4.3.1 Analysis of Wear Properties

Figure 4.1(a) and (b) are plots of friction coefficient as a function of number of cycles conducted on BOCLE for all six antiwear chemistries. In each case at least 5 repeat tests were conducted, shown here are representative tests for each case. The DDP-1 had the worst performance of all six of the antiwear additives as it failed prior to 6000 cycles in all tests. Its friction coefficient varies rapidly and exhibits a rapid breakdown of the protective tribofilm. The near contact temperature shown in figure 4.1(c) also increases a sharply coincident with the increase in friction indicating the loss of the protective tribofilm at the interface. On the other hand, the DDP-2 was the best antiwear agent. It showed stable and low friction coefficient for the entire duration of the test with no breakdown of the tribofilm. This is also reflected in the measurement of temperature as a function of cycles that shows a stable and graduate increase as the test progresses after an initial spike at 1000 cycles associated with the breakdown of the DDP-2 and formation of the protective tribofilm. The extent of wear is also very small as evidenced by the shallow wear scar in figure 4.1(d) that is about 1 μ m deep. The amine phosphate (AP-1) also survived the 15,000 cycle duration of the test.



* All tests for DDP-1 failed

Figure 4.1 Wear Properties of Six Different Ashless Antiwear Agents. a) Friction Coefficient of DDPs and AP, b) Friction Coefficient of TPPTs, c) Test Temperature of All Samples, and d) Profilometric Traces of the Wear Traces of All Six Tests.

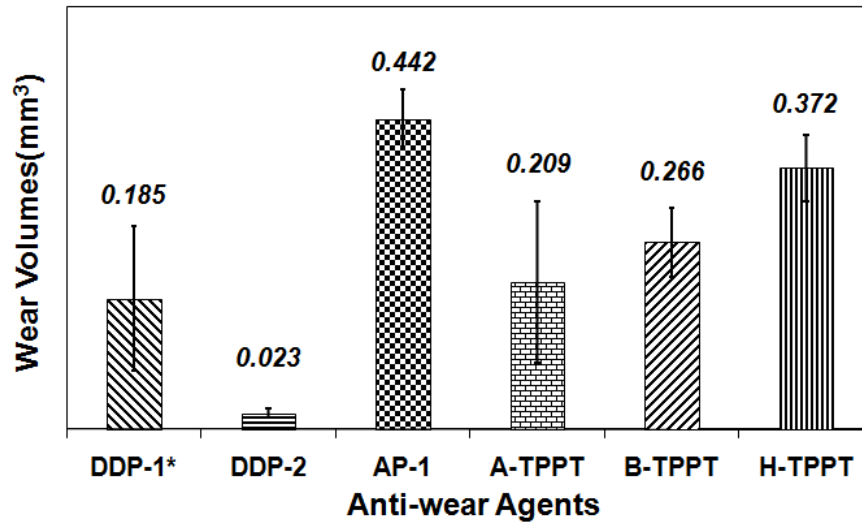


Figure 4.2 Wear Volume of All Six Ashless Antiwear Additives All Tested at a Load of 24Kg for a Period of 15000 Cycles. (* DDP-1 was measured at the failed point.)

However, as shown in figure 4.1(a) the plot of friction coefficient as a function of number of cycles shows a behavior that is typical of stick-slip behavior where there is repeated formation and breakdown of the protective tribofilm. These results in significant debris formation and rapid increase in wear as evidenced in figure 4.1(d) that shows a deep wear scar of 10 μm . In case of wear volume measurement (figure 4.2), the DDP-2 has the best wear performance and lowest wear volume while the DDP-1 has the worst performance as it failed in all cases prior to 6000 cycles. The answer for this early stage failure can be obtained from the research of Ribeaud. [19] He reported that the ashless DDP-1 has high levels of phosphorous volatility when it is compared with a DDP-2, an AP-1, and triphenyl phosphorothionates (TPPTs) by thermo gravimetric analysis (TGA) and flame ionization detection (FID) testing. [19] Therefore, the early failure of tribological test with neutral ashless DDP-1 is supported by its volatile property. In terms of amine phosphate (AP-1), it does not contain any sulfur an important ingredient in the formation of stable tribofilm and hence results in very poor wear performance as reflected by the large wear volume at the end of the test as shown in figure 4.2.

The triphenyl phosphorothionates with three different chain lengths all completed test duration of 15000 cycles. When three triphenyl phosphorothionates are compared the best wear performance is exhibited by alkylated triphenyl phosphorothionate (A-TPPT) followed by butylated triphenyl phosphorothionate (B-TPPT) and triphenyl phosphorothionate (H-TPPT). This is reflected in the wear profiles shown in figure 4.1(d). In addition comparison of figure 4.1(b) and (c) indicates that the friction coefficient and the near contact temperature are larger than DDP-2 and AP-1. Wear volume calculations in figure 4.2 indicate a trend similar to the profilometric traces that indicate that wear performance of the three triphenyl phosphorous compounds are in the order; A-TPPT→B-TPPT→H-TPPT (Good→Bad). Antiwear films on tribosurfaces form as a consequence of the decomposition of the antiwear additive with the formation of glassy films composed of Fe-S-P-O. The flash temperatures of the triphenyl additives are in the increasing order of A-TPPT→B-TPPT→H-TPPT with A-TPPT being the lowest, however, the temperature for 50% decomposition are in the opposite order with H-TPPT→B-TPPT→A-TPPT resulting in A-TPPT having the largest temperature range for decomposition and H-TPPT the least. The alkylated triphenyl phosphorothionate with the lowest flash temperature coupled with the largest range of decomposition temperature has the best wear performance among three triphenyl phosphorothionate compounds. Heuberger et al. in their paper [108] investigated that longer chain phosphorothionates enhance their oil solubility at low temperature (30°C and 80°C), so fewer additive molecules are available in the tribological contact. However, at high temperature (150°C), the temperature of the solution is high enough to thermally decompose the molecule in solution. The reaction temperatures in the BOCLE usually reach around 120°C or higher. In this temperature, thermal stability is more important factor than solubility. Thus, in spite of high solubility for oil solution, the A-TPPT thermally unstable has the best wear protection.

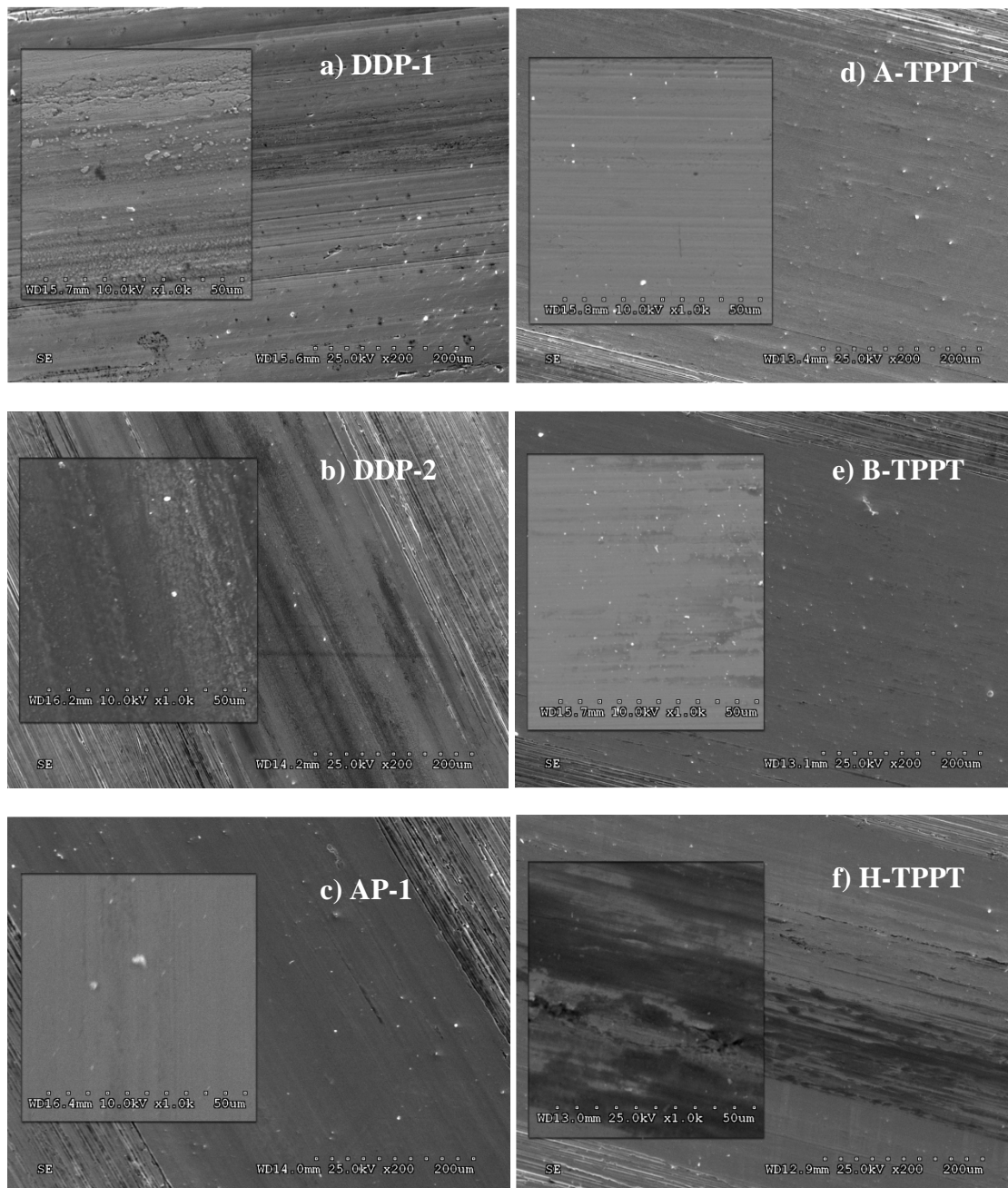


Figure 4.3 Secondary Electron Scanning Electron Microscopy Images of the Wear Track for Six Different Additives. Each Picture Consists of 25 KeV 200X SEM Image (Bigger Picture) and 10KeV 1,000X SEM Image (Smaller Picture). a) DDP-1, b) DDP-2, c) AP-1, d) A-TPPT, e) B-TPPT, and f) H-TPPT

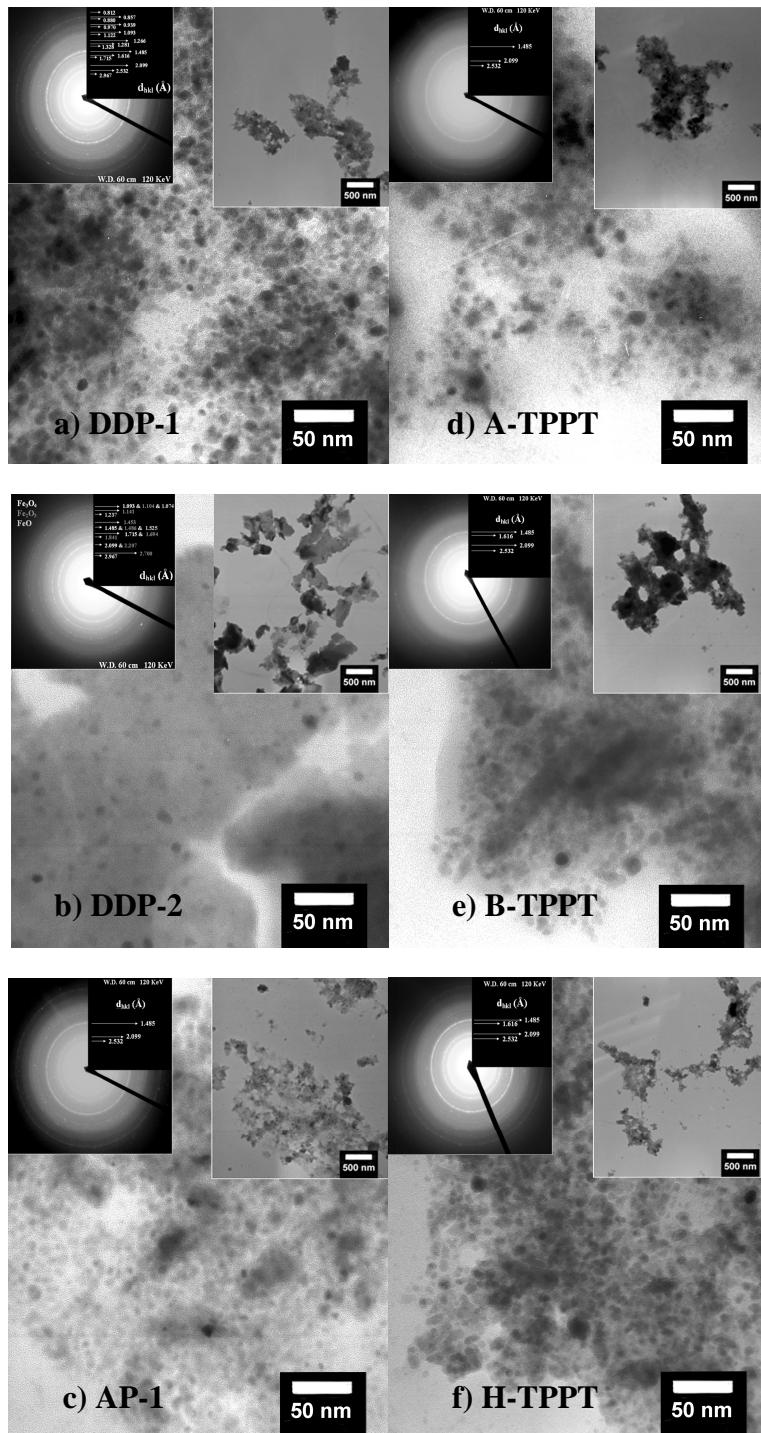


Figure 4.4 TEM Images of the Wear Debris after 5000 Cycles Test for All Six Ashless Antiwear Additives. 20,000 X Low Magnification, 200,000 X High Magnification, and the Diffraction Pattern. a) DDP-1, b) DDP-2, c) AP-1, d) A-TPPT, e) B-TPPT, and f) H-TPPT

4.3.2 SEM Analysis of Wear Track

Figure 4.3 displays the secondary electron SEM micrograph of the wear track of ring lubricated by additives with base oil. Each SEM figure consists of two images; 25 KeV 200 X magnification image of wear track and 10 KeV 1,000 X magnification image of center of wear track. The width of the wear track of the DDP-2 like figure 4.3(b) is the narrowest of all the six antiwear agents as reflected in the wear profile (figure 4.1(d)) and wears volumes (figure 4.2). Well developed Patch-like tribofilms on the wear track are investigated. However, at the other samples, very thin tribofilms, various scratches generated by abrasive wear, and well-polished bare surfaces are observed. Even adhesive wears occur under the boundary lubrication condition as shown at figure 4.3(a) DDP-1 and (f) H-TPPT.

4.3.3 TEM Analysis of Wear Track

Tribological tests were conducted with each of the chemistries at a phosphorous composition of 0.1 wt.%. The tests were conducted at a load of 24 Kg with 50 μ l of oil for duration of 5000 cycles in each case. The duration of 5000 cycles was chosen to ensure that none of the tests had failed and each of the tests would have sufficient time to form a stable tribofilm on the surface and some debris would be generated that would be representative of the tribofilm. The debris harvested at the end of 5000 cycles was examined in transmission electron microscope. The low magnification (20,000X) high magnification (200,000X) and selected area diffraction are shown in figure 4.4. In all six cases we can see that tribofilms are formed, however the particle size of the debris is the largest and best defined for DDP-2 compared to the other chemistries. Higher magnification bright field images of the chemistries all show the formation of very small (<20 nm) particles embedded within a larger amorphous film.

Regarding the analysis of diffraction pattern, the selected area diffraction of the samples indicates that the crystalline phases are oxides of iron, preferentially Fe_3O_4 . Mourhatch and Aswath [27] through the diffraction pattern analysis found the iron oxides in their wear debris are preferable to become Fe_3O_4 . The results of diffraction pattern analysis in this study

also support their finding. However, the ring pattern of DDP-2 that has the best antiwear performance is different from the others. The debris of L-DDP is composed of FeO, Fe₂O₃, and Fe₃O₄. This result explains the process of forming Fe₃O₄ as final iron oxides from Fe by way of FeO and Fe₂O₃ as intermediate stages during the tribological test. The detailed mechanism of formation of oxide nano-particles in the wear debris is well explained in the previous chapter 4.

The films that offered the best protection i.e. ones formed from DDP-2 have the smallest number of these oxides. A short chain ashless dialkyl dithiophosphate that offered one of the poorest wear performances exhibited some of the largest number of these oxide particles. The Fe₃O₄ particles in addition to being crystalline are also known to be quite abrasive resulting in the eventual breakdown of the protective film. A comparison of the three triphenyl phosphorothionate compounds indicate that the best wear performance was exhibited by the alkylated triphenyl phosphorothionate (A-TPPT) and the worst wear performance was exhibited by triphenyl phosphorothionate (H-TPPT). A comparison of the three tribofilms indicates that A-TPPT had the least number of oxide particles while H-TPPT had the most.

In order for an ashless antiwear chemistry to be efficient, not only does it have to decompose and react with the tribological surface and form a protective tribofilm, it also should minimize the oxidation of the Fe present in the underlying substrate and in the amorphous tribofilm.

4.4 Conclusion

Based on the above results, we can draw the following conclusions.

First, the tribofilm formed when DDP-2 is used as the antiwear agent is strong and stable. It offers the best wear performance as evidenced by the lowest coefficient of friction and smallest wear scar and wear volume. The surface of this wear film was the only one that exhibited phosphorous and the bright field TEM of the wear debris indicated that it was largely

amorphous with very few of the crystalline oxide particles suspended in it. Therefore, the DDP-2 is an excellent ashless antiwear alternative to ZDDP.

Second, the DDP-1 is the worst chemistry because it never completed the 15000 cycles in any of the tribological tests. The DDP-1 is much more volatile than the DDP-2. [19] The amine phosphate (AP-1) also has poor wear protection because of the absence of sulfur which helps protect the extreme pressure condition. Therefore, the volatility and the composition of the antiwear additive are important factors for the formation of stable tribofilm. The AP-1 and DDP-1 chemistries showed large number of embedded oxide particles in the tribofilms and offer wear poor wear protection and antioxidant characteristics.

The three triphenyl compounds generally performed poorer than the DDP-2. The triphenyl phosphorothionate (H-TPPT) had the worst friction and the poorest wear performance of the three and the alkylated triphenyl phosphorothionate (A-TPPT) had the best friction and wear performance of the three. A-TPPT is thermally the least stable with the lowest flash temperature and H-TPPT is the most stable with the highest flash temperature and as a consequence A-TPPT forms the most effective tribofilm with the smallest number of oxide particles and H-TPPT the most with the butylated triphenyl phosphorothionate (B-TPPT) in-between.

CHAPTER 5

XANES ANALYSIS OF THERMAL FILMS FORMED FROM ASHLESS ANTIWEAR COMPOUNDS COMPARING WITH ZDDP: ASHLESS DIALKYL DITHIOPHOSPHATES

Tribofilms formed at contacting surfaces protect the surfaces by creating a layer whose chemistry and properties are dependent on the chemistry of the additives used in the lubricant as well as the tribological conditions responsible for the formation of the tribofilms that include temperature and shear stress. Many studies have shown that a thermal route to form films using zinc dialkyl dithiophosphates (ZDDPs) provide a valuable insight into the mechanism of formation of tribofilms. In this study a thermal approach was used to study the mechanisms of thermal films formed on ferrous substrates for a variety of antiwear chemistries that include zinc dialkyl dithiophosphate (ZDDP) and four different ashless dithiophosphates with different alkyl groups. The thermal films were deposited on ferrous substrates by immersion in oil containing these additives at a nominal concentration of 0.08 wt. % phosphorous for durations ranging from 1 min to 4 hours (1, 5, 10, 30 min., and 1, 4 hour). The morphology and film thickness measurement were observed by the secondary electron microscope (SEM) and the optic profilometer. The chemistries of the films were analyzed using X-ray absorption near edge structure spectroscopy (XANES). Phenomenological models were developed to explain the formation of thermal films from ashless thiophosphates.

5.1 Introduction

Zinc dialkyl dithiophosphates (ZDDPs) have been widely used as multifunctional additives in industrial and automotive lubricants for lots of long time. More recently a number of ashless phosphorus containing additives have also been used in the lubricating oil. [118]

Recently with the drive towards lower emissions, the development of environmentally friendly oil additives has gained ground. [16,18,31,119] Ashless thiophosphates that has similar chemical structure as ZDDP with phosphorus and sulfur which play important roles for antiwear performance have been recommended as common possible alternatives to ZDDP. [31,47]

There have been many studies on ashless antiwear additives over the last couple of decades [2, 5-10, 21]. In the early 1980s, some studies reported that ashless thiophosphate and dithiophosphate have promising antifriction and antiwear properties when tested in a four ball tester. [90] Sarin et al. found amino diaryl dithiophosphate has similar antiwear and antifriction performance like metal containing dithiophosphates after testing several different types of dithiophosphates. [91] Fu et al. compared ashless neutral thiophosphates, $(RO)_2PSSR$ and $(RO)_3PS$, with ZDDP. They found that ashless neutral thiophosphates exhibit better load carrying capacity, thermal oxidation, and hydrolytic stabilities than ZDDP. [119] Schumacher and Zinke in their research [120,121] synthesized and tested several types of isogeometrical phosphorus compounds like phosphate, monothiophosphate, and dithiophosphate with different hydrocarbon groups. They determined that both mono- and di-thiophosphates have similar friction and wear properties and their thermal stabilities which are related to antiwear performance of the compounds strongly depend on their hydrocarbon groups.

Recently, various surface analytical techniques have provided fruitful information on both tribofilms and thermal films formed from oil additives. [7,21] In particular, X-ray absorption near edge structure (XANES) spectroscopy has been used to provide chemical and structural characterization of tribological films which mainly consist of phosphorus and sulfur. [15,22-24,26,28,45,57] Najman et al. studied the characteristics of tribological films generated from three different thiophosphate compounds in a couple of studies using XANES. [31,47,51] They found that acidic and neutral dithiophosphates and neutral monothiophosphate generated short chain iron phosphate films and iron sulfates with only traces of reduced sulfur through the films. Acidic dithiophosphate initially have worse wear performance than neutral dithiophosphate and

monothiophosphate, however, at longer period it has better antiwear performance. In case of both neutral di- and mono-phosphates, their phosphate film thicknesses are increased with increased rubbing time and wear is also increased. They found the difference of tribological behavior between acidic and neutral additives. [31,47] Zhang et al. compared ashless neural dithiophosphate with ZDDP using XANES spectroscopy. They found that chemistry variation of films formed from different solutions. The main cation of tribofilm of ZDDP is Zn while the main cation of ashless dithiophosphate is Fe. The tribofilm formed from ZDDP has various chain lengths of phosphates while ashless DDP has only short chain iron phosphates. [3,4]

Thermal decomposition has so far been accepted as a primary mechanism of antiwear film formation even though several mechanism models have been suggested. [21,23] Many studies related to antiwear and extreme pressure (EP) additives on boundary lubrication begin with an examination of the mechanism of thermal decomposition, in which thermal-oxidative decomposition products are absorbed from solution to form the film. [32,43] Yin [24,45], Suominen Fuller [23,57], Zhang [3,4], Nicholls [46], Najman [31,47,51], Pereira [22,28], and Aswath and Ramoun [27,48,76] all based the thermal decomposition as the first step of film formation in spite of a slightly different mechanism of film formation under tribological condition. If it were not for the decomposition process of oil additives, no tribological performance exists on the metal substrates. Therefore, to understand the growth mechanism of thermal film generated from oil additives can become the cornerstone of understanding the whole mechanism for antiwear performance of oil additives.

In order to understand the mechanism of thermal films formed from ashless thiophosphates, four different ashless dithiophosphates were studied along with a secondary ZDDP used for comparison. In this study, XANES spectra for elemental and chemical structural properties of thermal films, SEM for measurement of thermal film thickness, and optic profilometer for surface morphology have been combined to draw the comprehensive model for the mechanism of thermal film of ashless antiwear thiophosphates.

Table 5.1 Chemical Structures and Properties of Samples [112,113,122-125]

Additives	Chemical Structure	Flash Point (°C)	Density (g/cm ³)	TAN Test (mg, KOH/g)
ZDDP		185	1.079	-
DDP-1 Neutral Ashless DDP		114	1.1	-
DDP-2 Acidic Ashless DDP		162	1.104	167
DDP-3		100	1.01	2.0~8.0
DDP-4		142	1.08	-

R1 and R2 - Alkyl

5.2 Experimental Procedure

5.2.1 Materials and Sample Preparations

Four different type of ashless dialkyl dithiophosphates were studied in this study, comparing with zinc dialkyl dithiophosphate (ZDDP). Their chemical structures and properties are shown in table 5.1. All compounds were diluted to 0.08 wt% phosphorus with 100 neutral mineral oil in order to stay within the maximum limit of phosphorus in engine oil for current ILSAC GF-4 and future ILSAC GF-5 standards. All densities of samples are similar while the flash points of DDP-1 and DDP-3 are lower than the others. DDP-2 is a little acidic due to the carboxyl group (COOH).

Thermal films for chemical and morphological analyses were produced on AISI 52100 bearing steel coupons. Thermal films for thickness analysis were prepared on AISI 1075 steel coupons. The chemical compositions of steel coupons and the sizes for experiment are described in table 5.2. The coupons were polished with 5 μm alumina powders. All coupons were ultrasonically cleaned in hexane.

Table 5.2 Chemical Composition and Size of Steel Coupons

Coupons	AISI 52100 Steel	AISI 1075 Steel
Composition	C : 0.98~1.10 Mn : 0.25~0.45 P : max 0.025 S : max 0.025 Si : 0.15~0.35 Cr : 1.3~1.6	C : 0.70~0.80 Mn : 0.40~0.70 P : max 0.04 S : max 0.05
Coupon Size	Disc Type 12.7 mm (1/2 in) Diameter 4.23 mm (1/6 in) Thickness	Plate Type 2 mm X 5 mm 0.05 mm Thickness

In order to prepare thermal films, steel coupons were hung in a glass beaker containing the oil solution which was preheated up to 170 $^{\circ}\text{C}$ in the furnace. Two different types of coupons were heated together in a silicon oil bath at 170 $^{\circ}\text{C}$ for each desired time. In case of ZDDP, DDP-1, and DDP-2, total twelve coupons were immersed together in each container and

two coupons were taken out at each desired interval, 1, 5, 10, 30 minutes, 1 hour and 4 hours, to study the growth mechanism of thermal film. The coupons in DDP-3 and DDP-4 solutions were baked only for 4 hours. Thus, the final stage of thermal films was compared with one another. After immersion, all coupons were gently rinsed with hexane prior to each XANES, SEM, and optic profilometer analysis.

5.2.2 Data Acquisition and Analysis

Thicknesses of thermal films were measured from cross sections using a Hitachi 3000S scanning electron microscope (SEM) operating at 20 KeV in secondary electron mode. XANES spectroscopy was used to analyze the phosphorus and sulfur chemistry in the thermal films. The K edge data of both phosphorus and sulfur were obtained on the Canadian double crystal monochromator (DCM) beamline at the Synchrotron Radiation Center (SRC) of the University of Wisconsin–Madison in Stoughton, Wisconsin. The end station has the energy range of 1500 to 4000 eV and P and S spectra were acquired with a step size of 0.3 eV. The P and S L-edge spectra of lower energy range were collected on the variable line spacing plane grating monochromator (VLS-PGM) beamline at the Canadian Light Source (CLS) facility in Saskatoon, Saskatchewan, Canada. The PGM beamline covers between 5.5 and 250 eV and spectra were acquired with a 0.1 eV scan step for both P and S edges. Both high energy K edge and low energy L edge spectra have two different detection modes. The total electron yield (TEY) mode provides the chemical information of the surface layers. The fluorescence yield (FLY) mode provides the information of the bulk in thermal film.

All surface morphology images were collected using an optical profilometer; Wyko NT9100 Surface Profiler, which is a non-contact method to examine the surface morphology of the tested samples. The basic interferometric principle that light reflected from a reference mirror combines with light reflected from a sample to produce interference fringes, where the best-contrast fringe occurs at best focus, is used in the optical profilometer.

5.3 Results and Discussion

5.3.1 Thermal Film Thickness

All thermal films for thickness measurement were formed on 50 μm of thin AISI 1075 steel coupons (2 mmX5 mm). Each coupon was immersed in the preheated solution (170°C), baked for desired time and then removed individually. The scanning electron microscope (SEM) was used to take the cross section image of thermal film formed on the steel surface. In order to understand the mechanism of thermal film growth, three different ashless dithiophosphate compounds were examined. Figure 5.1 shows the thicknesses of thermal films produced from ZDDP, ashless additive DDP-1, and DDP-2 for different baking times. These thicknesses were measured at least at 20 different spots and averaged. Figure 5.2(a) is a plot that shows the growth of thermal films as a function of time. As the baking time increases, thermal film thicknesses of all three chemistries also increase even though each chemistry has different growth rate and mechanism. The growth kinetics of the thermal films can be broken down into either two steps or three steps. In the first step that lasts approximately 10 minutes, there is a very rapid increase in film thickness followed by a slowdown of the growth rate as shown in Figure 5.2(a). There are two differences in the growth kinetics of thermal films formed from ZDDP and DDP-1 (i) The initial growth rate of the film is much higher in DDP-1 compared to ZDDP resulting in a thicker films at the end of the first stage (≈ 10 minutes) and (ii) Mechanistically the film formed with ZDDP continues to grow after the first stage at a reduced growth rate while the film formed from DDP-1 saturates rapidly and there is minimal growth after the initial phase. In comparison with DDP-2, it behaves differently from ZDDP and DDP-1. DDP-2 does show an initial burst growth similar to ZDDP and DDP-1. However, after this phase the growth is steady state and continues till the 4 hour point yielding the thickest of the thermal films of all three chemistries. In all cases the growth of the tribofilms follows an exponential type growth pattern which can be modeled by the following equation.

$$d = d_0 * e^{kt} \quad \text{(Equation 5.1)}$$

where d is the thickness of thermal film, d_0 is the constant, t is the baking time, and k is the growth rate. By taking natural logarithms on both sides it yields a linear relationship between $\ln(d)$ and time (t) with the slope giving the rate constant, this equation becomes:

$$\ln(d) = \ln(d_0) + kt \quad (\text{Equation 5.2})$$

Figure 5.2(b, c, d) are the plots of $\ln(d)$ Vs. t . Clear variation of growth rates (slope, k , unit: $\mu\text{m}/\text{min.}$) is observed in these plots. In case of ZDDP in figure 5.2(b), two different growth rates are observed. Thermal films of ZDDP nucleate and grow fast until 11.26 minutes with a thickness of $2.459 \mu\text{m}$ and growth rate $k=0.1905 (\mu\text{m}/\text{min.})$ following which the growth rate slows down to $k=0.0012 (\mu\text{m}/\text{min.})$. Thermal films of DDP-1 have three different rates as shown in figure 5.2(c). Initially, its thickness increases rapidly with $k=0.4062 (\mu\text{m}/\text{min.})$ which is twice that of ZDDP until 7.61 minutes and thickness of $3.239 \mu\text{m}$ and the growth rate reduces to $k=0.0088 (\mu\text{m}/\text{min.})$ through 44.98 minutes and thermal film thickness of $5.185 \mu\text{m}$. After about 45 minutes, its growth rate is close to zero. Both secondary ZDDP and DDP-1 likely decomposed rapidly at $170 \text{ }^\circ\text{C}$, and their decomposed products react with steel surface rapidly in the initial stage. Subsequently, the availability of active decomposition product is reduced and the rate of formation of the thermal film is reduced with the more severe outcome seen in DDP-1.

In addition, it is probable that chemical rearrangement or reorganization of thermal films may occur inside the thermal films during this period. The thermal film of ZDDP grows continuously, but at a slower pace. However, the thermal film growth of DDP-1 stops increasing in thickness after 45 minutes. The rapid initial growth coupled with saturation of thickness of DDP-1 may be attributed to the exhaustion of available decomposition product as DDP-1 is not thermally stable with lower flash point ($114 \text{ }^\circ\text{C}$) than ZDDP ($185 \text{ }^\circ\text{C}$) and DDP-2 ($162 \text{ }^\circ\text{C}$). Only structural rearrangement of inside film of DDP-1 through oxidization or hydrolyzing is possible in this region. The plot of DDP-2 in figure 5.2(d) is slightly different from the others. It has three different growth rates like DDP-1. However, the initial growth with $k=0.0799 (\mu\text{m}/\text{min.})$ and $1.606 \mu\text{m}$ thickness at 7.71 minutes is slower than previous two cases.

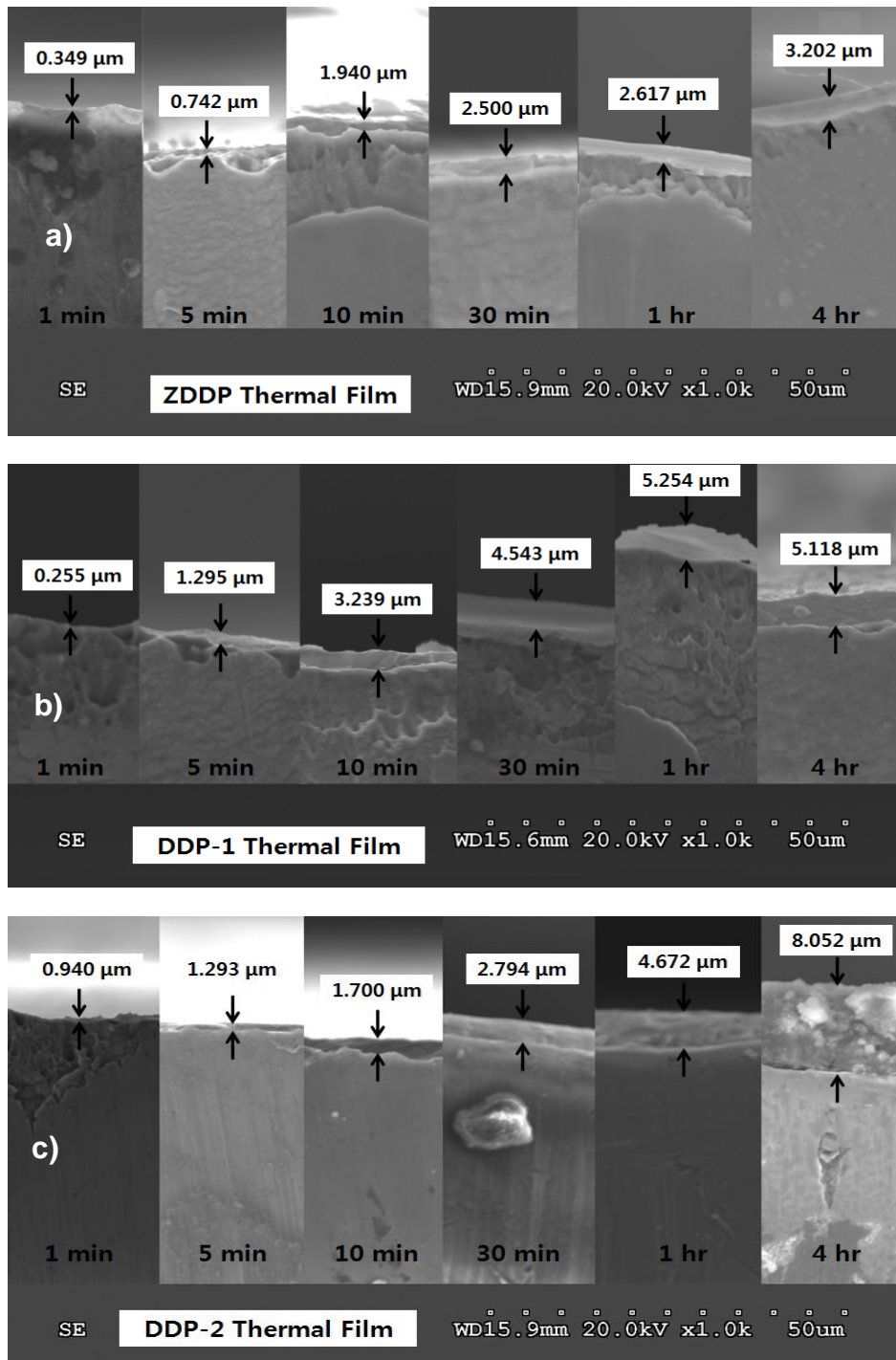


Figure 5.1 Cross-Section Images of Thermal Film Thicknesses Formed from Different Chemistries with the Variation of Time. a) the Thickness of Thermal Film of ZDDP, b) the Thickness of Thermal Film of DDP-1, and c) the Thickness of Thermal Film of DDP-2.

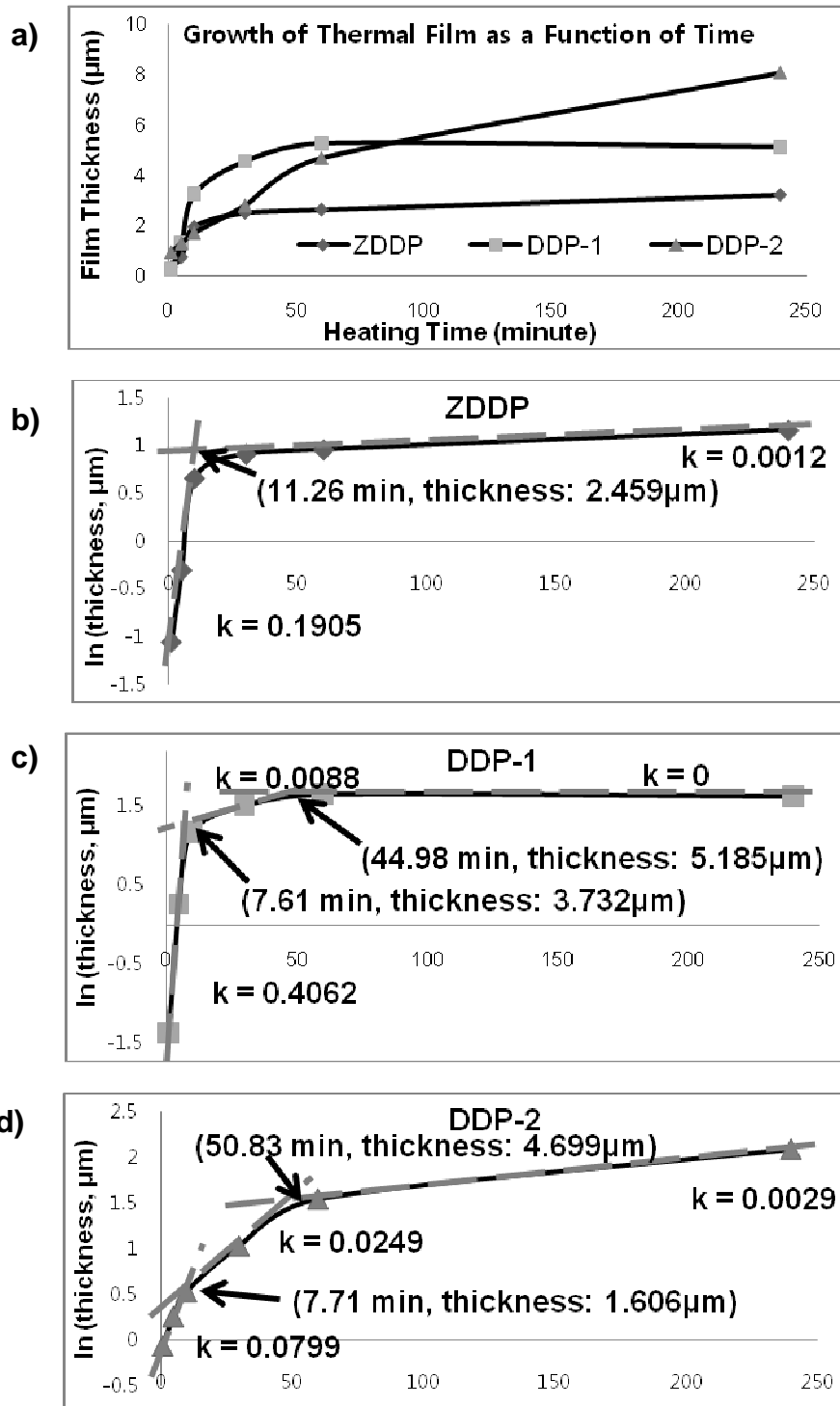


Figure 5.2 Plots of Thermal Film Growth as a Function of Time. a) the Plots of Thermal Film Growth of Three Different Chemistries, b) the Logarithm of Thickness of Thermal Film Formed from ZDDP, c) the Logarithm of Thickness of Thermal Film Formed from DDP-1, and d) the Logarithm of Thickness of Thermal Film Formed from DDP-2.

The intermediate stage is also different. The intermediate growth rate k value ($k=0.0249$ ($\mu\text{m}/\text{min.}$)) has not highly dropped as much as in the case of the previous two additives. This means that its thermal film grows steadily on the steel substrate to around 51 minutes with a thickness of $4.699 \mu\text{m}$ thickness. After 51 minutes, the thermal film of DDP-2 continuously forms with a slower growth rate of $k=0.0029$ ($\mu\text{m}/\text{min.}$), yielding a final thickness at 4 hours of $8.052 \mu\text{m}$. While the flash temperature of DDP-2 is comparable to ZDDP, the activity of the decomposed products is large enough to foster continuous deposition of the thermal film with increased baking time.

Figure 5.3 provides details of the role of chemistry variation on thermal film thickness after 4 hour baking. DDP-3 and DDP-4 have $8.923 \mu\text{m}$ and $6.219 \mu\text{m}$ thickness. Unfortunately, their growth rate and information as time goes on cannot be obtained because only 4 hour thermal films are made. However, as compared with final thicknesses of thermal films from earlier three additives, DDP-3 and DDP-4 may follow the thermal film growth of DDP-2.

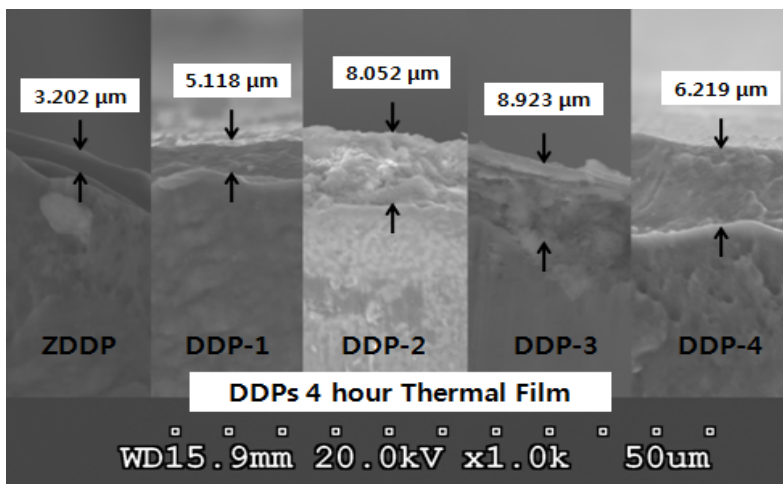


Figure 5.3 Cross-Section Images of Thermal Film Thicknesses Formed from Different Chemistries at 4 Hour.

5.3.2 XANES Analysis of Thermal Film

While thickness measurements provide quantitative information regarding the growth kinetics of thermal films, they do not provide information regarding the local changes of

chemistry of the thermal film as a function of time. X-ray absorption near edge structure (XANES) spectroscopy is appropriate to investigate the chemistry of tribological films formed from lubricant additives. Two different types of XANES spectra are usually acquired. Total electron yield (TEY) mode captures information from the near surface region while fluorescence yield (FLY) mode captures information from the bulk area. The sampling depths of the TEY and FLY at the L edge are around 5 nm and around 50 nm respectively. [47] The sampling depth of the TEY of the K edge is about 50 nm. However, the sampling depth of FLY at the K edge is in the diversity of opinion. Kasrai et al. mentioned bigger than 1 μm in their papers. [3,57,126] Suominen Fuller et al. [23] calculated to be over 10 μm depths. Ferrari and his colleagues insisted around 12–24 μm of the penetration depth. [25] Totir et al. [127] said that the corresponding fluorescence depth would be 3 μm . We believe a reasonable estimate for the sampling depth for K edge spectra for P and S is between 1–3 μm .

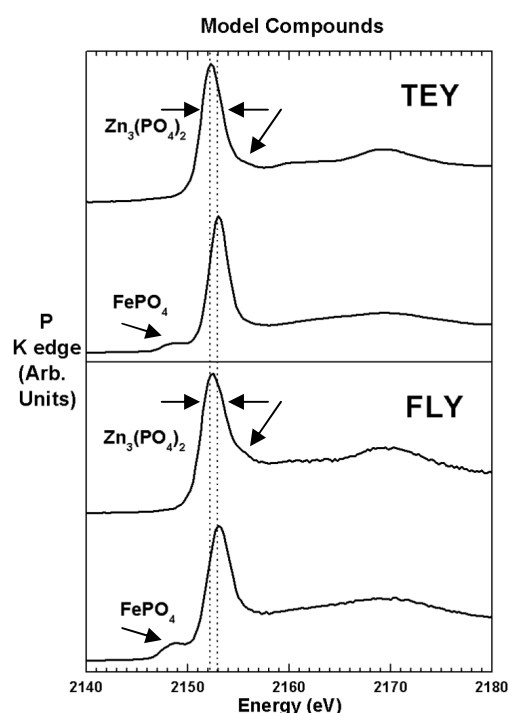


Figure 5.4 XANES Spectra of the TEY and FLY modes at the K edge of Phosphorus Model Compounds: $\text{Zn}_3(\text{PO}_4)_2$ and FePO_4 .

5.3.2.1 Phosphorus Characterization

K edge of Phosphorus

In order to identify the chemical property of samples, the XANES spectra of all thermal films were compared to those of model compounds. Figure 5.4 shows the K edge spectra of phosphorus model compounds respectively. Zinc phosphate ($\text{Zn}_3(\text{PO}_4)_2$) and iron phosphate (FePO_4) were used as model compounds. In figure 5.4, there are a couple of clear differences between two model compounds at both the TEY and FLY modes. The main peak of zinc phosphate is observed at 2152 eV, while one of iron phosphate is located at 2153 eV. In case of $\text{Zn}_3(\text{PO}_4)_2$, it has the shoulder at the right side of main peak and its main peak is a little wider than iron phosphate. In the spectra of FePO_4 , clear pre-edge is observed at the left side of main peak.

In figure 5.5, the phosphorus K edge spectra of thermal films generated from ZDDP at each reaction time are presented. In both TEY and FLY modes, 1 min. film is not well developed. After 5 minutes, the relative intensities of main peak are gradually increased until 1 hour. A 10 minute TEY spectrum was noisy and unstable because of temporary TEY detector error or near-surface contamination. It was removed. After 1 hour, the thermal film formed from ZDDP is well developed as evidenced by the well developed stable spectra at 1 and 4 hours. In fact, with SEM image of the cross section of the thermal films, we know the thermal film of ZDDP continued to grow between 1 and 4 hours even though the growth rate slows down. At all times, the right side shoulder and wide main peak that are the characteristics of zinc phosphate are observed. However, main peak positions are a little changed. The TEY peak of ZDDP thermal film is located at ~2152.5 eV and the FLY peak is at ~2152.7 eV. Thermal films formed from ZDDP baked at 170 °C are mixture of zinc phosphate and iron phosphate with zinc phosphate being the dominant phase in the film with the near surface dominated by zinc phosphates and smaller amounts of iron phosphate in the interior.

Figure 5.6 shows the phosphorus K edge spectra of thermal films generated from DDP-1 as a function of time. The white line peaks are located at 2153 eV which is indicated as an iron phosphate. The narrow width of main peak is also indicative of iron phosphate.

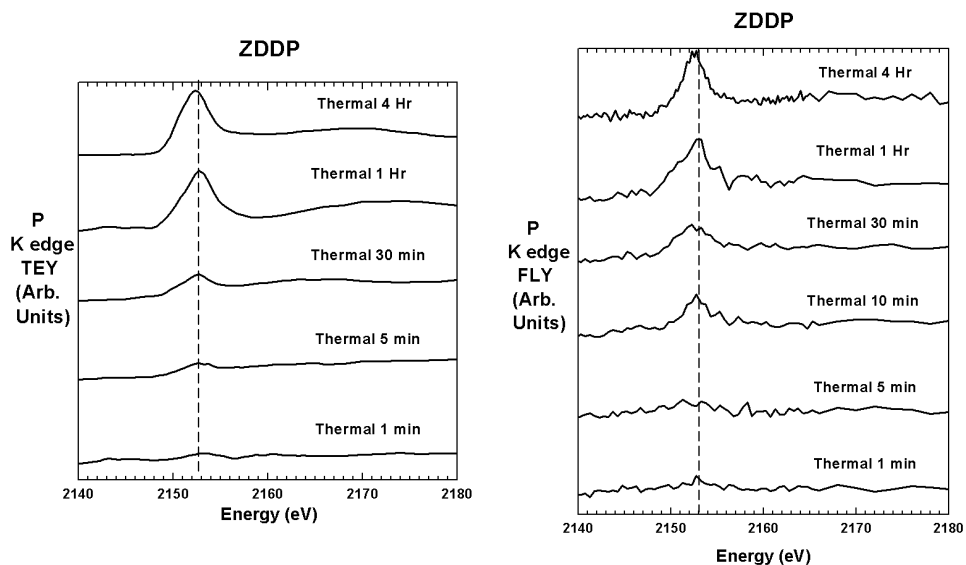


Figure 5.5 XANES Spectra of the TEY and FLY modes at the P K edge of Thermal Films Formed from ZDDP as Baking Time.

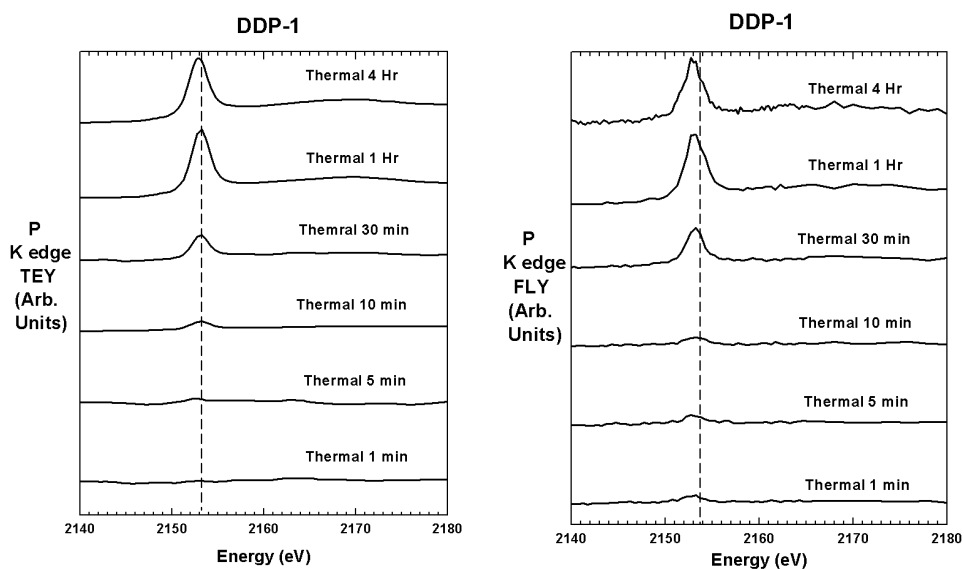


Figure 5.6 XANES Spectra of the TEY and FLY modes at the P K edge of Thermal Films Formed from DDP-1 as Baking Time.

However, these peaks don't have the pre-edge peak which is a characteristic of FePO_4 . Najman et al. in one of their papers [47] tested two different chain lengths of iron phosphates using XANES. They found that only FePO_4 has the pre-edge peak at the K edge of phosphorus but a longer chain phosphate, $\text{Fe}_{10}\text{P}_{18}\text{O}_{55}$, doesn't. The phosphate of thermal films of DDP-1 may be a longer chain iron phosphate rather than an iron ortho-phosphate. During early stages of film formation like the 1 min. test, the thermal films formed are not very stable as evidenced by the very small peaks at the P and S edge. The thermal films grow rather quickly until 1 hour after which the growth stagnates with the spectra from the 1 hour and 4 hour films being very similar. The thickness of post 1 hour thermal film is over 3 μm which indicates that the FLY spectra is only providing information on the top 3 μm of the film with the region underneath not being analyzed in XANES.

The XANES spectra of acidic DDP-2 are shown at figure 5.7. The 1 minute thermal film is unstable. The thickness of thermal film of DDP-2 gradually increased from 5 min. to 1 hour. After 1 hour, SEM images related with the thickness of film provide the evidence of film growth while XANES analysis provides insight into the chemical structure. All the spectra except the 4 hour film have the pre-edge peak clearly. This indicates the thermal film from DDP-2 mainly consists of FePO_4 until 1 hour. Then, this pre-edge disappeared at 4 hour peak. This means that fresh iron phosphates might continuously be generated by active and enough decomposed intermediate product of DDP-2 until 1 hour and after 1 hour, molecular rearrangement of iron phosphates might occur becoming a longer chain iron phosphate. Thermal films continue to grow until the end of the 4 hour test, resulting in a film that is twice as thick as the 1 hour film.

Figure 5.8 presents the K edge spectra of phosphorus for thermal films baked for 4 hours of five different chemistries. DDP-3 and DDP-4 were tested for only 4 hour in order to understand the effect of chemistry variation. In this figure, P K edge spectra of four ashless DDPs are similar and only the spectrum of thermal film of ZDDP shows the indication of zinc

phosphate. Therefore, this explains the variation of alkyl group in oil additives doesn't affect the formation of film at longer term tests but the variation of cation species does.

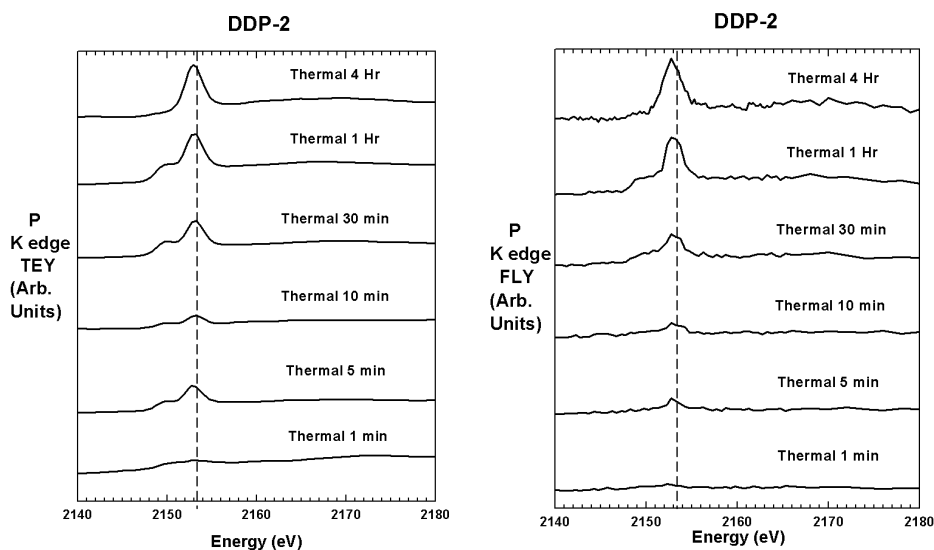


Figure 5.7 XANES Spectra of the TEY and FLY modes at the P K edge of Thermal Films Formed from DDP-2 as Baking Time.

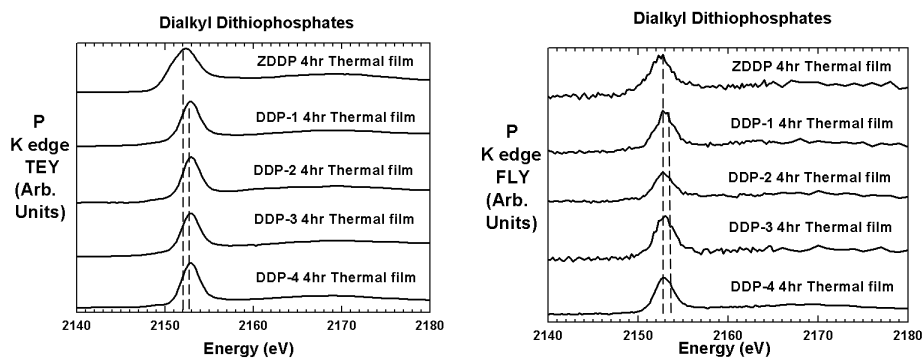


Figure 5.8 XANES Spectra of the TEY and FLY modes at the P K edge of 4 hour Thermal Films Formed from ZDDP and Four Different Ashless Thiophosphates.

L edge of Phosphorus

Figure 5.9(a) is the XANES spectra at L edge of phosphorus model compounds. Zinc phosphate ($Zn_3(PO_4)_2$) and two iron phosphates ($FePO_4$ and $Fe_4(P_2O_7)_3$) are plotted in the graph as model compounds. The FLY mode spectrum of $Fe_4(P_2O_7)_3$ were provided by the center for tribology research in the university of western Ontario. The spectra of phosphates are

composed of four different peaks from (a) to (d). In previous L edge XANES studies for phosphate glasses, all peaks at L edge spectra of phosphorus were characterized by its fine structure which resulted from the spin orbit splitting of the 2p level electrons and the local symmetry of the phosphorus. [67,68,128,129] The peaks (a) and (b) at the low energy side are generally separated by about 1eV and are assigned to the transition of spin orbit split 2p electrons between $2p_{3/2}$ (L3 edge) and $2p_{1/2}$ (L2 edge). The change in intensity of the doublet (a and b peak) is due to the distortion of the phosphate tetrahedral. The main peak (c) has been attributed to transitions to 3p orbitals which are sensitive to the presence of other elements such as oxygen and other cations like Fe or Zn. Peak (d) is due to transitions to 3d orbital in phosphorous. The intensity of peak (d) is also related to four coordinated oxygen. In comparison of the white line (c) peaks of model compounds, zinc phosphate has a slightly lower energy state at 138.7 eV than two iron phosphates at 139.0 eV of FePO_4 and at 139.3 eV of $\text{Fe}_4(\text{P}_2\text{O}_7)_3$. Also, zinc phosphate has a slightly lower pre-edge (a) peak. Between two iron phosphates, $\text{Fe}_4(\text{P}_2\text{O}_7)_3$ has a little stronger intensity of (a) peak and wider white line (c) peak than FePO_4 . Figure 5.9(b) is the FLY spectra of phosphorus L edge of unreacted raw materials which were prepared by dipping transparent plastic films into 50 % diluted by hexane solutions of dithiophosphate additives and drying at the air environment under the sun shine. TEY spectra of raw materials aren't detectable because of non-conductive properties at the surface area. All raw materials except DDP-1 raw material have critical features in comparison of inorganic model compounds. The positions of all peaks are similar with one of zinc phosphate. However, two pre-edge (e) and (f) peaks are higher than the white line (g) peak. This may result from the environmental structure differentiation around phosphorus atom caused by P=S and P-S bonds in undecomposed oil additives instead of P-O bonds of phosphate. On the other hand, P L edge spectra of raw DDP-1 is pretty close to zinc phosphate or iron phosphate with small two pre-edges. It indicates that thermally unstable DDP-1 is already decomposed by sun shine and is oxidized and hydrolyzed by oxygen and moisture atmosphere, then finally becomes phosphoric

acid, H_3PO_4 . That is the reason why DDP-1 raw material look like inorganic metal phosphate.

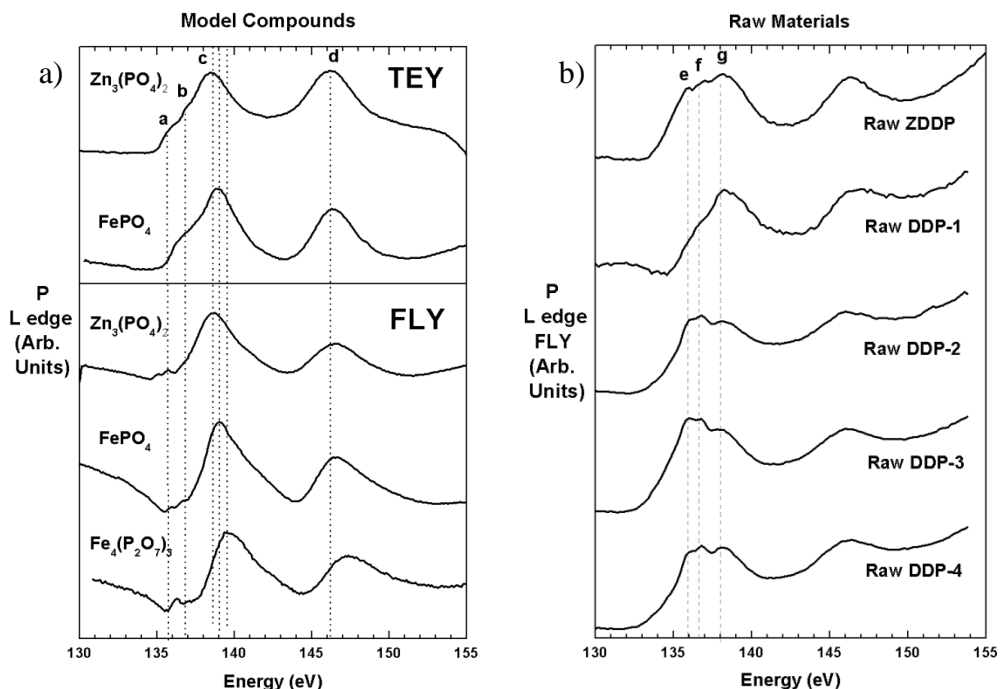
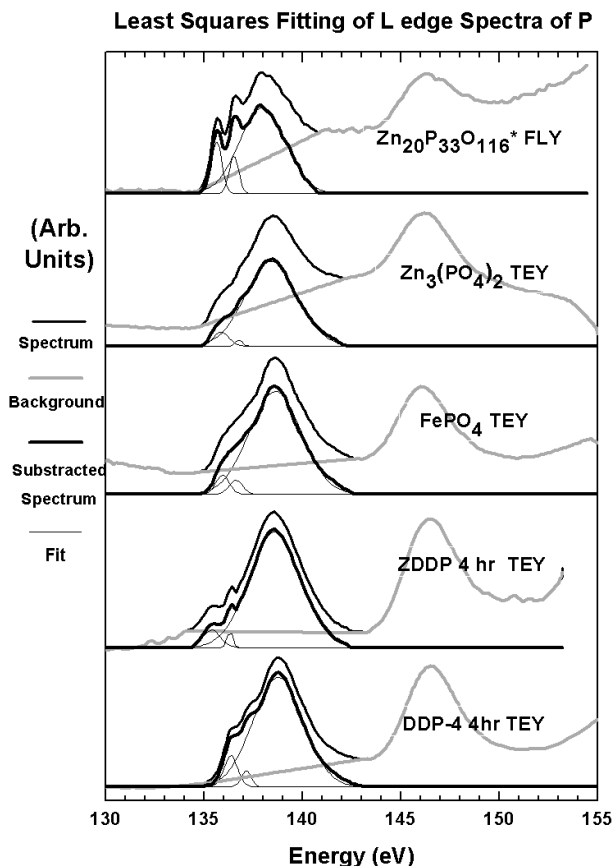


Figure 5.9 XANES Spectra of the TEY and FLY modes at the L edge of Phosphorus Model Compounds. a) TEY and FLY modes of Model Compounds: $Zn_3(PO_4)_2$, $FePO_4$ and $Fe_4(P_2O_7)_3$, b) FLY mode of Raw Materials.

The intensity of peaks (a) and (b) relative to peak (c) has been found to depend on the polyphosphate chain length. [24,67,128] Yin et al. in their paper [128] have shown the relative intensities of peak (a) and (b) are sensitive to the number of phosphorus in the linear polyphosphate glasses using various chain lengths of sodium phosphate glasses. In order to obtain accurate peak positions, widths, and intensities, their all spectra were fitted to Gaussian function using a least-squares program. These peaks have been subtracted by arctangent base lines to consider the excitonic states which are observed in certain solids. However, in this study, the linear background subtraction has been used instead of the arctangent function because the results are not much different and it is much simpler. Another reason is because the analyzed results using the deconvolution by the linear background subtraction can distinguish between orthophosphate, pyrophosphate, and short chain polyphosphate, while ones by the arctangent

background subtraction can't. Figure 5.10 shows five XANES spectra of three different phosphate model compounds and two different thermal films as examples of linear background subtraction and least squares fitting. All spectra consist of clear three different peaks, (a), (b), and (c).

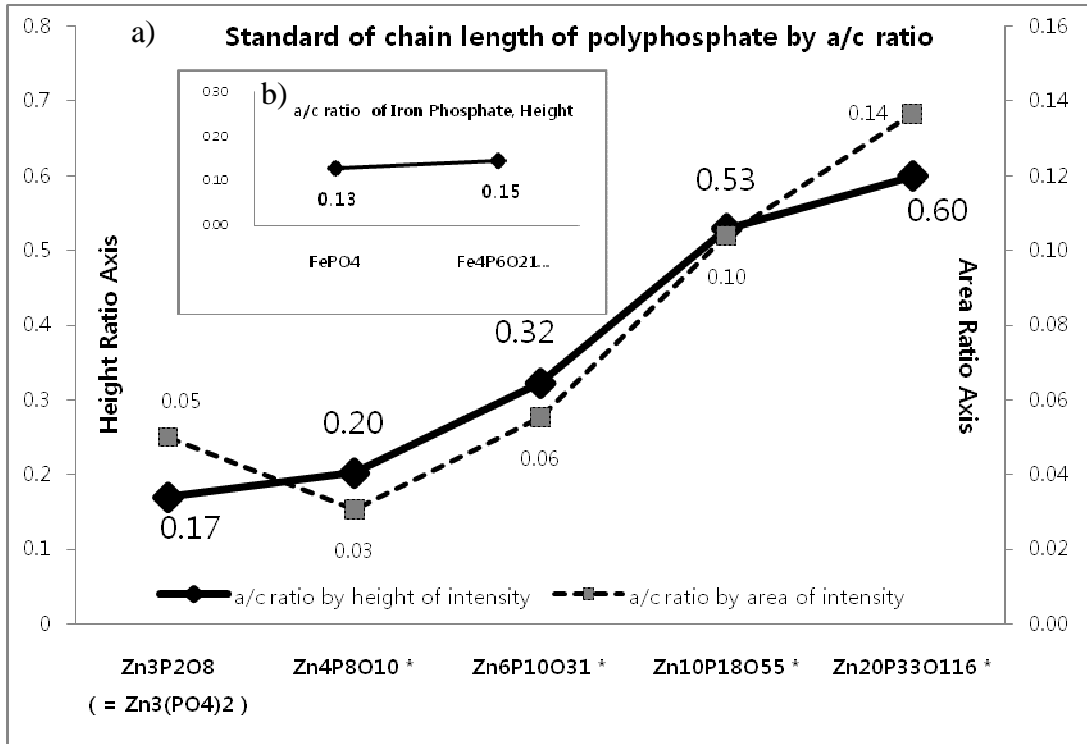


* : this spectrum of model compound was provided by Kasrai et al.

Figure 5.10 The Linear Background Subtraction and the Deconvolution of Polyphosphate Spectra of Three Model Compounds and Two Different Thermal Films: $Zn_{20}P_{33}O_{116}$, $Zn_3(PO_4)_2$, $FePO_4$, ZDDP 4 hour Thermal Film, and DDP-4 4 hour Thermal Film (from Top to Bottom).

The intensity of peak (a) of each sample is differentiated as a different chain length of phosphate samples. In order to compare the chain length of tribological films, the standard for the comparison of chain length is first required. All model compounds were analyzed with this

process and plotted in figure 5.11. Five different zinc polyphosphates which have various chain lengths in figure 5.11(a) (the spectra of polyphosphates marked as a symbol of star * came from the center for tribology research in the university of western Ontario.) and two different short chain iron phosphates in figure 5.11(b) are compared. There are two kinds of relative intensities normalized to peak (c). One is the relative intensity normalized by the areas of peaks. Another is the relative intensity normalized by the heights of peaks.



* : this spectrum of model compound was provided by Kasrai et al.

Figure 5.11 Standard of Chain Length of Polyphosphate Using the a/c Ratio, Relative Peak (a) Intensity Normalized to Peak (c) at P L edge Spectra. a) Two Different Relative a/c Ratios of Various Chain Length of Zinc Polyphosphates, the Left Y Axis is Related to Height a/c Ratio and the Right Y Axis is for the Area a/c Ratio. b) Relative Height a/c Ratios of Iron Phosphate and Iron Pyrophosphate as Two Model Compounds of Iron Phosphate.

The trends of both relative intensities for zinc model compounds are quite similar as presented in figure 5.11(a). Recently, the a/c ratio by the height of peak (a) and (c) have been mainly used in many studies for characterization of tribofilms. [23-25,47,50,68,130] In this study, relative a/c

ratios characterized by the height of peaks will be used as a method to compare the chain length of polyphosphate glasses. In case of iron model compounds, their a/c ratios are also shown in figure 5.11(b). Unfortunately, longer iron polyphosphates as model compounds haven't been tested. Thus, all values of a/c ratio generated from various zinc phosphates are used as the standard of comparison of phosphate chain length. Zhang et al. [4] and Nicholls et al. [130] have used the rule for the phosphate chain length: an a/c ratio of about 0.3 is short chain length polyphosphate, and the a/c ratio of about 0.6 indicates a long chain polyphosphate. Because the linear background subtraction was used in this study instead of arctangent function, the results of a/c ratios have to be changed. In this study, the new standard of chain length of polyphosphate to be suitable for this deconvolution method is used. The a/c ratio below 0.2 means common orthophosphate or pyrophosphate. The value between 0.2 and 0.35 indicates the short chain polyphosphate and the value from 0.35 to 0.55 is the medium chain length of polyphosphate. The polyphosphate with above 0.55 a/c ratio is called as the long chain polyphosphate.

Figure 5.12 to 5.15 show the phosphorus L-edge XANES spectra in TEY and FLY modes of thermal films generated from ZDDP and 4 different ashless DDP. These figures indicate the changes of chain lengths of phosphate thermal films with baking time. 1 minute thermal films of all additives are unstable because their P L edge peaks are noisy. Although the delineation of L edge peak position is not as sharp as the K edge, the positions of white line peak of ZDDP thermal films indicate the composition to be close to zinc phosphate. All main peaks of thermal films formed from ashless DDPs are located near the position of iron phosphate. There is no possibility of remaining undecomposed additives due to small two pre-edge spectra.

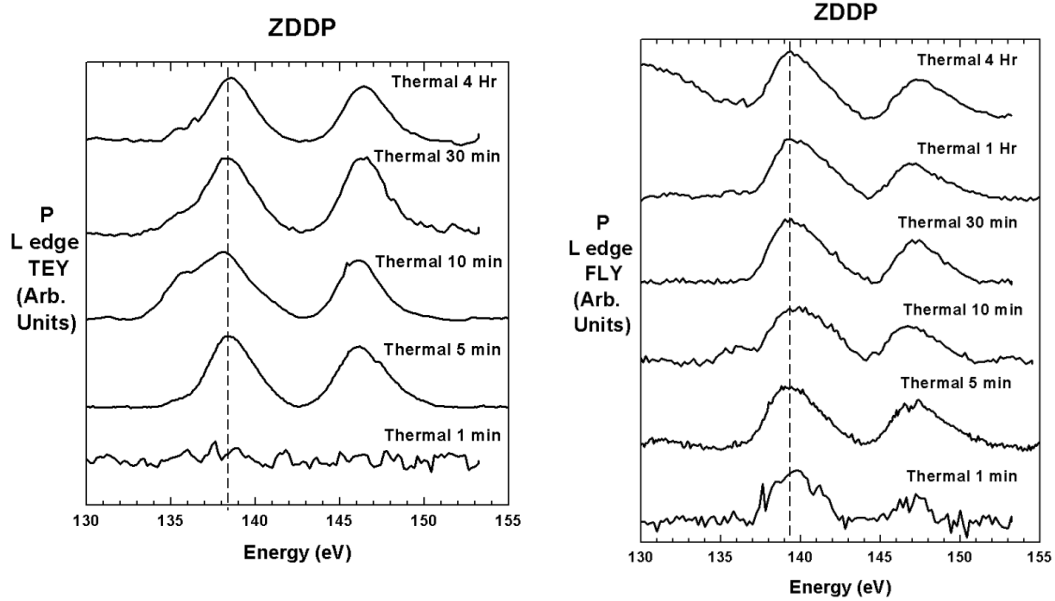


Figure 5.12 XANES Spectra of the TEY and FLY modes at the P L edge of Thermal Films Formed from ZDDP as Baking Time.

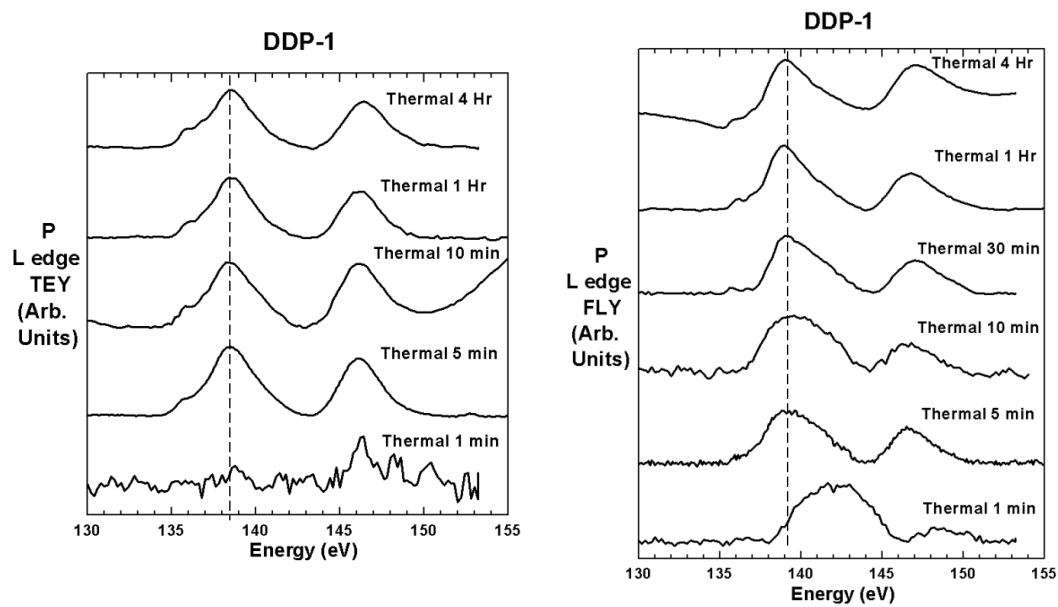


Figure 5.13 XANES Spectra of the TEY and FLY modes at the P L edge of Thermal Films Formed from DDP-1 as Baking Time.

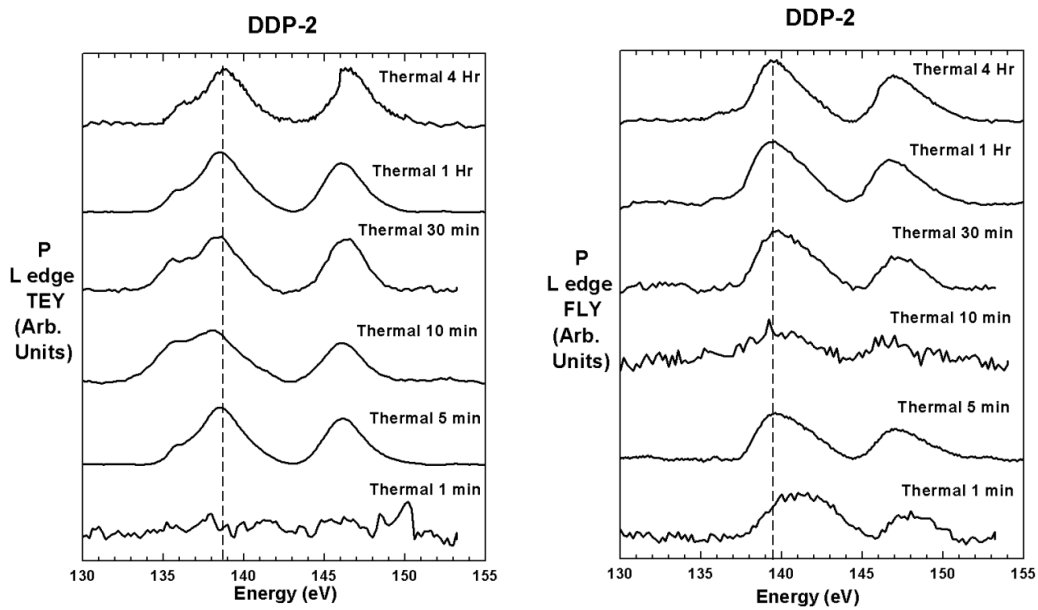


Figure 5.14 XANES Spectra of the TEY and FLY modes at the P K edge of Thermal Films Formed from DDP-2 as Baking Time.

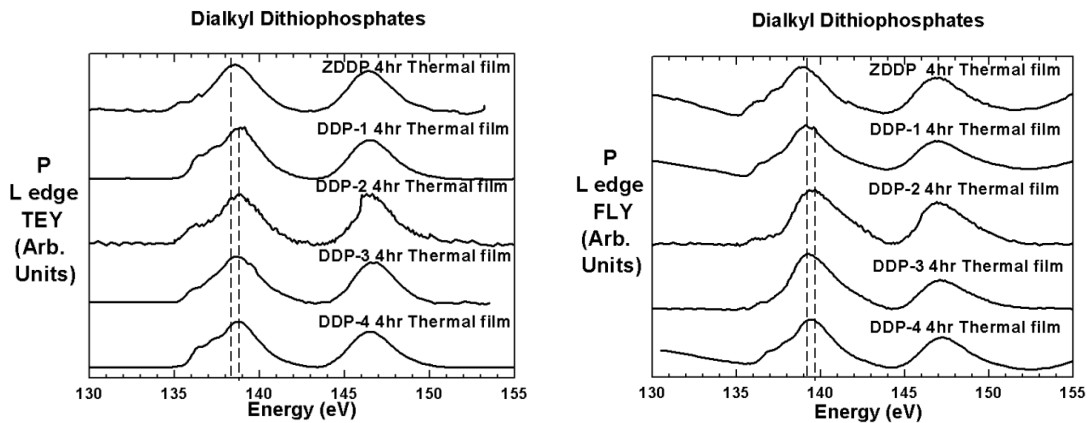


Figure 5.15 XANES Spectra of the TEY and FLY modes at the P L edge of 4 hour Thermal Films Formed from ZDDP and Four Different Ashless Thiophosphates.

In order to compare the chain length of phosphate glass films, all thermal films were treated as described above and plotted separately in figure 5.16. The relative intensity of peak (a) is more meaningful than the relative intensity of peak (b). Only a/c ratios of all thermal film are presented in the graphs. In all cases, TEY analyses for 1 minute samples of thermal films

aren't presented here because of initial instability. In case of ZDDP samples, all thermal films at both TEY and FLY modes except 10 minute sample have a/c ratio that is below 0.2. This means all phosphates in these thermal films are composed of zinc orthophosphates with a small amount of iron ortho- or pyro-phosphates. The 10 minute mark is the transition from rapid growth rate to a much slower growth rate of the thermal film as detailed in figure 5.2. The thermal film present at the 10 minute point for ZDDP has medium chain length Zn polyphosphates near the surface (~5 nm) and short chain length of Zn polyphosphates in 50~70 nm deep region from the surface, in addition, a small amount of Fe polyphosphates may also be present. L edge spectra are acquired from the top 50~70 nm of the thermal film and provide information only from this region. The phosphates in bulk area are determined to be ortho- or pyrophosphates using the K-edge spectra and FLY spectra at L-edge. The difference between DDP-1 and ZDDP is that in DDP-1 the thermal film contains iron phosphates. The analysis of iron phosphate chain length of DDP-1 indicates that it is similar to the zinc phosphate chain length of ZDDP.

The initial growth rate and decomposition rate of DDP-2 until around 8 minute are slower than what is exhibited by ZDDP and DDP-1. Analysis of the XANES spectra indicates that it has medium chain of iron polyphosphate in the near-surface region and short chain iron polyphosphate depths of 70 nm in the thermal film formed after 10 minutes. In case of DDP-2, these thermal films continue to grow after the initial 10 minute period all at two different growth rates both of which are slower than the initial growth rate as seen in figure 5.2. The thermal film present at 30 minute largely consists of iron polyphosphates of medium chain length. The thermal films formed at 1 hour and 4 hour in the near surface region are short chain of polyphosphates, but still polyphosphates because of continuous supply of decomposed additives that are depositing on the surface.

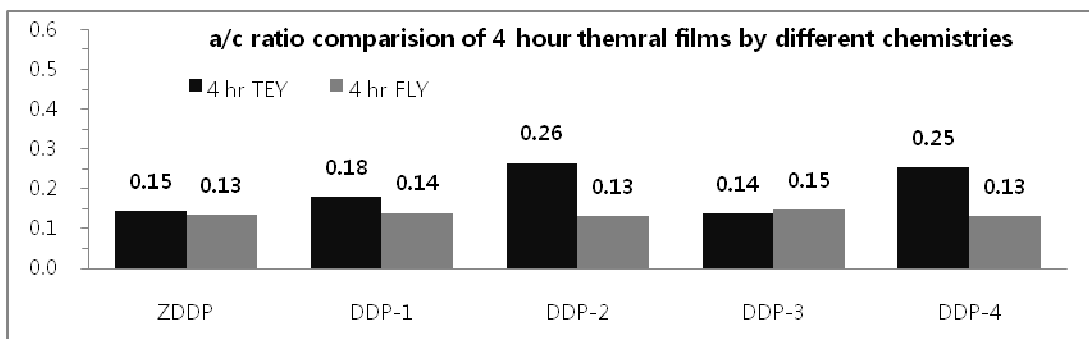
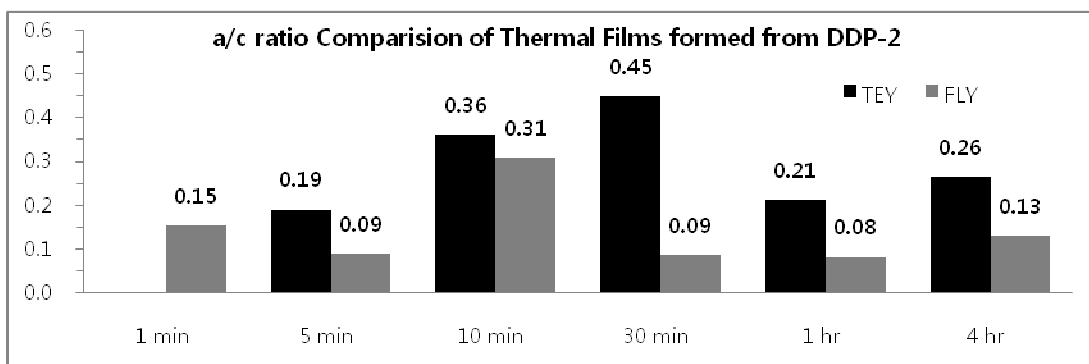
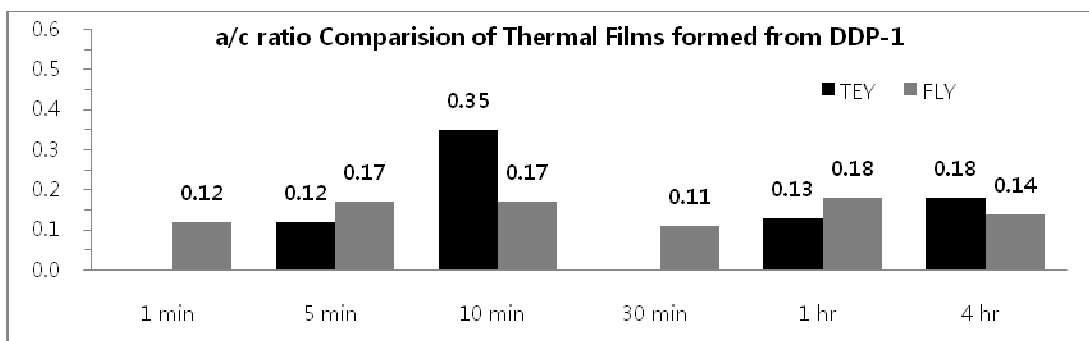
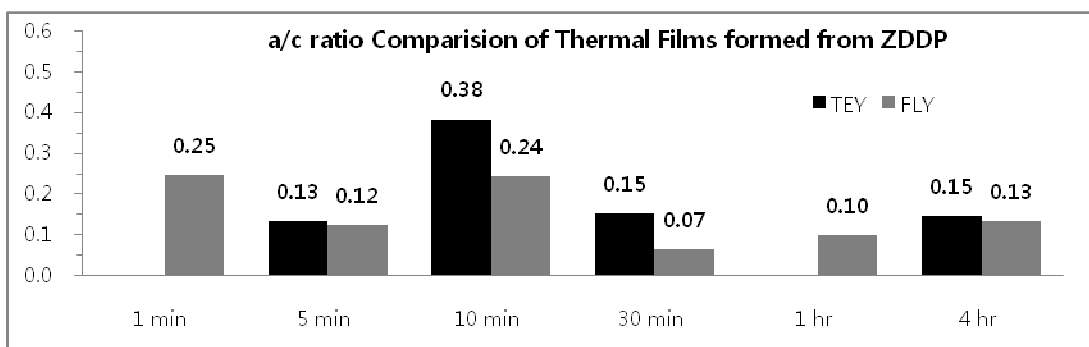


Figure 5.16 Chain Length Comparisons of Phosphate Films by a/c Ratio Comparison as Different Chemistries with Time. The Relative Ratios are Presented in order of ZDDP, DDP-1, DDP-2 and All 4 hour Thermal Films from Top to Bottom.

The last graph at the bottom of figure 5.16 provides the *a/c* ratio that is related to the chain length of thermal films from different thiophosphate additives formed at 4 hours. The 4 hour data was used to evaluate the chemistry and structure of well developed thermal films. In this analysis, antiwear chemistries can be divided into two categories according to pattern of reaction and growth for thermal films. ZDDP, DDP-1, and DDP-3 are one group and DDP-2 and DDP-4 are in another group based on the chemistry of the films. However, DDP-3 looks like that initial reaction and decomposition may be very active like ZDDP and DDP-1 and then after some time, it may grow slow or stop growing and may reorganize their chemical bonding and structure. DDP-4 may keep growing during all test time with opulent decomposed intermediate products like DDP-2. That is the reason why DDP-4 has short chain length of polyphosphates at the surface area at 4 hour test.

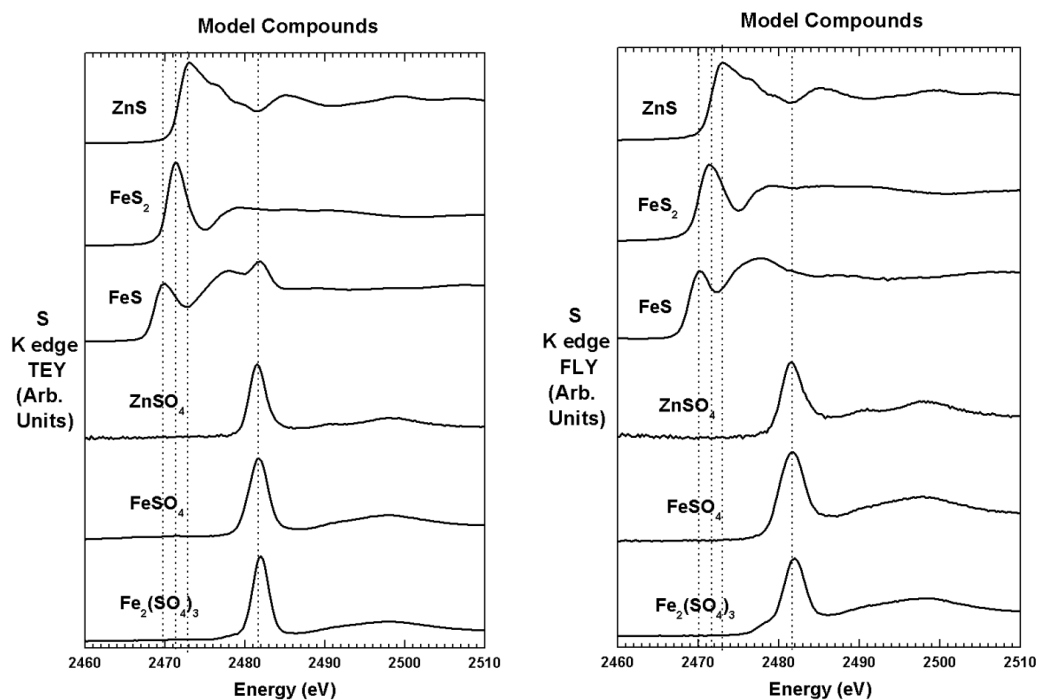


Figure 5.17 XANES Spectra of the TEY and FLY modes at the S K edge of Model Compounds.

5.3.2.2 Sulfur Characterization

K edge of Sulfur

Total six model compounds of sulfur species were analyzed and are shown in figure 5.17. First three model compounds are related to sulfide species. Zinc sulfide (ZnS), iron sulfide (FeS), and pyrite (FeS₂) belongs to first group. The other three are sulfate species like zinc sulfate (ZnSO₄), ferrous sulfate (FeSO₄), and ferric sulfate (Fe₂(SO₄)₃). The K edge spectra of sulfur model compounds are complex, however, only the positions of white line peaks are largely considered for analysis. In sulfides, positions of main peak are clearly distinguished. ZnS is located at 2470 eV, FeS₂ is at 2471.5 eV, and FeS is placed at 2473 eV. On the other hand, all sulfates are located at same position of 2481.5 eV. The sulfate peak cannot be used to differentiate between different cation species. However, one can clearly differentiate between sulfates and sulfides. Figure 5.18, 19, 20, and 21 are the S K edge XANES spectra of thermal films generated different chemistries at different baking time. All thermal films of ZDDP in figure 5.18 have sulfates. We can see the relative increase in intensity of the peaks as a function of time in these plots. After 1 hour of thermal exposure, the intensity of the sulfate peak is similar to the 4 hour sample indicating that the thermal films are not much changed after 1 hour exposure. Sulfide peaks are observed after 10 minute in FLY mode and after 30 minutes in TEY mode. Both peaks in TEY and FLY are close to zinc sulfide. At 4 hour baking, sulfides disappeared. Probably, through oxidation process, sulfur elements are changed from reduced form (sulfide) to oxidized form (sulfate). In case of DDP-1 in figure 5.19, no sulfide is observed at any point of the thermal exposure process. The increase of relative intensity of sulfate is shown as time is changed. After 30 minute testing, sulfate peaks are similar, which indicates that the chemistry of the thermal film has stabilized. Figure 5.20 shows the S K edge spectra of DDP-2. After 1 minute, both sulfide and sulfate are shown and the growth of sulfur species with time is observed. Sulfates appear to dominate in the all thermal films as evidenced by the strong relative intensity compared to sulfides. All 4 hour thermal films of different

thiophosphates shown in figure 5.21 look very similar. These films are all composed of sulfate species. In addition, small amount of sulfide are observed in DDP-2 and DDP-3.

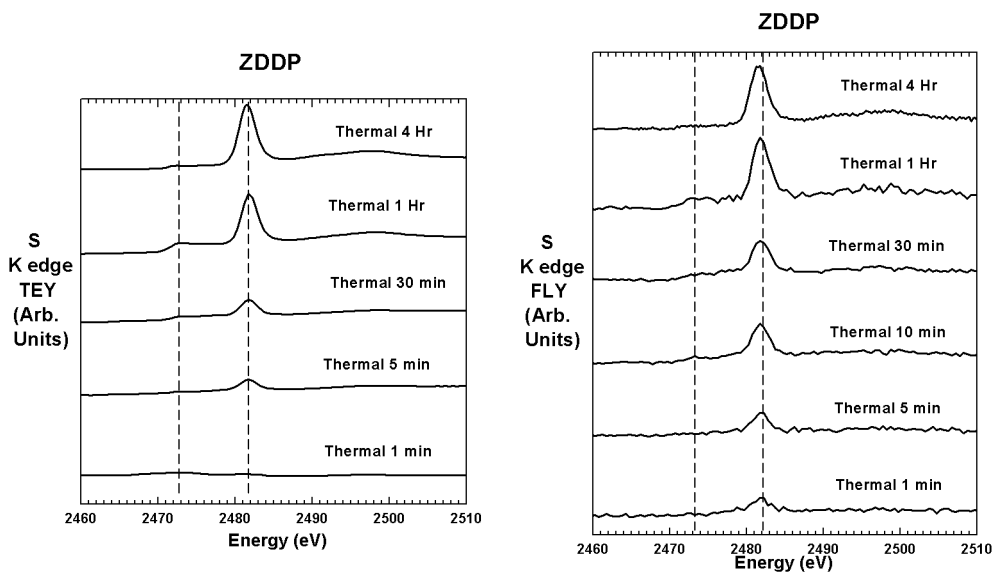


Figure 5.18 XANES Spectra of the TEY and FLY modes at the S K edge of Thermal Films Formed from ZDDP with Baking Time.

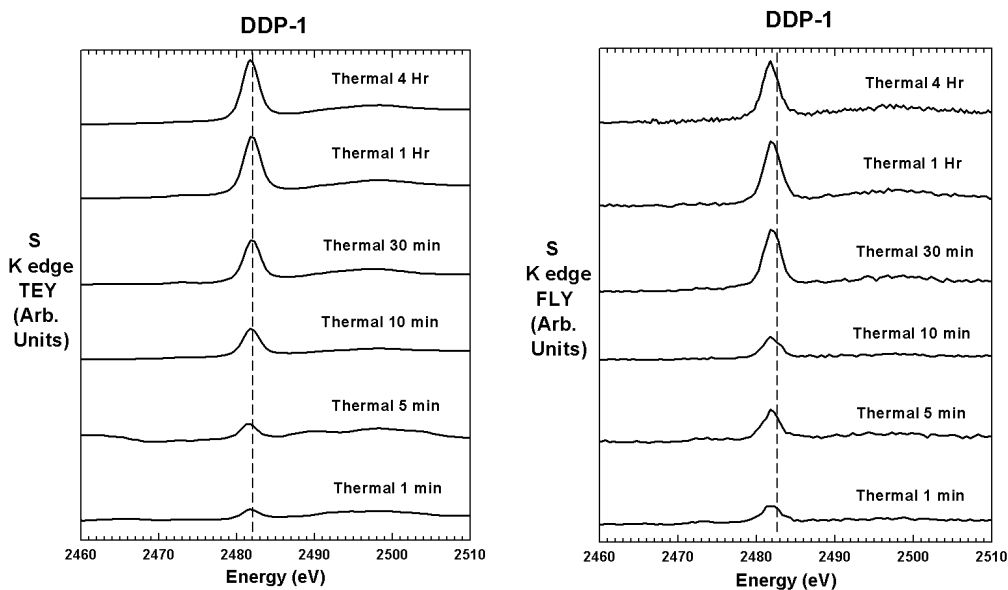


Figure 5.19 XANES Spectra of the TEY and FLY modes at the S K edge of Thermal Films Formed from DDP-1 with Baking Time.

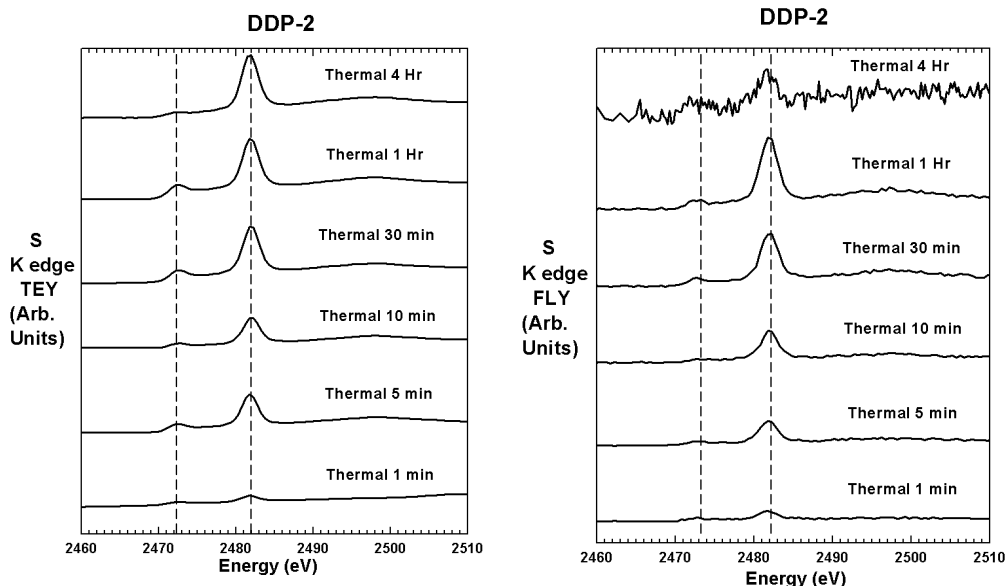


Figure 5.20 XANES Spectra of the TEY and FLY modes at the S K edge of Thermal Films Formed from DDP-2 with Baking Time

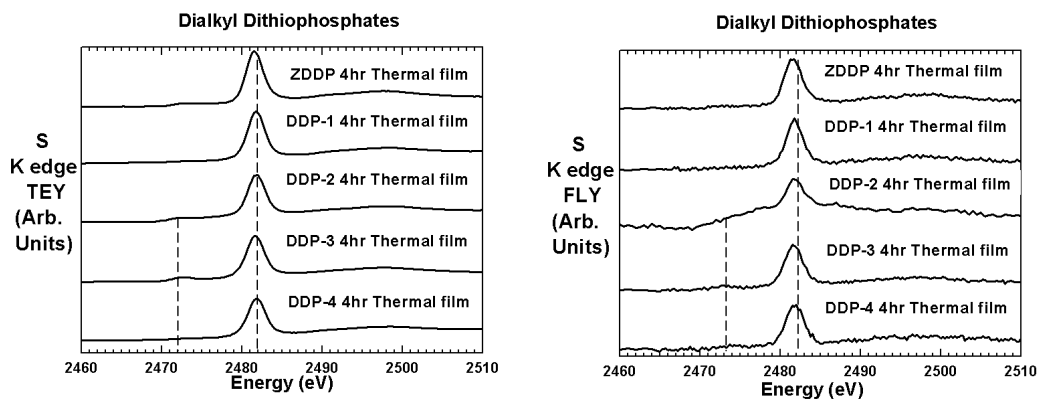


Figure 5.21 XANES Spectra of the TEY and FLY modes at the S K edge of 4 hour Thermal Films Formed from ZDDP and Four Different Ashless Thiophosphates.

It is difficult to get quantitative information from XANES spectra from multiple samples because the flux of photons are different at different times, however, if one is interested in determining the relative amounts of two constituents that are close in atomic number, it is possible to use the ratio of integrated intensity below the peaks to get a relative proportion of the two species. Sulfur and phosphorous are close together in the periodic table and the flux of

photons would likely not change much between the two peaks and can be used to characterize the relative proportion of P and S in the film. Figure 5.22 is an example of the sulfur and phosphorus peaks. Phosphorus and sulfur relative ratio was calculated by their integral area of white line peaks. Sulfur is separated into two species, sulfide and sulfate. The amount of sulfur was considered to be by the sum of sulfide and sulfate. In addition, the relative proportion of sulfide in sulfur species was also determined.

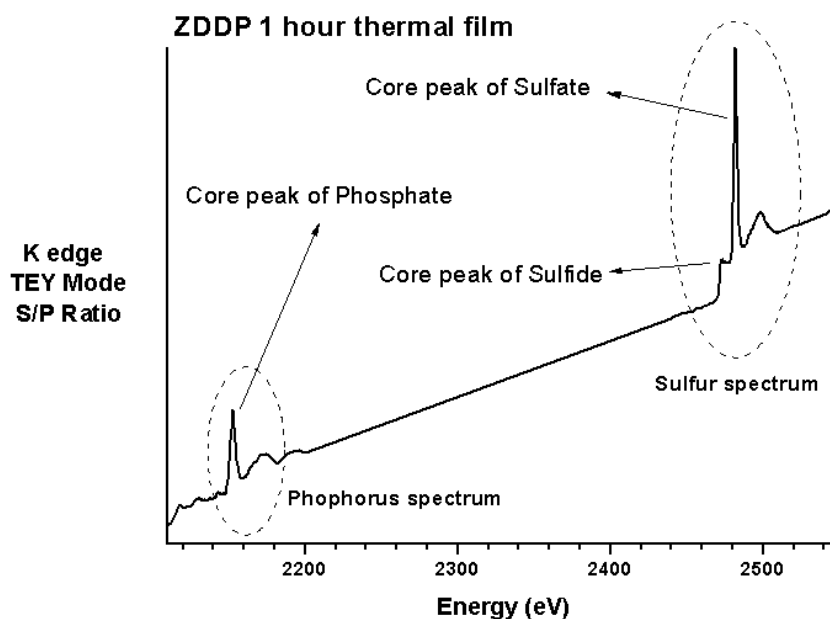


Figure 5.22 Example of K edge XANES Spectra where Both Phosphorus and Sulfur Coexist.

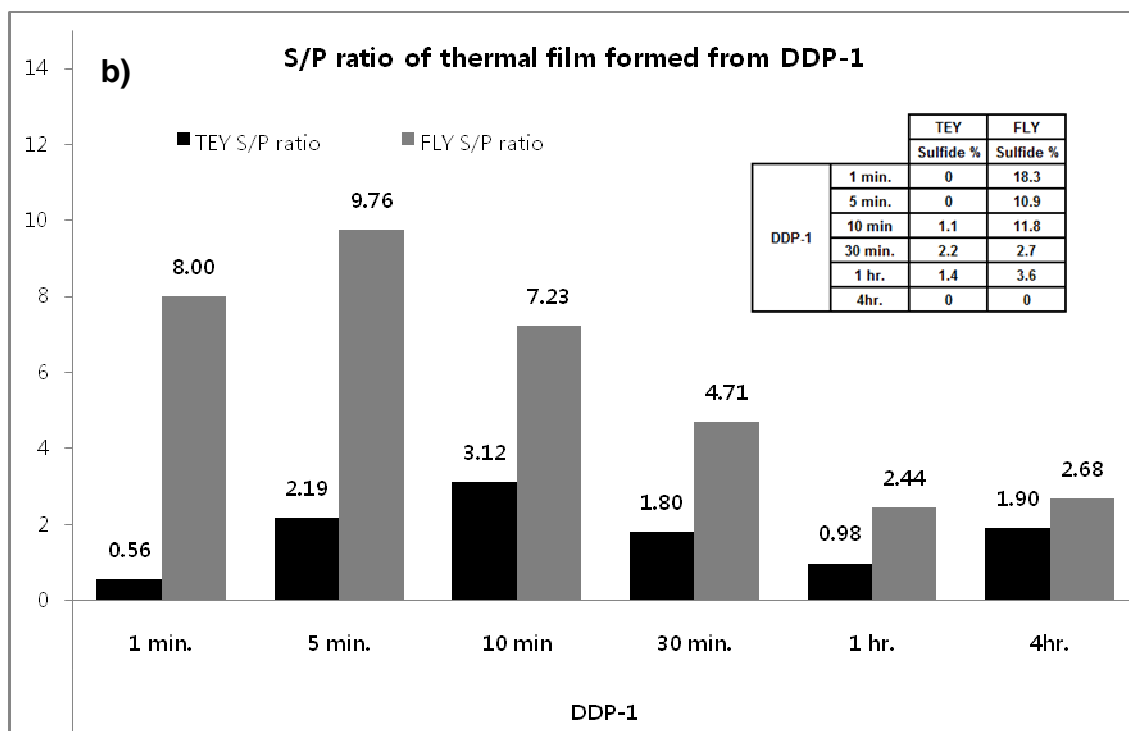
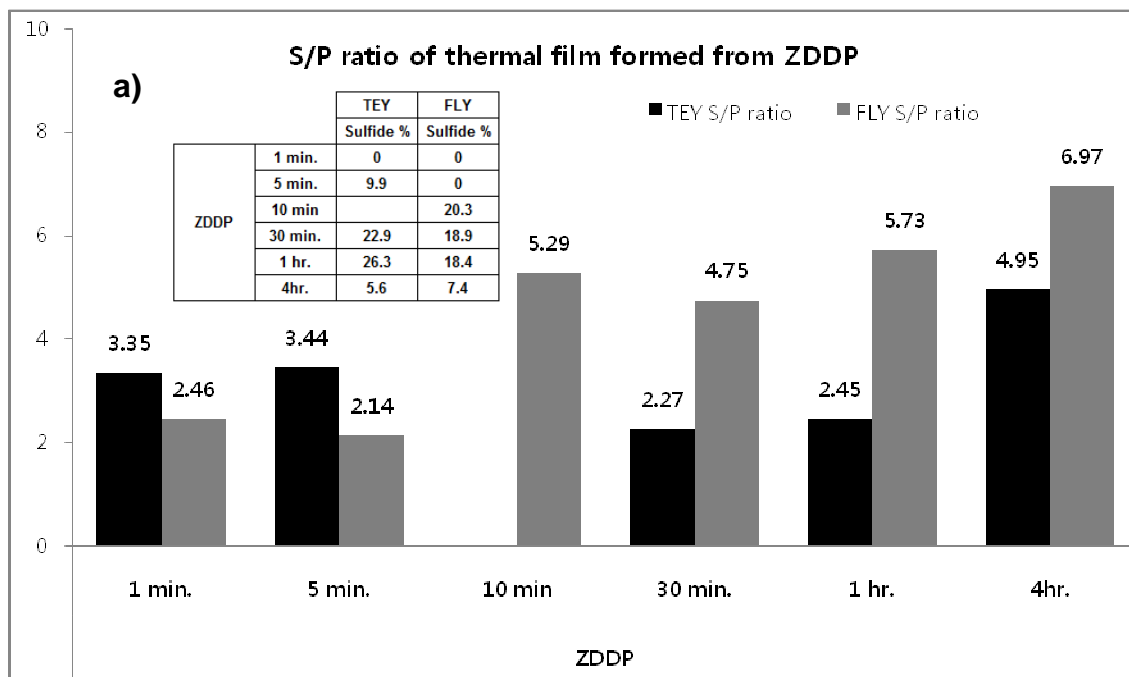
Figure 5.23 and 5.24 shows the relative S/P ratio of all thermal films generated from various thiophosphate additives and the proportion of sulfide to sulfate species in thermal films. All thermal films of ZDDP as depicted in figure 5.23(a) have significantly more sulfur species than phosphates. At 1 and 5 minute baking times, sulfates are more in surface region (50–70 nm) than in bulk region. With fast and active decomposition of ZDDP, sulfates are actively generated at the surface area by the reaction with the sulfur containing decomposed intermediates. Then, from 10 minutes to 1 hour, sulfates move into bulk area and phosphates

are likely formed at surface with plenty of decomposed products based on phosphorus. That is the reason that S/P ratio in FLY mode increases up to 5 ~ 7 and even though sulfur is still more than phosphorus, the S/P value in TEY mode decreases to about 2. Sulfides begin to be made up during these times with 20 percentages of total sulfur species. At 4 hours the thermal films and the oils are oxidized, so sulfates increase at both surface and bulk area together. Sulfides are also decreased at this point.

Ashless DDPs have different pattern of reaction from ZDDP thermal films. First, in case of DDP-1 shown in figure 5.23(b), the initial decomposition of chemistries and initial growth rate of thermal film are high. Thus, the initial formation of sulfur compounds is very active and presents both in the surface and bulk regions while the phosphates are present more in the surface regions. Examining the spectra in FLY mode, it is evident that sulfur compounds are dominant in thermal films formed at 5 minute (9.76 times than phosphorus), then their proportion is gradually reduced as exposure time is increased to 1 hour. This indicates that iron phosphates are more actively generated and form a greater part of the thermal film with increasing time. After 1 hour, S/P ratios in the FLY mode decreases to 2.5. The sulfides are formed in the first 30 minutes of thermal exposure after which they are oxidized to sulfates. In the early stages of formation of thermal film examined in the TEY mode, it is evident that the relative amount of sulfur increases compared to P until 10 minutes then decreases by 1 hour to approximately 1 to 1 ratio before increasing to a 2:1 ratio. This indicates that the phosphates stay near the top of the thermal films. In addition the change in chemistry of the thermal film even when there is not a significant increase in thickness indicates that the thermal film is reconstituting with time after the 1 hour period in the ZDDP and DDP films. Second ashless thiophosphate additive, DDP-2, have a large amount of sulfur compounds inside thermal films as shown in figure 5.24(a). Sulfur compounds are more reactive than phosphorus compounds. After 5 minutes of exposure, a S/P ratio of 11.56 in FLY indicates that in the top 3 μm of the thermal film there is a large amount of sulfur present when DDP-2 is used. The S/P ratio for

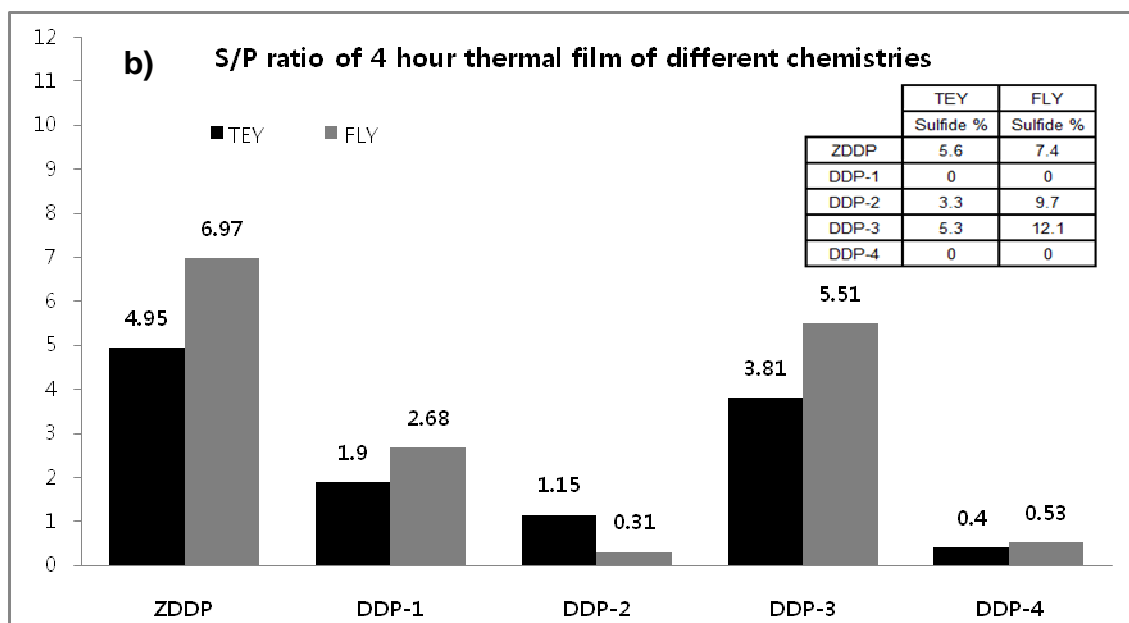
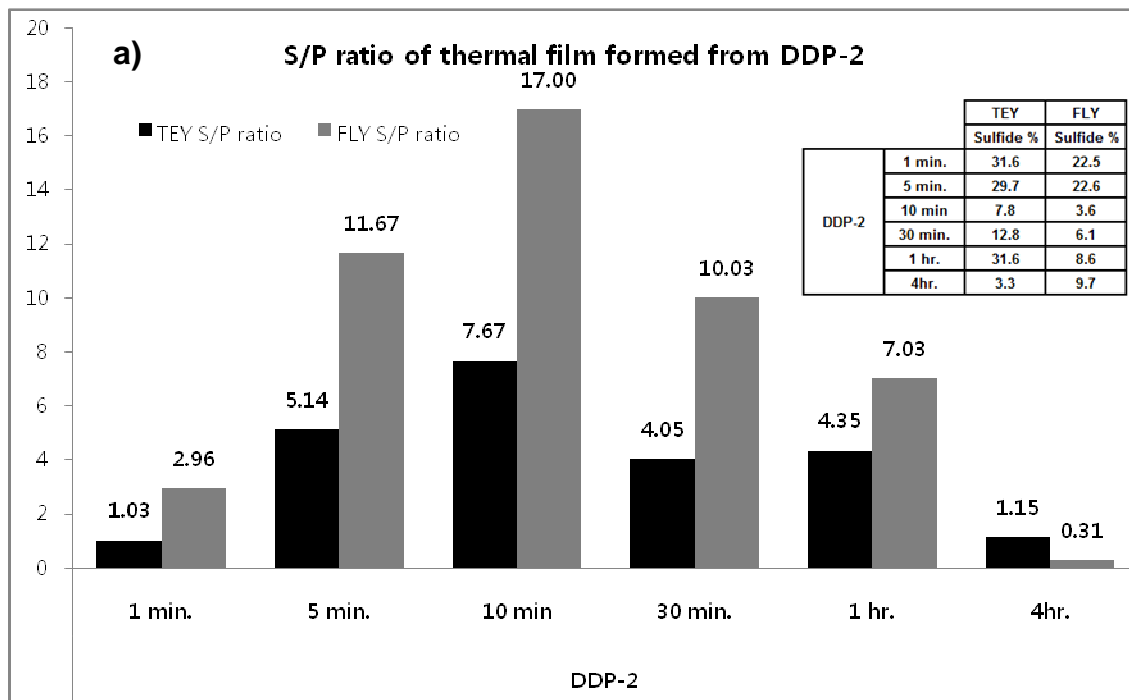
TEY is around 5 at 5 minutes which also indicates a larger amount of S near the surface (top 50 nm). Sulfides make up about 30 percentages of sulfur species located at surface area and in the bulk (3 μm) about 22 percentages of sulfides out of the total sulfur compounds. This initial growth rate of thermal film is not as high as ZDDP and DDP-1. Therefore, DDP-2 has a maximum S/P ratio at 10 minutes in both TEY (S/P=7.67) and FLY (S/P=17.00). After 10 minutes, these relative ratios of sulfur versus phosphorus keep decreasing until 4 hour. This indicates that phosphorus species accelerate to form phosphates with metal cations and then move to the top of thermal films and this trend increases as the thermal exposure increases to 4 hours. In case of DDP-2, the proportion of sulfur present as sulfides in the TEY falls below 10% at 10 minutes. However, after 1 hour, the amount of sulfide increases to 31 % with no significant increase in thickness of the thermal film. The FLY mode of DDP-2 has same trend in spite of different percentage of sulfides (3.6% \rightarrow ~9%). This indicates that a reconstitution of the thermal film is in progress with sulfates being reduced with oxygen being scavenged to form phosphates. This is supported by the fact that con-current with the increase in sulfide/sulfate ratio and also with a decrease in the S/P ratio. Thus, finally iron phosphates are dominant in thermal films after 4 hour test.

Comparing all 4 hour thermal films of thiophosphates in figure 5.24(b), it is hard to conclude the mechanisms of thermal film formation from DDP-3 and DDP-4 because those have limited information. However, through the S/P ratio of 4hour thermal film, DDP-3 seems to be close to the performance of ZDDP or DDP-1. In order to classify DDP-3 exactly, there are more experiments to be needed. DDP-4 is likely to follow the behavior of DDP-2 because its thermal film consists of mostly iron phosphates with below 1 point of S/P ratio after 4 hour. These results coincide with the result of a/c ratio analysis at P L edge spectra.



Sulfide % : $\text{sulfide}/(\text{sulfide}+\text{sulfate}) \times 100$

Figure 5.23 Relative S/P Ratio-1 of All Thermal Films Generated from Various Thiophosphate Additives and the Percentage of Sulfide at Sulfur Species in Thermal Films. a) Relative S/P Ratio and Sulfide % of ZDDP and b) Relative S/P Ratio and Sulfide % of DDP-1



Sulfide % : sulfide/(sulfide+sulfate)*100

Figure 5.24 Relative S/P Ratio-2 of All Thermal Films Generated from Various Thiophosphate Additives and the Percentage of Sulfide at Sulfur Species in Thermal Films. a) Relative S/P Ratio and Sulfide % of DDP-2 and b) Relative S/P Ratio and Sulfide % of 4 hour Thermal Films of Different Chemistries.

L edge of Sulfur

Figure 5.25(a) and (b) shows sulfur L edge spectra of six model compounds of sulfur. There are three sulfide model compounds, Zinc sulfide (ZnS), iron sulfide (FeS), and pyrite (FeS₂), and three sulfate model compounds, zinc sulfate (ZnSO₄), ferrous sulfate (FeSO₄), and ferric sulfate (Fe₂(SO₄)₃). Like the analysis of K edge spectra of sulfur, main peak's position and shape are used for analysis. All spectra of sulfates are very similar although their pre-edge peaks are slightly different due to cation species and condition. Clear feature of all sulfates are the two big broad peaks at ~172.5 eV and ~181 eV. Kasrai et al. found these two broad main peaks are mostly due to the presence of the oxidation product using several inorganic and organic sulfur compounds in order to characterize coals. [131] Sulfur L edge signal of thermal films are weaker than the signal of sulfur model compounds. Their pre-edges are hard to be distinguished. Thus, only common main peak positions of sulfates are used for analysis in this study. In case of sulfides, each sulfide model compound has characterized peaks such as figure 5.25(a, b). Common among them are the first two peaks between 162.5 eV and 164 eV. Figure 5.25(c) shows the FLY spectra at sulfur L edge of raw dithiophosphate additives. Clear different features of raw materials are two small peaks at 164 eV and at 166 eV indicating P=S and P-S bonds in the chemistries. However, raw DDP-1 has a different sulfur pattern among DDPs which looks like a certain sulfate. This peak may result from the presence of sulfuric acid (H₂SO₄). It might be formed on the plastic surface after DDP-1 was decomposed by the sun light, and then hydrolyzed and oxidized by air environment.

ZDDP 1 minute thermal film is unstable as shown in figure 5.26. After 5 minute, two broad and big peaks which indicate sulfates are observed together with a small amount of sulfides. The peaks of sulfides in the 4 hour thermal films are non-existent. Sulfur L edge of DDP-1 as figure 5.27 shows that sulfur mostly exists as a sulfate in the thermal film although a few sulfides are sometimes found in FLY mode. 1 minute sample looks unstable according to unusual FLY spectrum. Thermal film formed from DDP-2 shown in figure 5.28 is also similar.

Sulfates are dominant everywhere and every time with small amounts of sulfides present in all of the thermal films formed from DDP-2. In all 4 hour thermal film comparison of figure 5.29, all samples have mostly sulfates. DDP-2, and DDP-4 have a little more sulfides than ZDDP, DDP-1 and DDP-3, but this is not clear. This indicates that at the end of 4 hours, in the top $\approx 3\mu\text{m}$ of the thermal film the sulfur present is oxidized into sulfates while deeper down it is possible that some of the sulfur is still present in the form of sulfides. All DDPs have small amount of undecomposed raw materials at 1 minute test, however, after 1 min. no spectra for raw materials are detected.

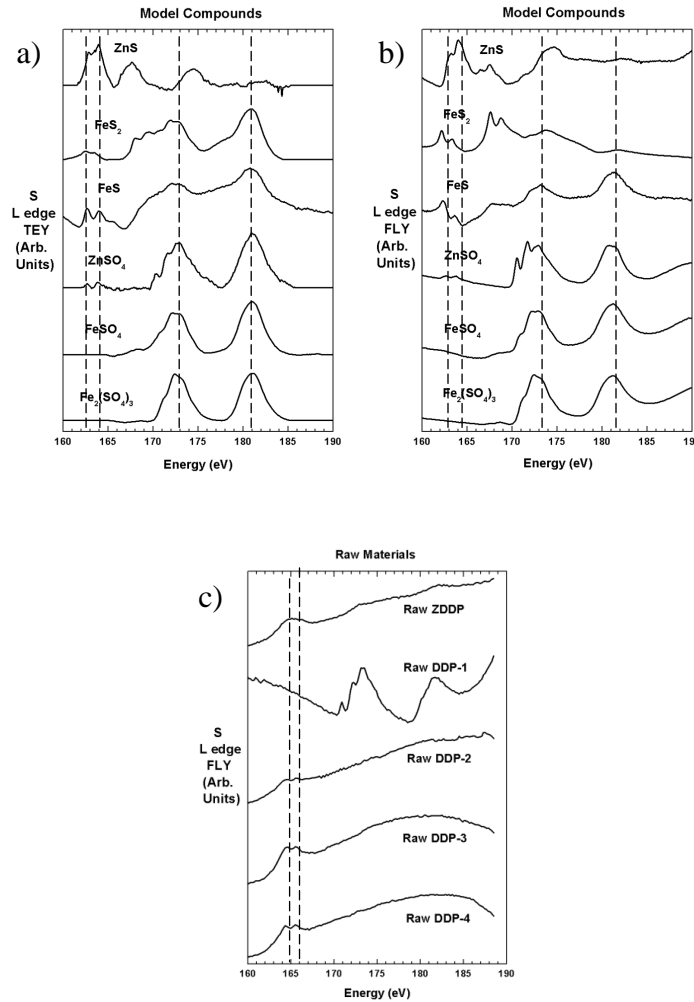


Figure 5.25 XANES Spectra of the (a) TEY and (b) FLY modes at the S L edge of Model Compounds and (c) FLY modes at the S L edge of Unreacted Raw DDPs.

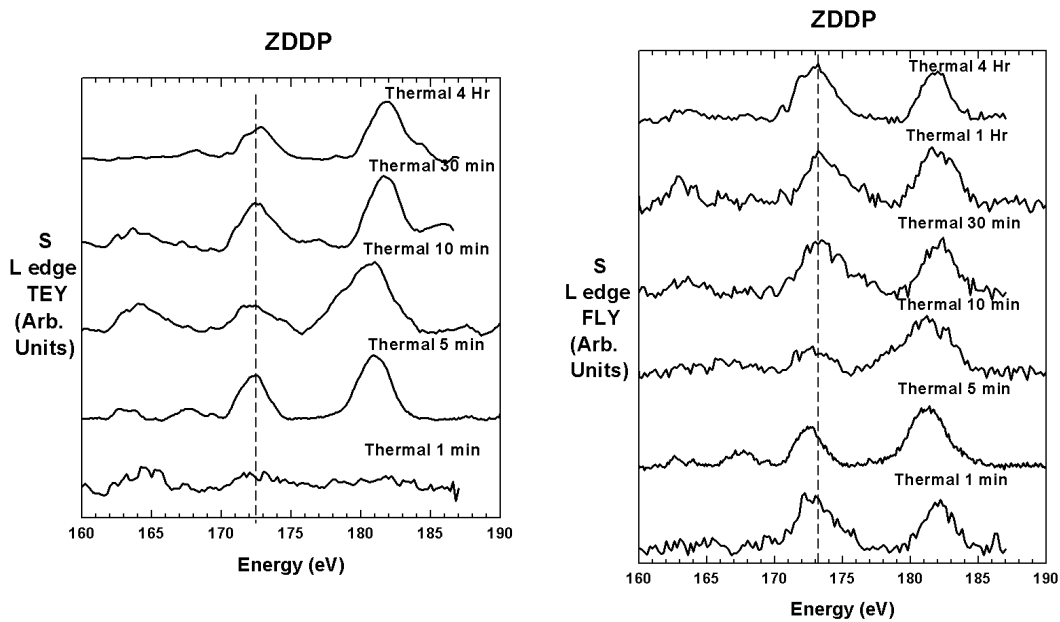


Figure 5.26 XANES Spectra of the TEY and FLY modes at the S L edge of Thermal Films Formed from ZDDP as Baking Time.

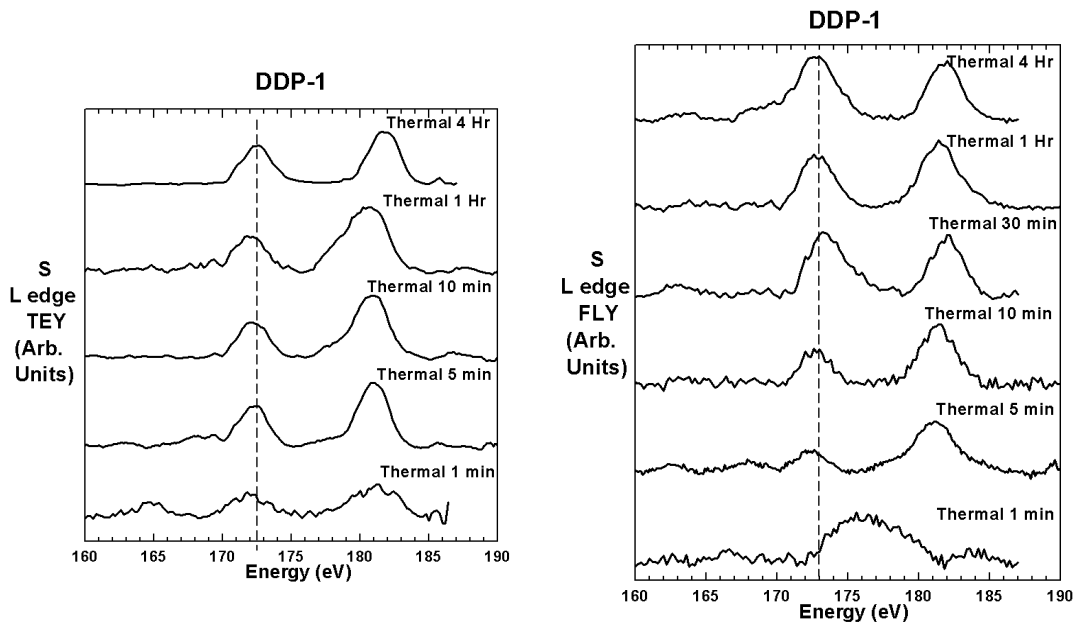


Figure 5.27 XANES Spectra of the TEY and FLY modes at the S L edge of Thermal Films Formed from DDP-1 as Baking Time.

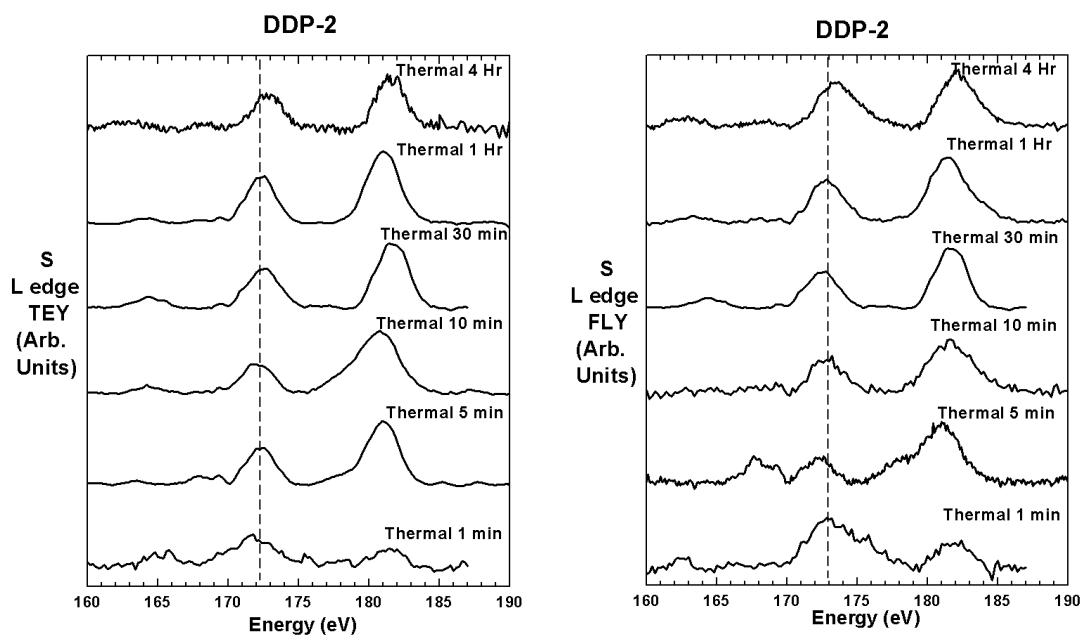


Figure 5.28 XANES Spectra of the TEY and FLY modes at the S L edge of Thermal Films Formed from DDP-2 as Baking Time

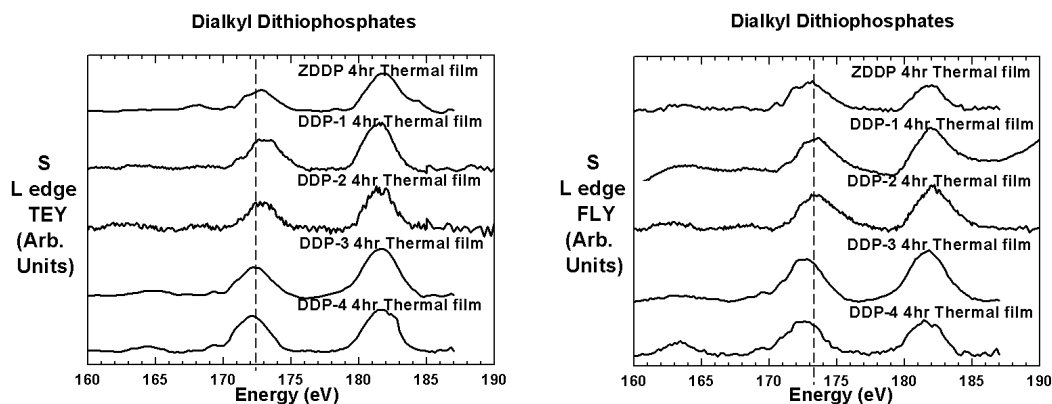


Figure 5.29 XANES Spectra of the TEY and FLY modes at the S L edge of 4 hour Thermal Films Formed from ZDDP and Four Different Ashless Thiophosphates.

5.3.3 Surface Morphology

Images of the topography of thermal films were recorded using a Wyko NT9100 Optical Profiler. Only 4 hour thermal films formed from ZDDP, DDP-1, and DDP-2 were examined. The bare steel sample prior to deposition of thermal film was polished down to 5 μm alumina and an image of the surface is shown in Figure 5.30.

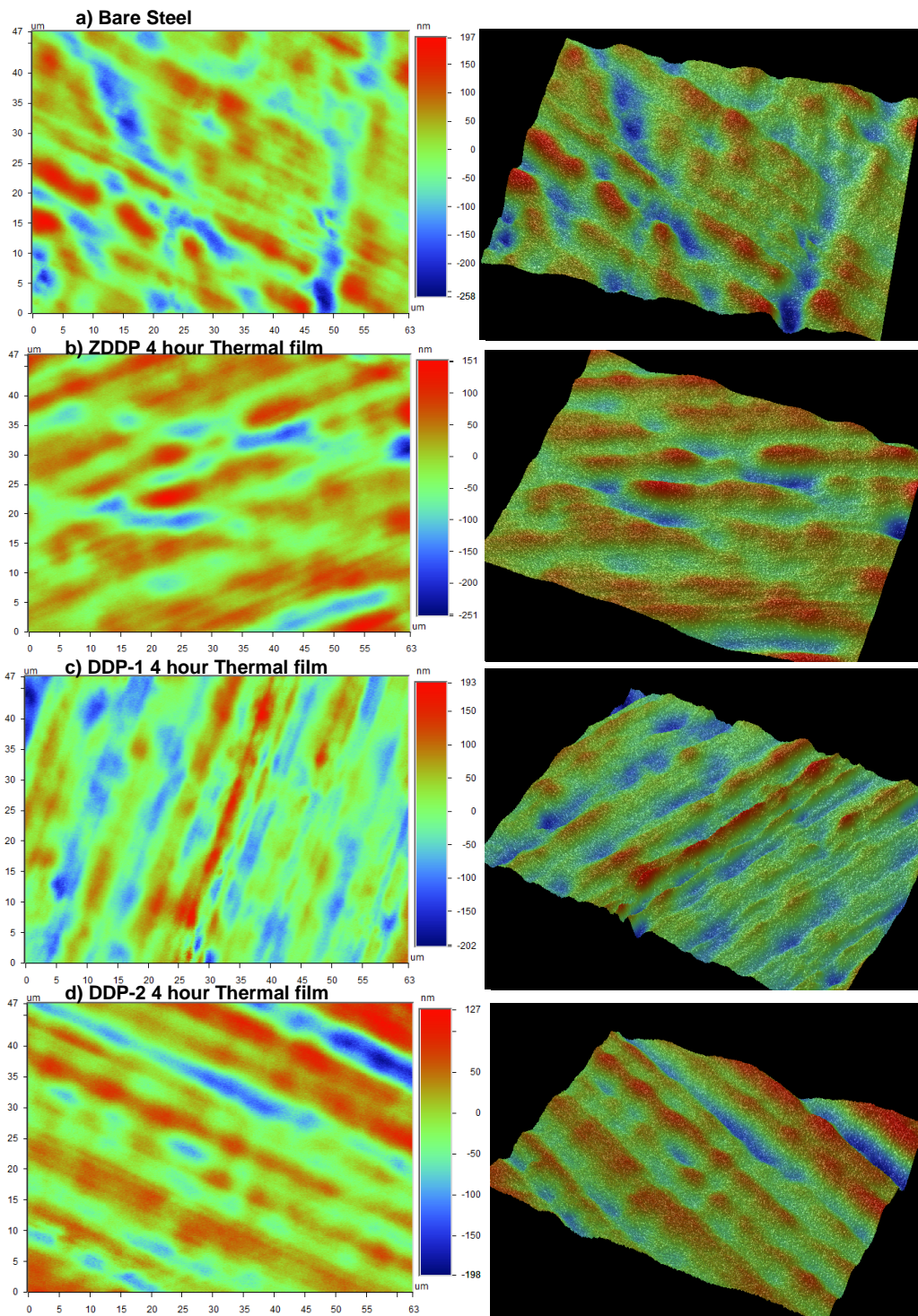


Figure 5.30 Optic Images of Surface Morphology of 4 hour Baked Thermal Films Using the Optic Profilometer, Wyko NT 9100. Magnification is 100X. a) Bare Steel Surface, b) ZDDP 4 hour Thermal Film, c) DDP-1 4 hour Thermal Film, and d) DDP-2 4 hour Thermal Film.

An important observation is the similarity of the images of bare steel and the surfaces of 4 hour thermal film. All the 4 hour thermal films are at least 3 μm thick or more (ZDDP: 3,202 μm , DDP-1: 5,118 μm , and DDP-2: 8,052 μm). The morphology of the thermal films show the same roughness as the starting steel which indicates that the film grows uniformly in all regions including the hills and valleys of the initial polished surfaces.

5.3.4 Mechanism of Thermal Film Formation and Phenomenological Model

Using the P and S L edge and K edge XANES technique, we have been able to develop an understanding of the growth of thermal films from zinc dialkyl dithiophosphate and other ashless thiophosphate additives. We have been able to detect the chain length of polyphosphates on the surface area until 50~70 nm deep with the a/c ratio analysis of P L edge spectra. Also, with the S/P ratio analysis of P and S K edge spectra, the chemical composition and structure of thermal films have been studied. Determination of the sulfide/sulfate ratio has provided insight into the oxidation state of sulfur in the thermal films. The measurement of thermal film thickness using the SEM, the changes of thickness of thermal films as a function of time and thermal film growth rate at each transition point have been determined. From all these observations, the mechanisms of thermal film formation, generated from ZDDP and four different ashless DDPs, can be described. In addition, phenomenological models were developed using the data acquired from each characterization technique.

In order to help understand the chemical structure and composition of thermal films in the phenomenological models, simplified symbols for inorganic model compounds were used. Table 5.3 shows the chemical name, formula, real 2D structure, and simplified model of inorganic compounds which are used at the phenomenological models. Zn is a big white circle, Fe is a big black circle, P is a small black dot, and S is a small white dot. O is not shown, so it looks like just a line. Phosphates species have dark surroundings. Sulfur compounds have white background. Real line means the connection between two atoms in a molecule. Dot line is the connection with other molecules outside.

Table 5.3 Inorganic model compounds for the phenomenological models

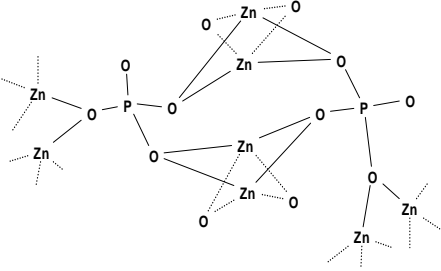
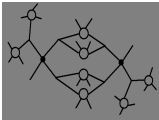
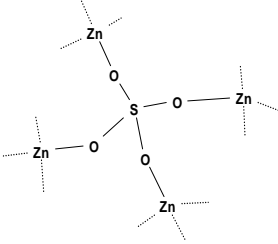
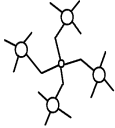
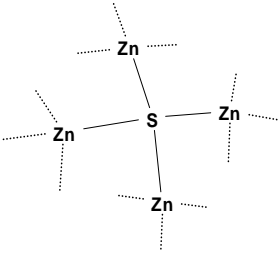
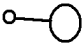
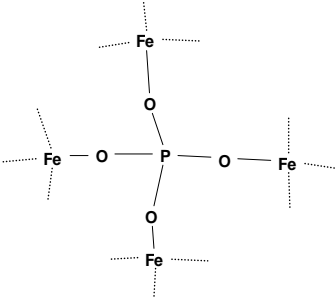
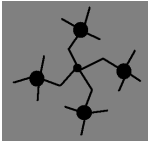
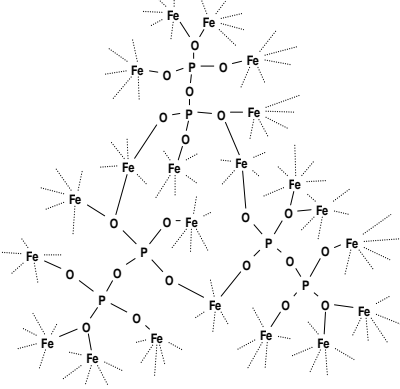
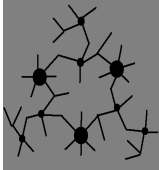
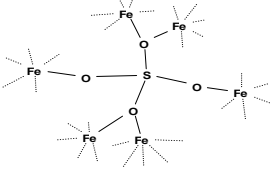

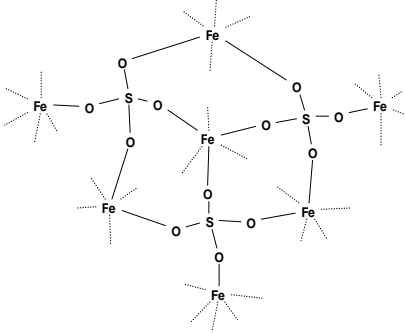
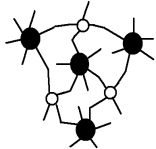
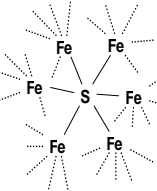

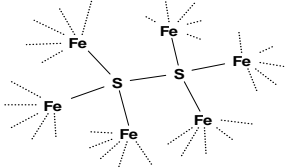
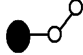
Name	Formula	Structure	Simplified Symbol
Zinc Phosphate	$Zn_3(PO_4)_2$		
Zinc Sulfate	$ZnSO_4$		
Zinc Sulfide	ZnS		
Iron Orthophosphate	$FePO_4$		

Table 5.3 - continued

<p>Iron Pyrophosphate</p>	<p>$\text{Fe}_4(\text{P}_2\text{O}_7)_3$</p>		
<p>Iron (□) Sulfate</p>	<p>FeSO_4</p>		
<p>Iron (□) Sulfate</p>	<p>$\text{Fe}_2(\text{SO}_4)_3$</p>		
<p>Iron Sulfide</p>	<p>FeS</p>		
<p>Pyrite</p>	<p>FeS_2</p>		

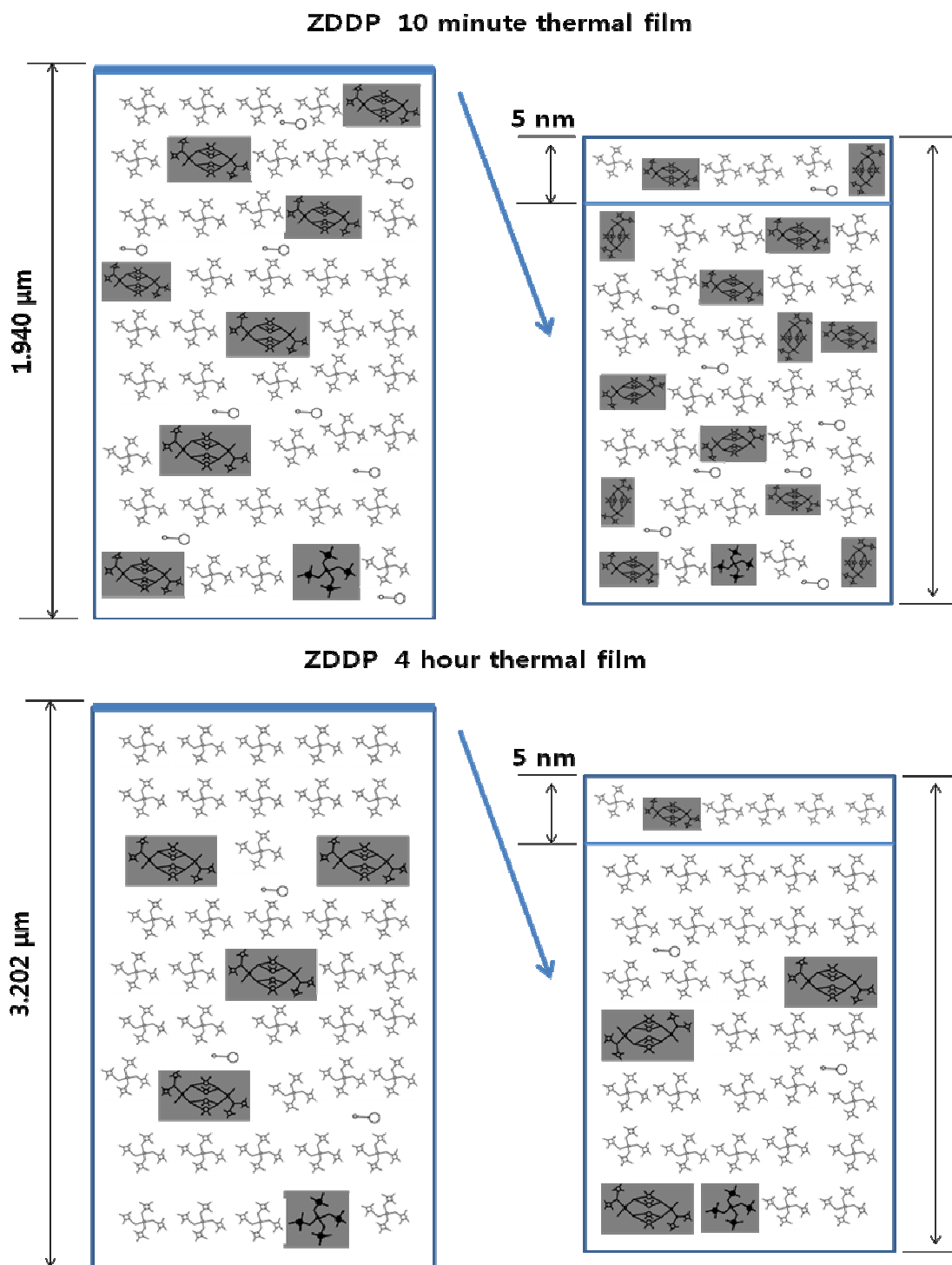


Figure 5.31 Phenomenological Model of ZDDP Thermal Films. Top Picture is 10 minute ZDDP Thermal Film and Bottom Picture is 4 hour ZDDP Thermal Film.

• **ZDDP Thermal Film**

1 min.: Some decomposed ZDDP products by preheating process at 170 °C start to react with metal cations (mainly Zn with few Fe) and to deposit on the surface. Zn/Fe sulfates and phosphates are observed. The formation of sulfate is preferable to one of phosphate. The chemical structure and reaction are not stable.

5 min.: The growth rate is very high. Film thickness also increases very fast. Sulfide starts to show up at the surface. Phosphates are ortho- or pyrophosphates. The reaction becomes stabilized.

10 min.: The thermal film growth rate is still fast. The cross linking of phosphate starts by plenty of active phosphorus containing decomposed products: medium chain length at top surface (5 nm) and short chain length at near surface (50~70 nm). Sulfur species are more than phosphates everywhere. Sulfur compounds are found more in the bulk (S/P ratio: 5.29). Sulfides occupy 20 %. (K edge TEY mode of 5 min. ZDDP thermal film was not available, so we assumed it as same as the data of 30 minute.) The phenomenological model for 10 minute ZDDP thermal film is drawn in figure 5.31 (Top).

First Step: $Zn[(RO)_2PS_2]_2$ (solution) \rightarrow $Zn(RO)_2P_2S_4$ (decomposed by preheating) + O_2 (in oil) + FeO or Fe_2O_3 (present on the surface of steel coupons) \rightarrow Zn/Fe ortho- and pyro-phosphate + $ZnSO_4/FeSO_4$ (or $Fe_2(SO_4)_3$) + ZnS (only surface, 10 %) \rightarrow Zn short chain polyphosphate (in 50~70 nm) and Zn medium chain polyphosphate (in top 5 nm) + $ZnSO_4$ \uparrow (in bulk) + ZnS (20% of the sulfur species)

30 min. and 1 hour: The growth rate decreases from $k=0.1905$ to 0.0012 ($\mu\text{m}/\text{min.}$) after 11 minutes. The thickness of thermal film increases gradually. During this period, decomposed products are gradually consumed, and oxidation and hydrolysis facilitated by high temperature, O_2 and H_2O in oil/environment is accelerated. However, thermal film continues to be deposited together with continued decomposition of ZDDP. The

proportion of sulfur compounds at 30 minutes and 1 hour are similar to the film formed after 10 minutes (S/P ratio: ~2.4 at surface and ~5 in bulk). Phosphates are formed as zinc ortho- or pyro-phosphate. Zinc sulfide remains at ~20 % of the sulfur content.

4 hour: After 4 hours of exposure the relative ratio of sulfates to phosphates is increased to ~5 times at surface (≈ 50 nm) and ~7 times in bulk (≈ 3 μ m). Thermal oxidation and hydrolysis processes of thermal films are accelerated. Sulfides are oxidized to sulfates. Phosphates are zinc ortho- or pyro-phosphates. Figure 5.31 (Bottom) illustrates the phenomenological model of the 4 hour ZDDP thermal film.

Second Step: $Zn(RO)_2P_2S_4$ (decomposed by preheating) + O_2 (in oil) + Zn polyphosphate (by hydrolysis $(H_2O) \rightarrow Zn$ phosphate + H_3PO_4) + $ZnSO_4$ + ZnS (by oxidation $\rightarrow ZnSO_4$) \rightarrow Zn ortho- and pyro-phosphate + $ZnSO_4 \uparrow$ + $ZnS \downarrow$ (5~7%)

• DDP-1 Thermal Film

1 min.: Decomposed DDP-1 products preheated at 170 °C begin to react with Fe and deposit on the surface. Fe sulfates, sulfides, and phosphates are observed. Sulfur species are very active. Phosphates are more than sulfur compounds at the surface area because of many decomposed DDP-1 products. The chemical structure and reaction are not stable.

5 min.: The growth rate is very high ($k=0.4062$ (μ m/min.)). Film thickness also increases very fast. Sulfur compounds are formed a lot and move deeper into the thermal film. Sulfide exists deeper in the tribofilm with sulfates near the surface. Phosphates are iron ortho- or pyrophosphates. DDP-1 is not thermally stable with a low flash point and decomposes easily yielding abundant active phosphorous and sulfur species to form thermal films. Sulfur containing compounds are more likely to deposit on the steel surface than P containing ones. However, at the very top layer, phosphates are dominant.

10 min.: The growth rate of the thermal film decreases dramatically as the active species in the oil are reduced due to the rapid decomposition. However, reconstitution of the

composition and structure of the thermal film proceeds. Medium chain length polyphosphates are formed near the top, but the bulk is still composed of iron phosphates. Overall, sulfur species are still dominant. The S/P ratio decreases from 9.76 to 7.23 in the bulk of the thermal film as calculated from the FLY spectra, while the near surface region (50 nm) has an S/P ratio of 3.12. The sulfate/sulfide ratio is 8 indicating most of the sulfur compounds are present as sulfates. A phenomenological model of the thermal film formed at 10 minutes is shown in Figure 5.32 (Top).

First Step: $(RO)_2PSS-C_2H_4CO_2R$ (solution) \rightarrow $(RO)_2PSSC_2H_4CO_2R$ (decomposed by preheating) + O_2 (in oil) + FeO or Fe_2O_3 \rightarrow Fe ortho- and pyro-phosphate + $FeSO_4$ (or $Fe_2(SO_4)_3$) + FeS(or FeS_2) (only Bulk, 11~12 %) \rightarrow Fe medium chain polyphosphate (in 5 nm) + Fe ortho- and pyro-phosphate (in Bulk) + Fe Sulfate \uparrow + Fe sulfide (in Bulk)

30 min. and 1 hour: After the initial rapid growth of the thermal film the growth rate slows down to almost 0. There is some reconstitution of the thermal film with the S/P ratio decreasing indicating that the sulfur species is migrating to the metal surface and the outer surfaces getting richer in phosphorous. This may also be made possible by the availability of active phosphorous species in the oil while sulfur species are reduced significantly. Sulfides are almost completely oxidized at this point.

4 hour: The thickness of thermal film is not changed. The reorganization and rearrangement of molecules inside thermal films continues. The proportion of S/P is ~2 at surface and ~2.7 in the bulk steadily. Phosphates are iron ortho- and pyro-phosphates. No sulfide is found.

4 hour thermal film model of DDP-1 can be seen in Figure 5.32 Bottom.

Second Step: $(RO)_2PSSC_2H_4CO_2R$ (decomposed by preheating) + O_2 (in oil) + FeO or Fe_2O_3 + Fe medium chain polyphosphate (by hydrolysis \rightarrow Fe phosphate) + Fe Sulfate (by hydrolysis(H_2O) \rightarrow Fe ion + H_2SO_4) + Fe Sulfide (by

oxidation \rightarrow FeSO_4 or $\text{Fe}_2(\text{SO}_4)_3$ \rightarrow Fe ortho- and pyro-phosphate \uparrow + Fe Sulfate \downarrow \rightarrow reorganization and rearrangement of thermal film

- **DDP-2 Thermal Film**

1 min.: Already preheated decomposed DDP-2 products begin forming thermal films on the steel surface. Fe sulfates, sulfides, and phosphates are observed. The ratio S/P ratio at the surface is 1 while in the bulk it is 3. Sulfate/Sulfide ratio in the thermal film is between 4-5. However, the initial thermal film of DDP-2 is unstable.

5 min.: The growth rate is not as fast as ZDDP or DDP-1 with a $k=0.0799$ ($\mu\text{m}/\text{min.}$). This means DDP-2 is a thermally stable and does not decompose as quickly. Sulfur-containing decomposed products are much more active with metal cation (Fe) resulting in the formation of sulfates and sulfides, which then migrate to the bulk. At this stage of the thermal film formation the S/P ratio is 12 in the bulk ($3\mu\text{m}$) indicating the dominant role played by the sulfur species, however closer to the surface the ratio is much smaller at 5 indicating the presence of more phosphates near the surface. Phosphates are Iron ortho- or pyrophosphates, but some short chain polyphosphates start to be observed by cross linking of phosphates. Sulfides continue to be present in the thermal film, though smaller in concentration than the sulfates.

10 min.: The growth rate of the thermal film changes after the initial film formation and growth rate reduces to 0.0249 ($\mu\text{m}/\text{min.}$). DDP-2 continues to decompose and provides active species for the growth of thermal films with sulfate being a dominant part of the film chemistry. At this stage the S/P ratio is 17 in the bulk and 7.6 at the surface and the extent of sulfides is decreased with increasing oxidation of the sulfides. Iron phosphates combine with each other resulting in chain extension to medium and short chain length polyphosphates at near the surface of film. We can see the 10 minute DDP-2 thermal film model at the top image of figure 5.33.

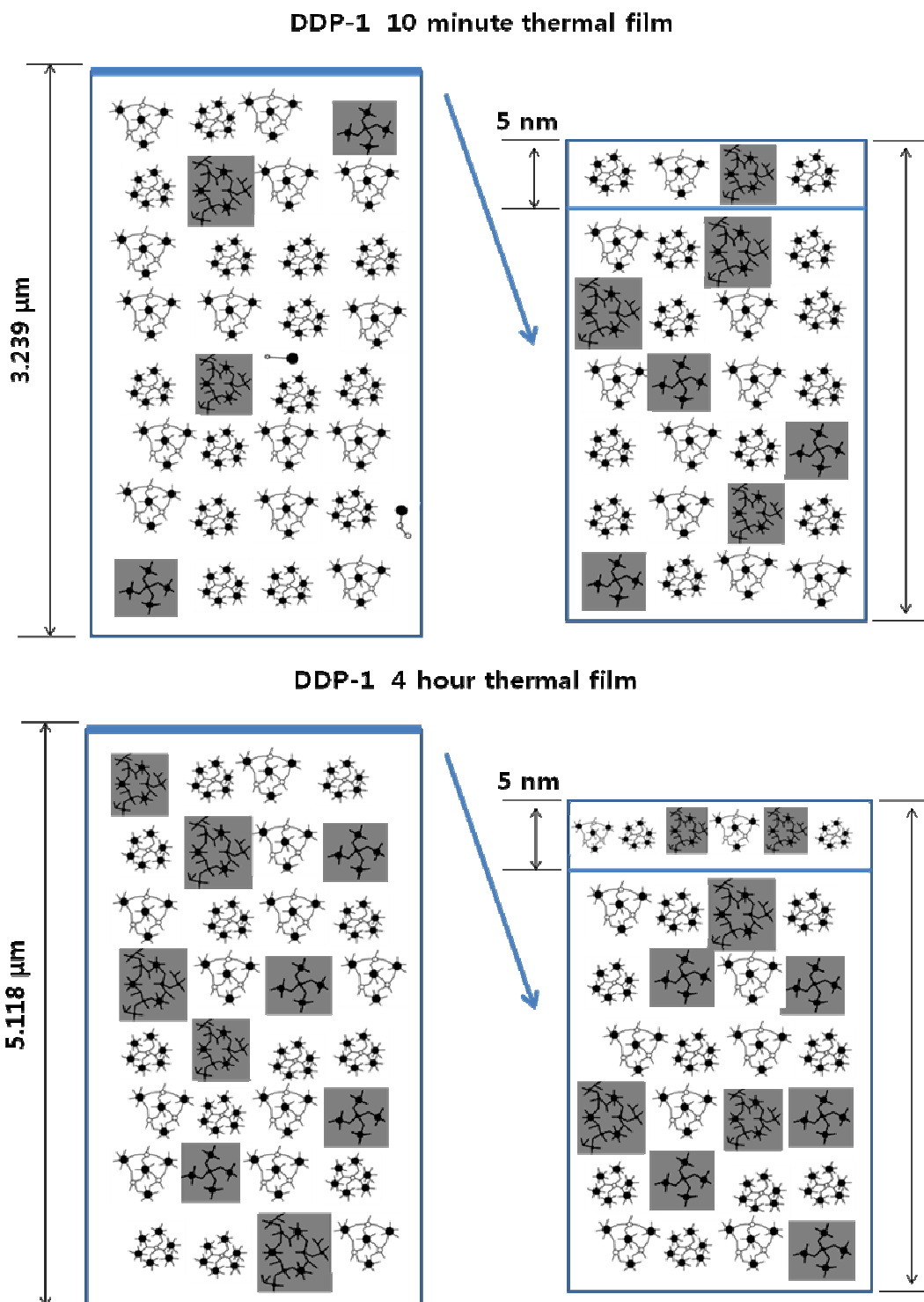


Figure 5.32 Phenomenological Model of DDP-1 Thermal Films. Top Picture is 10 minute DDP-1 Thermal Film and Bottom Picture is 4 hour DDP-1 Thermal Film.

First Step: (RO)₂PSS-C₂H₄COOH (solution) → (RO)₂PSSC₂H₄COOH (decomposed by preheating) + O₂ (in oil) + FeO or Fe₂O₃ → Fe ortho- and pyro-phosphate + FeSO₄(or Fe₂(SO₄)₃) + FeS(or FeS₂) → Fe short chain polyphosphate (in 50~70 nm) and Fe medium chain polyphosphate (in 5 nm) + Fe Sulfate↑+ Fe sulfide

30 min.: The reaction with P-containing decomposed products is accelerated. The S/P ratio decreases to 10 in the bulk and 4.05 near the surface. The phosphate glass near the surface continue to cross link near the surface yielding medium and long chain polyphosphates near the surface while in the bulk of the thermal film FePO₄ is present. Sulfides and sulfates are still present in the thermal film.

1 hour: At this stage the growth of the thermal film with DDP-2 slows down but continues at a steady pace unlike ZDDP and DDP-1 where the growth rate is substantially lower. The S/P ratio continues to drop indicating that phosphates continue to deposit and remain near the top of the thermal film. The lower S/P ratio may suggest that with increasing thickness of the thermal film, sulfur species present deeper down in the thermal film may not be analyzed (XANES K edge FLY mode cannot detect over 3000 nm depth). The surface of the thermal has short chain polyphosphates with iron orthophosphates are inside. But unlike the ZDDP and DDP-1 where the oxidation of sulfides to sulfates proceeds with time, there is an increase in the sulfide relative to sulfate at the surface. This possibly results in the reduction of the sulfates or deposition of sulfides.

4 hour: The thickness of thermal film consistently increases and iron phosphates become major compounds throughout the thermal film and extent of sulfur species on the surface is reduced. Small amount of sulfide remain in the bulk of the thermal film. The phosphate chain length remains similar to the film present at 1 hour with short chain Fe polyphosphate in the top 5 nm surface and iron ortho and pyrophosphate at 50~70 nm. 4 hour thermal film model of DDP-2 is shown in Figure 5.33 Bottom.

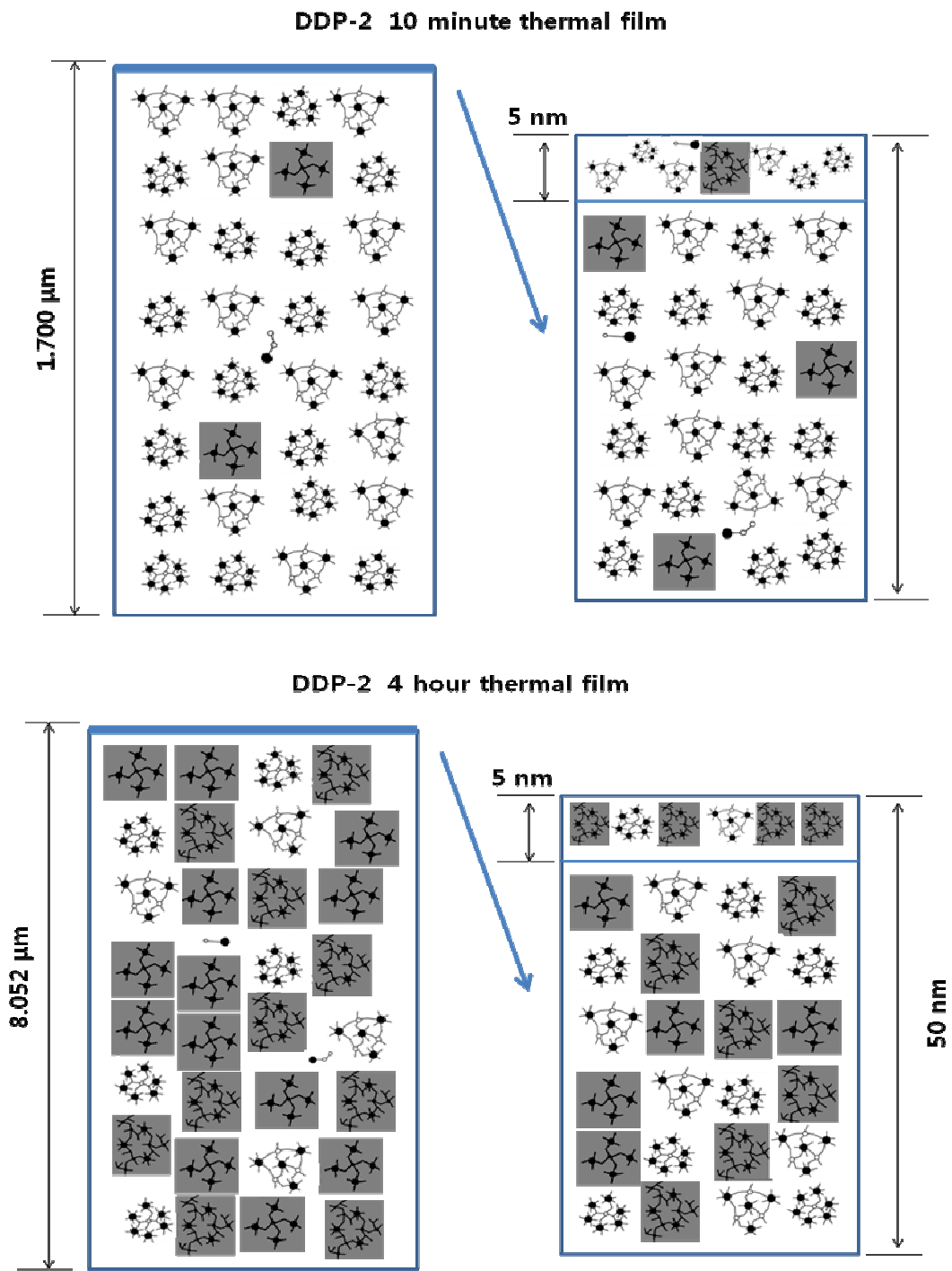


Figure 5.33 Phenomenological Model of DDP-2 Thermal Films. Top Picture is 10 minute DDP-2 Thermal Film and Bottom Picture is 4 hour DDP-2 Thermal Film.

Second Step: (RO)₂PSSC₂H₄COOH (decomposed by preheating) + O₂ (in oil) + FeO or Fe₂O₃ + Fe polyphosphate (by hydrolysis (H₂O)→Fe phosphate + H₃PO₄) + Fe Sulfate (by hydrolysis(H₂O)→Fe ion + H₂SO₄, and by the transition of oxygen to FePO₄) + Fe Sulfide (by oxidation→FeSO₄ or Fe₂(SO₄)₃) → Fe short chain polyphosphate (at the surface) + Fe ortho- and pyro-phosphate ↑+ Fe Sulfate↓ + Fe Sulfide↓

• DDP-3 and DDP-4 Thermal Film

Thermal films from DDP-3 and DDP-4 were only acquired after 4 hours of thermal exposure. The 4 hour thermal film models are provided in figure 5.34. It is difficult to understand the mechanism of formation of thermal film with limited information; however, the final constitution of their thermal films can be envisaged based on XANES data. However, based on evidence gathered with ZDDP, DDP-1 and DDP-2 a hypothetical model is proposed with some assumptions.

The formation of thermal film of DDP-3 appears to be similar to thermal films of DDP-1. The final S/P ratio is high value of 5.51 in the bulk and 3.81 at the surface. Sulfides are still observed inside the thermal films. All iron phosphates are ortho and pyro iron phosphates. Its final thickness is very high (8.923 μm). The closest thing is the thermal stability of both. Both have low flash points as mentioned in Table 5.1 and are easily decomposed. This property may explain why the thermal film formed by DDP-3 is very similar to the one formed by DDP-1 and may be dominated by the fact that both of them have low flash temperature.

The final 4 hour DDP-4 sample has many iron phosphates everywhere. At the surface area, short chain polyphosphates are also observed. Iron phosphorus compounds are mostly dominant in this thermal film. This result indicates DDP-4 may resemble the reaction of DDP-2. They both are more thermally stable as shown in Table 5.1.

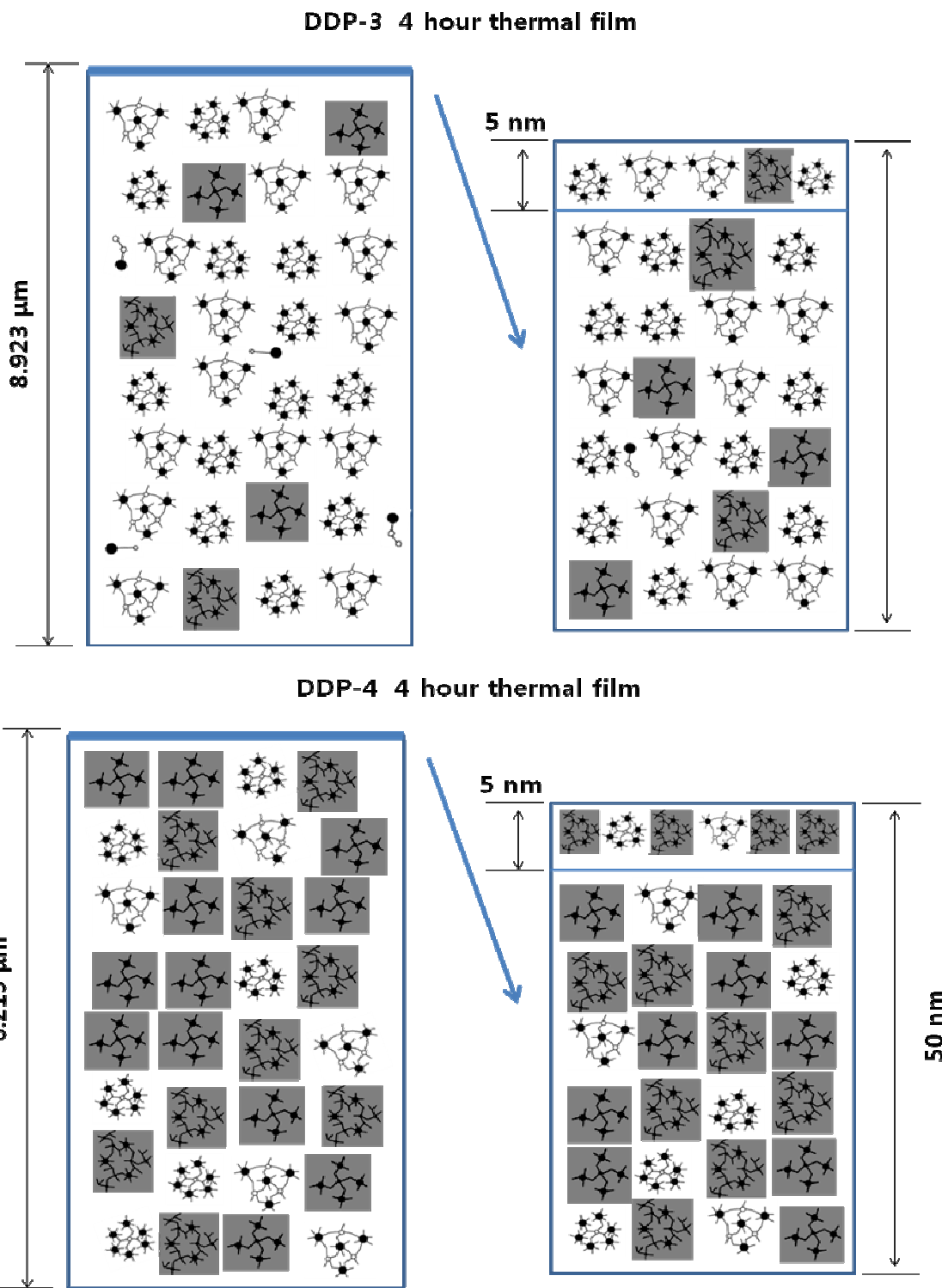


Figure 5.34 Phenomenological Model of DDP-3 and DDP-4 Thermal Films. Top Picture is 4 hour DDP-3 Thermal Film and Bottom Picture is 4 hour DDP-4 Thermal Film.

5.4 Conclusion

This study was undertaken to understand the mechanism of formation of thermal films generated from various metal and metal free dithiophosphate. For more detailed information, various time dependent thermal film samples have been used. The growth rate and the thickness of thermal film were obtained from SEM experiments. From P and S K and L edge XANES technique, fruitful chemical and structural information could be analyzed. With all analysis, the phenomenological models for thermal film structure have been proposed.

All thermal films are formed on the steel surface uniformly even if they grow to be several microns thick. These phenomena were found at the morphology images from the optic profilometer. There are three different patterns of formation of thermal films as different thiophosphate chemistries. The first case is the additives which have a lot of metal elements like ZDDP. The decomposed P- and S- containing products react with the metal surface forming thermal films. Second, ashless thiophosphates with low flash point was decompose very quickly with sulfur species forming very rapidly on the surface with sulfates dominating. Subsequently, phosphates are deposited and diffuse into the bulk of the thermal film. As the available active species are reduced over time the growth of the thermal film slows down and only oxidation and hydrolysis of thermal films were observed. Third, In case of ashless thiophosphates with high thermal stability, these additives decomposed slowly. At the initial stage many sulfur species deposited on the surface. However, with increasing time the phosphates are the dominant species in the thermal film. The reduction and reorganizations of sulfur species were carried out rather than hydrolysis.

CHAPTER 6

XANES ANALYSIS OF THERMAL FILMS FORMED FROM ASHLESS ANTIWEAR COMPOUNDS COMPARING WITH ZDDP: ASHLESS AMINE PHOSPHATES

Thermal decomposition has been accepted as the major mechanism of antiwear tribological film formation. A study of thermal films generated from various antiwear additives, provides valuable insights into the mechanism of tribofilm formation and the antiwear performance of additives can be indirectly understood. In this section, X-ray absorption near edge structure (XANES) spectroscopy has been used to characterize the chemistry of thermal films on steel substrates, which were generated from solutions of phosphorus containing additives, in particular in this study, three different amine phosphate additives were examined. Thermal films were formed at 170 °C by immersing steel coupons in oil containing these additives at a nominal concentration of 0.08 wt. % phosphorous for durations ranging from 1 minute to 4 hours (1, 5, 10, 30 min and 1, 4 hour). Using the secondary electron microscope (SEM), thermal film thickness was measured and the growth rate was calculated. The topography of thermal film surfaces was observed using an optical profilometer. The phosphorus K and L edge spectra and nitrogen K edge spectra show the chemical composition and structure of thermal films at the surface region as well as at the bulk region.

6.1 Introduction

A number of ashless phosphorus containing additives have been used in the lubricating oil industry as antiwear (AW) and extreme pressure (EP) additives for well over the past 50 years even though the zinc dialkyl dithiophosphates have been widely used as main antiwear additives in both automobile and industrial oils for many years. [49,118] In particular, phosphate esters have become popular among the various types of organo-phosphorus

compounds used to protect wear as an alternative to ZDDP at some tribological applications. [50] Phosphate esters generally react with various machined surfaces in order to form a protective film that mostly consists of iron polyphosphates, iron phosphates, and organic phosphates. [118] Xu et al. tested tricresyl phosphate (TCP) and triphenyl thiophosphate (TPPT) at the four ball tester and they found both are good anti-scurf, antiwear, and antifricition agents. [132] Zhang et al. [133] studied the interaction between diaryl phosphate (DPP) and dispersants and Najman et al. [50] investigated the interaction between diaryl phosphate (DPP) and triaryl phosphate (TPP) and sulfur containing extreme pressure (EP) agents. In addition to the studies of organophosphate additives like TCP, and DPP, the tribological effect of different substituent groups, especially adding amine groups have attempted. Minami et al. found the wear protection of amine salts of phosphate was better than one of phosphate alone because the alkyl groups from the amine group increased the overall solubility resulting in increasing its lubricity. [134] However, at higher loads, the antiwear properties of amine phosphates were decreased. [135] Wan et al. also insisted that amines reduced the antiwear properties of P-containing additives. [136] In spite of this controversy, amine phosphates are still widely used in various industrial applications. Hence, a detailed study of tribofilm formation from amine phosphates would provide insights into their behavior.

While amine phosphates have been used extensively as antiwear additives, the exact mechanism by which they afford wear protection is still poorly understood. It is generally accepted that there are several steps of the formation of tribofilm. First step and the most important step of this process is the thermal and thermo-oxidative decomposition of antiwear additives in oil solution. The chemical properties and even film growth pattern of tribofilm can be influenced by this thermal decomposition process as already studied at the previous chapter 5. Therefore, the thermal film formed by immersing steel coupons in oil formulation becomes important to study the mechanism of the tribological formation of film from ashless amine phosphates.

In this study, three different amine phosphates as ashless antiwear additives have been examined to understand the mechanism of thermal formation of film formed from organic phosphates containing functional group, here amine group, comparing with secondary ZDDP. Phosphorus K and L edge XANES spectra and nitrogen L edge XANES spectra have been used for elemental and chemical structural properties of thermal films. To measure the thickness of thermal films, the secondary electron microscope (SEM) has been tested. The topographical tests for thermal films have been done at the optic profilometer. Finally phenomenological models for thermal film generated from amine phosphates are developed.

6.2 Experimental Details

6.2.1 Materials and Sample Preparations

Three different ashless amine phosphates were studied in this study and compared with zinc dialkyl dithiophosphate (ZDDP). Figure 6.1 shows the common chemical structures of amine phosphate. Amine phosphates can be dibasic, mono basic structure, or mixture of both structure. Their properties are shown in table 6.1. All compounds were diluted to 0.08 wt% phosphorus with 100 neutral mineral oil. An amine phosphate usually consists of a phosphate and an amine group, which are connected by hydrogen bond. AP-1 and AP-3 have lower density than water (1 g/cm^3) while AP-2 is slightly higher (1.02 g/cm^3). In amine phosphate compounds, the functional groups (hydrocarbons) are meaningful in point of the thermal stability. AP-2 is a little acidic according to the result of TAN test.

All thermal films were formed by the static immersion of a steel coupon in 0.08 wt% solution in a preheated oil bath at $170 \text{ }^\circ\text{C}$ for 1, 5, 10, 30 minutes, 1 hour, and 4 hours. Detailed procedure is explained in previous chapter. All samples for thermal films were gently rinsed with hexane prior to each XANES, SEM, and optic profilometer analysis.

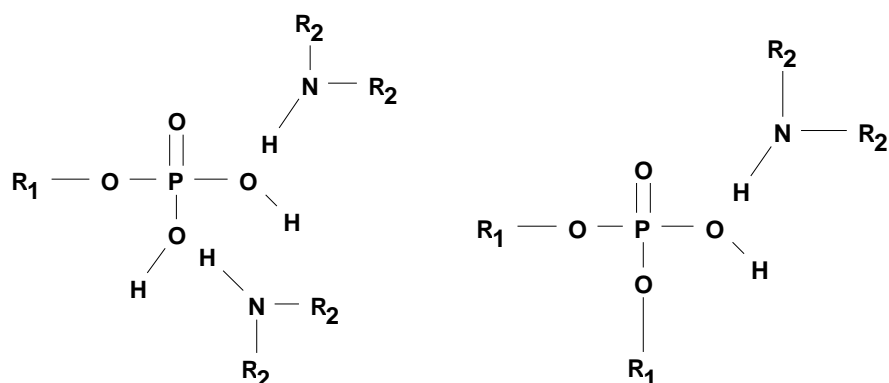


Figure 6.1 Common Chemical Structure of Amine Phosphate. Phosphate and Amine Group are Connected by Hydrogen Bond. a) Dibasic Amine Phosphate and b) Monobasic Amine Phosphate.

Table 6.1 Properties of Ashless Amine Phosphates. [49,117,137-140]

Additives	R ₁	R ₂	Flash Point (°C)	Density (g/cm ³)	TAN Test (mg, KOH/g)
AP-1	hexyl (aryl)	C11-C14 branched	135	0.92	-
AP-2	mixed methyl and butyl (isobutyl)	mixed methyl and butyl (isobutyl)	113	1.02	245-275
AP-3	alkyl	alkyl	96	0.94	-

6.2.2 Data Acquisition and Analysis

Thickness measurements for thermal films were conducted using secondary electron imaging in a Hitachi 3000 scanning electron microscope (SEM). Topographical surface images were taken using a Wyko NT9100 Surface Profiler.

The XANES spectroscopy was used to analyze phosphorus and nitrogen in the thermal films formed on steel coupons by three different amine phosphate solutions. The K edge data of phosphorus were obtained on the Canadian double crystal monochromator (DCM) beamline at the Synchrotron Radiation Center (SRC) of the University of Wisconsin–Madison in Stoughton, Wisconsin. These spectra has the energy range of 1500 to 4000 eV with 0.3 eV for P and 0.5 eV for S scan step of resolution. The P L-edge spectra of lower energy range were collected on the variable line spacing plane grating monochromator (VLS-PGM) beamline at the

Canadian Light Source (CLS) facility in Saskatoon, Saskatchewan, Canada. The PGM beamline covers between 5.5 and 250 eV with 0.1 eV scan step of resolution. In case of nitrogen (N) K-edge, the high resolution spherical grating monochromator (SGM) beamline in the CLS facility was used. It covers the energy range between 250 to 2000 eV with 0.1 eV scan step in 1000 μm by 100 μm spot size. In all XANES spectra, the total electron yield (TEY) mode for the information of surface region and the fluorescence yield (FLY) for the information of the bulk region were collected.

6.3 Results and Discussion

6.3.1 Thermal Film Thickness

All thermal films for thickness measurement were formed on thin AISI 1075 steel coupons (50 μm X 2 mm X 5 mm). The scanning electron microscope (SEM) was used to take the cross section image of thermal film formed on the steel surface. Thermal films of AP-1 were baked for various times ranging from 1 min to 4 hours while AP-2 and AP-3 were only backed for 4 hours. Figure 6.2(a, b) show the average thicknesses of thermal films generated from AP-1 and ZDDP at 20 different spots as a function of time. Figure 6.4(a) is the plot of thickness growth of thermal film versus time. Thermal film of ZDDP was used as a reference to compare with the thermal films of the amine phosphates. In case of AP-2 and AP-3, only the 4 hour data is shown. In the first 10 minutes, a very rapid increase in film thickness is shown in Figure 6.4(a). Then, the growth rate of the thermal film slows down and is steady state till the end of test (4 hour) with final thickness of 6.54 μm in case of AP-1 and of 3.20 μm in ZDDP. The growths of the tribofilms of AP-1 and ZDDP also follow an exponential type growth pattern. The growth kinetics of the thermal film generated from AP-1 can be broken down into three steps while one of ZDDP is two steps. Figure 6.4(b) is the plot of $\ln(\text{thickness})$ versus time related with AP-1. AP-1 has different growth pattern from ZDDP and ashless DDPs. Two clear transition points for the growth rate are observed in figure 6.4(b). Initially, its thickness increases rapidly with

$k=0.4632$ ($\mu\text{m}/\text{min.}$) until 5.0 minutes and thickness of $2\ \mu\text{m}$ and the growth rate reduces to $k = 0.0268$ ($\mu\text{m}/\text{min.}$) through 30 minutes and thermal film thickness of $3.86\ \mu\text{m}$. After about 30 minutes, the thermal film of AP-1 continues to with a slower growth rate of $k=0.0025$ ($\mu\text{m}/\text{min.}$) with a final thickness of $6.54\ \mu\text{m}$ at 4 hours. Subsequently, the availability of active decomposition product is reduced and the growth rate of thermal film is reduced. Shown in figure 6.4(c) is the growth of a ZDDP thermal film where two different growth rates are observed. Thermal films of ZDDP grow fast until 11.26 minutes with a thickness of $2.459\ \mu\text{m}$ and growth rate $k=0.1905$ ($\mu\text{m}/\text{min.}$) following which the growth rate slows down to $k=0.0012$ ($\mu\text{m}/\text{min.}$). In comparison, AP-1 decomposed rapidly at $170\ ^\circ\text{C}$, and its decomposed products react with steel surface rapidly in the initial stage. However, in AP-1 after the initial fast growth rate the rate drops rapidly but it still has more active species than ZDDP resulting in a thicker film compared to ZDDP.

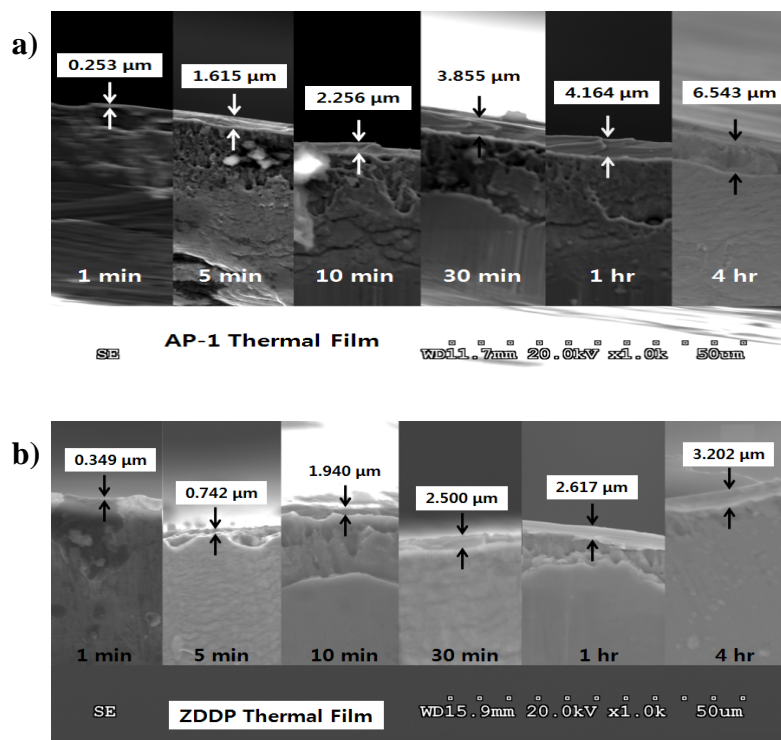


Figure 6.2 Cross-Section Images of Thermal Film Thicknesses Formed from a) AP-1 and b) ZDDP

Figure 6.3 provides thermal film thickness after 4 hour baking for the different amine phosphates and ZDDP. The thickness of 4 hour thermal film from AP-2 is 7.085 μm and AP-3 is 3.795 μm . All the data shown here is for the final thickness at 4 hours and hence growth patterns cannot be deduced. However, based on final thickness one can deduce AP-2 may follow the growth of AP-1 and AP-3 may be closer to ZDDP.

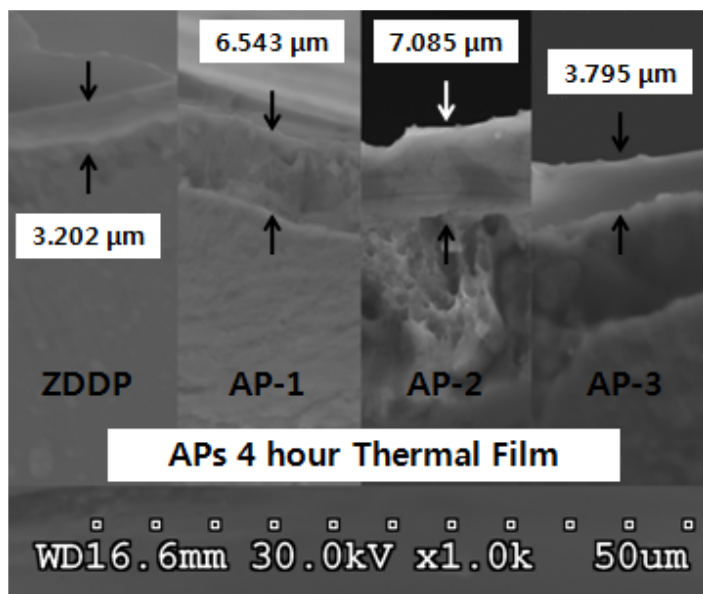


Figure 6.3 Cross-Section Images of Thermal Film Thicknesses Formed from Different Chemistries at 4 hour.

6.3.2 XANES Analysis of Thermal Film

X-ray absorption near edge structure (XANES) spectroscopy was used to characterize the chemical makeup of the thermal films. Total electron yield (TEY) and fluorescence yield (FLY) spectra of Phosphorus K and L edge and nitrogen K edge were collected. TEY which has the information of near surface area covers approximately 5 nm depths at L edge and 50 nm depths at K edge. FLY which has the information of bulk area covers approximately 50 nm depths at L edge and 1000–3000 nm depths.

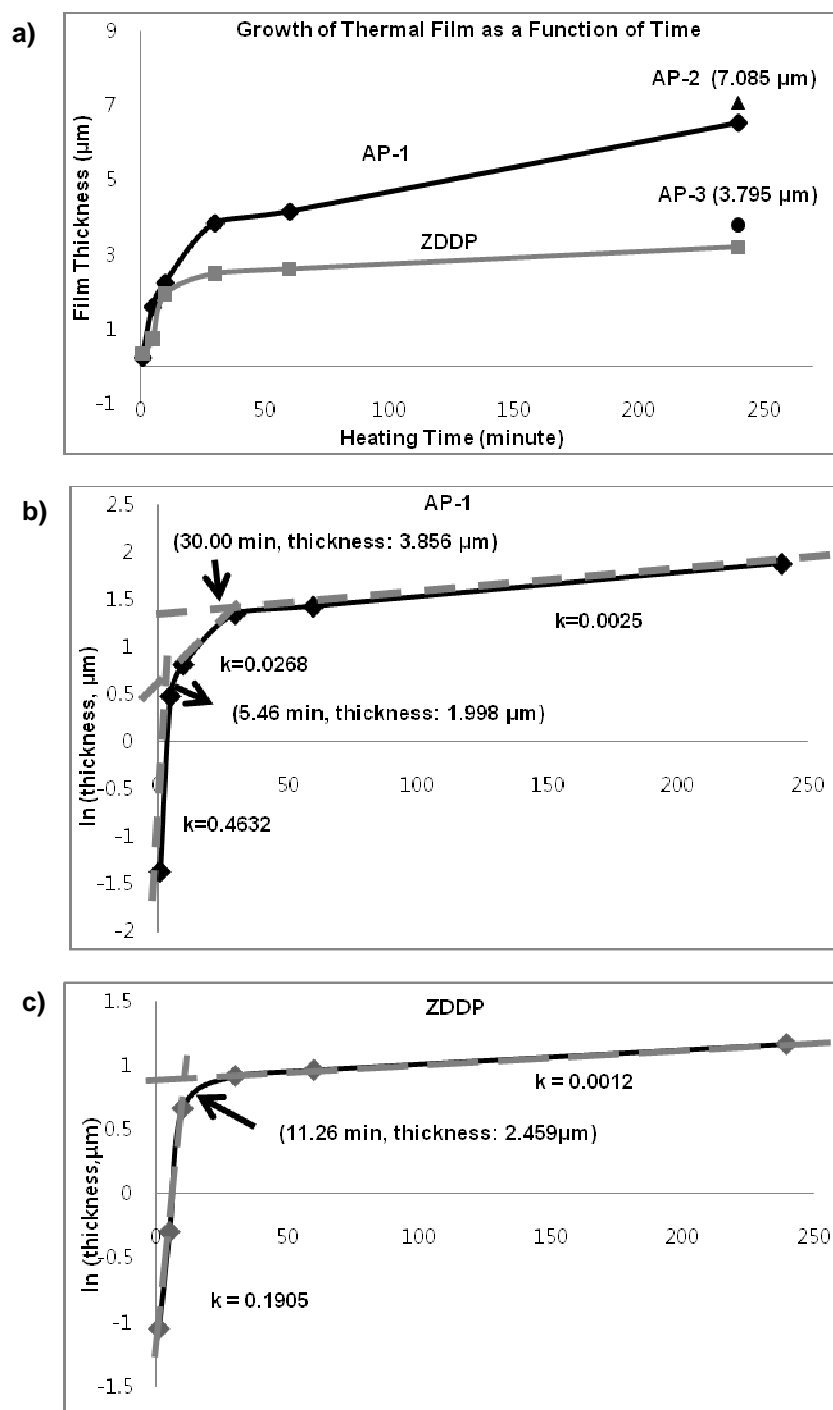


Figure 6.4 Plots of Thermal Film Growth as a Function of Time. a) Plots of Thermal Film Growth of Three Different Amine Phosphate Chemistries and ZDDP, b) Logarithm of Thickness of Thermal Film Formed from AP-1, and c) Logarithm of Thickness of Thermal Film Formed from ZDDP.

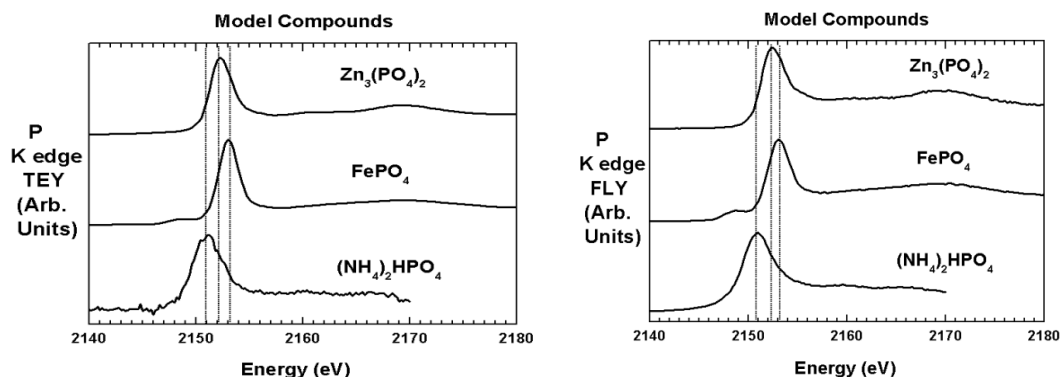


Figure 6.5 XANES Spectra of the TEY and FLY modes at the P K edge of Model Compounds: $Zn_3(PO_4)_2$, $FePO_4$, and $(NH_4)_2HPO_4$

6.3.2.1 Phosphorus Characterization

K edge of Phosphorus

In figure 6.5, phosphorus K edge XANES spectra of three model compounds: $Zn_3(PO_4)_2$, $FePO_4$ and $(NH_4)_2HPO_4$, are shown. The main peak of zinc phosphate is observed at 2152 eV, while one of iron phosphate is located at 2153 eV. Ammonium phosphate has its white line at about 2151 eV. $Zn_3(PO_4)_2$ has the shoulder at the right side of main peak and its main peak is a little wider than iron phosphate. $FePO_4$ has clear pre-edge at the left side of main peak. The width of main peak of $(NH_4)_2HPO_4$ is the widest among three model compounds.

Figure 6.6 shows P K edge spectra of all thermal films formed from AP-1 as a function of baking time. Comparing with model compounds, the white line peaks of all thermal films of AP-1 are close to the main peak of iron phosphate. None of the main peaks of thermal films can be identified to either ammonium phosphate or zinc phosphate. Hence, in this study, thermal films formed from AP-1 through thickness are mainly comprised of iron phosphates. The intensities of white line of thermal films in figure 6.6 increase with baking time indicating the thickness of thermal film increase.

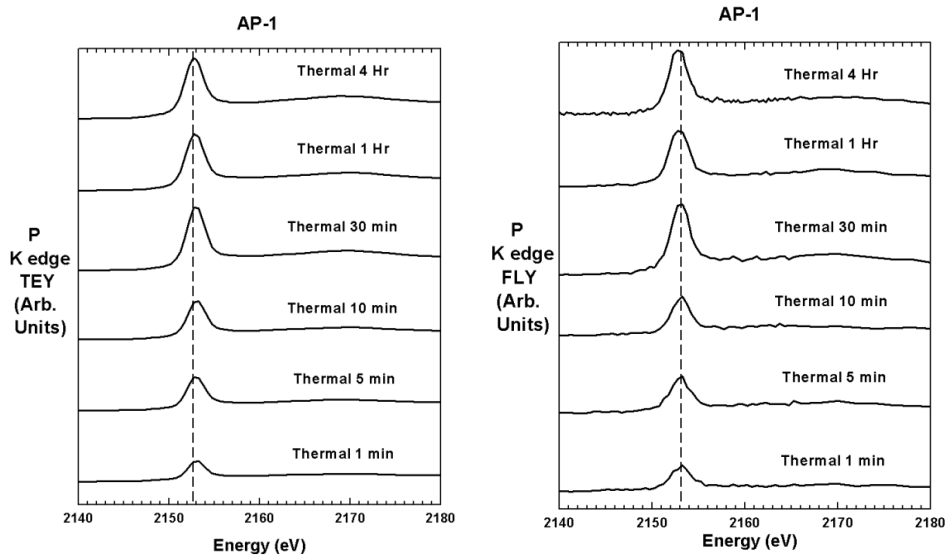


Figure 6.6 XANES Spectra of the TEY and FLY modes at the P L edge of Thermal Films Formed from AP-1 as Baking Time.

Figure 6.7 shows XANES spectra of the TEY and FLY modes at the P K edge of thermal films formed from three different amine phosphate additives. All 4 hour thermal films formed from three amine phosphates have the white peak which is placed at approximately 2153.0 eV, indicating iron phosphates. They have thermal films consisting of iron phosphates while the thermal film of ZDDP mainly has zinc phosphates with the main peak of 2152.0 eV.

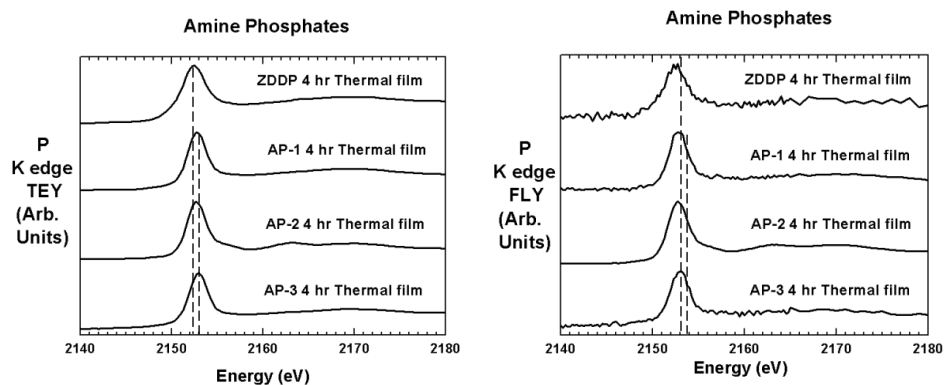


Figure 6.7 XANES Spectra of the TEY and FLY modes at the P K edge of 4 hour Thermal Films Formed from Three Different Amine Phosphate Additives Comparing with ZDDP 4 hour Thermal Film.
L edge of Phosphorus

Figure 6.8(a) is the XANES spectra at L edge of phosphorus model compounds. Zinc phosphate ($Zn_3(PO_4)_2$), iron phosphate ($FePO_4$), and ammonium phosphate ($(NH_4)_2HPO_4$) are plotted in the graph as model compounds. The spectra of phosphates are composed of four different peaks from (a) to (d). In this chapter, the explanation about the implication of each peak is skipped as it is already detailed in chapter 5. When comparing the white line (c) peak of model compounds, it is evident that ammonium phosphate has the lowest energy peak at approximately 138.2 eV and zinc phosphate has a slightly higher energy state at 138.7 eV and iron phosphate occurs at the highest energy at 139.0 eV. In addition, zinc phosphate has lower pre-edge peaks whose position is similar to the pre-edge of ammonium phosphate. In case of ammonium phosphate, its pre-edge peak (peak (a)) is at a lower energy at about 135.8 eV than pre-edge peaks of iron phosphates (peak (a')) at about 136.2 eV. The position of peak b of $(NH_4)_2HPO_4$ is at approximately 137.0 eV. This location is similar to the (b) peak of iron phosphate. The clear feature of ammonium phosphate is the intensity of two pre-edge peaks (a) and (b). These peaks are strong, and look like the peaks of longer chain polyphosphate, especially zinc and iron polyphosphates. Figure 6.8(b) is the plots of phosphorus L edge FLY spectra for undecomposed raw amine phosphate materials. Samples were prepared by being coated on the transparent films by dip coating method and by being dried at the air environment. Because of non-conductive property of organic materials, only FLY mode spectra were detectable. All amine phosphates additives have similar spectra at both two pre-edges and the white line similar to ammonium phosphate model compound. To distinguish between ammonium phosphate and undecomposed amine phosphates, their FLY phosphorus L edge peaks are de-convoluted and a/c ratio was calculated. Figure 6.9 shows the a/c ratio comparison of model compounds as well as amine phosphate raw materials in the FLY mode. The model compounds all have a/c ratio's that are below 0.19 while all the raw amine phosphates have an a/c greater than 0.33.

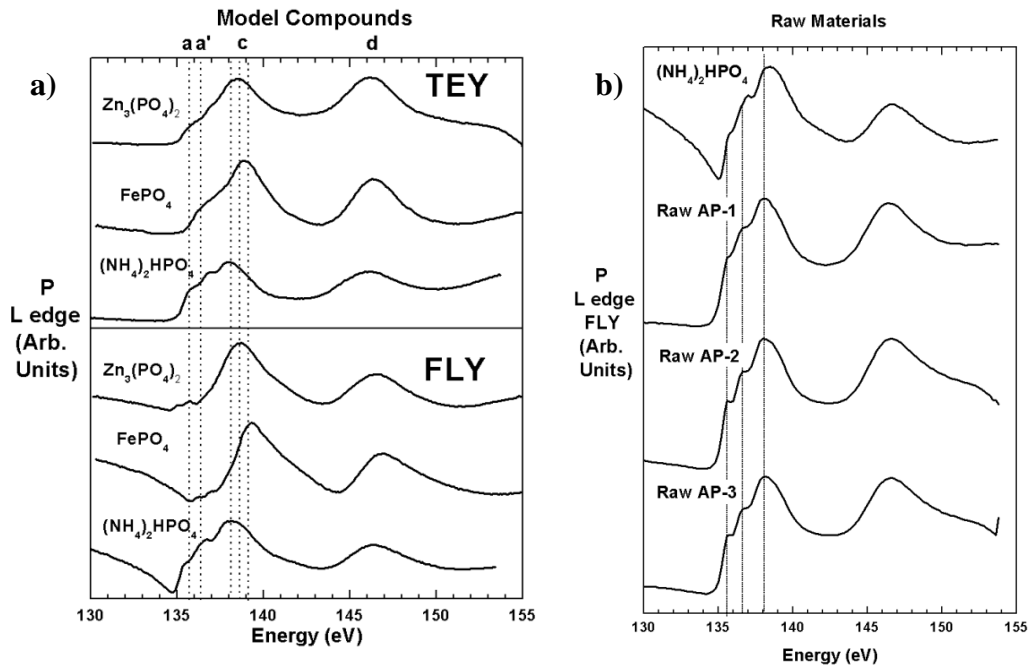


Figure 6.8 XANES Spectra of the TEY and FLY modes at the P L edge of Model Compounds as well as of Raw Amine Phosphate Additives. a) TEY and FLY Spectra of Model Compounds: $Zn_3(PO_4)_2$, $FePO_4$, and $(NH_4)_2HPO_4$ and b) FLY Spectra of Three Different Amine Phosphate Raw Materials.

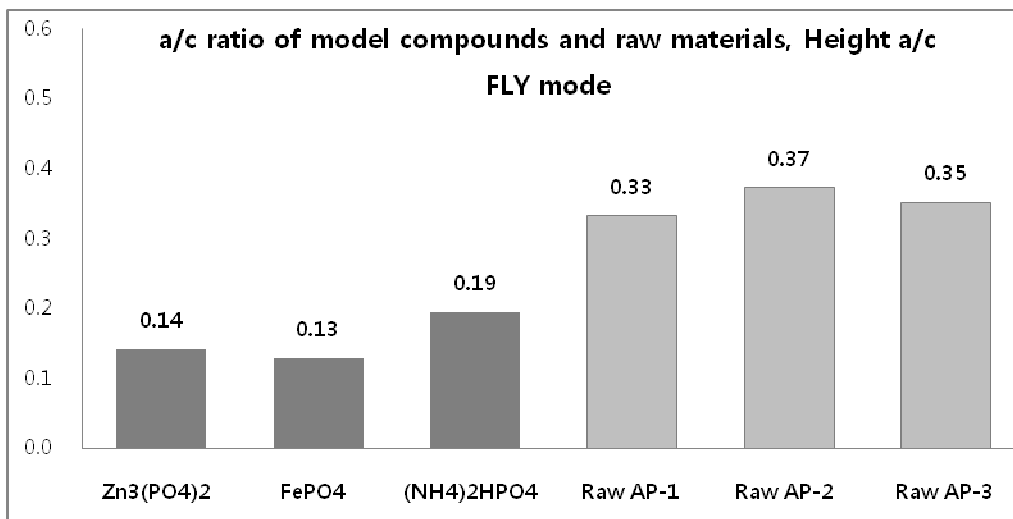


Figure 6.9 The a/c Ratio Comparison of Model Compounds and Raw Materials at the FLY mode.

Figure 6.10 shows the phosphorus L-edge XANES spectra in TEY and FLY modes of thermal films generated from AP-1. Well developed thermal films can be observed from 1 min to

4 hour by examining P L edge spectra at both TEY and FLY mode. The main core peak and two pre-edge peaks of all AP-1 thermal films are close to the peaks of ammonium phosphate model compound. However, by the analysis of phosphorus K edge spectra of thermal films, the composition of thermal film produced by AP-1 is found to be only iron phosphates. Therefore, the energy shift to lower level undoubtedly results from another reason instead of the ammonium phosphate. Najman et al. [49] in their study showed energy shift of the white line peak of iron phosphates resulting from the variation of chain length of iron phosphate. A longer chain iron polyphosphate has lower energy of main peak as shown in figure 6.11. Therefore, all thermal films of AP-1 in this study consist of longer chain iron polyphosphates.

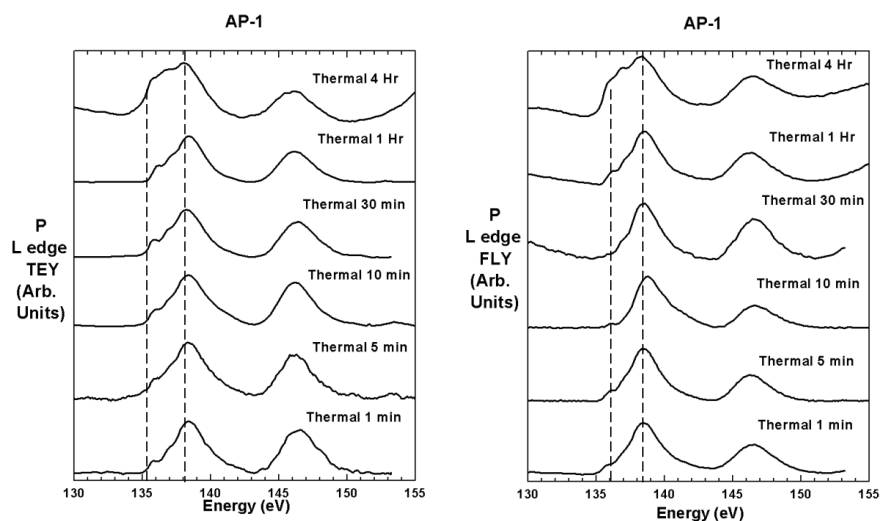


Figure 6.10 XANES Spectra of the TEY and FLY modes at the P L edge of Thermal Films Formed from AP-1 as Baking Time.

Figure 6.12 shows the *a/c* ratio analysis of thermal films formed from AP-1, which give an indication of the chain length of the polyphosphates. The way to analyze and calculate the *a/c* ratio from phosphorus L edge spectra was detailed in an earlier chapter and will not be repeated here. Characterization of the chain length of polyphosphate is based on the following analysis that was detailed in chapter 5: The *a/c* ratio below 0.2 corresponds to common orthophosphate or pyrophosphate. The ratio between 0.2 and 0.35 indicates the short chain

polyphosphate and the value from 0.35 to 0.55 is the medium chain length of polyphosphate. The polyphosphate with a/c ratio above 0.55 are long chain polyphosphate. At the near surface area of 5 nm depth determined from TEY spectra of the L-edge of the thermal films formed by baking for 10 min, the ortho- or pyrophosphates and short chain polyphosphates are deposited on the surface with decomposed amine phosphate compounds. For baking times longer than 10 minutes, the cross linking and chain extension of polyphosphates increase gradually. Finally, medium chain iron polyphosphates occupy the surface area at 4 hour with 0.40 a/c ratio. In the FLY mode that provides information over the top 50~70 nm when L-edge is used, it is evident that in the first 30 minutes the value of a/c ratio decrease indicating the proportion of ortho or pyro phosphate is increased, and then after 30 min, the a/c ratio increases again up to 0.35 at 4 hour. This means that cross linking and chain extension of phosphate compounds continues after the initial 30 min when much of the deposition occurs. Thermal film of 4 hour baking is majorly composed of medium chain length iron polyphosphates and short chain iron polyphosphates. In addition, more complex linked polyphosphates are preferably present in near the top of the thermal film.

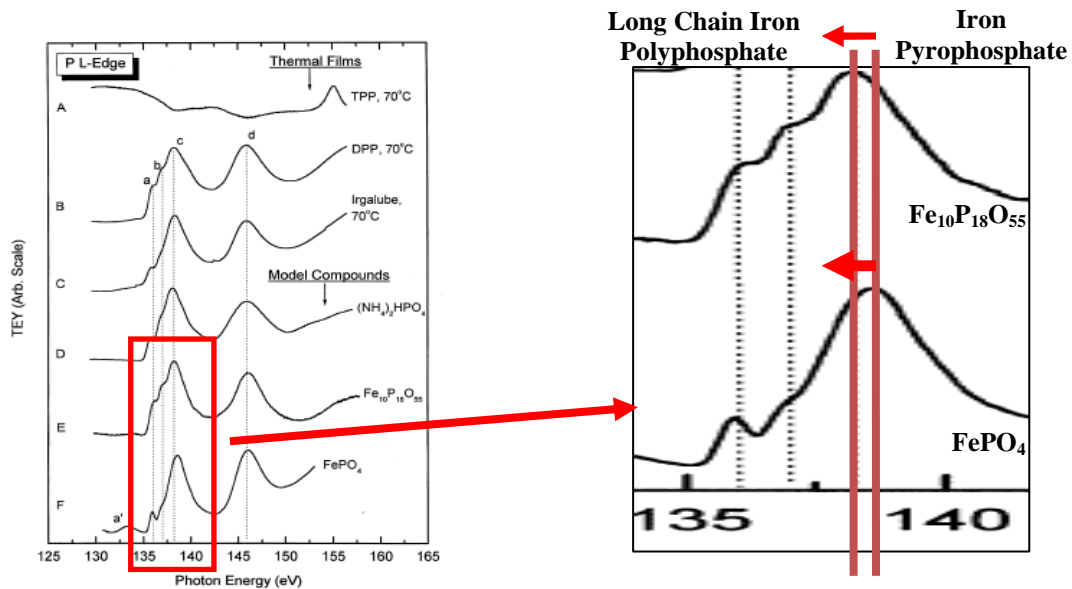


Figure 6.11 Example for Energy Shift of the White Line Peak Because of the Variation of Chain Length of Iron Phosphate. A Longer Chain Iron Polyphosphate Has Lower Energy Range of Main Peak. [49]

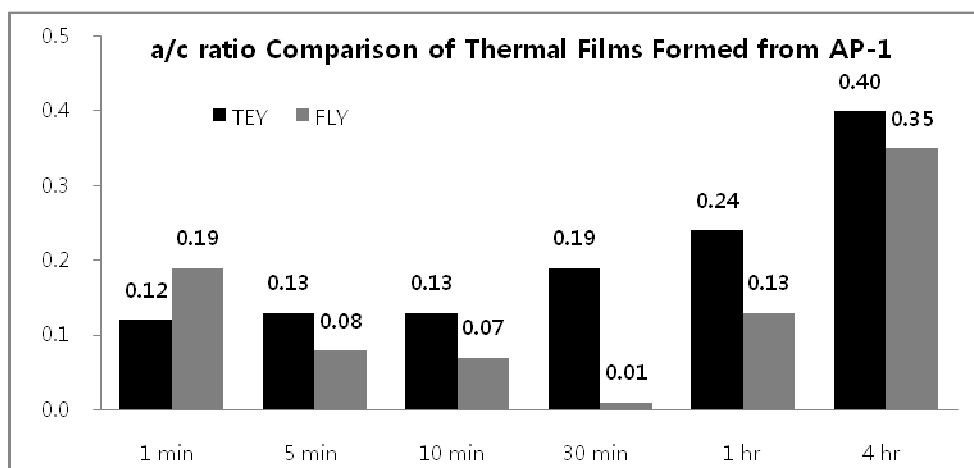


Figure 6.12 The a/c Ratio Comparison of AP-1 Thermal Films as a Function of Time at the TEY and FLY mode.

Figure 6.13 is plots of P L edge XANES spectra of all 4 hour thermal films formed from ZDDP and three different amine phosphates. In both TEY and FLY modes, all white lines of thermal films from amine phosphate species are close to the main peak of short or medium chain polyphosphate while the white peak of ZDDP is identical to zinc phosphate. Figure 6.14 shows the a/c ratio analysis of three different 4 hour thermal films of three amine phosphates. The a/c ratio values of AP-2 and AP-3 are smaller than AP-1. Hence, thermal films of AP-2 and AP-3 are mainly comprised of iron polyphosphates with short chain length.

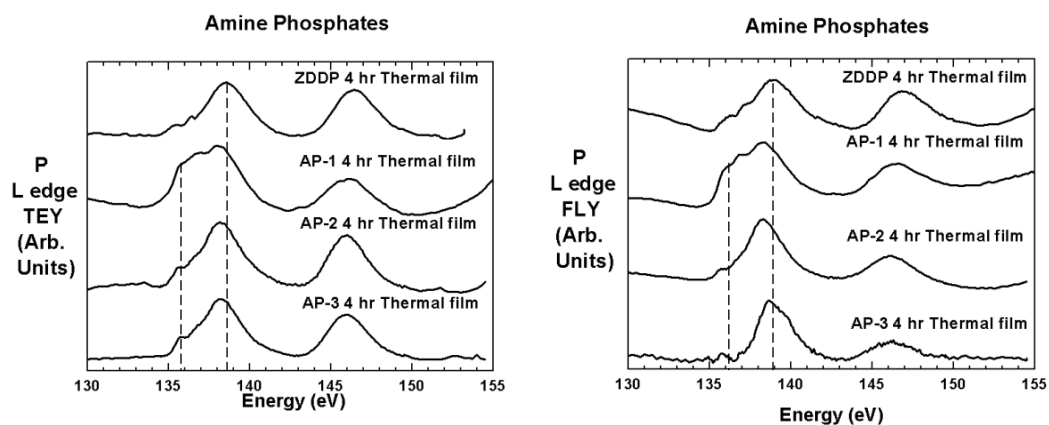


Figure 6.13 XANES Spectra of the TEY and FLY modes at the P L edge of 4 hour Thermal Films Formed from ZDDP and Three Different Ashless Amine Phosphates.

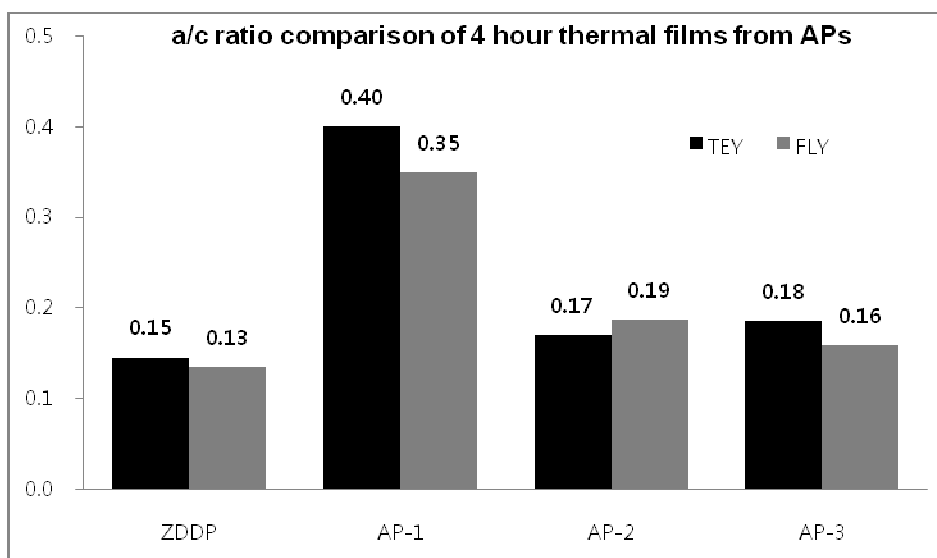


Figure 6.14 The a/c Ratio Comparison as Different Chemistries at 4 hour. The Relative Ratios are Presented in order of ZDDP, AP-1, AP-2 and AP-3.

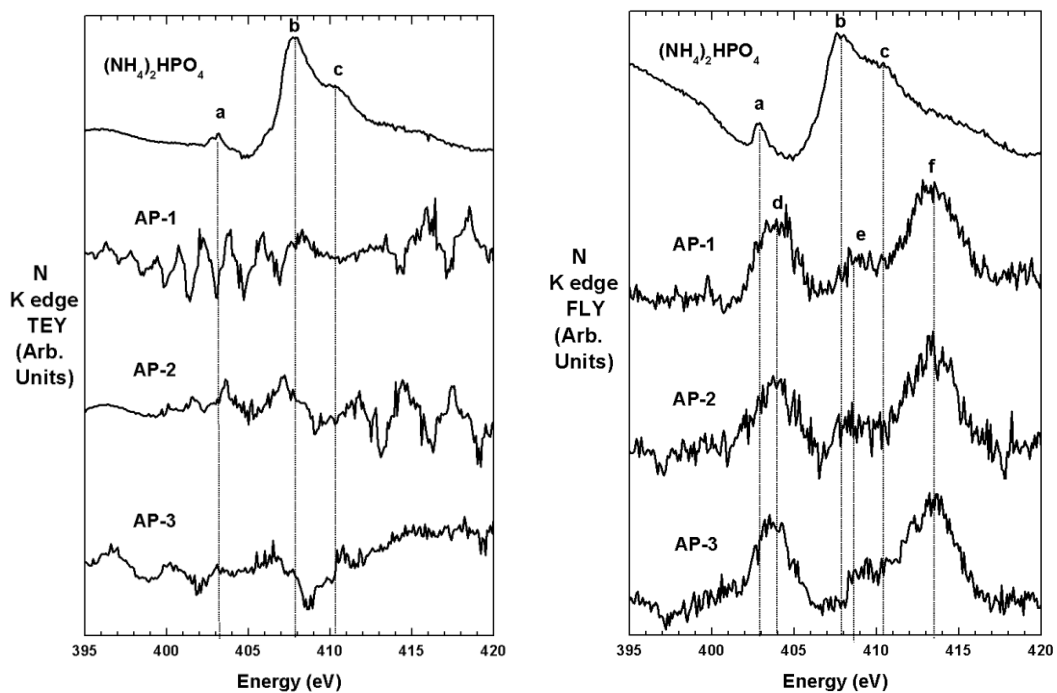


Figure 6.15 XANES Spectra of the TEY and FLY modes at the N K edge of Model Compound, $(\text{NH}_4)_2\text{HPO}_4$, and of 4 hour Thermal Films Formed from Three Amine Phosphates.

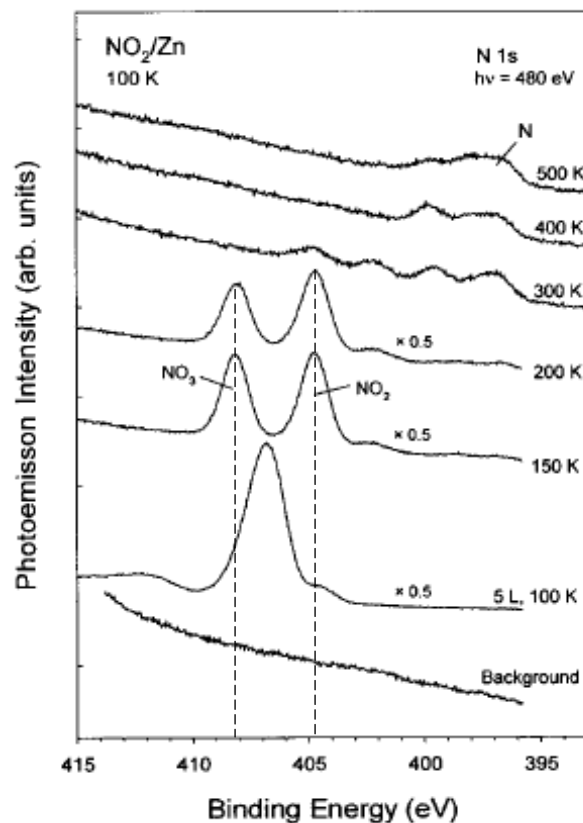


Figure 6.16 Nitrogen K edge XANES Spectra of NO_2 (Nitrite) and NO_3 (Nitrate). N and O 1s Photo Emission Spectra for the Adsorption of NO_2 on Polycrystalline Zinc at 100K. [141]

6.3.2.2 Nitrogen Characterization

K edge of Nitrogen

In order to understand the detailed chemical structure of thermal films generated from amine phosphates, nitrogen K edge XANES spectra have been examined. In figure 6.15, both TEY and FLY mode spectra of ammonium phosphate as a model compound and three different 4 hour thermal films of amine phosphates are plotted. The TEY spectra are noisy and not useful. However, FLY spectra of all 4 hour thermal films indicate the presence of nitrogen species. In comparison to ammonium phosphate, these thermal film spectra are not similar to $(\text{NH}_4)_2\text{HPO}_4$ because ammonium phosphate has the white peak at ~ 408 eV, the pre-edge peak at ~ 403 eV, and the right shoulder at ~ 410.5 eV, however, thermal films have a pre-edge peak 1 eV higher

(~404 eV) and main peak (~409 eV) and another big bump at ~413.5 eV. It indicates that all 4 hour thermal films formed from amine phosphate additives nitrogen in the thermal film, but not in the form of ammonium phosphates. Another study [141] of nitrogen K-edge XANES peaks of NO₂ and NO₃ on polycrystalline zinc are shown in figure 6.16. A nitrite peak is present at ~404.6 eV and a nitrate peak is present at ~408.2. In this study, the main cations are iron. Hence, there is some energy shift due to the variation of cation species. Possibly peak (d) and (e) are related to iron nitrite and iron nitrate although peak (f) is unknown. Therefore, nitrogen containing compounds are oxidized and deposited in the thermal film as oxidized conditions like iron nitrite or iron nitrate.

6.3.3 Surface Morphology

Figure 6.17 shows the topographical surface images of thermal films by using a Wyko NT9100 Optical Profiler. Only 4 hour thermal films formed from ZDDP, AP-1, AP-2, and AP-3 were observed. The bare steel sample prior to deposition of thermal film was also shown in figure 6.17(a). In the chapter 5, thermal films of both ashless thiophosphates and ZDDP are formed on the steel surface uniformly even if they grow to be several microns thick. It is because their optic images are similar with the surface image of bare steel. On the other hand, thermal films of amine phosphates are formed differently in comparison of dithiophosphate compounds. Wide and large patches are deposited on all around surface, whereas canyons between patches are observed with the depth of approximately 0.5~1 μm. No differentiation of functional alkyl groups in amine phosphate compounds is found.

6.3.4 Mechanism of Thermal Film Formulation and Phenomenological Model

All things considered, phenomenological model for thermal film formation of amine phosphate was developed as shown in figure 6.18. Also, the mechanism of formation of thermal generated from amine phosphate antiwear additives has been discussed in this section. The measurement of film thickness has given the growth kinetics of thermal film of amine phosphate compounds.

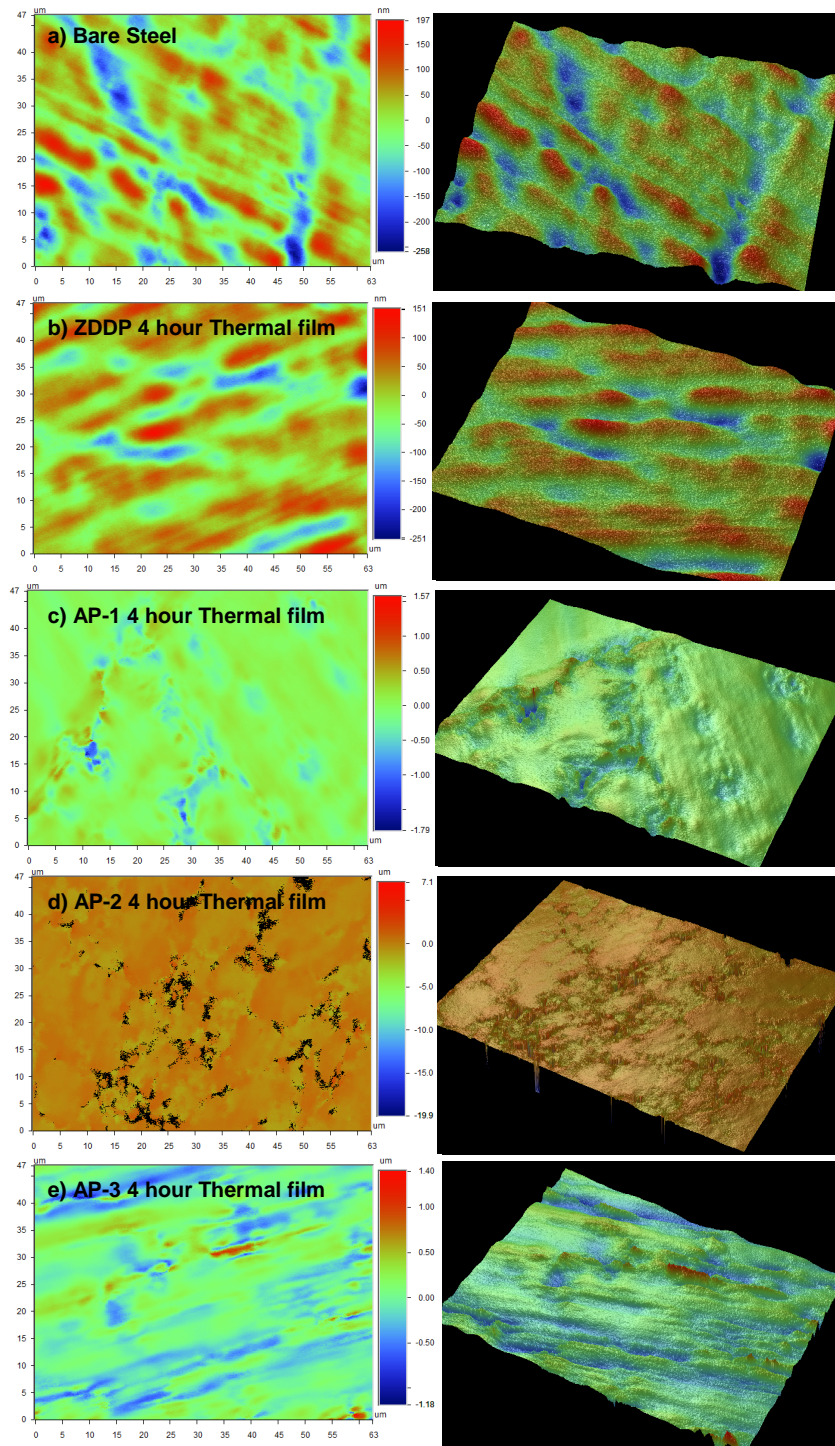


Figure 6.17 Topographical Surface Images (47 μm X 63 μm) of 4 hour Baked Thermal Films Using the Optic Profilometer, Wyko NT 9100. a) Bare Steel Surface, b) ZDDP 4 hour Thermal Film, c) AP-1 4 hour Thermal Film, d) AP-2 4 hour Thermal Film, and e) AP-3 4 hour Thermal Film.

Phosphorus K and L edge and nitrogen K edge XANES technique have been used for understanding the chemical structure and information of thermal films of amine phosphate species. All amine phosphates tested in this study have acted and reacted in the same manner even if there are some deviations of thickness measurement. Hence, only one phenomenological model is developed as a representative. All simplified symbols for modeling thermal films are exactly same as ones used in chapter 5. One new symbol was created with iron nitrite and iron nitrate being symbolized with the letter "Fe+NOx" in the circle in order to help understand the mechanism of film formation.

•AP-1 Thermal Film

1 min.: Decomposed AP-1 products preheated at 170 °C begin to react with Fe and deposit on the steel surface. The thermal film forms rapidly ($k=0.4632$ ($\mu\text{m}/\text{min.}$)). Even the chemical structure and reaction at 1 minute baking seem stable due to clear peaks in both P K and L edge spectra.

5 min.: The film growth is very fast ($k=0.4632$ ($\mu\text{m}/\text{min.}$)) until 5.46 minute with high thickness of 1.998 μm . Iron phosphates are actively deposited on the surface.

10 min.: The growth rate considerably decreases to a slow rate with $k=0.0268$ ($\mu\text{m}/\text{min.}$) after about 6 minutes. Thermal film consists of iron phosphates. On the surface of thermal film, short chain iron polyphosphates resulting from cross linking begin to be observed. Thickness of thermal film increases continuously. A phenomenological model of the thermal film formed at 10 minute is shown in figure 6.18(Top).

First Step: $(R_1O)_{1-2}PO(OH)_{2-1}\cdot(HNR_2)_{2-1}$ (solution) \rightarrow $(R_1O)_{1-2}PO(OH)_{2-1}\cdot(HNR_2)_{2-1}$ (decomposed by preheating) + O_2 (in oil) + FeO or Fe_2O_3 (present on the surface of steel coupons) \rightarrow Fe ortho- and pyro-phosphate + cross-linking of polyphosphate.

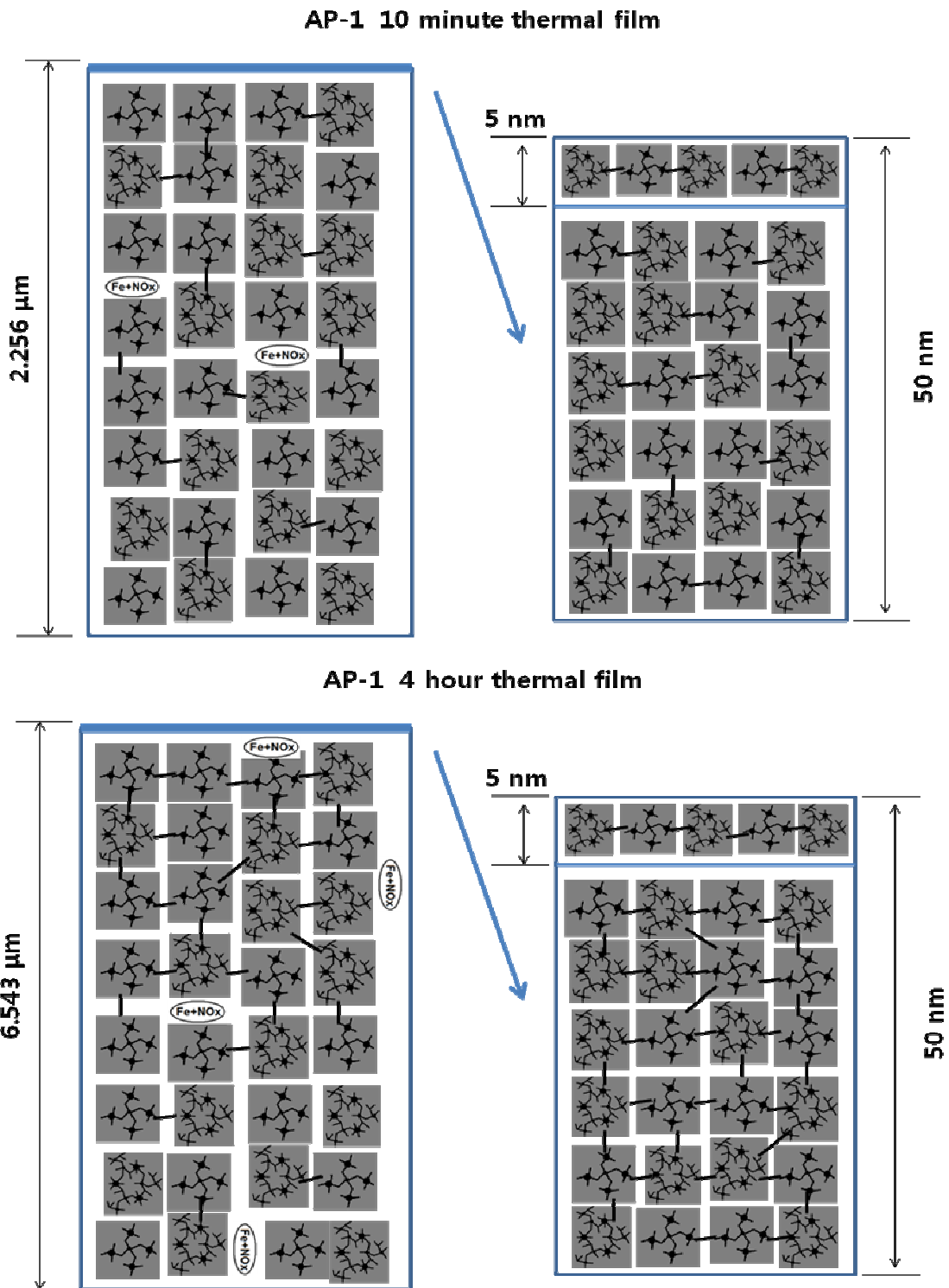


Figure 6.18 Phenomenological Model of AP-1 Thermal Films. Top Picture is 10 minute AP-1 Thermal Film and Bottom Picture is 4 hour AP-1 Thermal Film.

30 min.: The growth rate reduces to 0.0025 ($\mu\text{m}/\text{min.}$) after initial rapid growth of the thermal film.

Iron phosphates are main components of thermal film, while the proportion of cross linking among phosphates increase at the top surface layer by the result of the a/c ratio analysis. The oxidation of oil proceeds. Iron nitrite and iron nitrate begin to form and deposit at the thermal film.

1 hour: Film continuously forms with slow rate. The cross linking of phosphates increase at surface region (~ 5 nm) and also start to increase at the FLY region of L edge XANES spectra (~ 50 -70 nm). The oxidized nitrogen species increase.

4 hour: The thickness of thermal film consistently increases to 6.543 μm . Medium chain Iron polyphosphates are dominant at the surface region and short chain iron polyphosphate form in the bulk region. In bulk region, iron nitrate and nitrite compounds are present. 4 hour thermal film model of AP-1 is shown in figure 6.18(Bottom).

Second Step: $(\text{R}_1\text{O})_{1-2}\text{PO}(\text{OH})_{2-1}\cdot(\text{HNR}_2)_{2-1}$ (decomposed by preheating) + O_2 (in oil) + FeO or Fe_2O_3 + Fe ortho- and pyro-phosphate + cross-linking \rightarrow Fe short chain polyphosphate \uparrow (in bulk) + Fe medium chain polyphosphate \uparrow (in near surface) + Iron nitrate/nitrite (by oxidizing N-containing compounds)

6.4 Conclusion

This study was carried out to understand the mechanism of thermal film formation of various amine phosphate types of antiwear additives. The SEM has been used for the information of the growth kinetics of thermal films and the XANES spectroscopy has been used to collect the chemical information of thermal films. For topographical images of thermal films, the optic profilometer has been run. The results are summarized as follows.

Thermal films formed from amine phosphate antiwear additives have their own typical characteristics of film growth and chemical structure in the thermal film when compared with metal and metal free dithiophosphate additives (in the chapter 5). Their initial growth rate are

very fast, and then reduced quickly after 30 minute baking. Nonetheless, films are continuously formed on the surface until 4 hour test. Main component of thermal films formed from amine phosphates are iron phosphates and short and medium chain iron polyphosphates all through the thickness. In addition, iron nitrate and nitrite occurring from the oxidation of amine groups are observed in the thermal film. Thermal films of amine phosphates have wide and huge patch like shapes. Deep valleys or canons are also observed between thermal film patches resulting in high Ra value.

CHAPTER 7
TRIBOLOGICAL AND XANES ANALYSIS OF TRIBOFILMS FORMED
WITH NANOSCALE PTFE

PTFE (polytetrafluoroethylene) has diverse applications because of the low-energy and inert nature, for example, vessel coatings used in harsh chemical environments, human joint replacements, nonstick frying pans etc. PTFE is also used as antiwear additives or friction reducers in engine oil. [33,142,143] In this study, the interaction between the functionalized (Irradiated) PTFE and antiwear additives were examined. Nano scale functionalized PTFE and anti-wear additives such as F-ZDDP, secondary ZDDP, and ashless dithiophosphate were studied. This mixture of PTFE and one of antiwear additives were diluted at composition of 0.08 wt. % P and 0.33 wt. % PTFE in mineral base oil and wear performance was examined using a ball-on-cylinder type of tribotester. A limited quantity of oil (50 μ l) was used to observe the boundary layer. The mix of PTFE and additives have improved wear protection when compared with the AW additive or by PTFE itself. In presence of the functionalized PTFE, all tribofilms had more sulfide species and phosphate compounds and less abrasive species like iron oxides and iron/zinc sulfates with thin layer of PTFE on the top surface of tribofilms. Finally, the phenomenological models of tribofilms with/without PTFE were shown at the end of this chapter.

7.1 Introduction

It has been shown in the previous section that ashless antiwear additives demonstrate antiwear performance equal to or better than ZDDP and how these additives (both ashless additives and ZDDP) make films on the steel substrate using the formation of thermal films. Then, the question is whether there is any way to increase the efficiency of wear protection of ashless antiwear additives. Fluorinated hydrocarbons are examined as the possible candidate.

Unique properties such as excellent chemical resistance, low coefficient of friction and high temperature stability have resulted in polytetrafluoroethylene (PTFE) powders being used in various applications like bearings for machinery parts and biomedical joint replacements. [144-146] Moreover, PTFE powders are quite widely used as concentrated dispersions in liquid lubricants where they form pastes or greases. [33] Since the concept of adding PTFE to engine oil has been suggested in 1976 by F.R. Reick, some conventional motor oils with PTFE are currently marketed. [33,143] However, the function of PTFE particles in lubricated contacts is a matter of controversy. Some researchers have found no practical beneficial effects on either friction or wear by citing the researches from the NASA's Lewis Research Center and the GM's Fuels and Lubes department. [147] Palios et al. [33] found that large, micron sized PTFE particles appear to reduce friction and wear in reciprocating tests while very small PTFE particles in fully formulated oil appear to make no measurable contribution to friction and wear reduction. Other studies showed that PTFE powders remarkably reduce friction and wear in engines and other tribological systems. [142,143] However, only improvements have so far been shown without clear mechanism of antiwear performance. In this study, a functionalized polytetrafluoroethylene (PTFE) was used in conjunction with different antiwear additives.

7.2 Experimental Details

7.2.1 Test Materials

Functionalized (here, irradiated resulting in the formation of carboxyl groups) polytetrafluoroethylene (PTFE) powders (\varnothing : around 50 nm) were examined. Figure 7.1(a) shows the chemical structure of PTFE and figure 7.1(b) shows a schematic of a functionalized PTFE particle. This change in the roughness of the surface and in the contact area increases water repellence and the adhesion strength to deposited metal layers. [148] In fact, PTFE particles used in commercial engine treatments (or oils) have been bombarded with electrons. This electron irradiation makes the length of molecular chain shorter and reduces the size of the

particles. It also gives them an electrical charge to repel each other and to be chemically active. [142,143,147] It has been suggested that PTFE powders particularly in engine oil application can reduce friction and wear when suspended at quite low concentration. [33] They used the concentration of 0.33 wt% PTFE powder for their test. Three different antiwear additives were used to understand the synergetic or antagonistic effect between various types of antiwear additives and irradiated PTFE used at a concentration of 0.33 wt%. Normal ZDDP and ashless dithiophosphate (called as DDP-2 in this study) were run for the comparison. In order to study the effect of extra fluorine in oil, F-ZDDP which was developed in the University of Texas at Arlington was also examined. Detailed information about F-ZDDP can be referred at Parekh et al.'s [149] and Mourhatch et al.'s [39,48] papers. The concentrations of P in the oil samples was maintained at 0.08 wt % in a 100 neutral mineral oil.

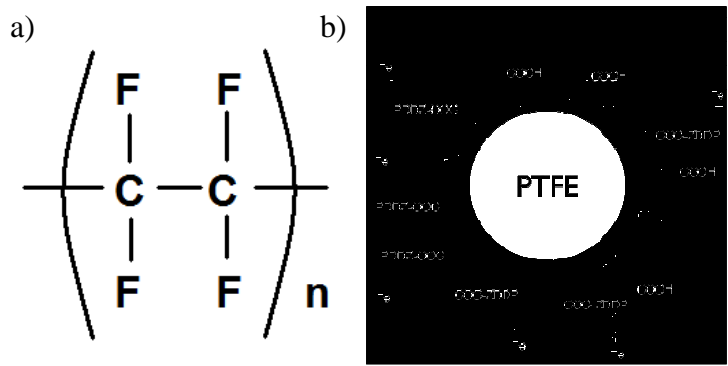


Figure 7.1 a) the Chemical Structure of Polytetrafluoroethylene (PTFE) and b) the Schematic of a Functionalized PTFE Particle

7.2.2 Tribological Tests and Tribofilm Analysis

Wear tests are performed on the home-made ball-on-cylinder evaluator. The same test condition of 24 Kg applied load (3.56 GPa Hertzian contact load with 1/4 inch dia. WC ball) and 15,000 cycles test are run at the lab-built BOCLE tester to compare with the previous wear tests in absence of PTFE.

The XANES spectroscopy was used to analyze the phosphorus, sulfur, zinc, iron, and oxygen components in the tribofilms tested using three different additives with and without irradiated PTFE. This analysis will help provide a better understanding of surface reaction of

antiwear additives when an additional additive, specifically a solid PTFE additive is present in oils revealing the interaction and the relationship between functionalized PTFE and antiwear additives. Phosphorus (P) and sulfur (S) K-edge spectra between 1500 and 4000 eV of energy range were collected from the Canadian double crystal monochromator (DCM) beamline at the Synchrotron Radiation Center (SRC) at the University of Wisconsin–Madison in Stoughton, Wisconsin. While P and S L-edge spectra between 5.5 and 250 eV were scanned at the variable line spacing plane grating monochromator (VLS-PGM) beamline at the Canadian Light Source (CLS) facility in Saskatoon, Saskatchewan, Canada. Especially, for new element spectra like Zinc (Zn) L-edge, oxygen (O) K-edge, and fluorine (F) K-edge, the high resolution spherical grating monochromator (SGM) beamline in the CLS facility was used. It covers the energy range between 250 to 2000 eV with 0.1 eV scan step in 1000 μm by 100 μm spot size. Using both the total electron yield (TEY) and fluorescent yield (FLY) modes at the DCM, the VLS-PGM, and the SGM beam lines, simultaneous information can be obtained on both the near surface and bulk chemical information of the films.

The morphological information of surfaces on all tested wear tracks were collected using both an optical profilometer; Wyko NT9100 Surface Profiler, and the scanning electron microscope (SEM), the Hitachi 3000.

7.3 Results and Discussion

7.3.1 Tribological Performance

The graph in figure 7.2 shows the wear performance of six different formulations in terms of wear volume from the lab-built lubricating tester. Each value of wear volume in each sample is an average of 18 measurements. In previous studies of lab colleagues [39,48,149], the wear protection of F-ZDDP was better than one of ZDDP. They explained that the fluorine of F-ZDDP makes thicker and more compliant tribofilms but have same hardness at the surface area. [39,48,149] These phenomena might result in better performance for antiwear action. The

wear results of ZDDP and F-ZDDP in this study are consistent with their results. The comparison of wear performance between ZDDP and ashless dithiophosphate (DDP-2) are already seen in chapter 3. Ashless DDP have better antiwear protection than ZDDP because it uniformly created about four times thicker but much more compliant tribofilms. All solutions mixed with irradiated PTFE in figure 7.2 have better wear protection than each solution without PTFE. It shows the beneficial role of functionalized PTFE in wear protection and indicates that irradiated PTFE powders provide a promising advantage in antiwear performance to oil samples containing only antiwear additives like ZDDP, F-ZDDP, and ashless dialkyl dithiophosphate.

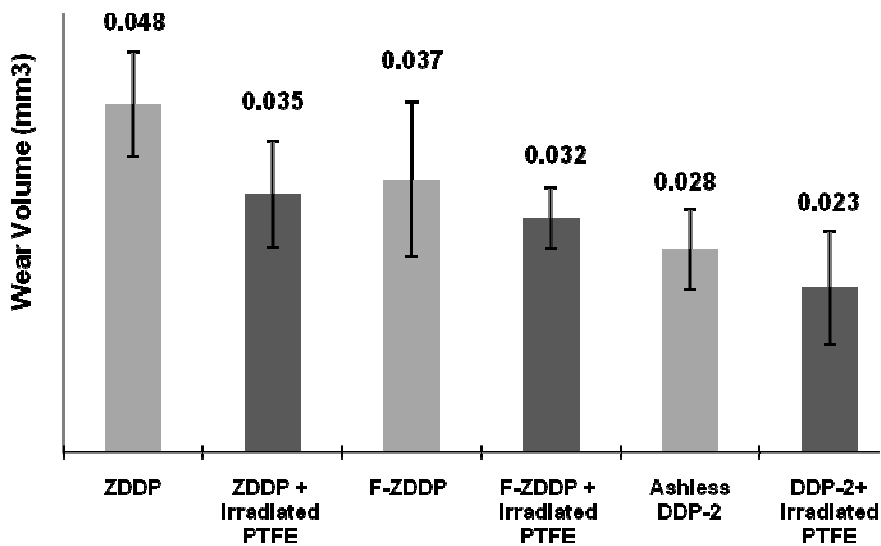


Figure 7.2 A Plot of Wear Volume Data vs. Type of Formulations. Three Different Types of Antiwear Additives, ZDDP, F-ZDDP, and Acidic Ashless Dithiophosphate, were Tested with 0.08 wt% P in Base Stock with/without 0.33 wt % irradiated PTFEs. Test Condition: a 1/4" Ball of WC on a 52100 Steel Cylinder, 24Kg Applied Load, and 15,000 Cycles.

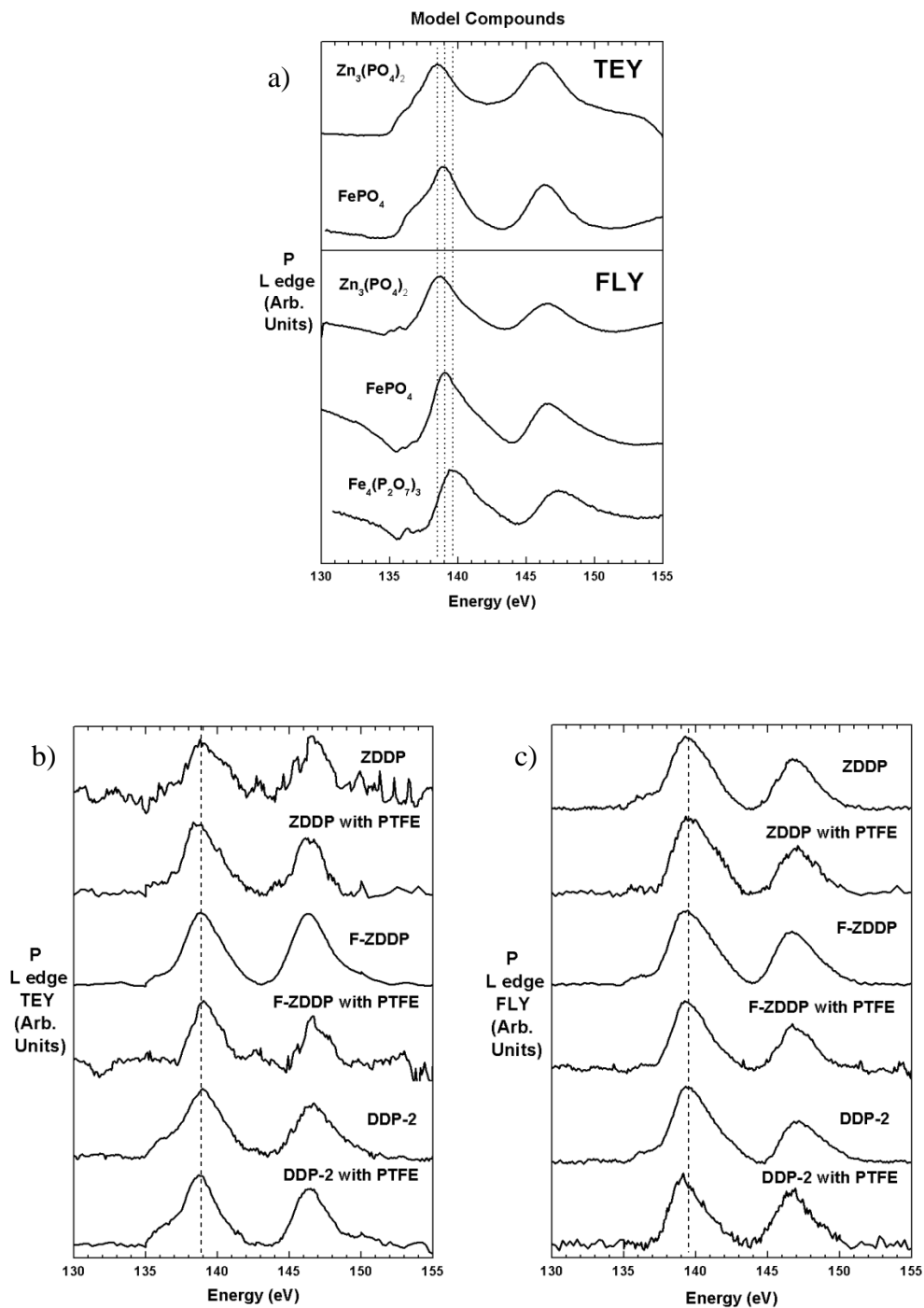


Figure 7.3 XANES Spectra of the TEY and FLY modes at the Phosphorus L edge. a) TEY and FLY mode of Model Compounds: $Zn_3(PO_4)_2$, $FePO_4$, and $Fe_4(P_2O_7)_3$, b) TEY mode of Tribofilms Formed from Six Solutions, and c) FLY mode of Tribofilms Formed from Six Solutions.

7.3.2 XANES Analysis of Tribofilm

7.3.2.1 Phosphorus and Sulfur Characterization

L edge of Phosphorus

Figure 7.3 shows the XANES spectra at L edge of phosphorus model compounds and of six tribofilms formed from six different solutions. In figure 7.3(a), zinc phosphate ($Zn_3(PO_4)_2$) and two iron phosphates ($FePO_4$ and $Fe_4(P_2O_7)_3$) are presented by TEY and FLY mode. The explanation about L edge XANES of model compounds is omitted in this chapter. Figure 7.3(b) and (c) are the phosphorus L-edge XANES spectra in TEY and FLY modes of tribofilms generated from ZDDP, F-ZDDP, and ashless DDP-2 with and without functionalized PTFE. At both the TEY mode of surface region and the FLY mode of bulk area of tribofilms, the positions of all white peaks of tribofilms are identical to the main peak of $FePO_4$ as 139 eV. All pre-edge peaks look small compared with the height intensity of main peaks. In figure 7.4, a/c ratios at both TEY and FLY mode of all samples are also calculated with same method used in chapter 5. All cases are located between 0.1 and 0.2. Value below 0.2 indicates films are composed of pyro- or ortho-phosphates. But, in case of DDP-2 and DDP-2 with PTFE, both a/c ratios of TEY peak are closer to 0.2 than other cases. Thus, the surfaces of the two samples with DDP-2 may have some short chain length of polyphosphates. To combine with two graphs, figure 7.3 and 7.4, all tribofilms tested under the extreme pressure conditions consist of iron pyro or orthophosphates with a small amount of zinc phosphates except tribofilms of DDP-2 and DDP-2 with PTFE. The presence of iron phosphates arises from the existence of plenty of Fe or iron oxides due to EP test conditions.

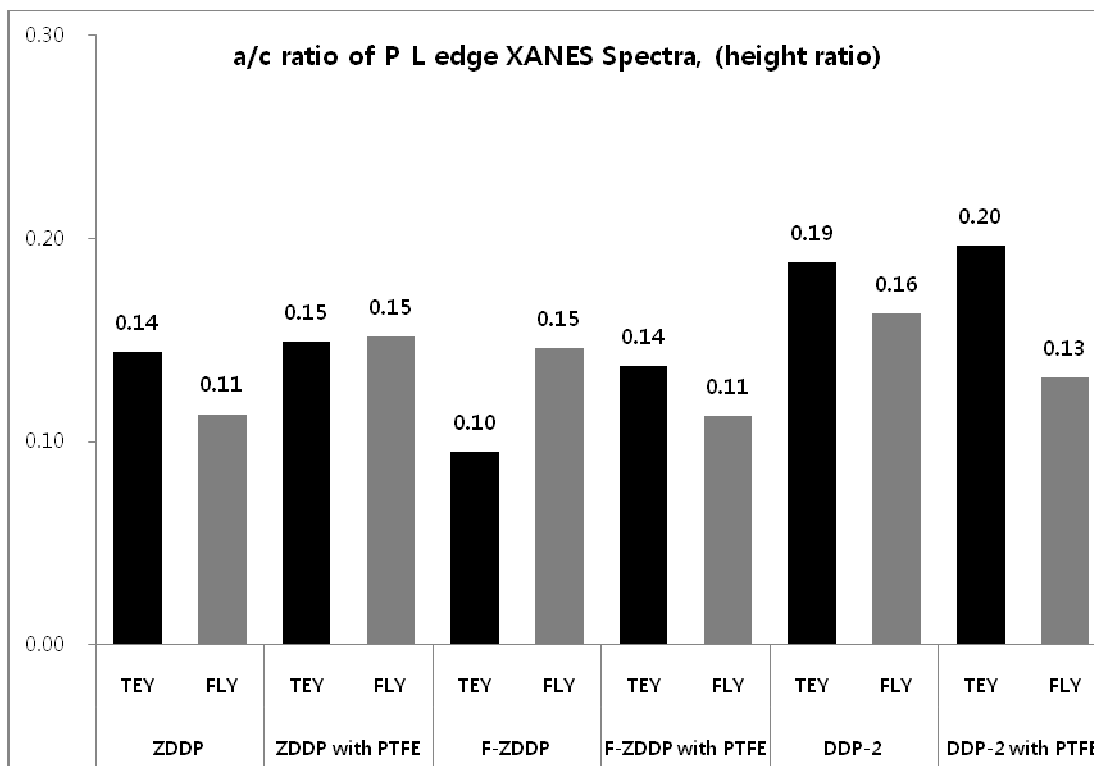


Figure 7.4 Relative a/c Ratios of P L edge TEY and FLY modes of Six Different Samples. The Height Intensity Ratio is Adopted like Previous Chapters

K edge of Phosphorus

Figure 7.5 shows the phosphorus K edge spectra of tribofilms generated from six different solutions and of two metal phosphate model compounds. The elucidation of K edge XANES spectra for model compounds is done in chapter 5 and hence is not repeated here. All the TEY and FLY mode spectra have similar position of white lines at around 2153 eV. The FLY mode of K edge includes the information of bulk area and the TEY mode of K edge has the information of 50 nm depth from the surface. This indicates all tribofilms generated from six different chemistries consist of iron phosphates.

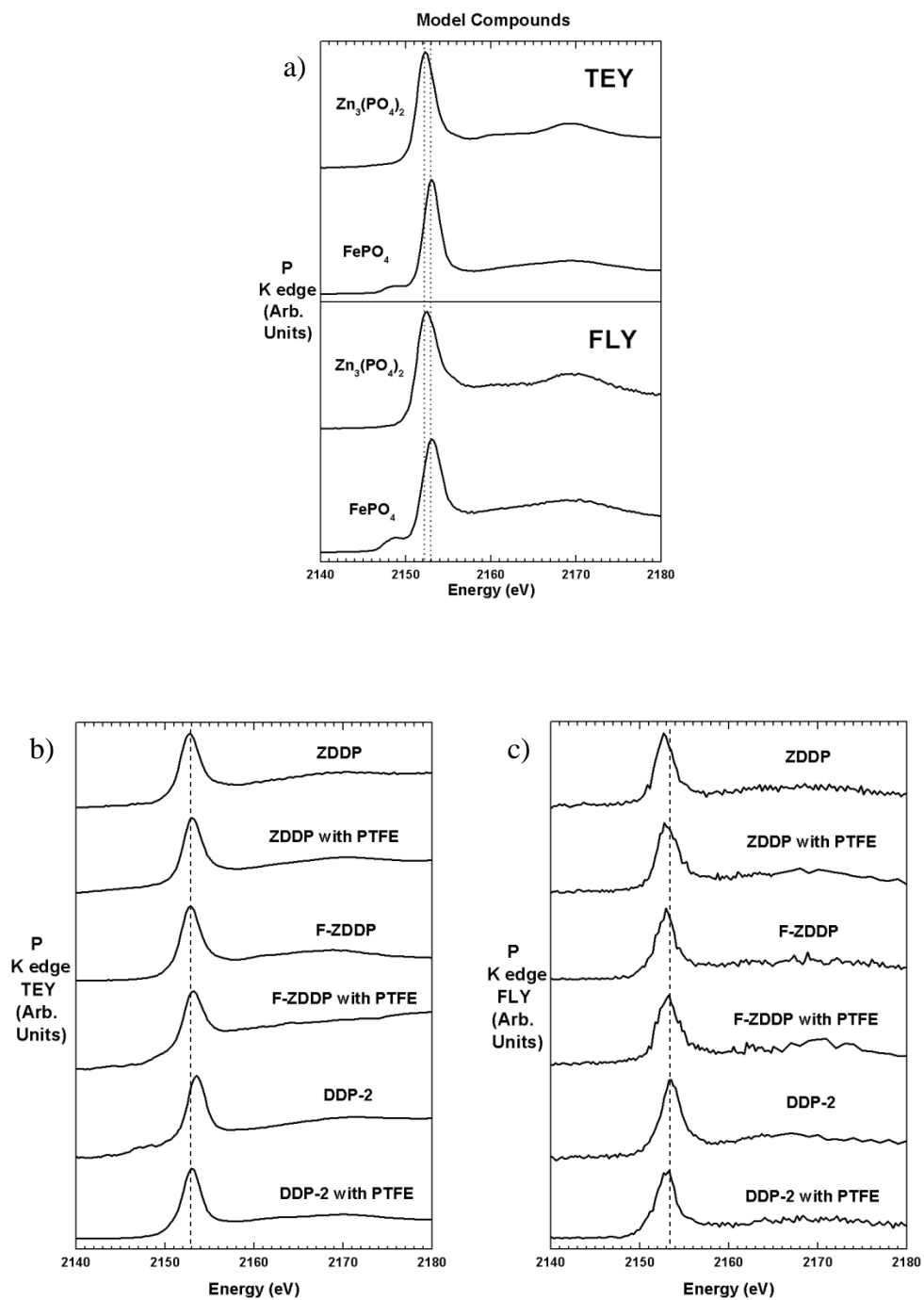


Figure 7.5 XANES Spectra of the TEY and FLY modes at the Phosphorus K edge. a) TEY and FLY mode of Model Compounds: $Zn_3(PO_4)_2$, and $FePO_4$, b) TEY mode of Tribofilms Formed from Six Solutions, and c) FLY mode of Tribofilms Formed from Six Solutions.

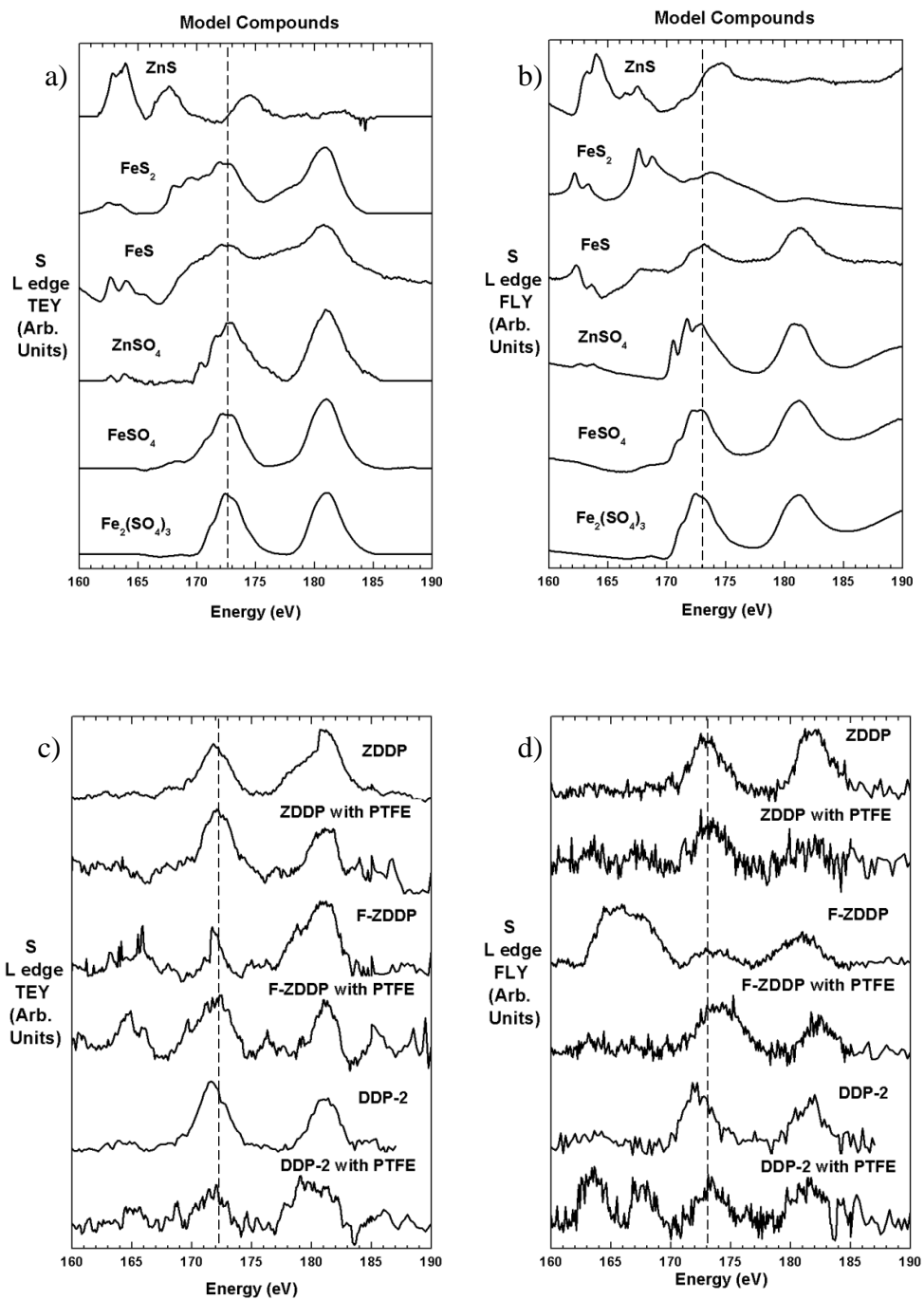


Figure 7.6 XANES Spectra of the TEY and FLY modes at the Sulfur L edge. a) TEY and b) FLY mode of Model Compounds: Three Metal Sulfides and Three Metal Sulfates, c) TEY mode of Tribofilms Formed from Six Solutions, and d) FLY mode of Tribofilms Formed from Six Solutions.

L edge of Sulfur

Figure 7.6(a) and (b) provide the TEY and FLY graphs of L edge XANES spectra related to sulfur model compounds. In figure 7.6(c) and (d), the TEY and FLY peaks of L edge of six different tribofilms formed from each solution are shown. Comparing L edge peaks of tribofilms with model compounds, all peaks of sulfur L edge are very weak and noisy. The sulfur spectra in this research are taken at energy range between 160 and 190 eV at the VLS PGM beam line in the Canadian Light Source using the high energy grating. The photon flux decreases in the range where sulfur is measured and is not high enough to get a good signal to noise ratio. Thus, particularly, in case of thin films like tribofilms, it is hard to get smooth sulfur L edge peaks. However, in these plots, some clear peaks at the position of sulfate white lines are observed even if these peaks are noisy. In addition, the existence of some sulfides species can be identified even though the cationic species is hard to isolate.

K edge of Sulfur

Figure 7.7 shows a series of XANES spectra at the S K edge for tribofilms formed from ZDDP, F-ZDDP, and DDP-2 with and without irradiated PTFE in both TEY and FLY modes. In order to help understand the analysis of sulfur K edge XANES spectra, the TEY and FLY mode of S K edge of six model compounds like zinc sulfide (ZnS), two iron sulfide (FeS and FeS₂), zinc sulfate (ZnSO₄), and two iron sulfates (FeSO₄ and Fe₂(SO₄)₃) are plotted at the top of graph together. All spectra of samples except tribofilm of F-ZDDP are similar in the TEY mode. The lower energy peak (a) located around 2470 eV is because of the formation of FeS whose main peak is associated to peak (a). Peak (b) located at about 2471.5 eV aligns well with the main peak of pyrite, FeS₂. Peak (c) is the main peak of ZnS, ZDDP with PTFE, F-ZDDP, and F-ZDDP with PTFE have this peak with small intensity. Only F-ZDDP has peak (d) situated at about 2477 eV. The peak (d) of tribofilm formed from F-ZDDP may originate from broad (d) peak of FeS or possibly a sulfite species which has the white peak at ~2477 eV [52]. At 2482 eV, sulfate species peak is clearly observed in every sulfur spectrum of tribofilms.

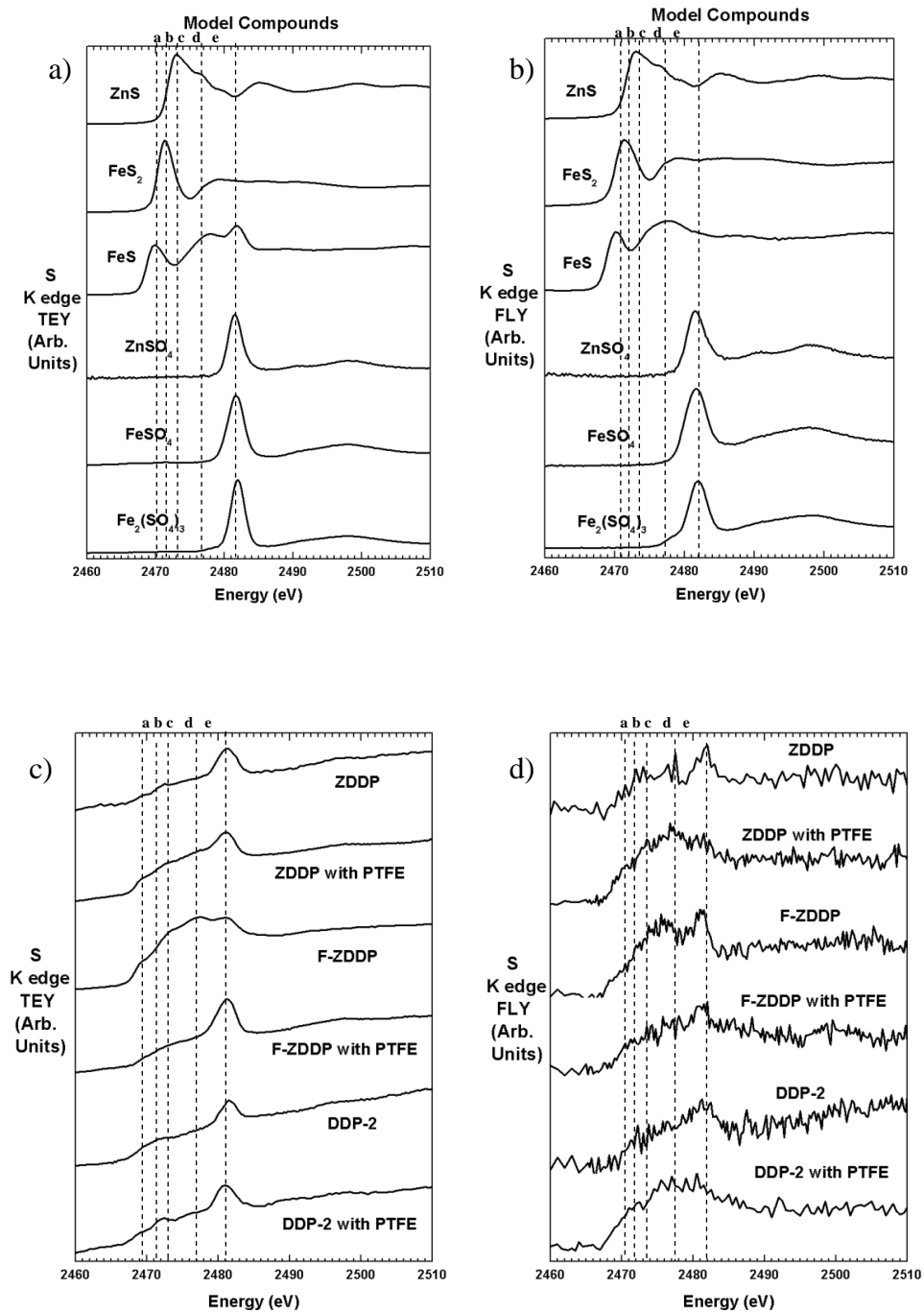


Figure 7.7 XANES Spectra of the TEY and FLY modes at the Sulfur K edge. a) TEY and b) FLY mode of Model Compounds: Three Metal Sulfides and Three Metal Sulfates, c) TEY mode of Tribofilms Formed from Six Solutions, and d) FLY mode of Tribofilms Formed from Six Solutions.

FLY modes of all samples also have similar patterns with the corresponding spectra obtained in the TEY. However, all peaks in the K edge FLY mode of sulfur species are somewhat noisy. With this FLY mode, we can conclude that both sulfide and sulfate species exist together deeper in the tribofilm.

Using both P and S K edge XANES spectra, the relative intensity ratio of sulfur versus phosphorus can be calculated like previous chapter 5. The proportion of sulfur and phosphorus species is examined in the surface area and the bulk area of tribofilms. The bar graphs in figure 7.8 show the S/P ratio of TEY and FLY modes at K edge. ZDDP have similar amount of sulfur species and phosphorus species everywhere with 0.95 in TEY and 1.15 in FLY of S/P ratio. Bulk area has 76 percentages of sulfides out of total sulfur species. At the surface, about 47 percentages of sulfides are present. It is reasonable that sulfates are more than sulfide at the surface area comparing with FLY mode because they are closer to oxygen environments. When irradiated PTFE is added in the solution, sulfur species increase in both TEY and FLY modes by two or three times. The reason is because sulfides increase at the surface area by twice (sulfide of 84.3 %) and at the bulk area the total amount of sulfur compounds increases by three times with huge amount of sulfides. These increased sulfide species help better protect the sliding surface at the extreme condition. DDP-2 has similar pattern of results like ZDDP and ZDDP with PTFE. Its S/P ratios are 0.71 at the TEY and 0.96 at the FLY indicating that phosphate species are slightly more than sulfur species. The sulfide percentage is 39 percentages at the TEY and 32 percentages at the FLY. This results from better activity of sulfur species out of the decomposed products of ashless DDPs as studied in chapter 5 of the study of thermal films from ashless dithiophosphates. In the presence of PTFEs, the amount of sulfur species at the FLY region rises to four times with the increase of sulfide species (53.3%). Even if the S/P value at the TEY are reduced to 0.42, the sulfides percentage increases to 45.3%. This indicates that phosphate compounds increase with the increase of sulfides, resulting in better antiwear performance. DDP-2 with PTFE has better antiwear performance with more sulfide species. F-

ZDDP has different pattern from ZDDP and DDP-2. When F-ZDDP itself is tested, its tribofilm has high S/P ratio (3.74) with 92 percentages of sulfide compounds at the FLY while the surface of tribofilm from F-ZDDP has 0.87 of S/P ratio with 47.7 % sulfide. Probably, these increased sulfides in the tribofilm may make better antiwear performance than the performance of ZDDP. In presence of PTFE, the S/P ratio of F-ZDDP at the TEY increases to 2.94 with 70 percentages of sulfides and the value of FLY mode decreases to 2.21 having still high amount of sulfide species (86.2%). This high amount of sulfide compounds makes better antiwear properties.

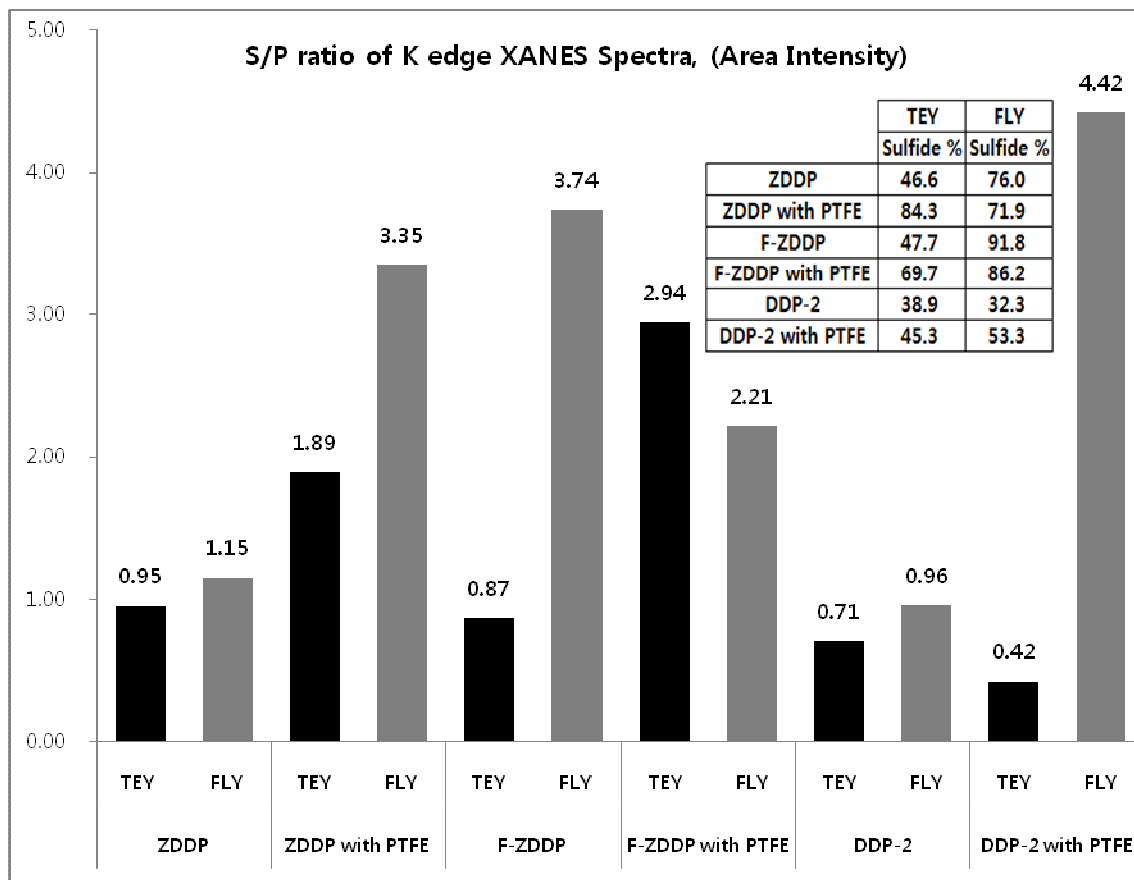


Figure 7.8 Relative S/P Ratios of K edge TEY and FLY modes of Six Different Samples and the Percentage of Sulfide out of Whole Sulfur Containing Compounds.

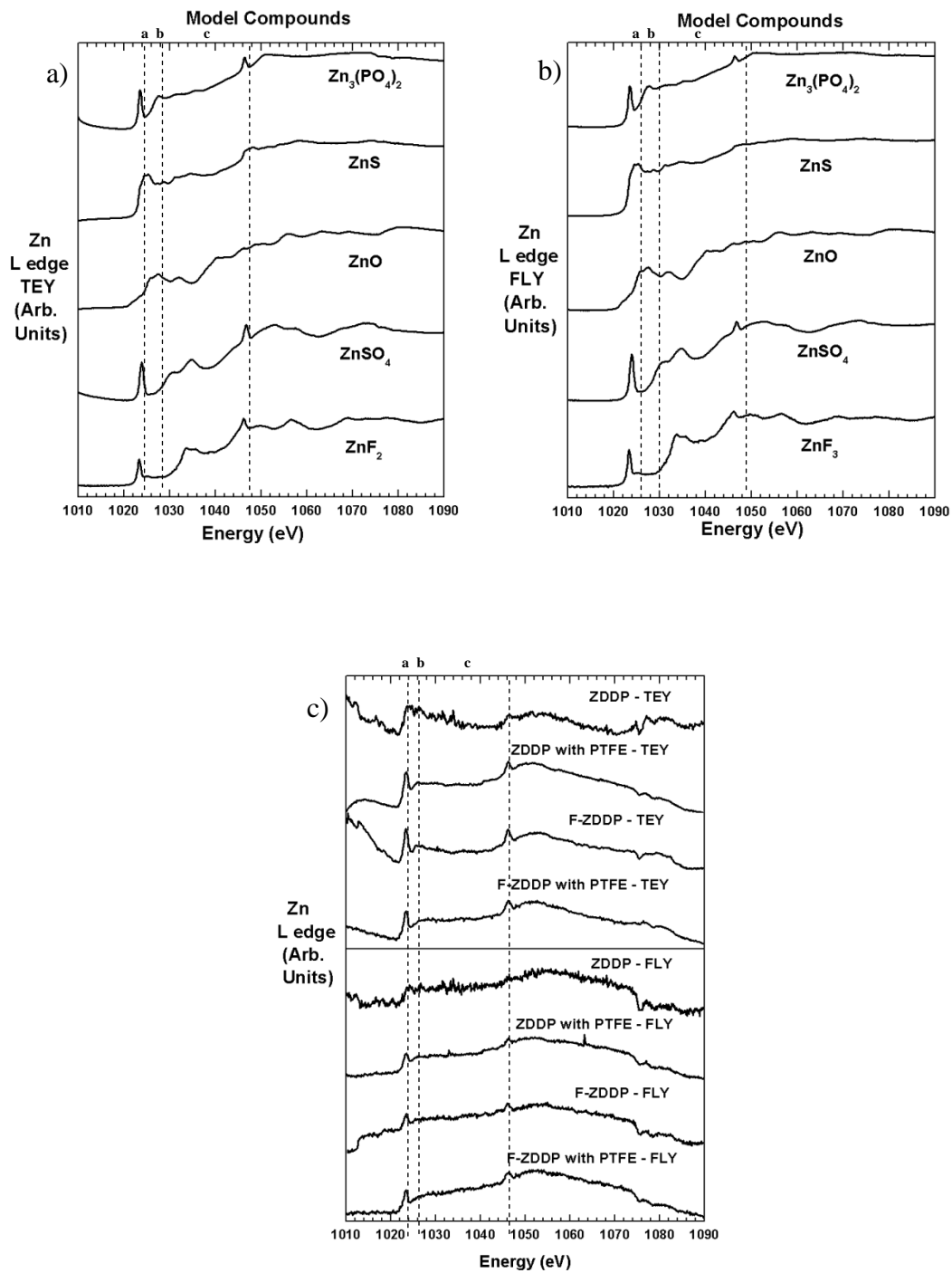


Figure 7.9 XANES Spectra of the TEY and FLY modes at the Zinc L edge. a) TEY and b) FLY mode of Model Compounds, c) TEY and FLY modes of Tribofilms Formed from ZDDP and F-ZDDP with and without PTFE.

7.3.2.1 Zinc, Oxygen, and Fluorine Characterization

L edge of Zinc

The Zn L edge spectra collected in TEY and FLY mode are shown in figure 7.9. All model compounds, $Zn_3(PO_4)_2$, ZnS, ZnO, $ZnSO_4$, and ZnF_2 , show intense peaks (peak (a)) at about 1024 eV in both TEY and FLY mode in figure 7.9(a) and (b) with the exception of ZnO. In XANES spectra of model compounds, peak (a) and (c) indicate the present of zinc phosphate, zinc fluoride, or zinc sulfate. However, peak (b) is clearly due to zinc phosphate. All Tribofilm samples of ZDDP and F-ZDDP with and without PTFE have peak (a), (b), and (c) together. This indicates that the tribofilms formed from these four different formulations have zinc phosphates. The spectrum of tribofilm of ZDDP itself is noisy but it also has recognizable intensities. Tribofilm generated from ZDDP may have less zinc phosphate than other.

K edge of Oxygen

Figure 7.10 is the TEY and FLY oxygen K edge spectra of the model compounds (in figure 7.10(a) and (b)) as well as the tribofilms formed from six different formulations (in figure 7.10(c) and (d)). $Zn_3(PO_4)_2$, $FePO_4$, ZnO, Fe_2O_3 , $ZnSO_4$, $FeSO_4$, and $Fe_2(SO_4)_3$ are used as model compounds for the XANES analysis. The oxide, sulfate, and phosphate peaks of oxygen are quite broad and diffuse as shown in figure 7.10. However, there are two clear differences at the pre-edge peak and at white line area. The zinc compounds do not have any lower energy pre edge like peak (a) (531 eV), (b) (532 eV), and (c) (533 eV) while iron compounds have. Iron phosphate has peak (b) and iron sulfate has peak (c). Iron oxide has broad peak between 531 eV (peak (a)) and 532.5 eV. Peaks (a), (b), and (c) in the spectra of the Fe containing model compounds are because of transition from O 1s to O 2p states hybridized with the partially filled Fe 3d band that is highly localized around the metal-atom sites. Due to the filled 3d orbital in Zn, zinc species don't have pre-edges. Broad white peaks of oxygen K edge at the right side of spectra are attributed to O 1s to O sp states hybridized with iron or zinc 4s and 4p states. [4] In model compounds, two oxides and $FeSO_4$ have the white peaks which are overall flat or

gradually increased. On the other hand, two phosphates, ZnSO_4 , and $\text{Fe}_2(\text{SO}_4)_3$ have the relative sharp main peaks. Obvious pattern in oxygen K edge from tribofilms of six solutions are obtained. In case of testing antiwear additives in absence of PTFE, they have iron oxide-like pre edge peaks and flat or gradually increased white peaks. This indicates their tribofilms have more oxide species with phosphates and sulfides which are already confirmed at the P and S analysis. Some iron sulfates (FeSO_4) are observed in the tribofilm of ZDDP itself by the position of peak (c). After adding irradiated PTFE, all tribofilms with PTFE are distinctly changed at two points. First, the pre-edge of iron oxide is clearly reduced. Second, their white peaks become relatively sharp (lower energy area increases at the broad white peak). This means in presence of PTFE oxide species (here, especially Fe_2O_3) are reduced and phosphates are increased. ZnSO_4 , and $\text{Fe}_2(\text{SO}_4)_3$ aren't considered because sulfides are more than sulfates in the tribofilms with PTFE by the S/P ratio analysis. In addition, the tribofilms of DDP-2 with and without PTFE do not have zinc cations. Hence, their iron oxide pre-edge peaks are bigger than cases of ZDDP and F-ZDDP with/without PTFE. However, the trends are same as the other two cases.

K edge of Fluorine

Figure 7.11(a) and (b) are the TEY and FLY XANES spectra of fluorine K edge for model compounds, FeF_3 , ZnF_2 , and PTFE, as well as three tribofilms formed from antiwear additives with PTFE powder. The white line spectra of model compounds are widely diffuse as shown in figure 7.11. FeF_3 has particular pre-edge peaks at about 685 eV (peak (a)) and 686 eV (peak (b)) and its main peak starts from approximately 693.5 eV. The white peaks of both ZnF_2 and PTFE begin at about 690.5 eV (peak (c)). The difference of two model compounds is the structure of near edge peaks. ZnF_2 had more complex peaks and one specific peak at about 696.5 eV (peak (d)). The TEY mode of tribofilms generated from antiwear additives with PTFE have white peaks at approximately 690.5 eV of peak (c), indicating the existence of PTFE or

ZnF₂. But the near edge structure of ZnF₂ is not detected. Hence, only PTFEs are formed at the surface of tribofilms. There are small pre-edge peaks shown at the position of peak (a) and (b).

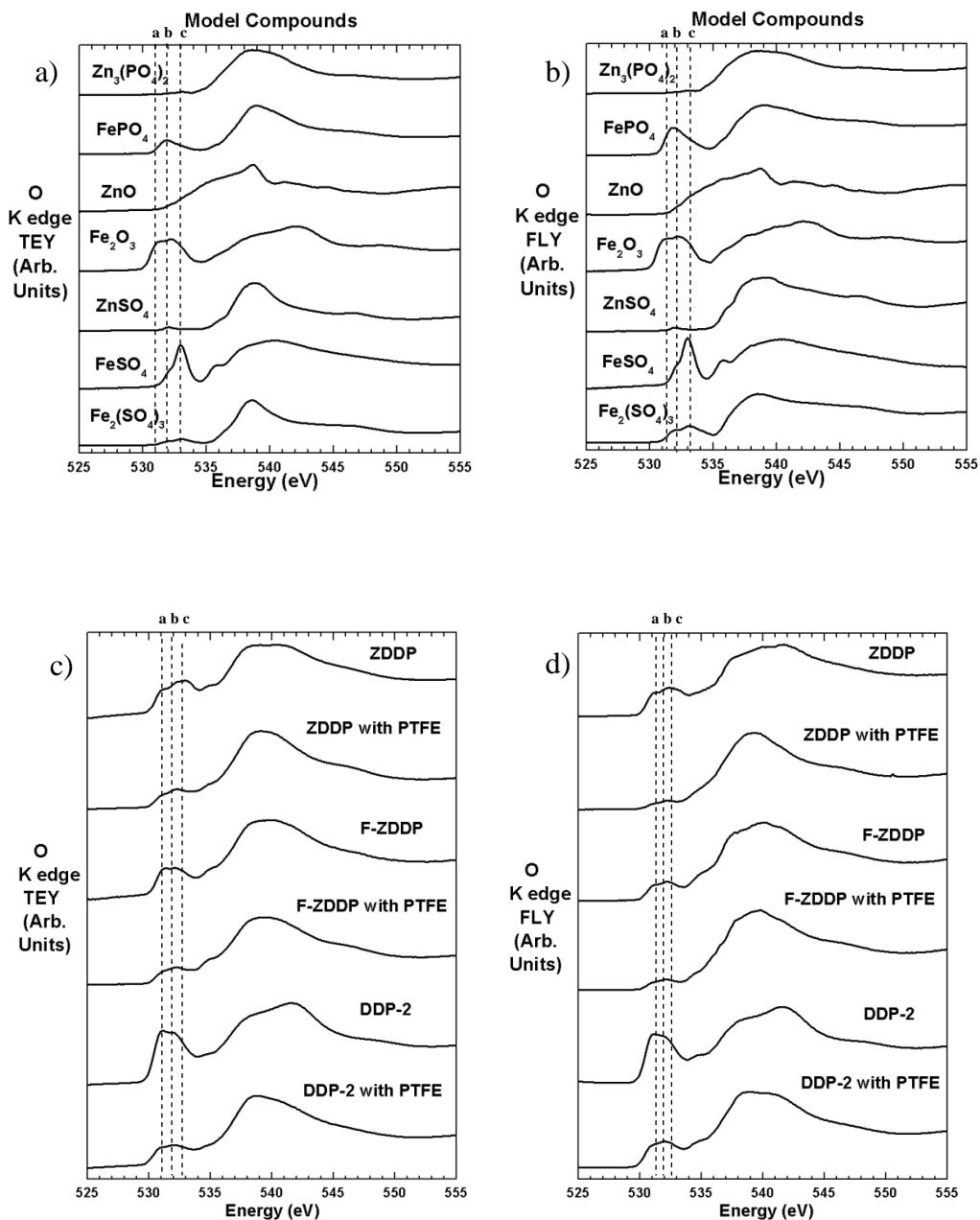


Figure 7.10 XANES Spectra of the TEY and FLY modes at the Oxygen K edge. a) TEY and b) FLY mode of Model Compounds, c) TEY mode of Tribofilms Formed from Six Solutions, and d) FLY mode of Tribofilms Formed from Six Solutions.

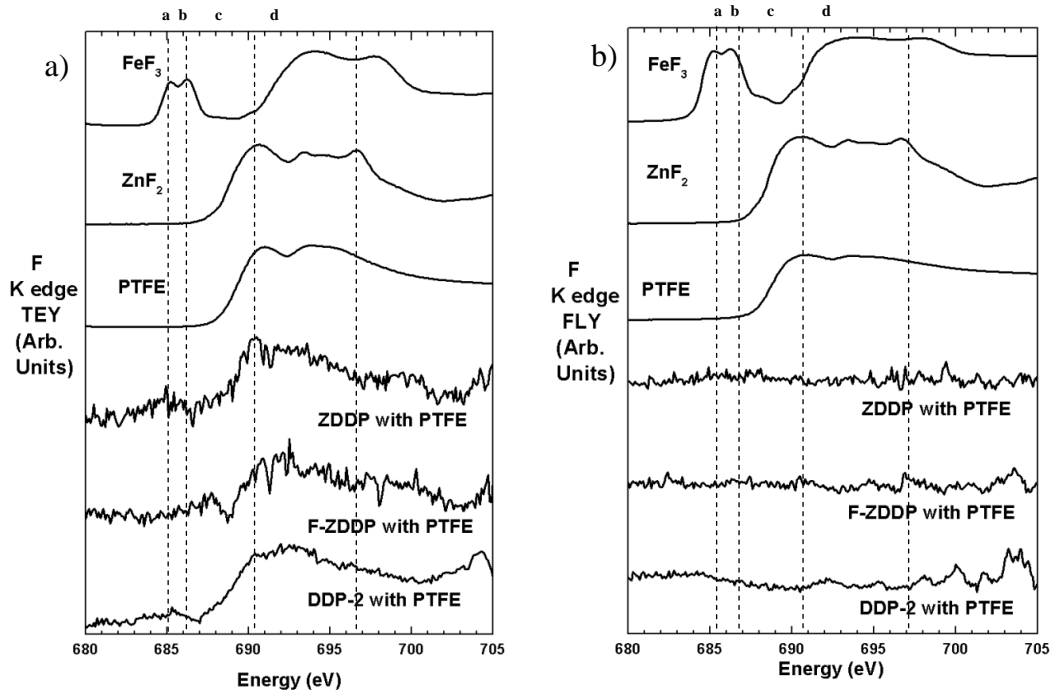


Figure 7.11 XANES Spectra of the TEY and FLY modes at the Fluorine K edge. a) TEY spectra of F Model Compounds as well as Tribofilms Formed from Antiwear Additives with PTFE and b) FLY Spectra of F Model Compounds as well as Tribofilms Formed from Antiwear Additives with PTFE.

However, TEY spectra of F K edge are noisy. Thus, we cannot conclude films are also composed of FeF_3 . At the FLY mode of F K edge spectra, all spectra for tribofilms are noisy and not detectable. Probably, because of small amount of fluorine and very thin PTFE layers, any fluorine spectra may not be observed at the FLY mode.

7.3.3 Morphology Analysis of Tribofilm

Figure 7.12 shows the surface images on the wear tracks tested with six different formulations using the SEM and the optic profilometer. Figures 7.12(a) to (e) are each 200X magnified SEM image of wear track. Picture (a), (c), and (e) are the images of tribofilms generated from only antiwear additives, ZDDP, F-ZDDP, and DDP-2. The images of wear tracks run by antiwear additives with PTFE powders are shown in the figure 7.12(b), (d), and (f). All

formulations have good wear protective properties even if there are variations of wear performance. All six samples have similar shape of wear track. In the middle of wear scar, well packed tribofilms are observed. As the representative of samples, tribofilms of F-ZDDP with PTFE are selected, and then investigated at the higher magnification using the SEM. Figure 7.12(g) and (h) shows the 2000X SEM images at these two different regions. Figure 7.12(i) and (j) are higher magnification images (5000X) for region-1 and region-2 of tribofilms of F-ZDDP with PTFE. The direction of wear test is detectable at both region-1 and -2. In the region-1, well developed, squeezed, and elongated antiwear pads are detected. On the other hand, the region-2 has very thick but swirl-like antiwear pads which were torn out and pushed up to same direction by one direction pressure. This indicates the extreme pressure condition occurs at the center of wear track and at a little far from the center of test, the wear tests for boundary lubrication condition are performed. Also, the topographical images from the optic profilometer as shown in figure 7.12(k) and (l) show the same images as the SEM study.

7.3.4 Mechanism and Phenomenological Model

The results of tribological tests have shown the synergetic effect between antiwear additives and functionalized PTFE powders. All XANES spectra, phosphorus K and L edge, sulfur K and L edge, zinc L edge, oxygen K edge, and fluorine K edge, have been used to study the mechanism of formation of tribofilms from antiwear additives like ZDDP, F-ZDDP, and DDP-2 in absence and in presence of nanoscale irradiated PTFE. The schematic models for the mechanisms of tribofilm formation, generated from ZDDP/F-ZDDP, and DDP-2 with and without irradiated PTFE, are shown in figure 7.13 and 7.14. For modeling, simplified symbols used in chapter 5 are used again. New simplified symbols for newly introduced compounds are added in table 7.1

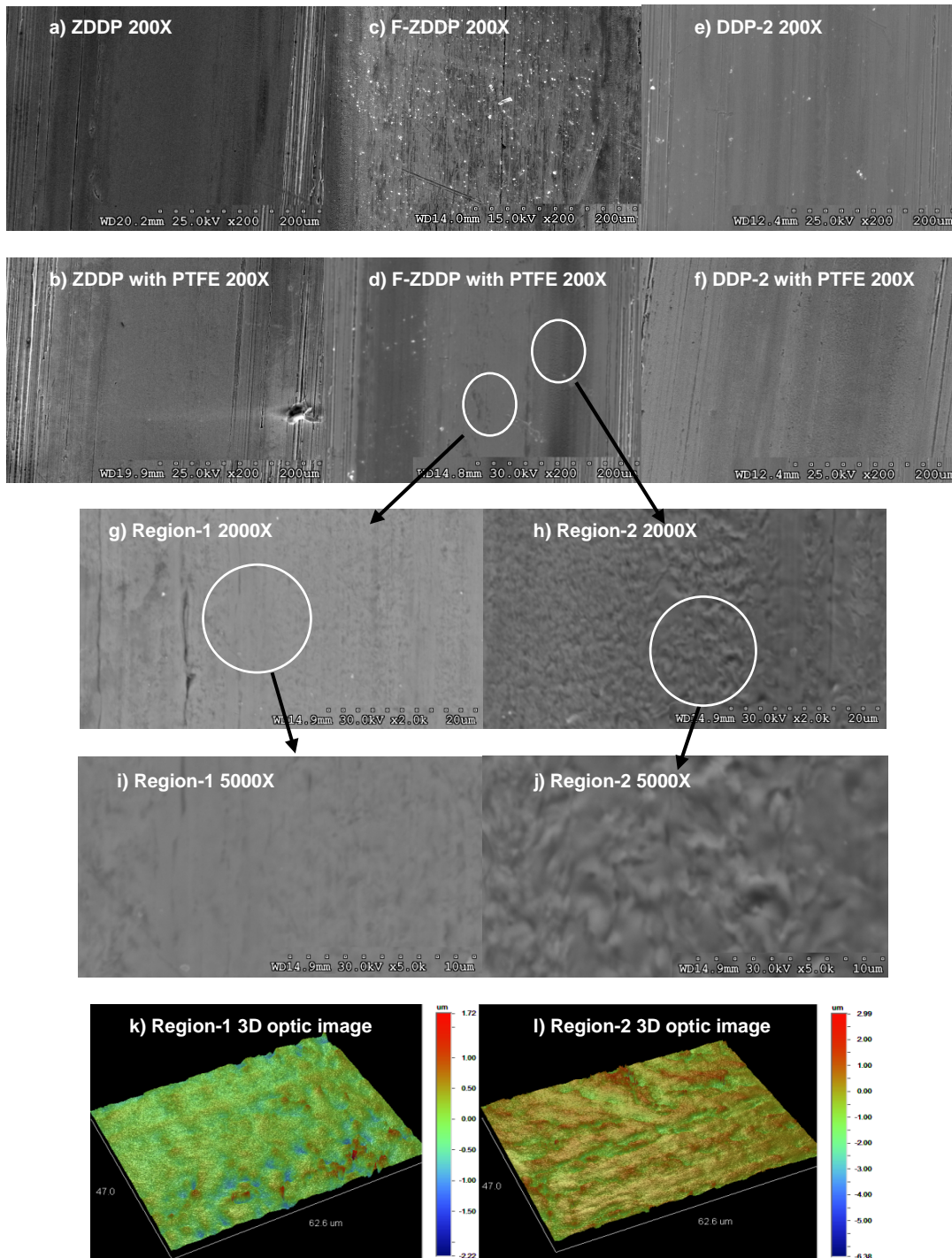
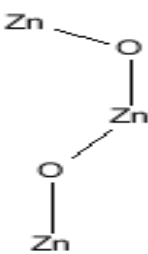
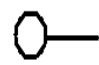
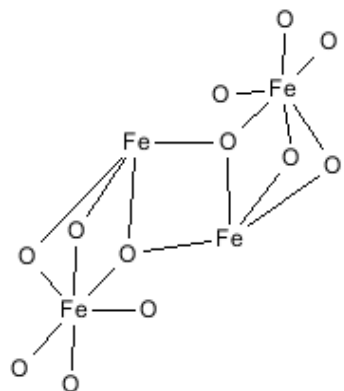
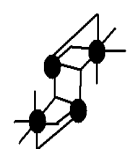


Figure 7.12 Morphological Images of Tribofilms Formed from Six Formulations. a)~f) 200X SEM Image of Each Antiwear Additive with/without PTFE, g) 2000X SEM Image of Region-1, h) 2000X SEM Image of Region-2, i) 5000X SEM Image of Region-1, j) 5000X SEM Image of Region-2, k) 3D Optic Profilometer Image of Region-1, and l) 3D Optic Profilometer Image of Region-2 at Tribofilm from F-ZDDP with PTFE.

Table 7.1 Inorganic Model Compounds for the Phenomenological Models

Name	Formula	Structure	Simplified Symbol
Zinc Oxide	ZnO		
Iron Oxide	Fe ₂ O ₃		

- In Absence of Irradiated PTFE

All phosphate species in tribofilms are pyro or orthophosphates from the a/c ratio analysis. Tribofilms are mainly comprised of iron phosphates and iron sulfides (including a pyrite) with some amount of iron sulfates. In case of ZDDP and F-ZDDP, small amount of zinc phosphates and zinc sulfides are also found. From O K edge XANES spectra, the existence of iron oxide in the tribofilm is clearly proved. The phenomenological model for tribofilms of ZDDP and F-ZDDP in absence of PTFE is drawn in figure 7.13 (Top) and one of ashless DDP-2 without PTFE is in figure 7.14(Top).

Antiwear Additives (in solution) → Decomposed antiwear additives (with thermal energy, shear force, and active surface energy) + O₂ (in oil) + Fe, FeO or Fe₂O₃ (present on the surface of steel coupons) → Iron Pyro- or Orthophosphate (with

Zinc Phosphate in presence of zinc cation) + Iron Sulfides (with Zinc Sulfide in presence of zinc cation) + Iron Sulfates + Fe, FeO, Fe₂O₃, or Fe₃O₄ (in Wear Debris and in the tribofilm)

- In Presence of Irradiated PTFE

When irradiated PTFEs are added in the formulations, sulfide species and phosphate compounds are increased while sulfate species are highly reduced. By oxygen K edge spectra, the decrease of iron oxides is obviously observed. The formation of PTFE layers or films is confirmed only at the top surface region using fluorine K edge XNAES spectra. PTFE thin layers protect the tribofilms from oxygen environment of outside. They hinder oxygen from reacting with sulfur and iron to be sulfate compounds and iron oxides which have abrasive characteristics. In addition, the lack of oxygen instigates the oxygen from oxides and sulfates to generate phosphate compounds and sulfide compounds by the reduction and the oxidation process. More sulfides and phosphates and less sulfates and oxides make better antiwear performance. Figure 7.13(Bottom) and 7.14(Bottom) show the phenomenological model of tribofilms formed from antiwear additives with irradiated PTFE powder.

Antiwear Additives (in solution) + PTFE → Decomposed antiwear additives (with thermal energy, shear force, and active surface energy) + O₂ (in oil) + Fe, FeO or Fe₂O₃ (present on the surface of steel coupons) + PTFE → PTFE thin layer (on the top surface of tribofilm) + Iron Pyro- or Orthophosphate ↑ (with Zinc Phosphate in presence of zinc cation) + Iron Sulfides ↑ (with Zinc Sulfide in presence of zinc cation) + Iron Sulfates ↓ + Fe, FeO, Fe₂O₃, or Fe₃O₄ ↓ (in Wear Debris and in the tribofilm)

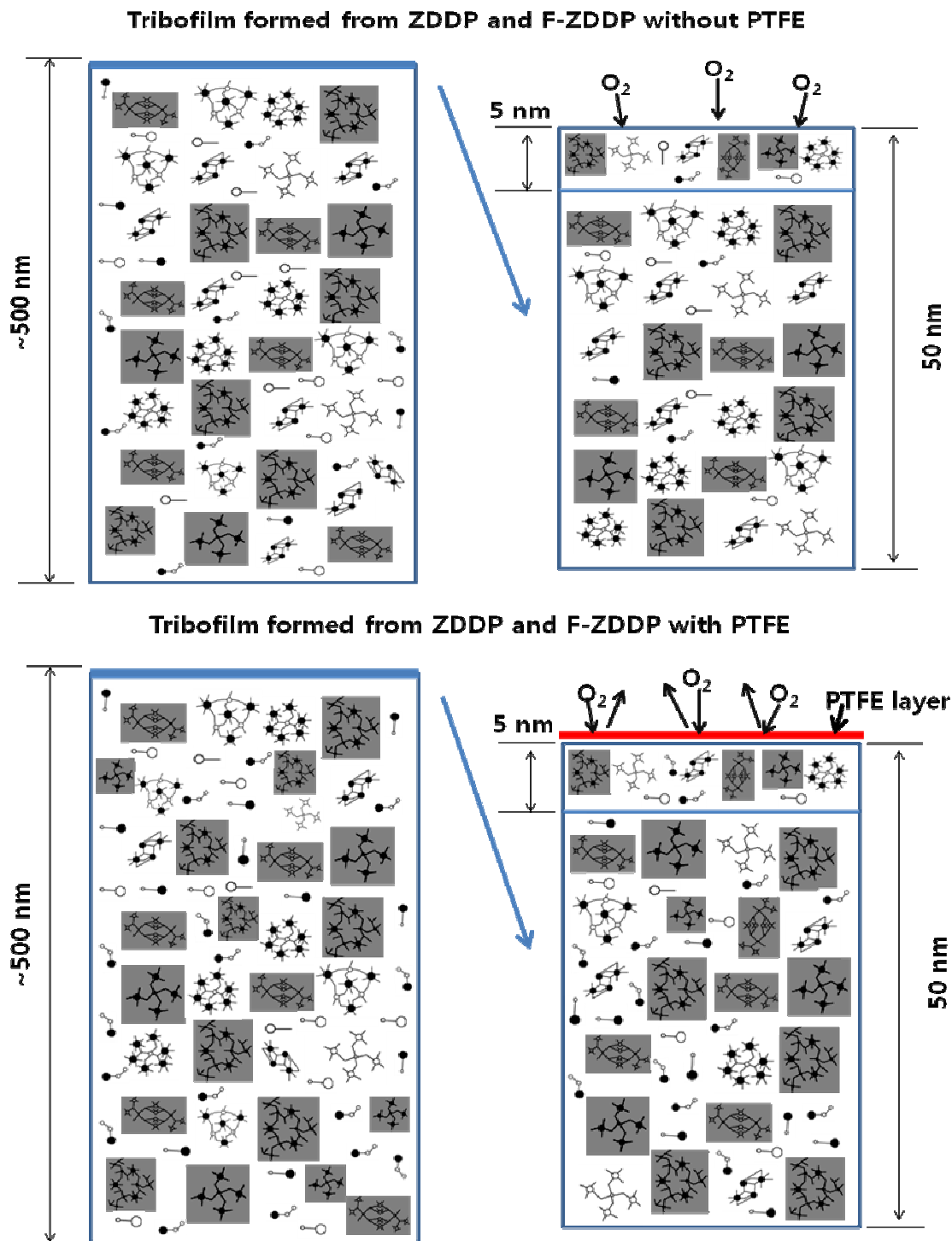


Figure 7.13 Phenomenological Model of Tribofilms Formed from ZDDP / F-ZDDP in Absence and in Presence of PTFE. Top Picture is Tribofilm of ZDDP/F-ZDDP itself and Bottom Picture is Tribofilm of ZDDP/F-ZDDP with PTFE.

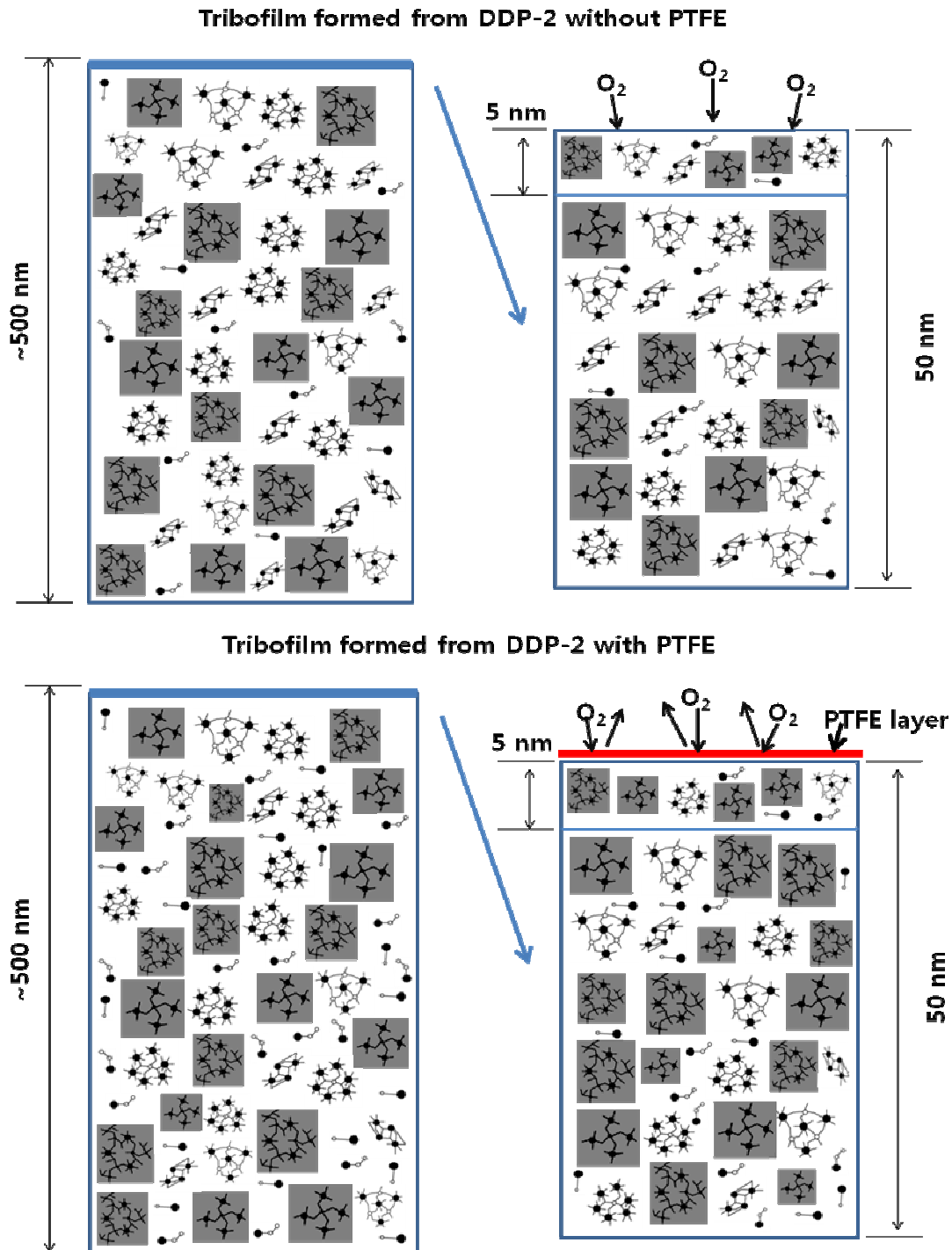


Figure 7.14 Phenomenological Model of Tribofilms Formed from DDP-2 in Absence and in Presence of PTFE. Top Picture is Tribofilm of DDP-2 itself and Bottom Picture is Tribofilm of DDP-2 with PTFE.

7.4 Conclusion

A detailed study was undertaken in order to investigate the effect between antiwear additives and irradiated PTFE powder. The synergetic effects have been observed at the tribological tests. For the chemical information, P, S, Zn, O, F XANES spectra have been analyzed. The results are summarized as follows.

1. Without functionalized PTFE, tribofilms consist of phosphate compounds and sulfur species of mixture of sulfates and sulfides. The percentage of sulfides at the sulfur compounds is high enough to protect the surface from wear. Oxides exist in the tribofilms.
2. With irradiate PTFE, PTFE layers of films form at the surface area, and then block the oxygen from reacting with metal cations and sulfur elements to create abrasive species. Amount of oxides and sulfates is reduced. Sulfides species are highly boosted and phosphates are also increased. This mechanism makes the better antiwear performance.
3. The presence of PTFE powder in the tribofilms doesn't make any topographical changes. However, it clearly makes the differentiation of chemical structure and composition at the tribofilm. The distinction of surface topography on the wear track is caused by the geometric and schematic variation of boundary contact condition.

CHAPTER 8

CONCLUSIONS

The objective of this research was to develop a fundamental understanding of how ashless compounds protect the tribological surfaces, how their films form, and the chemical properties and structure of films generated from ashless antiwear additives in comparison to ZDDP. In particular, this study has been divided into three parts in order to better understand the antiwear mechanisms of antiwear ashless additives. There are several major achievements in this dissertation.

In the first part of this research, the properties and mechanisms of tribofilms formed from ashless thiophosphates, amine phosphate, and triphenyl phosphorothionate antiwear additives under extreme pressure have been studied comparing with secondary ZDDP. The conclusions are following:

1. Ashless acidic dialkyl dithiophosphate (DDP-2 in this study) had better antiwear performance than ZDDP in the Ball on Cylinder tester under the extreme pressure conditions. The thickness of the ZDDP tribofilm is about 100 nm and it chemically consists of short chain pyrophosphates and iron sulfates with small amounts of iron and zinc sulfide. The surface region of this tribofilm is harder and stiffer while the bulk is softer and more compliant. This structure is the key to antiwear properties of ZDDP tribofilms since the harder crust protects the film from scratching and material removal while the compliant bulk dissipates the energy of possible impact on the tribofilm. On the other hand, the ashless acidic DDP-2 forms tribofilms which are significantly thicker (400 nm) and are similar to ZDDP tribofilms in chemical structure. The tribofilm of DDP

is uniform and compliant (compared to the steel substrate) through its thickness as thus protects the surface by protecting the surface by effectively covering the substrate.

2. Under extreme pressure conditions, ashless acidic DDP-2 has the best antiwear performance with the smallest wear volume and the lowest coefficient of friction among all ashless antiwear additives tested in this study. Ashless neutral dialkyl dithiophosphate (DDP-1) has the worst wear protection because it is thermally unstable and volatile under severe conditions. The amine phosphate (AP-1) also has poor wear protection because of the absence of sulfur which helps protect the extreme pressure condition. Therefore, the volatility and the composition of the antiwear additive, in particular sulfur, are important factors for the formation of stable tribofilm.
3. The three triphenyl compounds generally performed poorer than ashless dialkyl dithiophosphate (DDP-2). The triphenyl monothiophosphate groups tribologically performed in order of the facility of thermal decomposition (low flash point). The H-TPPT with the highest flash point had the worst friction and the poorest wear performance while the A-TPPT with the lowest flash point had the best friction and wear performance. Through the comparison of triphenyl mono-thiophosphates, the thermal stability, particularly decomposition temperature, is also confirmed as one of the critical factors for tribological performance.
4. From TEM study, wear debris generated from wear test are comprised of amorphous glass films and crystalline oxide particles. The number of crystalline oxide particles is the indication of antiwear performance. Wear debris resulting from poor wear protection have a lot of Fe_3O_4 which is the final stage of iron oxide. In case of better wear protection, some of intermediate stage of oxidation, FeO and Fe_2O_3 , are observed with major Fe_3O_4 .

In the second part of this research, in order to better understand the mechanism of tribofilm formation from metal free additives, fundamental issues related to thermal decomposition of ashless antiwear chemistries and their influence on thermal film formation have been studied.

1. In case of the additives which have a lot of metal elements like ZDDP, the decomposed P- and S- containing products react with the metal surface and their own metal cations forming thermal films. Sulfur species preferably deposit and diffuse into the thermal film near the steel substrate.
2. Ashless thiophosphates with low flash point like DDP-1 was decomposed very quickly with sulfur species forming very rapidly on the surface with sulfates dominating. Subsequently, phosphates are deposited and diffuse into the bulk of the thermal film. As the available active species are reduced over time the growth of the thermal film slows down and only oxidation and hydrolysis of thermal films were observed.
3. Ashless thiophosphates with high thermal stability decomposed slowly. At the initial stage many sulfur species deposited on the surface. However, with increasing time the phosphates are the dominant species in the thermal film. The reduction and reorganizations of sulfur species were carried out rather than hydrolysis. These additives have thick thermal films due to active film formation.
4. In case of ashless amine phosphate species, their initial growth rate is very fast, and then reduced quickly. Nonetheless, films are continuously formed on the surface during experiment time. Hence, amine phosphate compounds have high thickness of thermal films. Main component of thermal films formed from amine phosphates are iron phosphates and short and medium chain iron polyphosphates all through the thickness. In addition, iron nitrate and nitrite occurring from the oxidation of amine groups are observed in the thermal film.

The third part of this research, examined how ashless fluorinated compounds, in particular nano-scale PTFE powder, influence the formation and the characteristics of tribofilms and in proxy, the wear properties.

1. In absence of functionalized PTFE, tribofilms consist of similar amount of phosphates and sulfur species. The percentage of sulfides as sulfur compounds is high enough to protect the surface from wear. Some oxides exist in the tribofilms.
2. In presence of functionalized PTFE, thin film of PTFE form at the surface, and block the oxygen from reacting with other elements to create abrasive species. Amount of oxides and sulfates is reduced. Sulfides are highly increased and amount of phosphates are slightly increased. This phenomenon results in a synergetic effect between antiwear additives and functionalized PTFE powder causing in lower wear.

REFERENCES

- [1] D. Dowson, History of Tribology, Professional Engineering Publishing, London and Bury St Edmunds, UK, 1998.
- [2] G.W. Stachowiak, A.W. Batchelor, Engineering Tribology, Butterworth Heinemann, 2001.
- [3] Z. Zhang, E.S. Yamaguchi, M. Kasrai, G.M. Bancroft, Tribofilms generated from ZDDP and DDP on steel surfaces: Part 1. Growth, wear and morphology. Tribology Letters 19 (3) (2005) 211-220.
- [4] Z. Zhang, E.S. Yamaguchi, M. Kasrai, G.M. Bancroft, X. Liu, M.E. Fleet, Tribofilms generated from ZDDP and DDP on steel surfacUniversity Parkes: Part 2, chemistry. Tribology Letters 19 (3) (2005) 221-229.
- [5] S. Hironaka, Boundary Lubrication and Lubricants. Three Bond Technial News (1984) 1-6.
- [6] W. Castro, D.E. Weller, K. Cheenkachorn, J.M. Perez, The effect of chemical structure of basefluids on antiwear effectiveness of additives. Tribol. Int. 38 (2005) 321-326.
- [7] G.C. Smith, Surface analytical science and automotive lubrication. J. Phys. D 33 (2000) R187-R197.
- [8] E.P. Becker, Trends in tribological materials and engine technology. Tribol. Int. 37 (2004) 569-575.
- [9] J. Hu, X. Wei, G. Dai, Y. Fei, F. Xie, Z. Zong, Tribological behaviors and mechanism of sulfur- and phosphorus-free organic molybdate ester with zinc dialkyldithiophosphate. Tribology International 41 (2008) 549-555.
- [10] MECA, Clean Air Facts - The catalytic Converter: Technology for Clean Air. 2009 3.
- [11] Japan Automobile Manufacturers Association, DaimlerChrysler Corporation, Ford Motor Company and General Motors Corporation., ILSAC GF-4 Standard for passenger car engine oils. (2004).
- [12] www.Lubrizol.com. What is GF-5? 2009 (2008).
- [13] G.A. Mazzamaro, ILSAC GF-5 Development - Better Late Than Never.
- [14] W.P. Taylor, ASPA Spring 2009 Meeting Engine Oil Update GF-5. (2009).
- [15] M.A. Nicholls, T. Do, P.R. Norton, M. Kasrai, G.M. Bancroft, Review of the lubrication of metallic surfaces by zinc dialkyl-dithiophosphates. Tribol. Int. 38 (2005) 15-39.

- [16] J. Zhang, W. Liu, Q. Xue, Friction and wear behaviors of S-[2-S-(2-hydroxypropyl)benthiazole]dioctyldithiocarbamic acid ester as additive in liquid paraffin. *Wear* 224 (1999) 50-55.
- [17] B.A. Khorramian, G.R. Iyer, S. Kodali, P. Natarajan, R. Tupil, Review of antiwear additives for crank case oils. *Wear* (1993) 87-95.
- [18] H. Camenzind, D. Clark, M. Dratva, J. Fletschinger, M. Reyes-Gavilan, M. Ribeaud, P. Rohrbach, New ashless, hydrolytically stable and FZG active antiwear agent. *STLE conference* (2002) 1-33.
- [19] M. Ribeaud, Volatility of phosphorus-containing anti-wear agents for motor oils. *Lubr Sci* 18 (2006) 231-241.
- [20] A.M. Barnes, K.D. Bartle, V.R.A. Thibon, A review of zinc dialkyldithiophosphates (ZDDPS): Characterisation and role in the lubricating oil. *Tribol. Int.* 34 (2001) 389-395.
- [21] H. Spikes, The history and mechanisms of ZDDP. *Tribology Letters* 17 (2004) 469-489.
- [22] G. Pereira, A. Lachenwitzer, M. Kasrai, G.M. Bancroft, P.R. Norton, M. Abrecht, P.U.P.A. Gilbert, T. Regier, R.I.R. Blyth, J. Thompson, Chemical and mechanical analysis of tribofilms from fully formulated oils. Part 1 - Films on 52100 steel. *Tribology* 1 (2007) 48-61.
- [23] M.L.S. Fuller, M. Kasrai, G.M. Bancroft, K. Fyfe, K.H. Tan, Solution decomposition of zinc dialkyl dithiophosphate and its effect on antiwear and thermal film formation studied by X-ray absorption spectroscopy. *Tribol. Int.* 31 (1998) 627-644.
- [24] Z. Yin, M. Kasrai, M. Fuller, G.M. Bancroft, K. Fyfe, K.H. Tan, Application of soft X-ray absorption spectroscopy in chemical characterization of antiwear films generated by ZDDP part I: the effects of physical parameters. *Wear* 202 (1997) 172-191.
- [25] E.S. Ferrari, K.J. Roberts, M. Sansone, D. Adams, A multi-edge X-ray absorption spectroscopy study of the reactivity of zinc di-alkyl-di-thiophosphates anti-wear additives. 2. In situ studies of steel/oil interfaces. *Wear* 236 (1999) 259-275.
- [26] M.I. De Barros, J. Bouchet, I. Raoult, T. Le Mogne, J.M. Martin, M. Kasrai, Y. Yamada, Friction reduction by metal sulfides in boundary lubrication studied by XPS and XANES analyses. *Wear* 254 (2003) 863-870.
- [27] R. Mourhatch, P.B. Aswath, Nanoscale properties of tribofilms formed With zinc dialkyl dithiophosphate (ZDDP) under extreme pressure condition. *Journal of Nanoscience and Nanotechnology* 9 (2009) 2682-2691.
- [28] G. Pereira, D. Munoz-Paniagua, A. Lachenwitzer, M. Kasrai, P.R. Norton, T.W. Capehart, T.A. Perry, Y. Cheng, A variable temperature mechanical analysis of ZDDP-derived antiwear films formed on 52100 steel. *Wear* 262 (2007) 461-470.
- [29] J.M. Martin, C. Grossiord, T. Le Mogne, S. Bec, A. Tonck, The two-layer structure of Zndtp tribofilms, Part I: AES, XPS and XANES analyses. *Tribol. Int.* 34 (2001) 523-530.

- [30] M. Fuller, Z. Yin, M. Kasrai, G.M. Bancroft, E.S. Yamaguchi, P.R. Ryason, P.A. Willermet, K.H. Tan, Chemical characterization of tribochemical and thermal films generated from neutral and basic ZDDPs using X-ray absorption spectroscopy. *Tribol. Int.* 30 (1997) 305-315.
- [31] M.N. Najman, M. Kasrai, G.M. Bancroft, B.H. Frazer, G. De Stasio, The correlation of microchemical properties to antiwear (AW) performance in ashless thiophosphate oil additives. *Tribology Letters* 17 (2004) 811-822.
- [32] R.C. Coy, R.B. Jones, Thermal degradation and EP performance of zinc dithiophosphate additives in white oil. *ASLE transactions* 24 (1981) 77-90.
- [33] S. Palios, P.M. Cann, H.A. Spikes, Behaviour of PTFE suspensions in rolling/sliding contacts. *Tribology Series* 31 (1996) 141-152.
- [34] E.F. Rico, I. Minondo, D.G. Cuervo, The effectiveness of PTFE nanoparticle powder as an EP additive to mineral base oils. *Wear* 262 (2007) 1399-1406.
- [35] S.M. Hsu, Molecular basis of lubrication. *Tribol. Int.* 37 (2004) 553-559.
- [36] K. Parekh, Thesis, Interactions between antiwear agent and novel additive in engine oils. The University of Texas at Arlington (2005) 1-154.
- [37] D.M. Heyes, Molecular aspects of boundary lubrication. *Tribol. Int.* 29 (1996) 627-629.
- [38] S.M. Hsu, R. Munro, M.C. Shen, Wear in boundary lubrication. *Proc. Inst. Mech. Eng. Part J* 216 (2002) 427-441.
- [39] R. Mourhatch, Tribological and antiwear mechanisms of fluorinated zincdialkyl dithiophosphate in comparison to zinc diakyl dithiophosphate in engine oils. The University of Texas at Arlington (2008) 1-161.
- [40] A. Tonck, J.M. Martin, P. Kapsa, J.M. Georges, Boundary lubrication with anti-wear additives: study of interface film formation by electrical contact resistance. *Tribol. Int.* 12 (1979) 209-213.
- [41] K. Patel, Thesis, Development of low phosphorus engine oils. The University of Texas at Arlington (2004) 1-175.
- [42] P.A. Willermet, D.P. Dailey, R.O. Carter III, P.J. Schmitz, W. Zhu, Mechanism of formation of antiwear films from zinc dialkyldithiophosphates. *Tribology International* 28 (1995) 177-187.
- [43] H. Spedding, R.C. Watkins, Antiwear mechanism of ZDDP's - 1. *Tribol. Int.* 15 (1982) 9-12.
- [44] R.C. Watkins, Antiwear mechanism of ZDDP's - 2. *Tribol. Int.* 15 (1982) 13-15.
- [45] Z. Yin, M. Kasrai, G.M. Bancroft, K. Fyfe, M.L. Colaianni, K.H. Tan, Application of soft X-ray absorption spectroscopy in chemical characterization of antiwear films generated by ZDDP part II: the effect of detergents and dispersants. *Wear* 202 (1997) 192-201.

- [46] M.A. Nicholls, Micro-scale chemical and mechanical characterization of ZDDP antiwear films on steel and Al-Si alloys. The University of Western Ontario (2004) 1-208.
- [47] M.N. Najman, M. Kasrai, G.M. Bancroft, Chemistry of antiwear films from ashless thiophosphate oil additives. *Tribology Letters* 17 (2004) 217-229.
- [48] R. Mourhatch, K. Parekh, P.B. Aswath, A multi technique study of the tribological behavior and the tribofilms generated from fluorinated thiophosphate compounds in comparison to normal ZDDP. 2006 (2006).
- [49] M.N. Najman, M. Kasrai, G.M. Bancroft, A. Miller, Study of the chemistry of films generated from phosphate ester additives on 52100 steel using X-ray absorption spectroscopy. *Tribology Letters* 13 (2002) 209-218.
- [50] M.N. Najman, M. Kasrai, G.M. Bancroft, Investigating binary oil additive systems containing P and S using X-ray absorption near-edge structure spectroscopy. *Wear* 257 (2004) 32-40.
- [51] M. Najman, M. Kasrai, G. Michael Bancroft, R. Davidson, Combination of ashless antiwear additives with metallic detergents: Interactions with neutral and overbased calcium sulfonates. *Tribol. Int.* 39 (2006) 342-355.
- [52] M.N. Najman, M. Kasrai, G.M. Bancroft, X-ray absorption spectroscopy and atomic force microscopy of films generated from organosulfur extreme-pressure (EP) oil additives. *Tribology Letters* 14 (2003) 225-235.
- [53] E.S. Ferrari, D. Adams, A multi-edge X-ray absorption spectroscopy study of the reactivity of zinc di-alkyl-di-thiophosphates (ZDDPS) anti-wear additives: 1. An examination of representative model compounds. *Wear* 236 (1999) 246-258.
- [54] H. Fujita, H.A. Spikes, The formation of zinc dithiophosphate antiwear films. *Proc. Inst. Mech. Eng. Part J* 218 (2004) 265-277.
- [55] C.M. Taylor, Automobile engine tribology-design considerations for efficiency and durability. *Wear* 221 (1998) 1-8.
- [56] G.M. Bancroft, M. Kasrai, M. Fuller, Z. Yin, K. Fyfe, K.H. Tan, Mechanisms of tribochemical film formation: stability of tribo- and thermally-generated ZDDP films. *Trib. Lett.* 3 (1997) 47-47-51.
- [57] M.L. Suominen Fuller, L. Rodriguez Fernandez, G.R. Massoumi, W.N. Lennard, M. Kasrai, G.M. Bancroft, The use of X-ray absorption spectroscopy for monitoring the thickness of antiwear films from ZDDP. *Trib. Lett.* 8 (2000) 187-187-192.
- [58] S. Bec, A. Tonck, J.M. Georges, R.C. Coy, J.C. Bell, G.W. Roper, Relationship between mechanical properties and structures of zinc dithiophosphate anti-wear films. Volume 455 (1999) 4181-4181 - 4203.
- [59] Y. Li, Nanoscale studies of the prevention and measurement of wear in automobile engines. The University of Western Ontario (2008) 1-241.

- [60] J.E. Penner-Hahn, X-ray Absorption Spectroscopy, in: Anonymous Comprehensive Coordination Chemistry, Elsevier Science, 2003, pp. 159-186.
- [61] F. Jalilehvand, X-ray Absorption Spectroscopy (XAS).
- [62] www.canadianlight.com, X-ray absorption spectroscopy.
- [63] M. Newville, Fundamentals of XAFS. (2008).
- [64] www.wisconsin-med.edu, The Synchrotron Radiation Center (SRC).
- [65] www.canadianlight.com, The Canadian Light Source (CLS).
- [66] K. Varlot, M. Kasrai, G.M. Bancroft, E.S. Yamaguchi, P.R. Ryason, J. Igarashi, X-ray absorption study of antiwear films generated from ZDDP and borate micelles. *Wear* 249 (2001) 1029-1035.
- [67] M. Kasrai, M. Fuller, Z. Scaini, Z. Yin, R.W. Brunner, G.M. Bancroft, M.E. Fleet, K. Fyfe, K.H. Tan, Study of tribochemical film formation using x-ray absorption and photoelectron spectroscopies. *Lubricants and lubrication* (1995) 659-669.
- [68] Y. Li, G. Pereira, A. Lachenwitzer, M. Kasrai, P.R. Norton, Studies on ZDDP Thermal Film Formation by XANES Spectroscopy, Atomic Force Microscopy, FIB/SEM and ³¹P NMR. *Tribology Letters* 29 (2008) 11-22.
- [69] S. Bec, K. Demmou, J. Loubet, S. Pavan, C. Minfray, J. Martin, Mechanical properties of ZnDTP tribofilms measured by nanoindentation at controlled temperature. (2005) 823-824.
- [70] K. Komvopoulos, E.S. Yamaguchi, V. Do, P.R. Ryason, Nanomechanical and nanotribological properties of an antiwear tribofilm produced from phosphorus-containing additives on boundary-lubricated steel surfaces. (2004; 2004) 1631-1636.
- [71] W.C. Oliver, G.M. Pharr, Measurement of hardness and elastic modulus by instrumented indentation: Advances in understanding and refinements to methodology. *J. Mater. Res.* 19 (2004) 3-20.
- [72] W.C. Oliver, G.M. Pharr, Improved technique for determining hardness and elastic modulus using load and displacement sensing indentation experiments. *J. Mater. Res.* 7 (1992) 1564-1580.
- [73] User Manual for Ubi 1, Hysitron Incorporated.
- [74] O.L. Warren, J.F. Graham, P.R. Norton, Nanomechanical properties of films derived from zinc dialkyldithiophosphate. *Tribology Letters* 4 (1998) 189-198.
- [75] M.A. Nicholls, P.R. Norton, G.M. Bancroft, M. Kasrai, T. Do, B.H. Frazer, G. De Stasio, Nanometer Scale Chemomechanical Characterization of Antiwear Films. *Tribol. Lett.* 17 (2004) 205-205-216.

- [76] R. Mourhatch, P.B. Aswath, Mechanism of Boundary Lubrication with Zinc Dialkyl Dithiophosphate. Under Review; San Antonio, TX, USA (2006; 2006) IJTC-12054.
- [77] Y. Li, G. Pereira, M. Kasrai, P.R. Norton, The effect of steel hardness on the performance of ZDDP antiwear films: A multi-technique approach. *Tribology Letters* 29 (2008) 201-211.
- [78] M. Aktary, M.T. McDermott, G.A. McAlpine, Morphology and Nanomechanical Properties of ZDDP Antiwear Films as a Function of Tribological Contact. *Tribol. Lett.* 12 (2002) 155-155-162.
- [79] J.L. Reyes-Gavilan, P. Odorisio, A review of the mechanisms of action of antioxidants, metal deactivators, and corrosion inhibitors. *NLGI Spokesman* 64 (2001) 22-33.
- [80] W. Hua, L. Jing, Y. Hongling, Z. Xiangqiong, L. Lingbo, R. Tianhui, The tribological behavior of diester-containing polysulfides as additives in mineral oil. *Tribology International* 40 (2007) 1246-1252.
- [81] Y. Kim, K. Chung, N. Kim, D. Hwang, W. Cho, Synergetic lubricating effect of several ashless dithiocarbamates with mo-donor additives. *Tribology International* 40 (2007) 397-404.
- [82] V. Kroger, U. Lassi, K. Kynkaanniemi, A. Suopanki, R.L. Keiski, Methodology development for laboratory-scale exhaust gas catalyst studies on phosphorus poisoning. *Chem. Eng. J.* 120 (2006) 113-113-118.
- [83] Z. He, J. Lu, X. Zeng, H. Shao, T. Ren, W. Liu, Study of the tribological behaviors of S, P-containing triazine derivatives as additives in rapeseed oil. *Wear* 257 (2004) 389-394.
- [84] A.E. Jimenez, M.D. Bermudez, P. Iglesias, F.J. Carrion, G. Martinez-Nicolas, 1-N-alkyl-3-methylimidazolium ionic liquids as neat lubricants and lubricant additives in steel-aluminum contacts. *Wear* 260 (2006) 766-782.
- [85] X. Zeng, J. Li, X. Wu, T. Ren, W. Liu, The tribological behaviors of hydroxylcontaing dithiocarbamate-triazine derivatives as addtives in rapeseed oil. *Tribology International* 40 (2007) 560-566.
- [86] X. Zeng, H. Shao, W. Rao, Z. He, T. Ren, Tribological study of trioctylthiotriazine derivative as lubricating oil addtieve. *Wear* 258 (2005) 800-805.
- [87] Y. Gao, Z. Wu, Z. Zhang, Q. Xue, Study on tribological properties of 2,5-dialkoxymethylthio-1,3,4-thiadiazoles. *Wear* 222 (1998) 129-134.
- [88] W. Liu, C. Ye, Z. Zhang, L. Yu, Relationahip between molecular structures adn tribological properties of phosphazene lubricants. *Wear* 252 (2002) 394-400.
- [89] S.H. Roby, J.A. Supp, Effect of ashless antiwear agents on valve train wear and sludge formation in gasoline engine testing. *Lubrication Engineering* 53 (1997) 17-22.
- [90] A.B. Vipper, V.L. Lashkhi, P.S. Belov, V.A. Parfenova, I.V. Blokhina, Antifriction and antiwear efficiency of ashless thiophosphates and dithiophosphates. *Chem. Technol. Fuels Oils* 19 (1983) 136-139.

- [91] R. Sarin, D.K. Tuli, S. Prakash, K.K. Swami, A.K. Bhatnagar, Phosphorus components in lubricants: Structure-activity relationship. *Phosphorus, Sulfur and Silicon* 177 (2002) 1763-1766.
- [92] C. Kajdas, M.J. Furey, R. Kempinski, J. Valentino, New condensation-type monomer combinations as ashless antiwear compositions. *Wear* 249 (2001) 235-239.
- [93] R. Kapadia, R. Glyde, Y. Wu, In situ observation of phosphorous and non-phosphorous antiwear films using a mini traction machine with spacer layer image mapping. *Tribol. Int.* 40 (2007) 1667-1679.
- [94] K. Topolovec-Miklozic, T.R. Forbus, H.A. Spikes, Film thickness and roughness of ZDDP antiwear films. *Tribology Letters* 26 (2007) 161-171.
- [95] C. Minfray, J.M. Martin, C. Esnouf, T. Le Mogne, R. Kersting, B. Hagenhoff, A multi-technique approach of tribofilm characterisation. 447-448 (2004) 272-277.
- [96] A. Somayaji, R. Mourhatch, P.B. Aswath, Nanoscale mechanical properties of in-situ tribofilms generated from ZDDP and F-ZDDP with and without antioxidants. *Journal of Nanoscience and Nanotechnology* 7 (2007) 4378-4390.
- [97] Y. Li, G. Pereira, M. Kasrai, P.R. Norton, Studies on ZDDP anti-wear films formed under different conditions by XANES spectroscopy, atomic force microscopy and ³¹P NMR. *Tribology Letters* 28 (2007) 319-328.
- [98] Y. Li, G. Pereira, A. Lachenwitzer, M. Kasrai, P.R. Norton, X-ray absorption spectroscopy and morphology study on antiwear films derived from ZDDP under different sliding frequencies. *Tribology Letters* 27 (2007) 245-253.
- [99] A. Somayaji, P.B. Aswath, The role of antioxidants on oxidation stability of oils with F-ZDDP and ZDDP and chemical structure of tribofilms using XANES. *Tribology Transactions* 52 (2009) 511-525.
- [100] Y. Li, G. Pereira, A. Lachenwitzer, M. Kasrai, P.R. Norton, X-ray absorption spectroscopy and morphology study on antiwear films derived from ZDDP under different sliding frequencies. *Tribology Letters* 27 (2007) 245-253.
- [101] M. Kasrai, M.S. Fuller, G.M. Bancroft, E.S. Yamaguchi, P.R. Ryason, X-ray absorption study of the effect of calcium sulfonate on antiwear film formation generated from neutral and basic ZDDPs: Part 1 - Phosphorus species. *Tribology Transactions* 46 (2003) 534-542.
- [102] Z. Zhang, E.S. Yamaguchi, M. Kasrai, G.M. Bancroft, X. Liu, M.E. Fleet, Tribofilms generated from ZDDP and DDP on steel surfaces: Part 2. chemistry. (2005; 2005) 619-620.
- [103] M. Elgin, A. Rossi, N.D. Spencer, X-ray Photoelectron Spectroscopy Analysis of Tribostressed Samples in the Presence of ZnDTP: A Combinatorial Approach. *Trib. Lett.* 15 (2003) 199-199-209.
- [104] M. Kasrai, M.S. Fuller, G.M. Bancroft, E.S. Yamaguchi, P.R. Ryason, X-ray absorption study of the effect of calcium sulfonate on antiwear film formation generated from neutral and basic ZDDPs: Part 2 - Sulfur species. *Tribology Transactions* 46 (2003) 543-549.

- [105] M.Z. Huq, P.B. Aswath, R.L. Elsenbaumer, TEM studies of anti-wear films/wear particles generated under boundary conditions lubrication. *Tribol. Int.* 39 (2007) 111-111-116.
- [106] R.W.G. Wyckoff, *Crystal Structures*, 2nd ed. Robert, E. Krieger Publishing Co. Florida (1982) 85.
- [107] R.L. Blake, T. Zoltai, R.E. Hessevick, L.W. Finger, Refinement of hematite crystal structure. *American Mineralogist* 51 (1966) 123-129.
- [108] R. Heuberger, A. Rossi, N.D. Spencer, Reactivity of alkylated phosphorothionates with steel: a tribological and surface-analytical study. *Lubrication Science* 20 (2008) 79-102.
- [109] M.Z. Huq, P.B. Aswath, R.L. Elsenbaumer, TEM studies of anti-wear films/wear particles generated under boundary conditions lubrication. *Tribol. Int.* 40 (2007) 111-116.
- [110] J.M. Martin, J.L. Mansot, I. Berbezier, H. Dexpert, Nature and origin of wear particles from boundary lubrication with a zinc dialkyl dithiophosphate. *Wear* 93 (1984) 117-126.
- [111] J.M. Martin, Antiwear mechanisms of zinc dithiophosphate: a chemical hardness approach. *Tribology Letters* 6 (1999) 1-8.
- [112] Ciba Specialty Chemicals, Ciba IRGALUBE 63 MSDS and Specification. (2005).
- [113] Ciba Specialty Chemicals, Ciba IRGALUBE 353 MSDS and Specification. (2005).
- [114] Ciba Specialty Chemicals, Ciba IRGALUBE TPPT MSDS and Specification. (2005).
- [115] Ciba Specialty Chemicals, Ciba IRGALUBE 232 MSDS and Specification. (2005).
- [116] Ciba Specialty Chemicals, Ciba IRGALUBE 211 MSDS and Specification. (2005).
- [117] Ciba Specialty Chemicals, Ciba IRGALUBE 349 MSDS and Specification. (1997).
- [118] W.D. Phillips, Ashless phosphorus-containing lubricating oil additives, in: *Anonymous Lubricant Additives: Chemistry and Applications*, Dekker Media, 2003, pp. 45-111.
- [119] X. Fu, W. Liu, Q. Xue, The application research on series of ashless P-containing EP and AW additives. *Ind Lubr Tribol* 57 (2005) 80-83.
- [120] R. Schumacher, D. Landolt, H.J. Mathieu, H. Zinke, Surface reaction behavior of isogeometrical phosphorus compounds. *ASLE transactions* 26 (1983) 94-101.
- [121] R. Schumacher, H. Zinke, Tribofragmentation and antiwear behaviour of isogeometric phosphorus compounds. *Tribol. Int.* 30 (1997) 199-208.
- [122] Ciba Specialty Chemicals, Propanoic acid, 3-[[bis(2-methylpropoxy)phosphinothioyl]thio]-2-methyl-. STD/1013 (2002).

- [123] M. Fletschinger, P. Rohrbach, P.C. Hamblin, D. Clark, M. Ribeaud, Lubricant Compositions Comprising Thiophosphoric Acid Esters and Dithiophosphoric Acid Esters. (2003).
- [124] R.T. Vanderbilt, VANLUBE 727 MSDS and Specification. (2004).
- [125] R.T. Vanderbilt, VANLUBE 7611M MSDS and Specification. (2002).
- [126] M. Kasrai, W.N. Lennard, R.W. Brunner, G.M. Bancroft, J.A. Bardwell, K.H. Tan, Sampling depth of total electron and fluorescence measurements in Si L- and K-edge absorption spectroscopy. *Appl. Surf. Sci.* 99 (1996) 303-312.
- [127] D.A. Totir, M.R. Antonio, P. Schilling, R. Tittsworth, D.A. Scherson, In situ sulfur K-edge X-ray absorption near edge structure of an embedded pyrite particle electrode in a non-aqueous Li+-based electrolyte solution. *Electrochim. Acta* 47 (2002) 3195-3200.
- [128] Z. Yin, M. Kasrai, G.M. Bancroft, K.H. Tan, X-ray-absorption spectroscopic studies of sodium polyphosphate glasses. *Physical Review B: Condensed Matter* 51 (1995) 742-742.
- [129] D.G.L. Sutherland, M. Kasrai, G.M. Bancroft, Z.F. Liu, K.H. Tan, Si L edge and K edge x-ray absorption near-edge spectroscopy of gas-phase $\text{Si}(\text{CH}_3)_x(\text{OCH}_3)_{4-x}$: Models for solid-state analogs. *Physical Review B: Condensed Matter* 48 (1993) 14989-15001.
- [130] M. Nicholls, M.N. Najman, Z. Zhang, M. Kasrai, P.R. Norton, P.U.P.A. Gilbert, The contribution of XANES spectroscopy to tribology. *Canadian Journal of Chemistry* 85 (2007) 816-830.
- [131] M. Kasrai, J.R. Brown, G.M. Bancroft, Z. Yin, K.H. Tan, Sulfur characterization in coal from X-ray absorption near edge spectroscopy. *International Journal of Coal Geology* 32 (1996) 107-135.
- [132] M. Xu, D. Li, The properties of various antiwear and extreme-pressure additives in pentaerythritol ester. *J. Synth. Lubr.* 20 (2003) 25-37.
- [133] Z. Zhang, M. Najman, M. Kasrai, G.M. Bancroft, E.S. Yamaguchi, Study of interaction of EP and AW additives with dispersants using XANES. (2004) 341-351.
- [134] I. Minami, S. Kikuta, H. Okabe, Anti-wear and friction reducing additives composed of ortho-phenylene phosphate-amine salts for polyether type base stocks. *Tribol. Int.* 31 (1998) 305-312.
- [135] J.M. Hall, H. Ravner, Amine phosphates as antiwear additives in neopentyl polyol esters. *ASLE Transactions* 16 (1973) 291-296.
- [136] Y. Wan, W. Liu, T. Ren, Q. Xue, Effect of amines on the antiwear properties of P-containing compounds as oil additives. *Lubr Sci* 6 (1994) 283-290.
- [137] R.T. Vanderbilt, VANLUBE 672 MSDS and Specification. (2006).

- [138] R.T. Vanderbilt, VANLUBE 9123 MSDS and Specification. (2003).
- [139] B. Munoz, A. Margida, T. Karol, Organomolybdenum containing magneto rheological fluid. (1996).
- [140] M. Wisotsky, M. Beltzer, T. Ashcraft, P.J. Berlowitz, Rust resistant turbo oils containing monobasic amino phosphates and dicarboxylic acids. (1998).
- [141] J.A. Rodriguez, T. Jirsak, J. Dvorak, S. Sambasivan, D. Fischer, Reaction of NO₂ with Zn and ZnO: Photoemission, XANES, and Density Functional Studies on the Formation of NO₃. *J Phys Chem B* 104 (2000) 319-328.
- [142] B. Wilson, Slick 50 - A proven PTFE-based boundary lubricant for engines. *Ind Lubr Tribol* 47 (1995) 6-8.
- [143] B. Willson, PTFE as a friction modifier in engine oil. *Ind Lubr Tribol* 44 (1992) 3-5.
- [144] N.V. Klaas, K. Marcus, C. Kellock, The tribological behaviour of glass filled polytetrafluoroethylene. *Tribol. Int.* 38 (2005) 824-833.
- [145] DuPont, Dupont Zonyl - Fluorichemical Intermediates. (2001) 1-16.
- [146] X. Lu, K.C. Wong, P.C. Wong, K.A.R. Mitchell, J. Cotter, D.T. Eadie, Surface characterization of polytetrafluoroethylene (PTFE) transfer films during rolling-sliding tribology tests using X-ray photoelectron spectroscopy. *Wear* 261 (2006) 1155-1162.
- [147] B. Winfield, Oil additives: the pitch is slick, but do they work? *Letter to Car and Driver* (1994) 23.
- [148] T. Kobayashi, M. Iwaki, T. Ubagai, K. Terashima, Formation of carbon needles from fluoropolymer by ion irradiation followed by defluorination. *206* (2003) 184-188.
- [149] K. Parekh, X. Chen, P.B. Aswath, Synthesis of fluorinated ZDDP compounds. *Tribology Letters* 34 (2009) 141-153.

BIOGRAPHICAL INFORMATION

BoHoon Kim received the B.Eng. in Metallurgical Engineering from Korea University, Seoul, South Korea in 2000. He was honorably discharged on expiration of term of mandatory Korean military service for 30 months in 1997 as an air force. During 2000~2003, he was a semiconductor engineer in Samsung Electronics Co. Ltd, Kiheung, South Korea, where he worked on CVD Processing and Semiconductor Manufacturing. He received the M.S. degree in Finance from the University of Wyoming, Wyoming, U.S.A. in 2005. He has pursued a Ph.D. degree in Materials Science and Engineering Department at the University of Texas at Arlington since 2005 under the supervision of Dr. Pranesh B. Aswath. During his doctoral program at the UTA, he has served and volunteered for community outreach organizations such as American Society of Materials (ASM) International North Texas Student Chapter, Korean Scientists and Engineers Association (KSEA) North Texas Chapter, and UTA-Korean Student Association (KSA) as the president, the vice-president, and also a member. In 2007, he synchronously received three outstanding scholarships: the Korean Honor Scholarship, the KUSCO-KSEA Scholarship, and the ASM International Scholarship. In addition, he was awarded the Best Outstanding Student Organization Award from the UTA as the president of UTA Korean Student Association (KSA). He is the member of KSEA, ASM, ΦΚΦ (Phi Kappa Phi), ASE, STLE, and AOCS. His research interests include the mechanism and performance of ashless anti-wear additives in engine oil and the characterization of tribological film on the surface of engine to develop improved engine oil.